UNIVERSITÄT BONN
Physikalisches Institut

Dijets in Diffractive Photoproduction measured with the ZEUS Experiment

by
Roger Renner

The diffractive photoproduction of dijets in electron-proton scattering has been studied using 77.1 pb^{-1} of data taken with the ZEUS detector at HERA. The measurements have been made at a centre-of-mass energy $\sqrt{s} = 318\,\text{GeV}$ in the kinematic range $0.2 < y < 0.85$ and $x_{I\!P} < 0.025$, where y is the inelasticity and $x_{I\!P}$ is the fraction of the proton momentum taken by the diffractive exchange. The jets have been reconstructed using the k_T algorithm. The two jets with the highest transversal energy have been required to satisfy $E_T > 7.5$ and $6.5\,\text{GeV}$, respectively, and to be in the pseudorapidity range $-1.5 < \eta < 1.5$. Differential cross sections have been measured and been confronted with the predictions from leading order Monte Carlo simulations and next-to-leading order QCD calculations.

Post address:
Nußallee 12
53115 Bonn
Germany

BONN-IR-2006-13
Bonn University
Oktober 2006
ISSN-0172-8741

UNIVERSITÄT BONN
Physikalisches Institut

Dijets in Diffractive Photoproduction measured with the ZEUS Experiment

von
Roger Renner

Dieser Forschungsbericht wurde als Dissertation von der Mathematisch-Naturwissenschaftlichen Fakultät der Universität Bonn angenommen.

Referent:	Prof. Dr. E. Paul
Korreferent:	Prof. Dr. U. Thoma
Tag der Promotion:	Fr., 13. Oktober 2006

Diese Dissertation ist auf dem Hochschulschriftenserver der ULB Bonn `http://hss.ulb.uni-bonn.de/diss_online` elektronisch publiziert.

Erscheinungsjahr: 2007

Contents

Introduction

The final state in deep inelastic electron-proton scattering contains a scattered electron or neutrino and a parton – a quark or gluon – scattered off the proton. The proton remnant as well as the parton carry colour, and as they depart from each other, the strength of the strong force increases until the potential energy stored in the field between them is sufficient to produce secondary gluons or quark-antiquark pairs. Once the available energy of the initial process is split up among partons, the strong force becomes effective and the partons hadronise in colourless objects, e.g. baryons and mesons. In general these particles are bundled in phase space as so-called jets, whose directions and energies approximately represent those of the initial partons. Due to the strong force, the angular range between the jet originating from the proton remnant and the struck quark *(current jet)* is filled with soft particles, and the existence of a significant gap is exponentially suppressed.
However, this naïve picture fails to explain a considerable fraction of events in deep inelastic scattering (DIS) which display no hadronic activity between the proton remnant and the current jets. Such a topology indicates that some sort of colourless particle, denoted as Pomeron ($I\!P$), has been scattered off the proton.
This phenomenon, known as diffractive exchange, was found in a variety of scattering processes. In this analysis, diffraction in hard photoproduction (PHP) of dijets has been studied on data taken with the ZEUS detector at the electron-proton collider HERA. In PHP a quasi-real photon is emitted by the initial electron, i.e. the squared four-momentum transfer Q^2 is small, $Q^2 \lesssim 1\,\mathrm{GeV}^2$, and interacts with a Pomeron, the hypothetical particle of the diffractive exchange. The hard scale is provided by requiring two current jets with transverse energies $E_T^{jet\,1(2)} \geq 7.5(6.5)\,\mathrm{GeV}$.

The outline of the thesis is as follows: In Chapter 1, a brief introduction to the theory of diffraction is given. The experimental setup, i.e. the HERA collider, the ZEUS detector and the procedure of data acquisition, is described in Chapter 2. Information on the data sample and the Monte Carlo (MC) simulations can be found in Chapters 3 and 4, respectively. The reconstruction of kinematic variables and the selection cuts are described in Chapters 5 and 6. Contamination of the data sample with different sources of background is considered in Chapter 7. The tuning of the MC sample to the background-reduced data sample is described in Chapter 8. Chapter 9 contains details on subsequent data corrections and control plots, acceptances and efficiencies for a set of variables. Cross sections for these variables are presented and compared with leading order (LO) MC simulations in Chapter 10 and with next-to-leading order (NLO) QCD predictions in Chapter 12. The results of systematic checks are summarised in Chapter 11. Finally, conclusions from this analysis are drawn in Chapter 13.

Chapter 1

Theoretical framework

In this introduction to diffraction, a historical path is followed as far as appropriate. Motivated by diffraction in optics (Sec. 1.1), the main features of diffraction in particle physics (Sec. 1.2) – in particular the production of diffractive dijets (Sec. 1.3) – are sketched before kinematic variables corresponding to these processes are introduced (Sec. 1.4). Early studies on diffraction were limited to soft interactions (Sec. 1.5), and could be described by Regge theory (Sec. 1.6). Studies on hard diffraction became possible as colliders with higher centre-of-mass energy became available, and can be described by means of perturbative quantum chromodynamics (pQCD) (Sec 1.7). Cross sections of hard diffraction in DIS are expected to factorise into universal diffractive parton distribution functions (dPDFs) of the proton convoluted with cross sections of a partonic subprocess (Sec. 1.7.1). Recent results indicate the possibility of factorisation breaking for hard diffraction in hadron-hadron scattering (Sec. 1.7.2) and hence suggest implications for lepton-hadron scattering in the kinematic range of this analysis.

1.1 Diffraction in optics

The denotation of diffraction in particle physics is motivated by features it has in common with the phenomenon of diffraction in optics. As first noted by Francesco Maria Grimaldi [1] in the 17th century, *"light does not only propagate directly, reflectively and refractively, but also in a fourth manner, denoted as diffractively"*[1]. A plane light wave that passes a hole

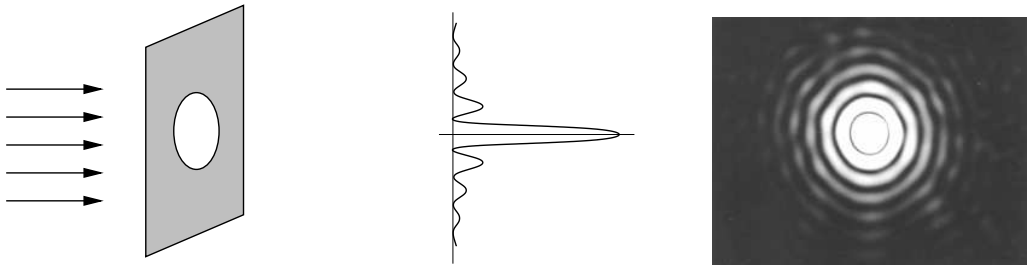

Figure 1.1: A plane light wave that passes a hole *(left)* becomes diffracted, hence leading to a pattern of constructive and destructive interference on a screen behind the hole *(middle, right).*

[1] *"Lumen propagatur seu diffunditur non solum directe, refracte ac reflexe etiam quodam quarto modo diffracte."*

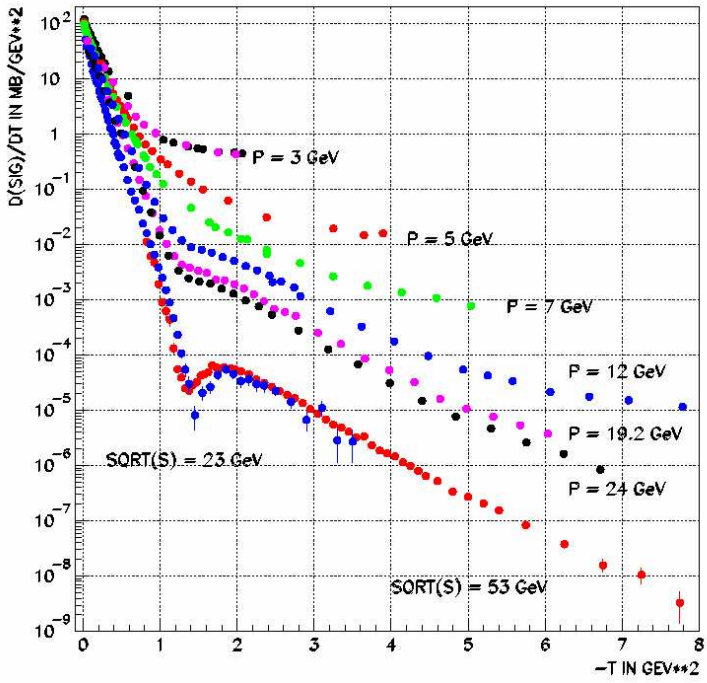

Figure 1.2: Cross sections for elastic p-scattering vs. the negative squared four-momentum transfer t of the proton for different p-momenta in fixed-target experiments ($P \leq$ 24GeV) and centre-of-mass energies $\sqrt{s}$ in colliding-beam experiments; a minimum followed by a second maximum is observed for $\sqrt{s} \geq 23\,\text{GeV}$ – taken from [2].

in an opaque screen (Fig. 1.1a), propagates non-linearly behind it; according to Huygens principle, each point of the light wave acts as a source of a spherical wave. The superimposition of these spherical waves leads to constructive and destructive interference. On a screen sufficiently far behind the hole, a central maximum is observed, surrounded by additional smaller maxima (Fig. 1.1b). The intensity of the maxima is found to decrease exponentially with $e^{-(R_0/2)^2\theta}$, where θ is the scattering angle and R_0 the radius of the hole.

1.2 Diffraction in particle physics

Early results on elastic proton-proton (pp) scattering (Fig. 1.2) revealed features which led to the connotation with diffraction in optics [3]:

- the total cross section σ_{tot} rises slowly with increasing centre-of-mass energy $\sqrt{s}$;
- the cross section falls exponentially with the squared four-momentum transfer $|t|$ between the incoming and outgoing proton: $d\sigma/dt \propto e^{-b|t|}$.
  Here t is related to the scattering polar angle θ in optical diffraction and $b = R_0^2/4$ can be interpreted as a constant associated with the radius of the interaction;
- with increasing t, a second diffractive maximum is observed for sufficiently large $\sqrt{s}$.

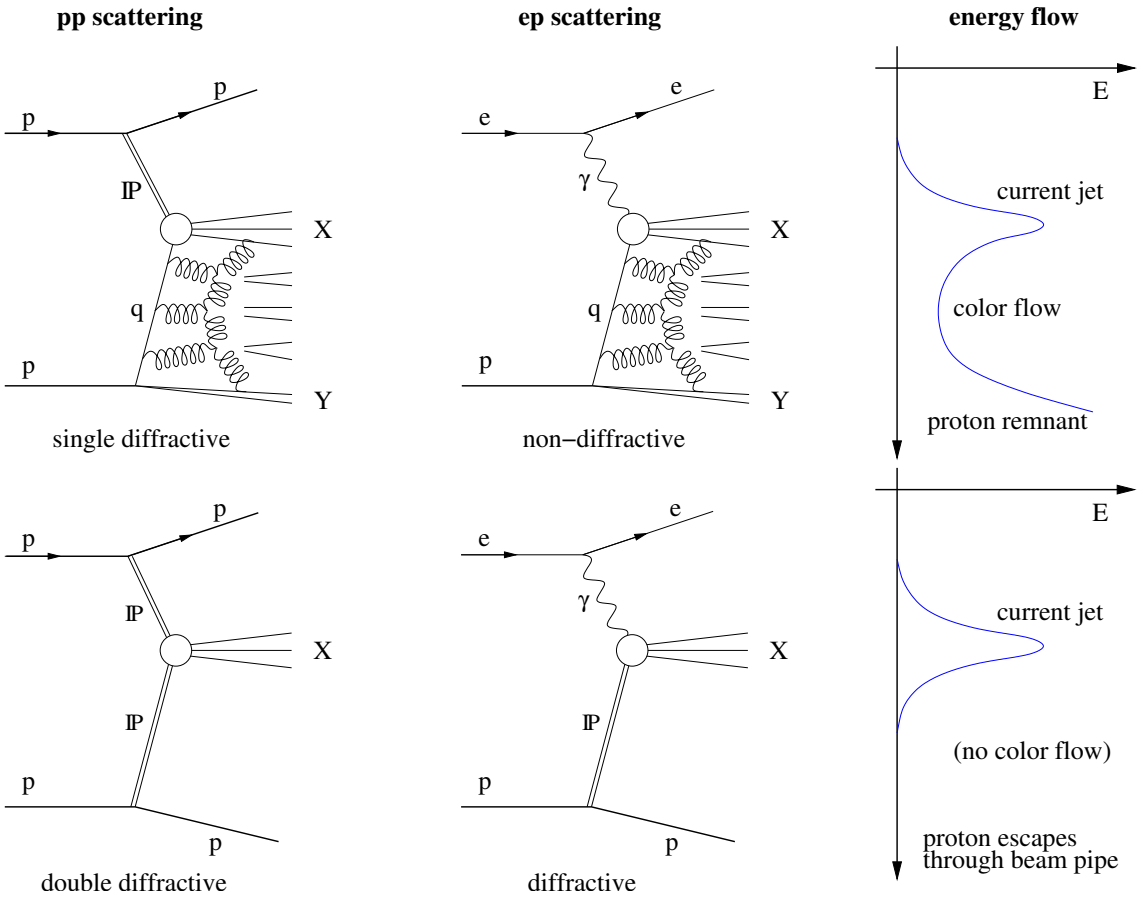

Figure 1.3: Single and double diffractive process in *pp* scattering *(left column)*, non-diffractive and diffractive scattering in *ep* collisions *(middle)*, and angular distribution of energy flow *(right)*.

In elastic *pp* scattering the initial and final state are identical: $pp \to pp$. In particular, no quantum numbers except angular momentum are exchanged. Diffractive *pp* scattering refers to processes where at least one proton stays intact and a hadronic system X is observed in the final state: $pp \to ppX$ or $pp \to pYX$ (Fig. 1.3, left column). In terms of Regge phenomenology (Sec. 1.6), this is explained by the exchange of a Pomeron $I\!P$, a hypothetical particle with zero quantum numbers.
In *ep* scattering with a hadronic system X in the final state, two distinct processes are possible (Fig. 1.3, middle column). In both cases the scattering process is moderated by a virtual photon γ (or by a Z^0) emitted from the electron. The upper graph in the middle column of Fig. 1.3 refers to inelastic scattering $ep \to eYX$, whereas the lower graph depicts diffractive scattering $ep \to epX$.
Such diffractive events account for $\sim 10\%$ of *ep*-scatterings at HERA energies [4, 5]. In the ZEUS-experiment (Sec. 2.3) this class of events is observed by a lack of particles in proton beam direction: Figure 1.4 shows the event distribution of $\eta^{\max}$, defined as the pseudorapidity (Sec. 1.4) of the particle closest to the proton beam direction. The distribution of ZEUS data is compared to Monte Carlo simulations (Sec. 4.1), that represent the final state configurations described in Fig. 1.3. Diffractive events at ZEUS dominate at values of $\eta^{\max} \lesssim 2.5$.

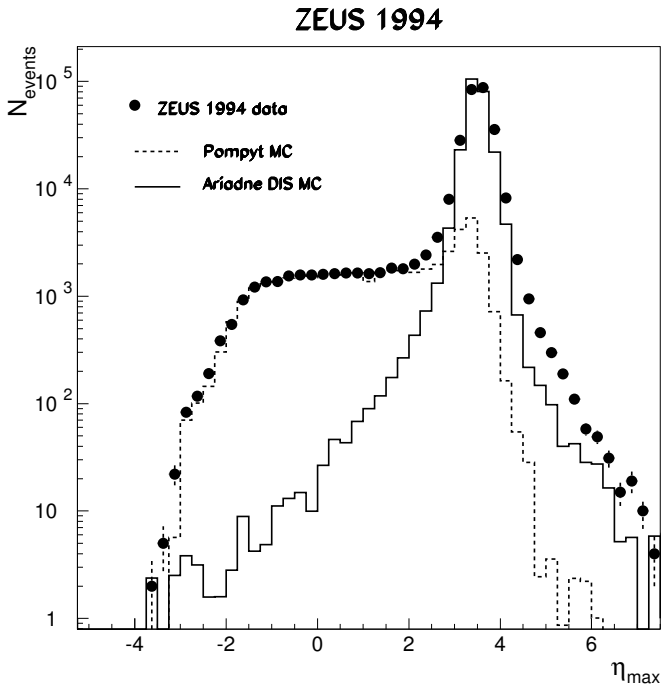

Figure 1.4: Event rates vs. η^{max} for ZEUS data in DIS compared with Monte Carlo simulated events for diffractive (POMPYT) and non-diffractive (ARIADNE) exchange; diffractive exchange is dominant for $\eta^{max} \lesssim 2.5$ – taken from [4].

1.3 Diffractive dijets

In this analysis, diffraction will be considered for processes in ep-scattering where a dijet system is observed. The two jets are assumed to result from partons produced in the initial diffractive process as described below. The concept of jets will be discussed in Sec. 5.3.

1.3.1 Diffractive dijets in DIS

In deep inelastic scattering (DIS) the electron is scattered through a large angle, indicating a large squared four-momentum transfer Q^2 between the incoming and outgoing lepton and hence the emission of a highly-virtual photon γ^*. Q^2 is also denoted as the photon virtuality and reflects the resolution Δb with which the scattered objects can be probed: $\Delta b \approx \lambda = \hbar c/\sqrt{Q^2}$.
Besides the lowest order scattering on a quark of the proton (Fig. 1.5 left), a diffractive process can occur (Fig. 1.5 middle, right) where the diffractive exchange particle $I\!P$ is interpreted to have a partonic substructure similar to the proton, i.e. with universal structure functions of gluons and quarks [6]. The emission of the diffractive particle $I\!P$ is followed by the interaction of a parton in the $I\!P$ with the virtual photon: either directly if the parton is a quark, or indirectly if the parton is a gluon which couples to a $q\bar{q}$-pair before interacting with the photon.
Two additional variables are required to describe diffractive scattering: $x_{I\!P}$ (or ξ in hadron-hadron scattering) gives the longitudinal momentum fraction of the proton taken by the

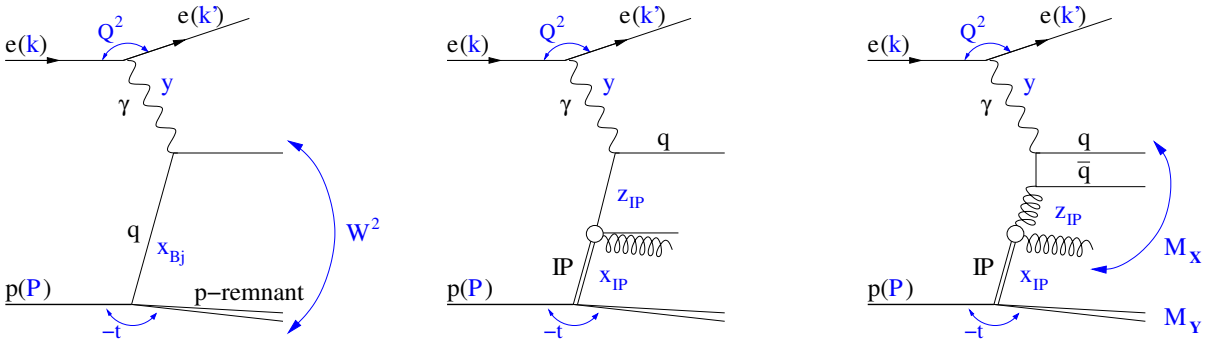

Figure 1.5: The LO graphs of DIS *(left)* and diffractive DIS *(middle, right)*, along with the kinematic variables used to describe them.

diffractive exchange, whereas $z_{I\!P}$, also denoted as β, corresponds to the Bjorken variable x_{Bj} in non-diffractive scattering and gives the longitudinal momentum fraction of the diffractive exchange taken by a quark or gluon evolving from it. As depicted in Fig. 1.5, the variable x_{Bj} is then replaced by the two variables $x_{I\!P}$ and $z_{I\!P}$ for the diffractive exchange:

$$x_{Bj} = x_{I\!P} \cdot z_{I\!P} \qquad (z_{I\!P} \equiv \beta) \tag{1.1}$$

Occasionally a direct contribution of the $I\!P$ is mentioned in literature, meaning $z_{I\!P} \simeq 1$. The kinematic variables describing the graphs in Fig. 1.5 are explained in Tab. 1.1.

1.3.2 Diffractive dijets in PHP

Most events at ZEUS are photoproduction events, i.e. the lepton is only scattered by a small angle, Q^2 is small (usually $Q^2 \lesssim 1\,\mathrm{GeV}^2$) and the photon is quasi-real. Like in DIS, the photon can interact directly with a $q\bar{q}$-system, referred to as *direct PHP* (Fig. 1.6 left). For quasi-real photons, however, Heisenberg's Uncertainty Principle also allows a fluctuation into a $q\bar{q}$-system, i.e. the resolved photon can interact via its partonic content. This is denoted as *resolved PHP* (Fig. 1.6 right). For the resolved process, one additional variable, x_γ, is required for the fraction of the longitudinal photon momentum taken by the parton which

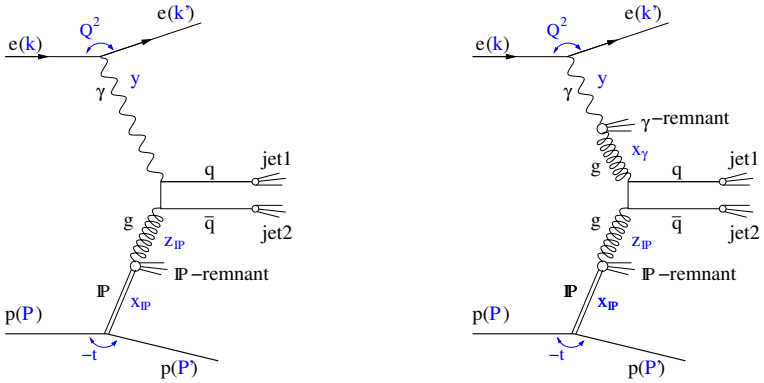

direct PHP resolved PHP

Figure 1.6: Main contributions to the production of diffractive dijets in PHP.

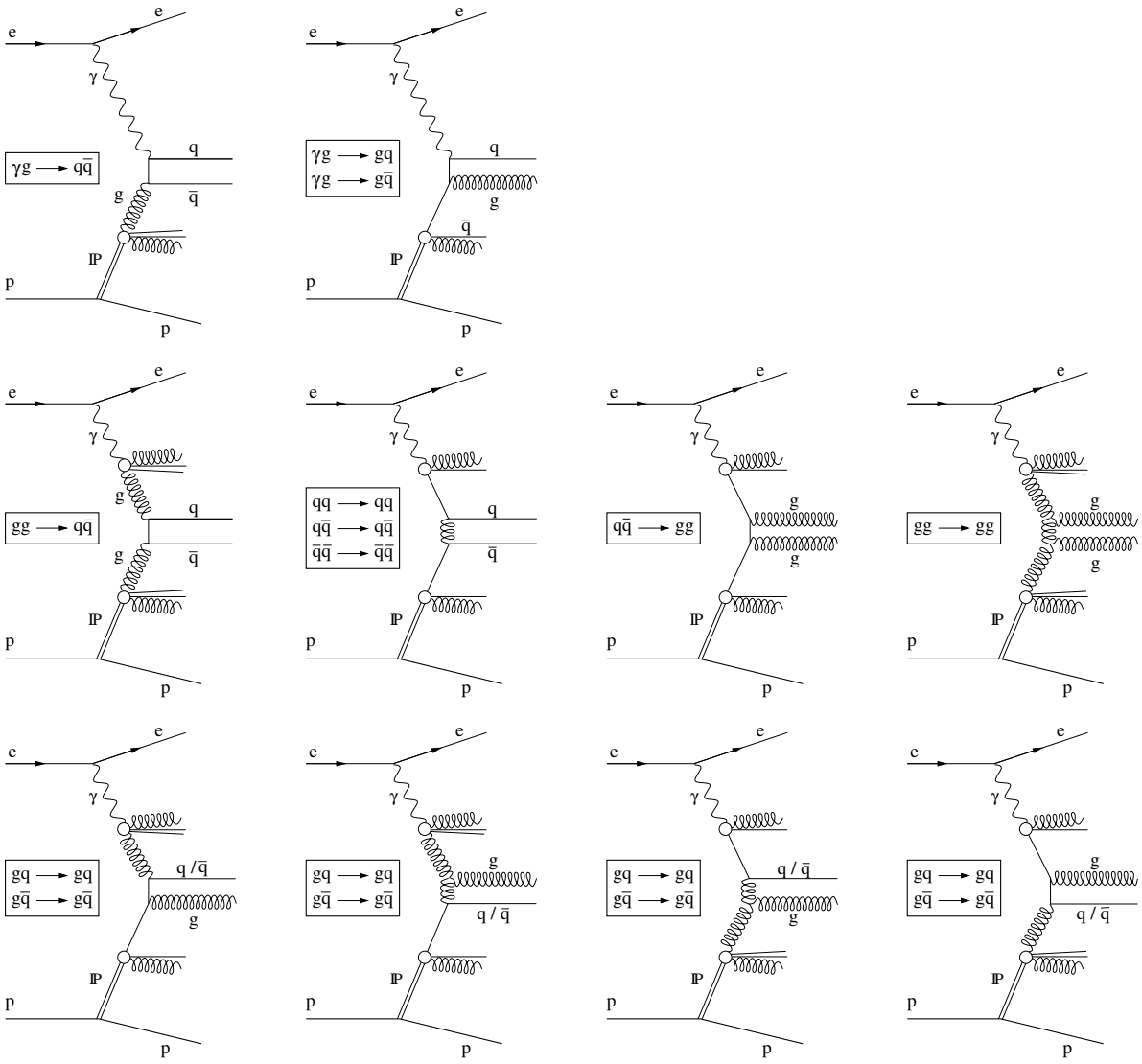

Figure 1.7: LO graphs for direct *(top row)* and resolved PHP *(middle and bottom row)* – the labelled partons in the centre are considered to form the dijet system whereas the partons starting from a circle symbolise the remnant resulting from the Pomeron or, in case of resolved PHP, from the photon.

evolves from the photon (see also Tab. 1.1). For *leading order* (LO) processes of direct PHP, it follows that $x_\gamma = 1$. Beyond LO, $x_\gamma \lesssim 1$ and the separation of direct and resolved PHP is not strict anymore.
An overview of LO-contributions[2] to the production of diffractive dijets is given in Fig. 1.7. The top row depicts processes for direct PHP: In the case that the diffractive exchange

[2]The abbreviation *LO* is ambiguous as it is often used for *leading order* as well as *lowest order*. Strictly speaken, the lowest order processes for diffractive dijets in resolved PHP in Fig. 1.7 are at least one order higher than the lowest order processes for diffractive dijets in direct PHP. The combination of both, however, is considered as the leading order contribution to the production of diffractive dijets in PHP.
In most circumstances both terms are interchangable, and the term *lowest order* will be used in this analysis only where misunderstandings could result.

contributes a gluon g, a $q\bar{q}$ system is produced (top-left diagram). If a quark q evolves from the diffractive exchange, a dijet system can be produced by QCD-Compton scattering (top-right diagram). The graphs in the second and third row refer to contributions from resolved PHP.

1.4 Kinematic variables

The kinematic variables used in this analysis are summarised in Tab. 1.1. Here $k = (E_e, \vec{k})$ and $P = (E_p, \vec{P})$ are the four-momentum of the initial electron e and proton p, respectively, and k' and P' those of the scattered e' and p'. Experimental observables for these variables are derived in Sec. 5.4.

Kinematic variables		
Squared centre-of-mass energy (cme)	$s = (k+P)^2 \simeq 4E_eE_p$	
Squared four-momentum transfer		
• at proton vertex	$t = (P-P')^2$	
• at lepton vertex (virtuality)	$Q^2 = -(k-k')^2 = -q^2$	
Squared mass of		
• system X	$M_X^2 = (q+P-P')^2$	
• proton p / diss. proton (Y)	$M_Y^2 = (P')^2$	
• total hadronic system	$W^2 = (P+q)^2 = ys - Q^2 + m_p^2$	
Inelasticity	$y = \frac{Pq}{Pk}$	$0 \leq y \leq 1$
Longitudinal momentum fraction of p taken by scattered parton	$x_{Bj} = \frac{Q^2}{2 \cdot Pq} = \frac{Q^2}{Q^2+W^2-m_p^2}$	$0 \leq x_{Bj} \leq 1$
Additional variable for PHP		
Longitudinal momentum fraction of γ taken by scattered parton with 4-momentum u	$x_\gamma = \frac{Pu}{Pq}$	
Additional variables for diffraction		
Longitudinal momentum fraction		
• of p taken by $I\!P$	$x_{I\!P} = \frac{(P-P')q}{Pq} = \frac{Q^2+M_X^2-t}{Q^2+W^2-m_p^2} \simeq \frac{Q^2+M_X^2}{Q^2+W^2}$	
• of $I\!P$ taken by scattered parton	$z_{I\!P} = \frac{Q^2}{2(P-P')q} = \frac{Q^2}{Q^2+M_X^2-t} \simeq \frac{Q^2}{Q^2+M_X^2}$	

Table 1.1: Description of main kinematic variables and calculation formulae.

Rapidity and pseudorapidity

Another important variable in collider physics, where the direction of the beam line is distinguished from all other directions, is the rapidity $\mathcal{Y}$ [7]:

$$\mathcal{Y} = \frac{1}{2} \cdot \ln \frac{(E + p_z)}{(E - p_z)},$$

where E is the energy of the particle and p_z its longitudinal momentum along the z-axis, chosen to be the beam line. In the non-relativistic limit the rapidity reduces to the longitudinal velocity v of a particle, but it is more practical as it is additive under Lorentz boosts along the z-axis.
In the limit of small masses or high energies, the rapidity reduces to the so-called pseudorapidity η [7]

$$\eta = -\ln \tan \frac{\theta}{2}, \tag{1.2}$$

where θ is the scattering polar angle with respect to the colliding beam direction. Like the rapidity, the pseudorapidity is additive under Lorentz boosts along the z-axis.
In this analysis, the pseudorapidity is used to describe the direction of *jets* η^{jet} (Sec. 5.3) as well as the direction of the particle which is closest to the beam direction, η^{max} (Sec. 5.4).

1.5 Soft vs. hard diffraction

In lowest order, the cross section for processes involving the strong force is proportional to α_S:

$$\alpha_s(Q^2) = \frac{4\pi}{\beta_0 \cdot \log(Q^2/\Lambda^2_{QCD})}, \tag{1.3}$$

where Q^2 is the scale parameter of the interaction and $\beta_0 = 11 - \frac{2}{3}N_f$. Since $\beta_0 > 0$ for the numbers of flavours $N_f = 6$, the Q^2-dependence allows the following conclusions:

- for $Q^2 \gg \Lambda^2_{QCD}$, α_S becomes small and the quarks and gluons can then be considered as asymptotically free. Q^2 provides a *hard scale* and it is possible to calculate cross section by means of perturbative QCD (pQCD);

- for $Q^2 \lesssim \Lambda^2_{QCD}$, the energy scale is of the order of $R = \frac{hc}{E} \gtrsim 1\,\text{fm}$ and allows only soft processes in elastic or diffractive scattering. This is the regime where Regge theory can be applied to calculate cross sections.

Hence, the value of Λ_{QCD} defines a boundary between hadrons on the one hand and quasi-free quarks and gluons on the other. Experimentally this value was found to be $\Lambda_{QCD} \approx 300\,\text{MeV}$. Perturbative calculations break down for smaller values of Q^2, but a hard scale might still be given by the transverse energy E_T^{jet} in jet production, the quark mass m_q in the production of heavy quarks or a large four-momentum transfer squared t.
In this analysis, diffractive PHP of dijets is studied at large transverse jet energies.

1.6 Diffraction in terms of Regge theory

Particle exchange in soft scattering processes can be described by Regge theory [3, 8]. It is based on the study of the analytic properties of the scattering amplitude $T(s,t)$. For high energies s and small four-momentum transfer squared t, the elastic amplitude of two hadrons a and b can be expressed as a function of a so-called *trajectory* $\alpha(t)$ which is exchanged between a and b:

$$T_{elast}^{ab\to ab}(s,t) \;=\; i\cdot s\,\beta_a(t)\cdot\left(\frac{s}{s_0}\right)^{\alpha(t)-1}\cdot\beta_b(t)\;.$$

Here $\beta_a(t)$ and $\beta_b(t)$ are form factors which account for the non-pointlike nature of the hadrons. For $t=0$, the forward elastic scattering cross section can be written as

$$\left.\frac{d\sigma_{elast}^{ab\to ab}}{dt}\right|_{t=0} \;=\; \frac{1}{16\pi s^2}\left|\,T_{elast}^{ab\to ab}(s,0)\,\right|^2 \;=\; \frac{1}{16\pi}\left(\beta_a(0)\beta_b(0)\right)^2\cdot\left(\frac{s}{s_0}\right)^{2(\alpha(t)-1)}\;.$$

An analogous relation to the Optical Theorem, based on the conservation of probability, connects the total cross section to the imaginary part of the forward elastic scattering amplitude:

$$\begin{aligned}\sigma_{tot}^{ab}(s) &= \frac{1}{s}\cdot\mathrm{Im}\,T_{elast}^{ab\to ab}(s,0)\\ &= \beta_a(0)\beta_b(0)\cdot\left(\frac{s}{s_0}\right)^{\alpha(t)-1}\;.\end{aligned}\qquad(1.4)$$

In terms of Regge theory, diffractive exchange refers to a special trajectory, denoted as the Pomeron trajectory. In addition, other, non-diffractive processes are possible where the Pomeron $I\!P$ in Fig. 1.3 is replaced by a meson (e.g. π^0, ρ^0, J/Ψ). These processes refer to the exchange of so-called Regge trajectories ($I\!R$). Both $I\!P$ and $I\!R$ trajectories are assumed to be linear in t [8]:

$$\alpha_{I\!P}(t) \;=\; \alpha_{I\!P}(0)+\alpha'_{I\!P}\cdot t \qquad\qquad \alpha_{I\!R}(t) \;=\; \alpha_{I\!R}(0)+\alpha'_{I\!R}\cdot t$$

The cross section in Eqn. 1.4 can be re-written as the sum of the exchange of $I\!R$- and $I\!P$-trajectories:

$$\sigma_{tot} = M\cdot s^{\alpha_{I\!R}(0)-1}+N\cdot s^{\alpha_{I\!P}(0)-1}$$

With $\alpha_{I\!R}(0)=1-\kappa$ and $\alpha_{I\!P}(0)=1+\varepsilon$, Donnachie and Landshoff [9] performed a fit of the form

$$\sigma_{tot} = M\cdot s^{\epsilon}+N\cdot s^{-\kappa}$$

to data of single-diffractive hadron-hadron collisions $pp\to pX$, where M, N, ϵ and κ are fit parameters. Their results led to a parametrisation of the Pomeron and Reggeon trajectories according to:

$$\begin{aligned}\alpha_{I\!R} &= 0.5475+0.93\,\mathrm{GeV}^{-2}\;\cdot\;t\\ \alpha_{I\!P} &= 1.0808+0.25\,\mathrm{GeV}^{-2}\;\cdot\;t\end{aligned}$$

In particular, the value of $\varepsilon\approx 0.08$ leads to a slow rise of the cross section for elastic scattering and therefore also for diffractive scattering. The t-dependent cross section $d\sigma^{ab\to ab}/dt$ falls exponentially with t in analogy to diffraction in optics.
As a consequence, Reggeon exchange refers to soft elastic scattering and its contribution to hard diffraction is small and has been neglected for this analysis.

1.7 Diffraction in pQCD

In terms of QCD, the exchange of a Pomeron refers to the exchange of a colour singlet. In LO this can be interpreted as a $2g$-exchange (Fig 1.8 middle) where the two gluons form a colour neutral state [10]. As a result of the interaction of gluons with themselves, a gluon ladder evolves at NLO and beyond (Fig 1.8 right).

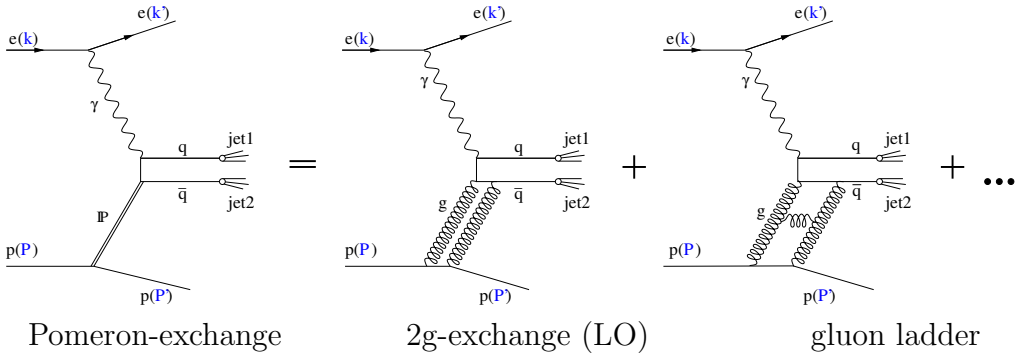

Figure 1.8: Diffractive process depicted as exchange of a Pomeron *(left)*, two gluons *(middle)* or a gluon ladder *(right diagram)* which form a colour singlet.

1.7.1 Factorisation

DIS cross section

The total cross section σ_{ep} for DIS is given by

$$\frac{d^2\sigma_{ep}}{dx_{Bj}\,dQ^2} = \frac{4\pi\,\alpha_{em}^2}{x_{Bj}\,Q^4}\left(\frac{y^2}{2}\cdot 2x_{Bj}F_1(x_{Bj},Q^2) + (1-y)\cdot F_2(x_{Bj},Q^2)\right). \tag{1.5}$$

From the QPM[3] it follows that in lowest order (Fig. 1.5 left)

$$\frac{d^2\sigma_{ep}}{dx_{Bj}\,dQ^2} = \sum_q \frac{d^2\sigma_{eq}}{dx_{Bj}\,dQ^2},$$

and the structure functions F_1 and F_2 are given by

$$\begin{aligned} F_1(x_{Bj}) &= \frac{1}{2}\cdot\sum_i q_i^2 f_i(x_{Bj}), \\ F_2(x_{Bj}) &= x_{Bj}\cdot\sum_i q_i^2 f_i(x_{Bj})\,, \end{aligned}$$

where f_i are the parton distribution functions of the parton with charge q_i. The emission of non-collinear gluons by quarks leads to a non-vanishing longitudinal cross section [12].

[3] In the *Quark Parton Modell* (QPM) introduced by Feynman, the proton is considered to consist of point-like constituents, suggested to be quarks and gluons [11].

The corresponding longitudinal structure function $F_L(x_{Bj})$ is defined by the violation of the Callan-Gross relation

$$F_L(x_{Bj}) \;=\; F_2(x_{Bj}) - 2x_{Bj} \cdot F_1(x_{Bj}) \tag{1.6}$$

and experimentally found to be small.

Diffractive DIS cross sections

In hard diffraction the Pomeron is considered as a single particle scattered off the proton. In the *resolved Pomeron model* by Ingelman & Schlein [6], this particle is assumed to have a partonic substructure and universal structure function of its constituents. The scattering can then be interpreted as a two-stage process:

1. the emission of a Pomeron $I\!P$ from the proton, followed by

2. the interaction of a parton with longitudinal momentum fraction $z_{I\!P}$ of the $I\!P$ with a probing particle, e.g. a virtual photon γ^* or a quark or gluon evolving from it (comp. Fig. 1.6).

Two additional variables, t and $x_{I\!P} = x_{Bj}/z_{I\!P}$ (Eqn. 1.1), are required to describe this process, and the four-fold differential cross section $\sigma_{ep}^{D(4)}$ for diffractive DIS (dDIS) can be written in an analogous way to Eqn. 1.5:

$$\begin{aligned}
\frac{d\sigma_{ep}^{D(4)}}{dx_{I\!P}\,dt\,dz_{I\!P}\,dQ^2} &= \frac{4\pi\,\alpha_{em}^2}{z_{I\!P}\,Q^4} \;\cdot\; \left(\frac{y^2}{2}\cdot 2x_{I\!P}F_1^{D(4)}(z_{I\!P},Q^2,x_{I\!P},t) + (1-y)\cdot F_2^{D(4)}(z_{I\!P},Q^2,x_{I\!P},t)\right) \\
&= \frac{4\pi\,\alpha_{em}^2}{z_{I\!P}\,Q^4}\cdot\left[\left(1-y+\frac{y^2}{2}\right)\cdot F_2^{D(4)}(z_{I\!P},Q^2,x_{I\!P},t) - \frac{y^2}{2}\cdot F_L^{D(4)}(z_{I\!P},Q^2,x_{I\!P},t)\right]
\end{aligned}$$

For the transformation in the second step, Eqn. 1.6 has been used. Due to the small contribution from F_L, this is often reduced to

$$\frac{d\sigma_{ep}^{D(4)}}{dx_{I\!P}\,dt\,dz_{I\!P}\,dQ^2} \;=\; \frac{2\pi\,\alpha_{em}^2}{z_{I\!P}Q^4}\cdot\left(1+(1-y)^2\right)\cdot\sigma_{red}^{D(4)}(z_{I\!P},Q^2,x_{I\!P},t)$$

with the reduced diffractive cross section $\sigma_{red}^{D(4)}$:

$$\sigma_{red}^{D(4)} \;=\; F_2^{D(4)} - \frac{y^2}{1+(1-y)^2}\cdot F_L^{D(4)} \;\approx\; F_2^{D(4)}\,. \tag{1.7}$$

If the scattered proton p' is not detected by the experiment, then t is not known. In this case an integration over t is performed to obtain the three-fold cross section and structure function:

$$\begin{aligned}
\sigma_{red}^{D(3)} &= \int dt\,\sigma_{red}^{D(4)} \\
F_2^{D(3)}(z_{I\!P},Q^2,x_{I\!P}) &= \int dt\,F_2^{D(4)}(z_{I\!P},Q^2,x_{I\!P},t)
\end{aligned}$$

F_2^D is constrained by the partonic structure functions in the Pomeron, f^D, which can be evoluted by the Dokshitzer-Gribov-Lipatov-Altarelli-Parisi (DGLAP) equations [13, 14]. According to the Ingelman-Schlein model, they factorise into two parts:

$$f^D(x_{I\!P}, t, z_{I\!P}, Q^2) = \underbrace{f_{I\!P/p}(x_{I\!P}, t)}_{\text{Pomeron flux}} \cdot \underbrace{f_{a/I\!P}(z_{I\!P}, Q^2)}_{\text{diffractive PDFs}}$$

The first factor can be interpreted as a Pomeron flux, giving the probability that at four-momentum transfer squared t a Pomeron with the momentum fraction $x_{I\!P}$ is found in the proton,

$$f_{I\!P/p}(x_{I\!P}, t) = \int_{t_{\min}}^{t_{\max}} dt\, e^{B_{I\!P} t} x_{I\!P}^{1-2\alpha_{I\!P}(t)}\,, \tag{1.8}$$

while the second part can be considered as a universal diffractive structure function, giving the probability to find a parton a with momentum fraction $z_{I\!P}$ in the Pomeron at energy Q^2 of the probing particle. Such a factorisation theorem for DIS was proven by J.C.B. Collins [15]. The proof holds for lepton-hadron scattering but fails for hadron-hadron scattering due to soft interactions between hadrons in both the initial and final state (Sec. 1.7.2).
As a consequence, all non-perturbative information would be contained in universal diffractive PDFs (dPDFs), i.e. dPDFs experimentally determined for one reaction would allow cross sections for any other hard diffractive processes to predicted by convolution according to the DGLAP equations with a hard scale.
In diffractive PHP, $Q^2 \lesssim 1\,\text{GeV}^2$ does not provide a hard scale. As stated in Sec. 1.5, a hard scale can alternatively be given by large transverse energies E_T^{jet} of particle jets. For the production of diffractive dijets in PHP, Kaidalov et al. [16] use

$$Q^2 \quad \longrightarrow \quad \mu^2 \;=\; Q^2 + \frac{1}{4}(E_T^{jet\,1} + E_T^{jet\,2})\,. \tag{1.9}$$

The cross section for diffractive dijet production in $ep \to e + 2\,jets + p\,(or\ Y)$ is considered to be the sum of direct and resolved contributions [16]

$$\sigma^D_{\text{PHP}} \;=\; \sigma^D_{\text{dir}} + \sigma^D_{\text{res}}$$

with

$$\begin{aligned}
\frac{d\sigma^D_{\text{dir}}(\mu^2)}{dt\,dx_{I\!P}\,dz_{I\!P}\,dy} &= \sum_a [f_{\gamma/e}(y) \quad \cdot \quad f_{I\!P/p}(x_{I\!P}, t) \cdot f_{a/I\!P}(z_{I\!P}, \mu^2)] \cdot \sigma(\gamma a \to 2\,jets) \\
\frac{d\sigma^D_{\text{res}}(\mu^2)}{dt\,dx_{I\!P}\,dz_{I\!P}\,dy\,dx_\gamma} &= \sum_{a,b} [f_{\gamma/e}(y) \cdot f_{b,\gamma}(x_\gamma, \mu^2) \cdot f_{I\!P/p}(x_{I\!P}, t) \cdot f_{a/I\!P}(z_{I\!P}, \mu^2)] \cdot \sigma(ba \to 2\,jets)\,.
\end{aligned}$$

Here a is the parton from the Pomeron, b is the parton in the resolved photon, $\sigma(\gamma a \to 2\,jets)$ and $\sigma(ba \to 2\,jets)$ are the cross sections for the production of two final state partons hadronising into 2 jets as depicted in Fig. 1.6. They were calculated in QCD by M. Klasen and G. Kramer [17] using diffractive parton distributions functions $f_{a/I\!P}$ which were obtained from experiments H1 and ZEUS (Sec. 1.7). For the calculations of the resolved processes, the parton distribution functions $f_{b/\gamma}$ were taken from GRV [18].

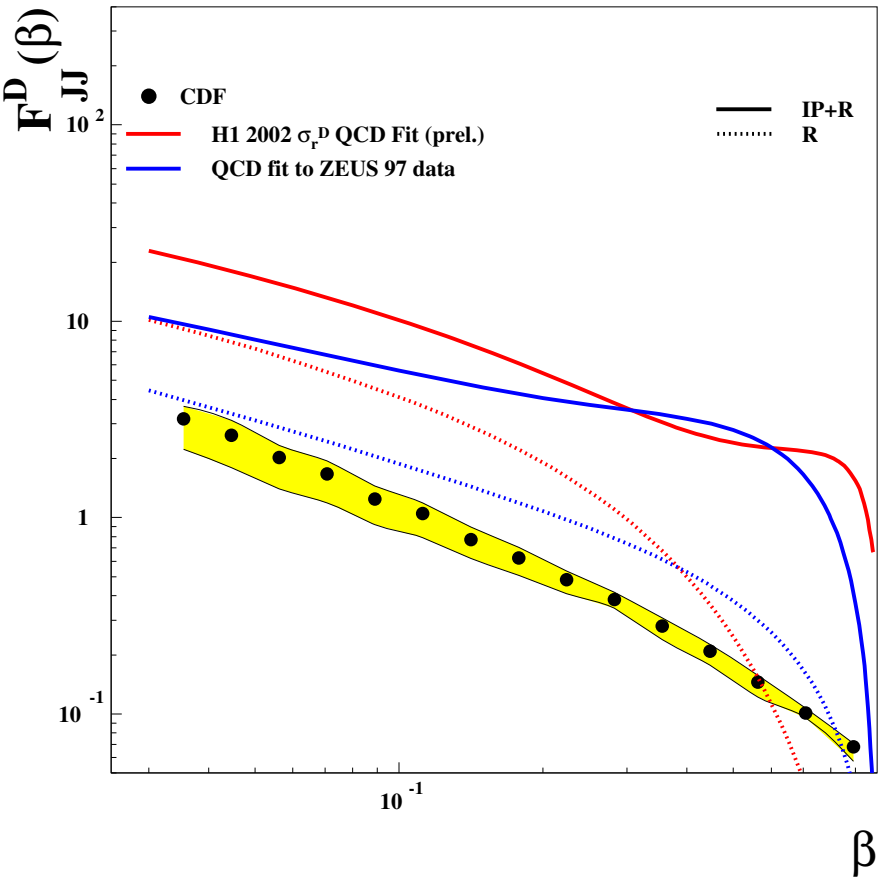

Figure 1.9: The diffractive dijet structure function F_{jj}^{D} over β $(= z_{I\!P})$ for CDF data obtained from single diffractive pp scattering and two fits *(red, blue)* including $I\!P$ and $I\!R$ contributions *(solid lines)*, and contributions from $I\!R$ exchange only *(dotted lines)* – taken from [19].

1.7.2 Factorisation breaking

Recent data on single inclusive scatterings $p\bar{p} \rightarrow pX$ taken in the CDF experiment at the TEVATRON collider have been compared to a prediction for single diffractive dijets [19]. This prediction used dPDFs of the H1 Collaboration (Sec. 1.8.1) which were extrapolated to the kinematical range of the CDF experiment. The predicted structure function overestimates CDF data by a factor of $\simeq 3 - 10$ (Fig. 1.9).
According to Kaidalov et al. [20], such a suppression factor is possible in diffractive hadron-hadron scattering due to multi-$I\!P$ exchange in the initial state or rescatterings between final state partons (Fig. 1.10). These effects reduce the rapidity gap survival probability [21]. Such higher order processes were calculated yielding a rather constant suppression factor [20] over the kinematical range as seen for the $\beta\,(= z_{I\!P})$ dependence in Fig. 1.9.
In direct PHP the photon interacts point-like as in diffractive DIS (Fig. 1.11, left diagram) so that Collins' proof of QCD factorisation is expected to hold. In resolved PHP the photon acts as source of partons and thus mimics hadronic scattering (Fig. 1.11, middle, right diagram) so

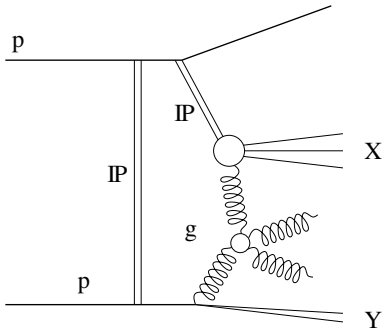

Figure 1.10: Initial state multi-$I\!P$ exchange and final state partons rescattering.

that factorisaton breaking is expected. Based on calculations assuming s-channel unitarity, Kaidalov et al. [16] predict a suppression factor of $R = 0.34$ for the cross section of hard resolved PHP in ep collisions, smeared for values of $x_\gamma > 0.3$. Hence hard diffractive PHP provides a unique possibility to study the interplay of factorisation validity versus factorisation breaking.
The NLO calculations by Klasen and Kramer [17] suggested that factorisation breaking for the resolved photon could be observed mainly as an overall suppression factor. The results of this analysis will be compared to NLO calculations based on Klasen and Kramer's model in Sec. 12.3.

1.8 Diffractive parton distributions

Diffractive Parton Distribution Functions (dPDFs) were determined from diffractive ep scattering in DIS events at HERA by the H1 and ZEUScollaboration. Diffractive events were selected according to three different signatures that are characteristic for diffraction:

- a large rapidity gap (LRG) devoid of any particles between the scattered

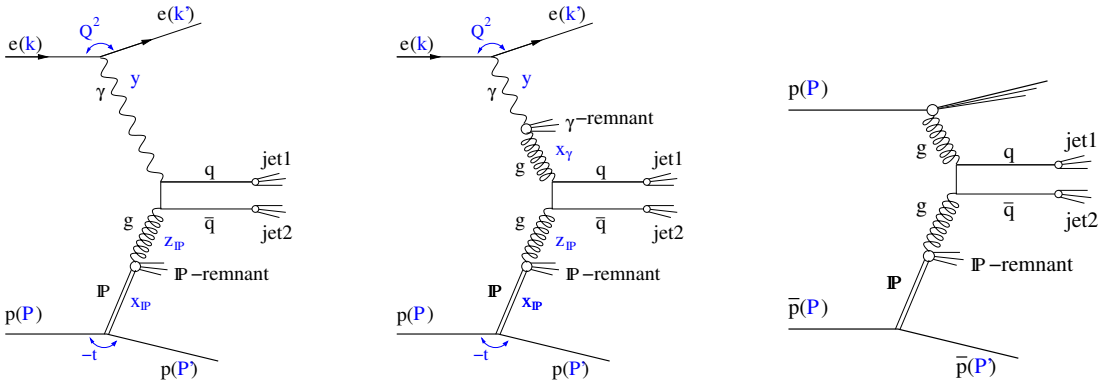

DIS / direct PHP resolved PHP hadronic scattering

Figure 1.11: Diffractive scattering in direct PHP and DIS *(left)*, resolved PHP *(middle)* and single diffractive scattering in $p\bar{p}$ collisions *(right)*.

proton (or system Y) and the diffracted system X; *(→ LRG method, Sec. 1.8.1)*

- an intact proton in the final state that loses only little of its inital momentum: $p' > 0.98p$, $x_L = 1 - x_{I\!P} > 0.95$; *(→ LPS method, Sec. 1.8.2)*
- a rather isolated hadronic system X with mass M_X separated from the scattered proton. *(→ M_X method, Sec. 1.8.3)*

These methods and the dPDFs derived from them will be described below.

1.8.1 LRG method – H1 LO fit 2, H1 2002 fit

According to a simplified model introduced by Feynman [22], particles produced in hadron collisions at high squared centre-of-mass energy s are distributed uniformly in rapidity within kinematic limits given by $\pm s/m_{parton}$ (Fig. 1.12 left). A LRG is then exponentially suppressed: $dN/d\,\Delta\mathcal{Y} \propto e^{-\Delta\mathcal{Y}}$. In contrast, the requirement of a colourless exchange in diffractive events [5, 23] results in a LRG between the hadronic system X with mass M_X and the scattered proton p (Fig. 1.12 right): $dN/d\,\Delta\mathcal{Y} \cong$ const.

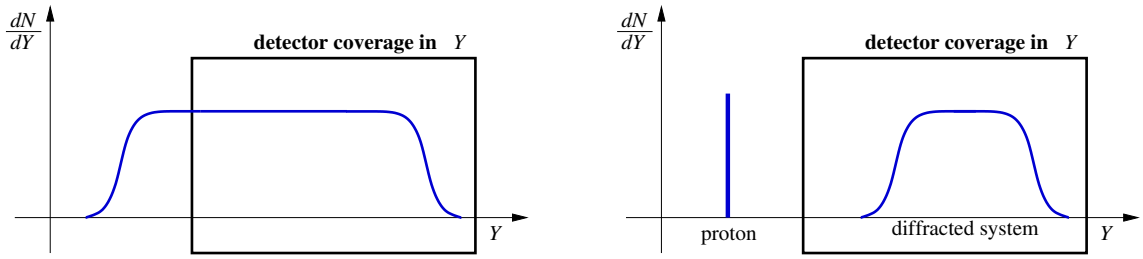

Figure 1.12: Schematic depiction of particle rates over rapidity Y for non-diffractive *(left)* and diffractive events *(right)*.

The size of the LRG in diffraction is related to the masses of the final state systems at each vertex: In the centre-of-mass system of $\gamma^* p$, the scattered p and the system X move in opposite directions with longitudinal momentum $p_L \approx W/2$. Then an upper limit for the rapidity gap can be estimated by the rapidities of the proton and the system X:

$$\begin{aligned}
\mathcal{Y}_p &= +\frac{1}{2}\cdot\ln\frac{E_p + p_L}{E_p - p_L} = +\frac{1}{2}\cdot\ln\frac{(E_p + p_L)^2}{E_p^2 - p_L^2} &&\approx &&+\frac{1}{2}\cdot\ln\frac{W^2}{m_p^2}\\
\mathcal{Y}_X &= -\frac{1}{2}\cdot\ln\frac{E_X + p_L}{E_X - p_L} = -\frac{1}{2}\cdot\ln\frac{(E_X + p_L)^2}{E_X^2 - p_L^2} &&\approx &&-\frac{1}{2}\cdot\ln\frac{W^2}{M_X^2}\\
\Longrightarrow\quad \Delta\mathcal{Y} &= \mathcal{Y}_p - \mathcal{Y}_X &&\approx &&\ln\frac{W^2}{m_p M_X}
\end{aligned}$$

This limit is likely to be reduced on both sides: The hadronisation products of the system X are spread in rapidity; typically $M_X < 100\,\text{MeV}$ and $\Delta\mathcal{Y}_X \lesssim 3$. The measurement of high proton rapidities is limited by the detector coverage.
Since a LRG in non-diffractive events is exponentially suppressed, background from such processes can be suppressed by requiring a sufficiently large gap. However, the diffractive

sample obtained hereby can still be enhanced with background from non-diffractive events with low multiplicity while diffractive events with high multiplicity are likely to be damped. The LRG method is sensitive to contributions from both Pomeron and Reggeon exchange, though the latter is expected to be small and usually not taken into account.
The H1 collaboration determined dPDFs from data on inclusive diffractive DIS measurement. The H1 LO fit2 [24] used an unexceptionally high value of $\alpha_{I\!P}(0)$: $\alpha_{I\!P}(0) = 1.17 > 1.08$. A more recent fit, denoted as H1 2002 fit [25], was performed by the H1 Collaboration on inclusive data in diffractive DIS and used a more conservative value for $\alpha_{I\!P}(0)$. This fit was not available in time for the production of MC events for this analysis, but was used for the calculation of NLO predictions.

1.8.2 LPS method – ZEUS LPS fit

The LPS-method [23, 26] selects diffractive events by tagging the intact, slightly scattered proton in the final state in a *leading proton spectrometer* (LPS), which is placed at small angles at large distance from the interaction point (Sec. 2.3). The energy of the scattered proton can be reconstructed by its track and diffractive events can be selected by requiring a sufficiently small t. The detector coverage limits the kinematic range at low t, i.e.the scattered proton p' might remain undetected for very small t.
The LPS method provides a cleaner diffractive sample than the LRG method because background from proton dissociation is highly suppressed. Since only neutral Reggeons can be exchanged, contributions from $I\!R$-exchange are smaller than for the LRG method. However, statistics are lower for the LPS method.

1.8.3 M_X method – ZEUS GLP fit

The M_X method [23, 26, 27] approximates the distribution of events over $(\ln M_X^2)$ (Fig. 1.13) by the form

$$\frac{dN}{d(\ln M_X^2)} = \underbrace{A}_{\text{diffractive}} + \underbrace{B \cdot exp(C \cdot \ln M_X^2)}_{\text{non-diffractive}},$$

where the Gaussian peak is due to non-diffractive exchange and the plateau A is due to diffractive exchange which is approximately proportional to $(\ln M_X^2)$. While the LPS and LRG method select diffractive events directly, the M_X method extracts the diffractive signal statistically by fitting the above formula to data and subtracting the non-diffractive contribution in each (W, Q^2)-bin.
The M_X method is not biased by low-multiplicity events but depends on a precise M_X^2 measurement and description of the exponential fall-off of the non-diffractive contribution. Furthermore, this method is only applicable up to a reasonable ratio of diffractive to non-diffractive contribution which restricts the measurement to small masses of $M_X \lesssim 35\,\text{GeV}$.

1.8.4 Comparison of dPDFs

The dPDFs of the LO fit 2 are shown in Figure 1.14, a comparison of the other dPDFs derived from above methods is shown in Fig. 1.15.

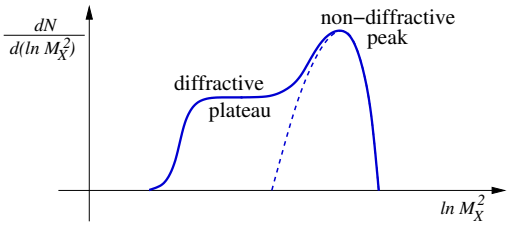

Figure 1.13: Schematic illustration of contributions from diffractive and non-diffractive events in the distribution of $(\ln M_X^2)$.

Compared to the H1 2002 fit, the H1 LO fit 2 is flatter at high $z_{I\!P}$ for both the the distribution of quarks and gluons. The dPDFs of the H1 2002 fit, the ZEUS LPS fit and GLP fit are similar in shape for quarks but differ considerably for gluons. Compared with the ZEUS LPS fit, the H1 2002 fit indicates the need of a normalisation factor of ~ 0.8. The gluon density from the ZEUS GLP fit is roughly a constant factor smaller than the H1 2002 fit. The differences between the dPDFs are still under investigation [28, 29].

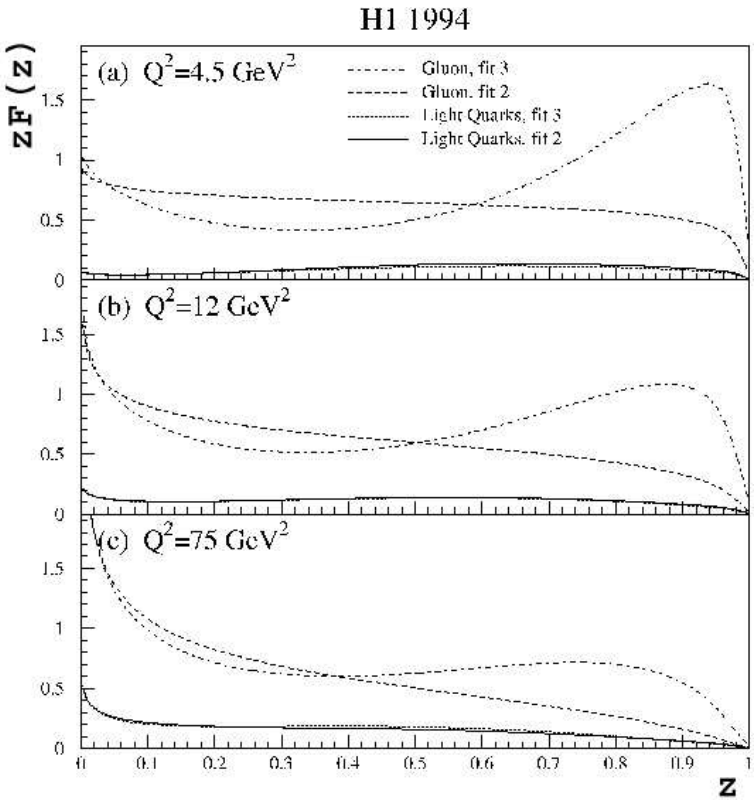

Figure 1.14: Diffractive PDFs of the H1 LO fit 2 vs. $z_{I\!P}$ – taken from [24].

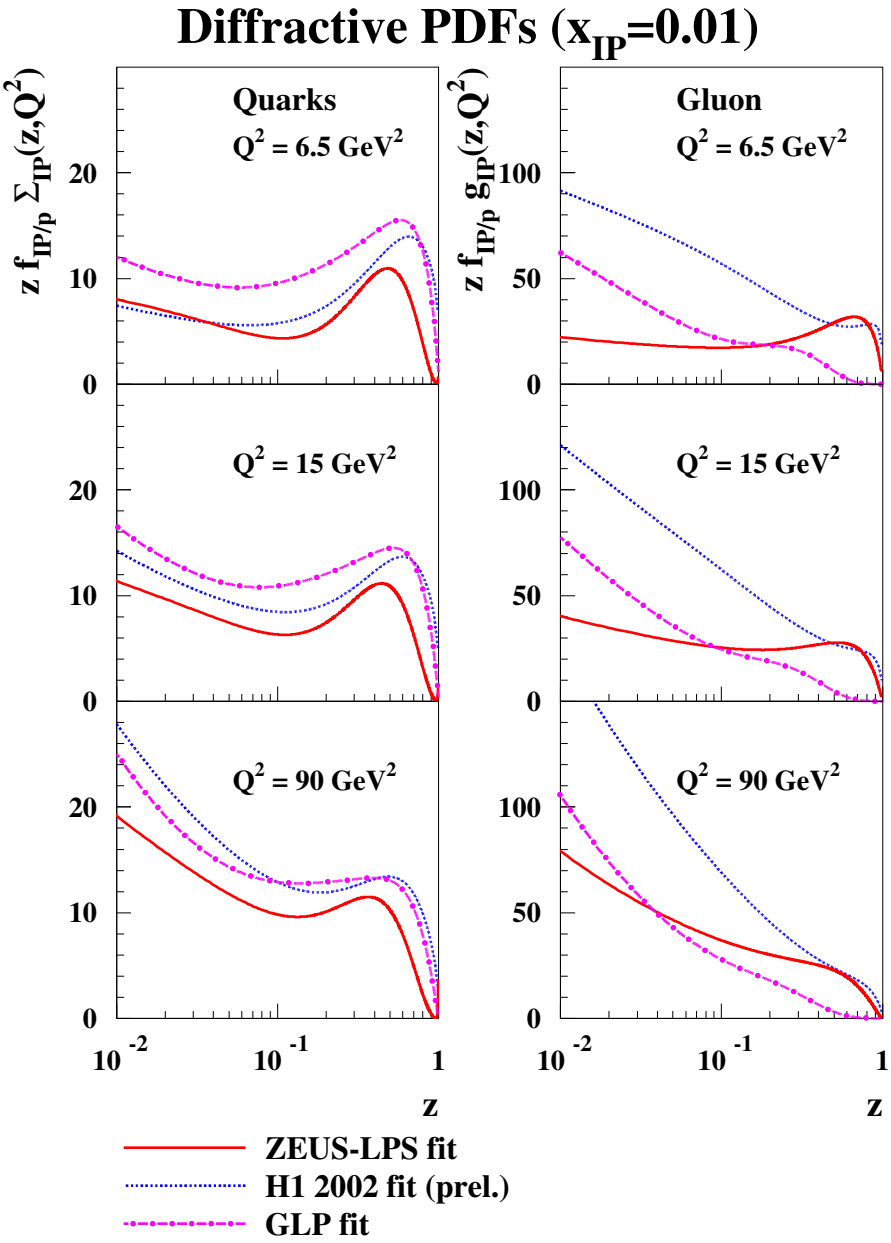

Figure 1.15: Comparison of dPDFs vs. $z_{I\!P}$ obtained from the LRG, LPS, and M_X method – taken from [30].

Chapter 2

Experimental setup

This analysis was performed with data taken with the ZEUS[1] detector at the *Hadron Electron Ring Accellerator* (HERA) at the *Deutsches Elektron Synchrotron* (DESY) in Hamburg. This chapter will give a short introduction to the purpose, design and function of these facilities.

2.1 DESY

DESY was founded on December 18, 1959, as an independent institution under civil law, and is a member of the Hermann von Helmholtz Association of National Research Centers. Its main objectives are

- the development, construction and operation of accelerator facilities;
- the investigation of the fundamental properties of matter and forces;
- the use of synchroton radiation in the fields of surface physics, material science, chemistry, molecular biology, medicine, and geophysics.

In its long history, a number of outstanding discoveries have been made, e.g. the observation of excited charmonium states in 1975 [32] and the detection of gluons in 1979 [33]. Over the past decades, basic research performed at DESY has continously increased knowledge on the standard model of particle physics.
Future projects include the design of a *Free Electron Laser* (X-FEL) and important contributions to the INTERNATIONAL LINEAR COLLIDER (ILC). The X-FEL will operate in X-ray band and hence enable direct observation of atoms and molecules in biological and chemical processes in real-time, e.g. for pharmacological purposes. The ILC will take advantage of technology originally invented for the construction of a *TeV–Energy Superconducting Linear Accelerator* at DESY. High energy electron-positron collisions at the ILC will possibly help to solve fundamental questions of modern particle physics, for instance the search for the Higgs boson and supersymmetric particles.

2.2 HERA

Fig. 2.1 depicts the main parts of the accelerator and pre-accelerator elements. Bunches of

[1] ZEUS is an acronym for *Ζητηρισις 'Ευριστικος 'Υποκειμενες Συμμετριας*, meaning 'Search for the Elucidation of Underlying Symmetries' and was certainly chosen to match with the acronym HERA [31].

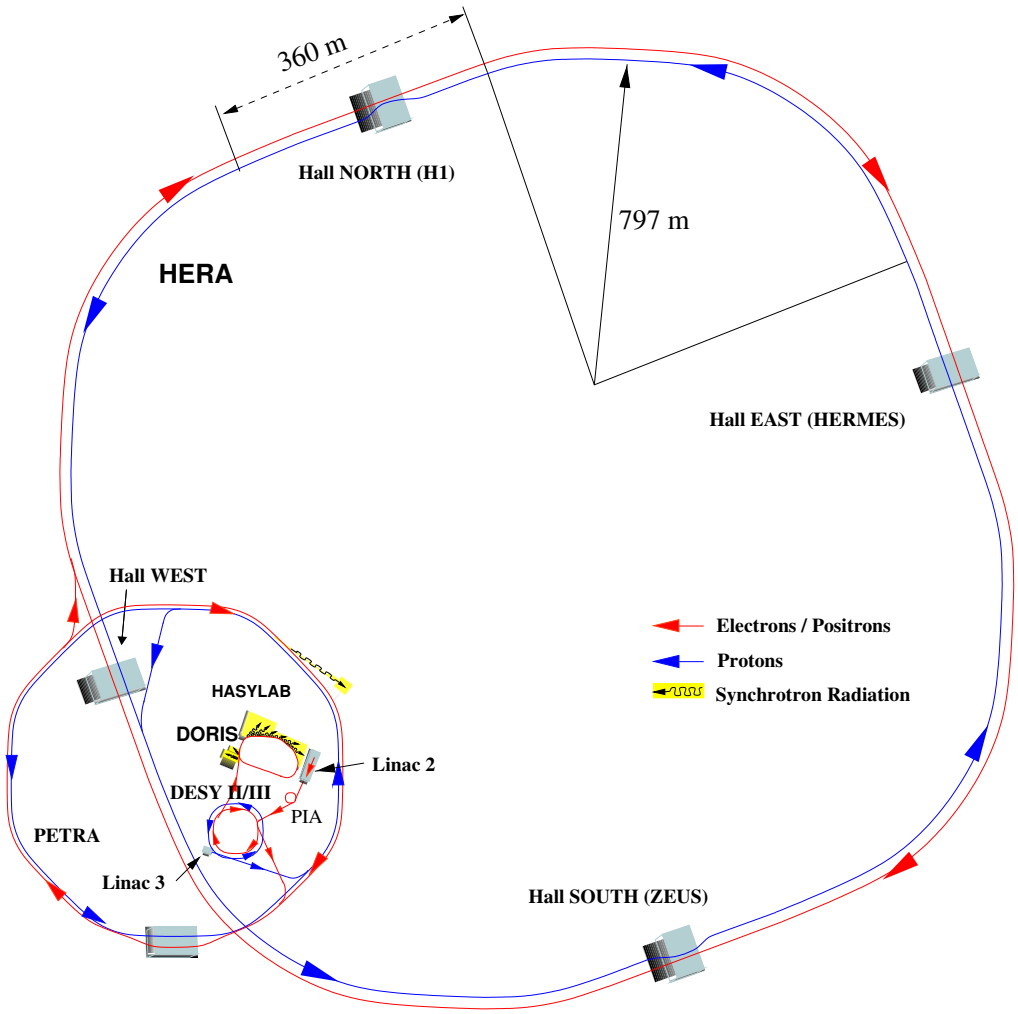

Figure 2.1: Accelerators and experiments at DESY.

electrons (or positrons[2]) and protons traverse the linear accelerators LINAC 2, LINAC 3 respectively, before being injected in the storage rings DESY II, DESY III respectively. Protons are pre-accelerated and then fed into the *Proton Electron Tandem Ring Accelerator* (PETRA). Here they are ramped up to 40 GeV before they are ejected counter-clockwise into the superconducting proton ring of HERA. Electrons run through the same cascade of accelerators and after protons have reached their nominal energy of 920 GeV, electrons are injected clockwise into the electron ring of HERA and ramped up to 27.5 GeV. At these energies, electrons and protons circulate in HERA with a velocity close to the speed of light. The acceleration process is summarised in Tab. 2.1.

There are four experiments located in the straight sections of the ring accelerator: HERA-B in the west, HERMES in the east, H1 in the north and ZEUS in the south. HERA-B (not in operation anymore) and HERMES are fixed target experiments designed for the research on heavy flavour production and the spin of the proton, respectively. H1 and ZEUS are colliding beam experiments used for a variety of studies in particle physics. At the interaction points of these detectors, the beampipes for electrons and protons merge into one and the beams are

[2]In the following the term *electrons* will be used for both electrons and positrons if not stated otherwise.

Accelerator	Electrons (positrons)	Protons
LINAC II/III	450 MeV	50 MeV
PIA	—	(accumulation)
DESY II/III	8 GeV	7.5 GeV
PETRA II	12 GeV	40 GeV
HERA	27.5 GeV	920 GeV

Table 2.1: Acceleration chain for HERA.

brought to collision at zero crossing angle.
The length of 6336 m of the HERA ring allows for 220 bunch buckets for both electrons and protons, resulting in a bunch crossing interval of 96 ns. In normal operation, a number of so-called *pilot bunches* remain unfilled or unpaired, i.e. without a counter-rotating partner, in order to estimate the background from gas in the beam pipe or cosmic events. Table 2.2 summarises the main parameters of the HERA design.

Operational parameters	Design values
proton beam energy E_p	920 GeV
electron beam energy E_e	27.56 GeV
centre-of-mass energy $\sqrt{s}$	318 GeV
proton beam current	140 mA
electron beam current	58 mA
bunch buckets	220
paired bunches	189
bunch crossing interval	96 ns
luminosity $\mathcal{L}_{inst}$	$1.4 \cdot 10^{31}\,\mathrm{cm}^{-2}\mathrm{s}^{-1}$

Table 2.2: Design parameters of HERA (run period I, 1994-2000).

2.3 The ZEUS detector

The ZEUS detector is in operation since 1992 and was significantly upgraded in 2000. A full view of ZEUS is shown in Fig. 2.2.
Its asymmetric design, more apparent in the longitudinal view of Fig. 2.4, accounts for the different beam energies which result in a Lorentz boost of the centre-of-mass system (CMS) in forward direction relative to the laboratory system[3].
The transverse view in Fig. 2.4 (top) shows the onion-like structure of the detector: A set of tracking detectors surround the *interaction point* (IP) of the ZEUS detector and measures the momentum of charged particles. These detectors are almost hermetically encased by a set of calorimeters which measure the energy of the particles. Additional detectors along the

[3]The ZEUS coordinate system is a right-handed Cartesian system with its origin in the nominal interaction point (IP) of the detector. The $x-$axis is pointing towards the centre of the HERA ring and the $z-$axis in proton direction, also referred to as *forward direction* (see Fig. 2.3).

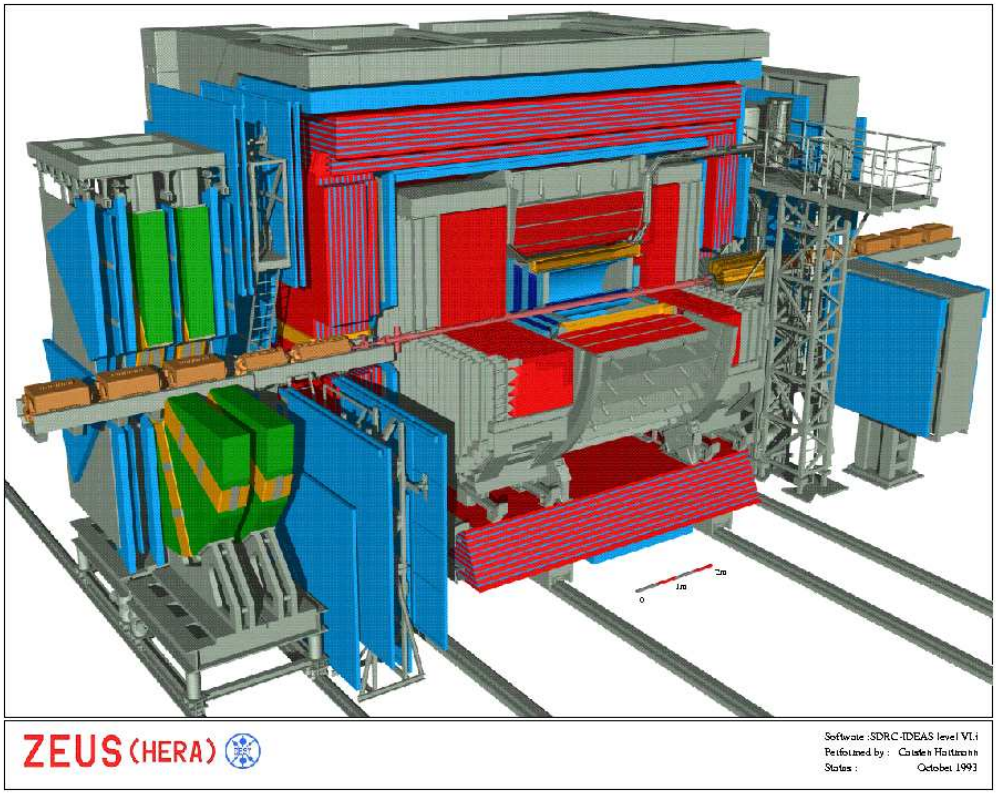

Figure 2.2: 3-Dimensional view of the ZEUS detector (before upgrade) — detector components are labelled in Fig. 2.4.

beamline detect softly scattered electrons and protons as well as bremsstrahlung photons that leave the detector at angles too small to be detected in the main ZEUS detector.
Detailed information on the complete ZEUS detector can be found elsewhere [34]. In the following, only the main detector components and those relevant for this analysis will be described in more detail.

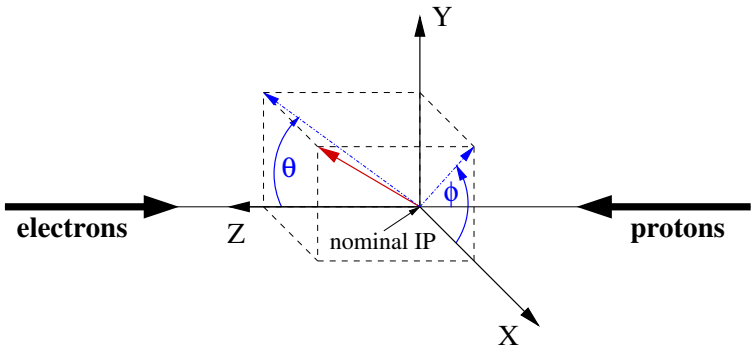

Figure 2.3: Coordinate system of the ZEUS detector.

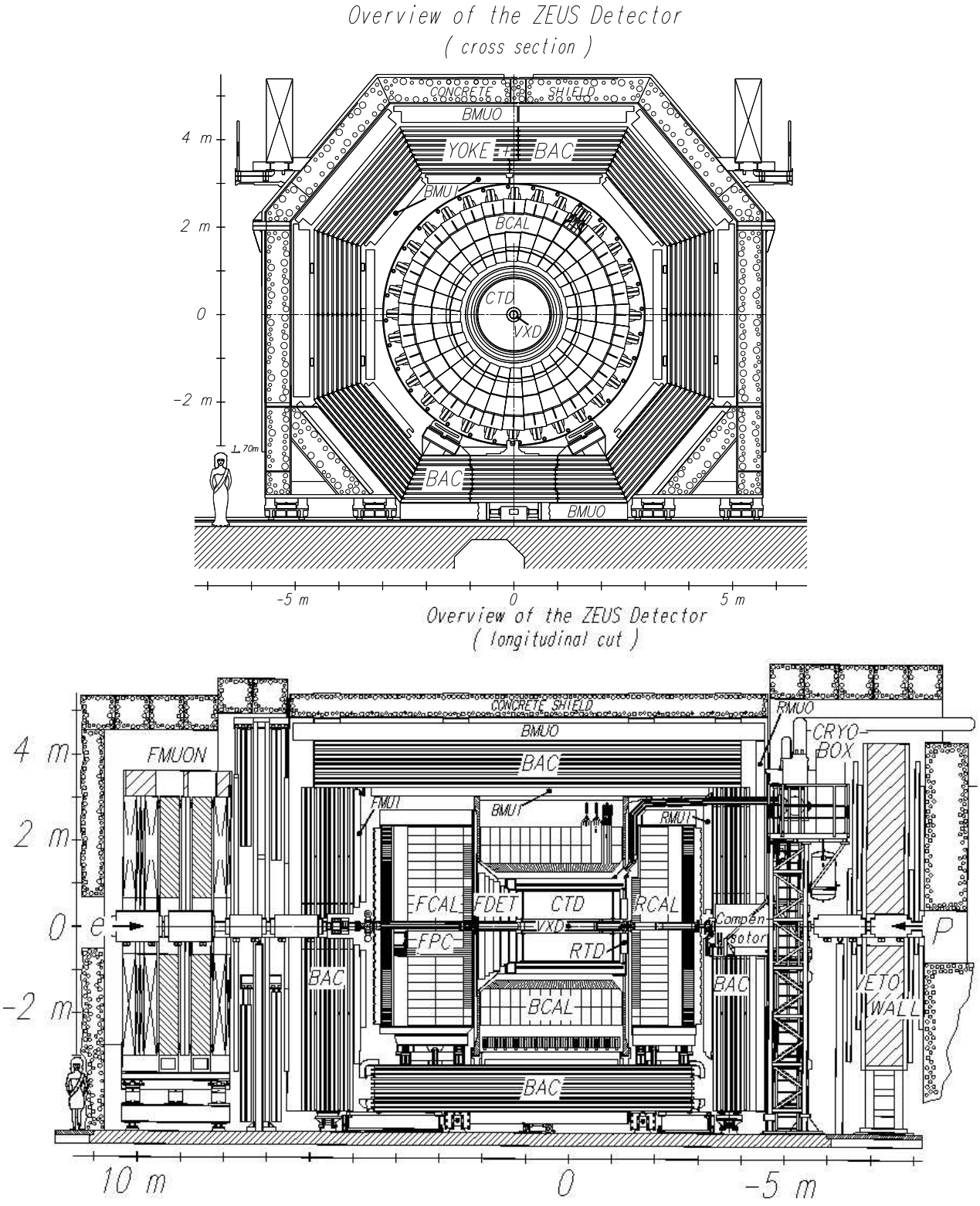

Figure 2.4: Transverse *(top)* and longitudinal view *(bottom)* of the ZEUS detector.

2.3.1 Tracking detectors

The ZEUS tracking detectors mainly consist of the central tracking device (CTD) and the forward detector (FDET). The vertex detector (VXD) was not in use anymore in the data taking for this analysis. A microvertex detector (MVD) and the straw-tube tracker (STT) were installed during the upgrade in 2000 and were therefore not available for this analysis.

The Central Tracking Device (CTD)

The CTD [35] is a cylindrical drift chamber which operates in the magnetic field of 1.43 T provided by the superconducting solenoid (see Sec. 2.3.3). The CTD surrounds the beampipe and covers a polar range of $15° < \theta < 164°$ and an azimuthal range of 360°. As depicted in Fig. 2.5, it is radially subdivided into 9 circular superlayers of 32 drift cells in the centre and up to 96 cells in the outer superlayer. Each cell has eight sense wires. In the superlayers with odd numbers, these sense wires run parallel to the beam axis whereas in superlayers with even numbers the sense wires have a small stereo angle with respect to the beamline to provide better information on the z-position of a track. The first, third and fifth superlayers are additionally instrumented with z-by-timing electronics, mainly for triggering purposes. The resolution in z is $1.0 - 1.4\,\text{mm}$, whereas in $r - \phi$ it is about 230 μm. This leads to a

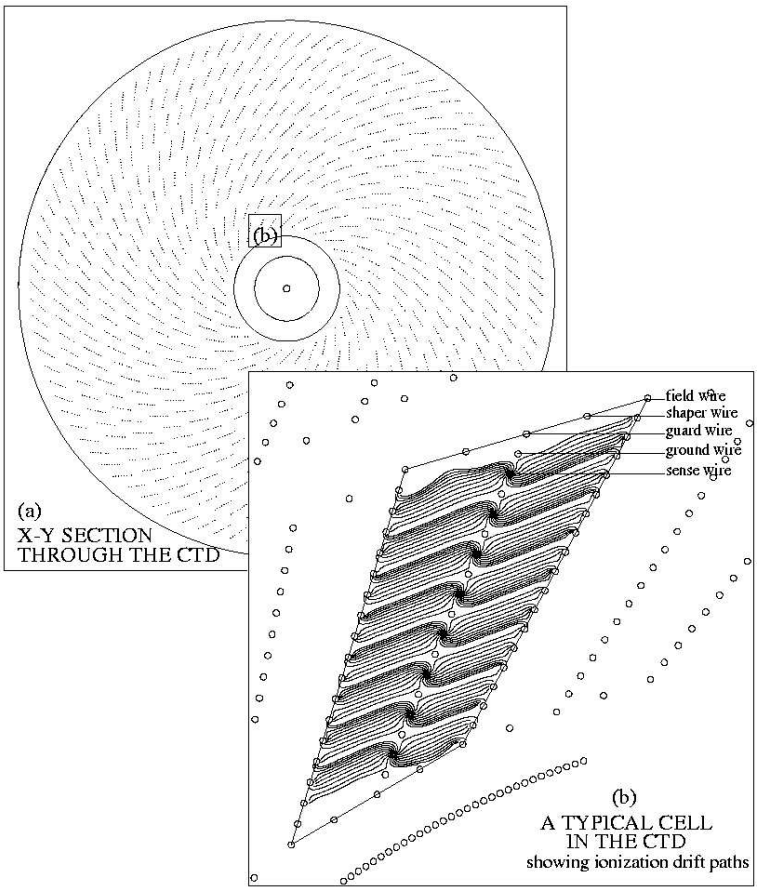

Figure 2.5: Transverse view of a CTD sector.

pseudorapidity resolution of

$$\frac{\sigma(\eta)}{\eta} = (0.2\,\eta \oplus 0.3)\,\%$$

for $p_T > 2\,\mathrm{GeV}$. The transverse momentum resolution was determined [36] as

$$\frac{\sigma(p_T)}{p_T\,[\mathrm{GeV}]} = (0.58\,p_T\,[\mathrm{GeV}] \oplus 0.65 \oplus \frac{0.14}{p_T\,[\mathrm{GeV}]})\,\%$$

The CTD uses a gas mixture of argon, carbon dioxide and ethane.

The Forward Detector (FDET)

The FDET comprises the forward/rear tracking detector (FRTD) and a transition radiation detector (TRD).
The FRTD [37] consists of three planar drift chambers in the forward (FTD) and one in the rear (RTD) direction. The FTD extends the tracking to small values of θ by its coverage of $7° < \theta < 28°$ (RTD: $160° < \theta < 170°$) and improves the track measurement in the forward direction where the highest particle densities are observed due to the Lorentz boost in proton direction. Each FTD module consists of three layers of drift cells which are rotated by $\pm 60°$ with respect to the first layer (Fig. 2.6, left). The drift cells are perpendicular to the beampipe. Each cell has six signal wires and a number of field forming wires (Fig. 2.6, right). The signal wire resolution is $120\,\mu$m. The FRTD operates with a gas mixture of argon, carbon dioxide and ethanol. The TRD consists of two modules placed in the gaps between the FTD modules. Detailed information on the TRD, which is not used in this analysis, can be found in [38]. The TRD was replaced by the STT [39] during the upgrade in 2000.

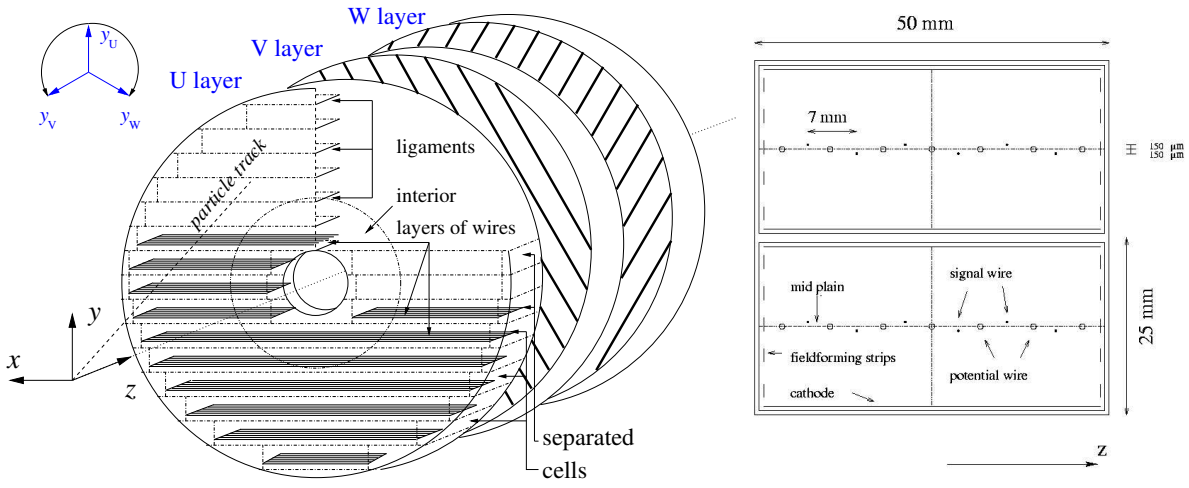

Figure 2.6: Layers of one FRTD chamber *(left)*; transverse view of a cell *(right)*.

2.3.2 Calorimeters

The Uranium Calorimeter (CAL)

The uranium-scintillator calorimeter [40] encloses the solenoid and tracking chambers. It is composed of three parts, the forward (FCAL), barrel (BCAL) and rear (RCAL) calorimeter and covers polar angles from $2.6° - 176.2°$ ($3.95 > \eta < -3.49$) and 99.7% of the total solid angle.
The CAL consists of 80 modules (Fig. 2.7). The modules of the FCAL and BCAL (RCAL) are longitudinally subdivided into one electromagnetic and two (one) hadronic sections. They consist of depleted uranium and scintillator plates laminated alternately, with a total radiation length of $25X_0$ and a absorption length of 6λ in the FCAL, 4λ in the BCAL and 3λ in the RCAL. The scintillator plates form cells of $5 \times 20\,\mathrm{cm}^2$ (RCAL : $10 \times 20\,\mathrm{cm}^2$) in the electromagnetic section and cells of $20 \times 20\,\mathrm{cm}^2$ in the hadronic sections. Light generated in the scintillator is collected on both sides of the module by wavelength shifters and converted into an electronic signal by photomultiplier tubes. The calibration of the photomultipliers is monitored with the signal from the radioactivity of the ^{238}U to a precision of $< 2\%$. The

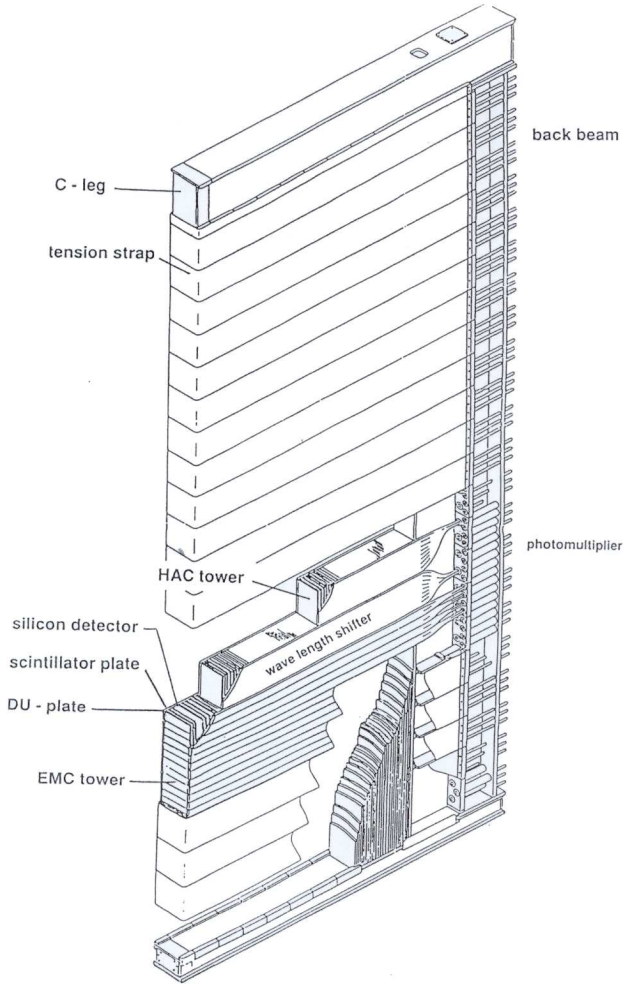

Figure 2.7: Schematic drawing of a CAL module.

CAL is compensating, i.e. electrons and hadrons of equal energy yield the same pulse height within 3% for momenta above 3 GeV/c. The energy resolution as measured in test beams is

$$\frac{\sigma}{E} = \frac{18\%}{\sqrt{E\,[\mathrm{GeV}]}} \oplus 0.2\% \qquad \text{for electrons and}$$
$$\frac{\sigma}{E} = \frac{35\%}{\sqrt{E\,[\mathrm{GeV}]}} \oplus 0.3\% \qquad \text{for hadrons.}$$

The calorimeter noise is dominated by the uranium radioactivity and is typically 15 MeV in the EMC cells and 25 MeV in the HAC cells. The calorimeter allows a time measurement with a resolution of

$$\frac{\sigma}{t} = \frac{1.5\,\mathrm{ns}}{\sqrt{E\,[\mathrm{GeV}]}} + 0.5\,\mathrm{ns}.$$

The Forward Plug Calorimeter (FPC)

The FPC [41] is a lead scintillator sandwich calorimeter which was installed in the beam hole of the FCAL in 1997 and extends the calorimetric coverage of the ZEUS detector from $\eta = 3.95$ to 5.33. It is located at a distance of $z = 226$ cm from the IP and covers an area of $19.2 \times 19.2\,\mathrm{cm}^2$ with a hole of 4.8 cm in diameter for the beampipe. Like the CAL, the FPC is compensating and longitudinally segmented into an electromagnetic (EMC) and a hadronic (HAC) section which are read out separately by wavelength shifting fibres and photomultipliers. The EMC (HAC) section consists of 60 (16) cells (see Fig 2.8) with a size of $24 \times 24\,\mathrm{mm}^2$ ($48 \times 48\,\mathrm{mm}^2$), and has an energy resolution of

$$\frac{\sigma_E}{E} = \frac{25\%}{\sqrt{E\,[\mathrm{GeV}]}} \oplus 3\%$$

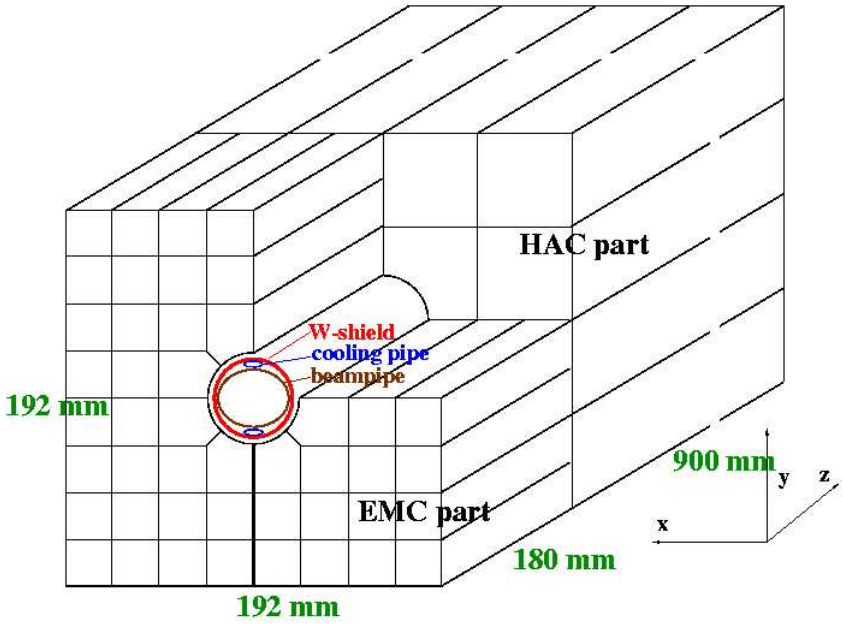

Figure 2.8: Schematic drawing of the FPC.

for electrons and

$$\frac{\sigma_E}{E} = \frac{50\%}{\sqrt{E\,[\mathrm{GeV}]}} \oplus 5\%$$

for hadrons. The radiation and absorption length of $26.5X_0$ and 5.08λ units respectively, were designed to be similar to those of the FCAL in order to minimize fluctuations of the energy measurements in the transition area.
The FPC improves the energy measurement in the forward direction where most particles are produced due to the large energy imbalance of the incident electron and proton and the resulting Lorentz boost. It also enables slightly scattered protons to be detected. In this analysis, a lack of signal in the FPC is used to identify more clearly events with a large rapidity gap in forward direction.

The Backing Calorimeter (BAC)

The proportional tube chambers of the BAC [34] are placed in the gaps of the iron yoke (Sec. 2.3.3) and measure particle momentum. Particles which are able to traverse the yoke are mostly muons. In this analysis, the BAC is used to reject background caused by cosmic muons (Sec. 7.2.2).

2.3.3 Other detector components

Magnets

The *solenoid* is a superconducting magnet which surrounds the CTD and provides the magnetic field which is necessary to bend charged particles detected in the CTD and measure their momentum from their track curvature. The material of the solenoid accounts for $0.9X_0$ of radiation length. The effect of the magnetic field on the beams is suppressed by a compensator shield provided by a second superconducting solenoid, the *compensator*, at the rear endcap of the *iron yoke*. The yoke has the shape of an octagonal cylinder and surrounds the inner ZEUS detector. It consists of iron plates welded together with spacer bars in between and is magnetised with a toroidal field of 1.5 T in the forward direction.

The Luminosity Monitor (LUMI)

The luminosity $\mathcal{L}$ measures the rate R of events per second for a given process with the cross section σ and is defined by the relation $R = \mathcal{L} \times \sigma$. A precise measurement of the luminosity is crucial for the correct calculation of cross sections and therefore requires

- a process with a clear experimental signature, and
- a cross section that is theoretically well known and
- large so that statistical uncertainties are small.

The latter criterion is also necessary to allow a continuous and fast monitoring of the luminosity at HERA which is essential for beam steering and focusing.
These requirements are satisfied by the bremsstrahlung process $ep \to e'\gamma p$, in which an incoming electron radiates a high energy photon γ in the electromagnetic field of the proton charge.

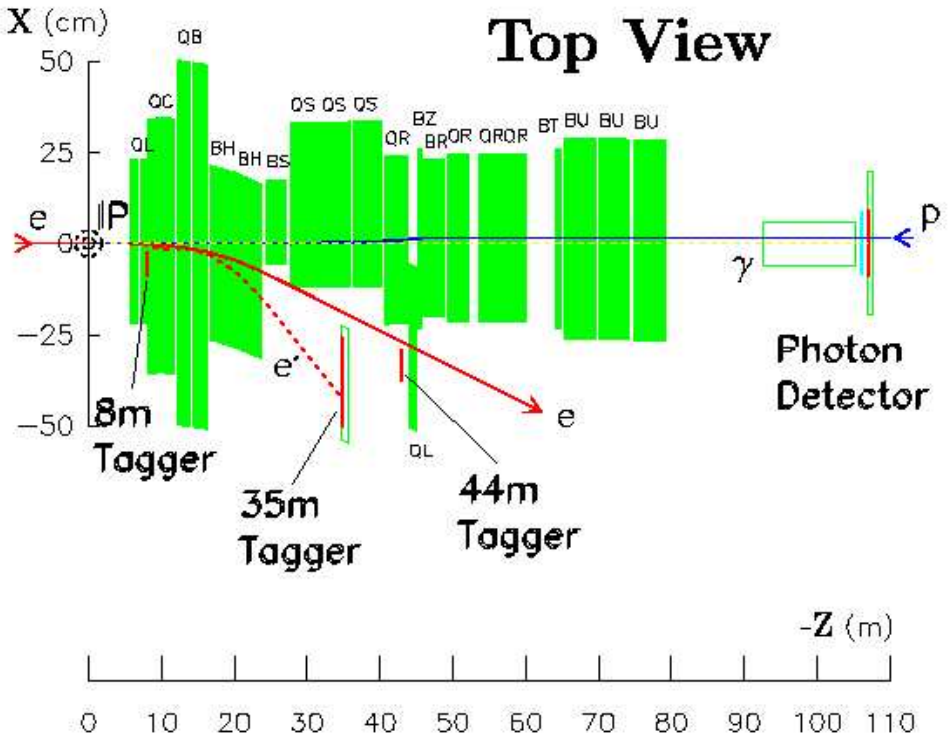

Figure 2.9: Schematic top view on the luminosity detector.

The scattered electron has less energy than the beam electrons and is therefore bent towards the centre of the ring by the electron beamline magnets. These electrons can be tagged at distances of $-8\,\mathrm{m}$, $-35\,\mathrm{m}$ or $-44\,\mathrm{m}$ from the interaction point. Their measurement is used as additional systematic check and for the estimation of background corrections.
The luminosity calculation is based on the rate of radiated photons that leave the beampipe through a copper-beryllium window and are measured with the LUMI detector [42] at a distance of $z = 92.5\,\mathrm{m}$ from the interaction point. After traversing a $12.7\,\mathrm{m}$ long vacuum pipe and a graphite absorber to shield against synchrotron radiation, the photon is detected in a lead-scintillator sampling calorimeter at a distance of $z = 107\,\mathrm{m}$. The detector has an energy resolution of $\sigma(E)/E = 0.23/\sqrt{E\,[\mathrm{GeV}]}$, corrected for event pile-up, electron-gas background and geometrical acceptance of bremsstrahlung photons. The total systematic uncertainty of the luminosity measurement is 2.25% for the data taken in 1999/2000..

2.4 Trigger and data acquisition

The number of events from *ep*-interactions is small (typically $\ll 0.1\%$) compared with the number of background events, e.g. from interaction of beam protons with residual gas in the beampipe or the wall of the beampipe itself.
At a bunch crossing interval of 96 ns, not all events can be reconstructed in detail and the data acquisition relies on an effective reduction of background events. At ZEUS this is accomplished with a three-fold trigger system [34], that consists of the First (FLT), Second (SLT) and Third

Level Trigger (TLT). On the first and second level, events are selected online by a system of component (*local*) triggers which send data to a *global* trigger (GFLT, GSLT). On the third level, events are reconstructed, selected and classified offline using computer farms.
Time-flow and event rates of the trigger system are sketched in Fig. 2.10 and summarised in Tab. 2.3.

Trigger	Input rate	Output rate
GFLT	10.4 MHz	1 kHz
GSLT	1 kHz	100 Hz
TLT	100 Hz	3 Hz

Table 2.3: Time flow of the ZEUS trigger system.

The First Level Trigger (FLT)

The GFLT has an input rate of 10.4 MHz, corresponding to the bunch crossing interval of 96 ns, and must reach a decision within 4.4 μs equivalent to 26 bunch crossings. Therefore all detector components need to store information for this time span. In case of a positive GFLT decision, all signal pipelines are stopped and the data for the corresponding bunch crossing is read out.
The GFLT decision is mainly based on analog information from the local FLT of the CAL and CTD, e.g. the energy deposits in different parts of the calorimeter and the existence of tracks originating close to the IP. The timing of signals from the FCAL and RCAL as well as the z-by-timing information (s. Sec. 2.3.1) from the CTD readout is used to reject background from beam gas events that occur upstream of the IP and deposit large amounts of energy in the detector. The output rate of the GFLT is less than 1 kHz.

The Fast Clear (FCLR)

The FCLR is an additional, intermediate level of the trigger system: Contrary to the other triggers, it solely provides a veto decision which is based on the FLT information of the CAL but as more time is available for the FCLR, additional calculations can be performed by the local FLT of the CAL. If the result of these calculations indicates a background event, the local FLT sends a request to the GFLT to abort the event. In case the positive GFLT decision was mainly based on CAL information, the GFLT sends an interrupt to all components. The FCLR thus reduces the busy-time of most components' readout and hence the average dead-time of the readout system.

The Second Level Trigger (SLT)

During the time span needed for a GFLT decision, data from most components are digitised and can be used by the GSLT for more advanced selection based on basic calculations. The local SLT of the CAL calculates the total transverse energy E_T and the missing E_T while the local SLT of the CTD determines the number and quality of tracks and vertex tracks and their corresponding charge, a closer calculation of the z-vertex and the track angles ϕ and θ including error estimates.
The GSLT must reach a decision within 10 ms and reduces the rate to about 100 Hz.

The Third Level Trigger (TLT)

In case of a positive GSLT decision, information from all components is transferred to the Event Builder (EVB). The final selection is reached by physics filters of the TLT, based on a first reconstruction of the event. The accepted events are recontructed in processor farms, classified with trigger bits and stored on tape.

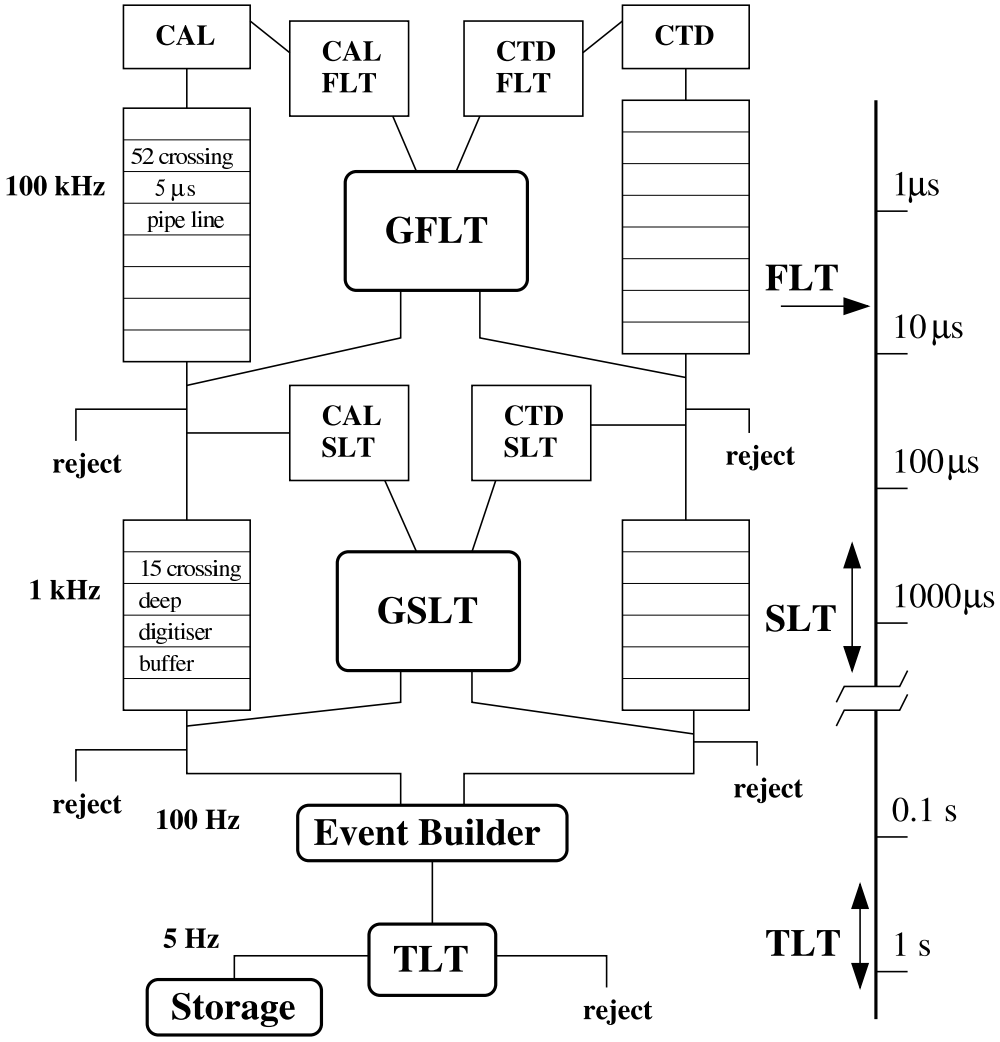

Figure 2.10: Data processing and trigger rates at the ZEUS detector.

Chapter 3

Data taking

This analysis was performed using data taken with the ZEUS detector in the years 1999 and 2000. The trigger selection will be discussed in Sec. 6.1. In 1999 HERA switched from e^-p to e^+p operation. All three data sets – $99e^-p$, $99e^+p$ and $00e^+p$ – were handled equally.

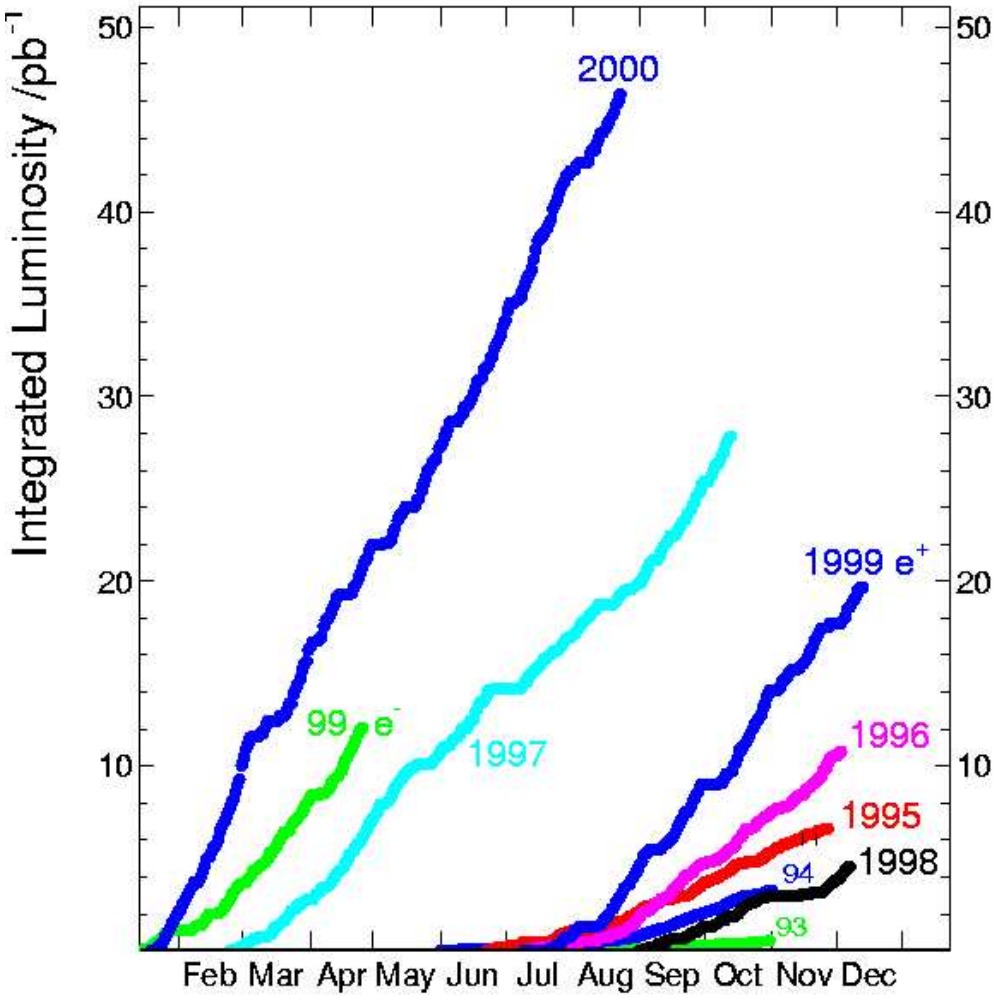

Figure 3.1: Integrated luminosity of ZEUS data for the years 1993-2000.

Events were selected by taking advantage of the flag EvTake (on) which allows also partially corrupted runs to be included. The luminosity of the three data sets is given in Tab. 3.1. For a number of runs (37588-37639), the nominal z-vertex was shifted; these runs were excluded. The integrated luminosity $\mathcal{L}_{tot}$ of all set sums up to $\mathcal{L}_{tot} = 77.1\,\mathrm{pb}^{-1}$ (see also Fig. 3.1).

	$99\,e^-p$	$99\,e^+p$	$00\,e^+p$	Total
Run range	31784-32906	33125-34486	35031-37715	31784-37715
with shifted vertex			37588-37639	
Runs	462	516	1042	2020
Runs w/o shifted vertex			1009	1987
Hera delivered	$17.119\,\mathrm{pb}^{-1}$	$28.537\,\mathrm{pb}^{-1}$	$66.411\,\mathrm{pb}^{-1}$	$112.07\,\mathrm{pb}^{-1}$
Zeus gated	$14.005\,\mathrm{pb}^{-1}$	$23.421\,\mathrm{pb}^{-1}$	$55.097\,\mathrm{pb}^{-1}$	$92.52\,\mathrm{pb}^{-1}$
Zeus on-tape	$12.607\,\mathrm{pb}^{-1}$	$21.615\,\mathrm{pb}^{-1}$	$51.790\,\mathrm{pb}^{-1}$	$86.01\,\mathrm{pb}^{-1}$
Zeus after EvTake	$12.079\,\mathrm{pb}^{-1}$	$19.649\,\mathrm{pb}^{-1}$	$46.221\,\mathrm{pb}^{-1}$	$77.95\,\mathrm{pb}^{-1}$
Zeus after EvTake				
w/o shifted vertex			$45.406\,\mathrm{pb}^{-1}$	$\boldsymbol{77.13}\,\mathrm{pb}^{-1}$

Table 3.1: Run ranges and integrated luminosites of data subsets.

Chapter 4

Monte Carlo simulation

4.1 Purpose

Parton interactions are described theoretically by means of pQCD. Partons, however, are not directly observable, only the final state products are, i.e. hadrons and their decay products. More precisely, from an experimental point of view all information about initial state parton interactions is limited to and drawn from detector responses which measure hadrons (see Fig. 4.1). In the following, the terms *Parton Level* (PL), *Hadron Level* (HL) and *Detector Level* (DL) will be used to refer to the subsequent steps of the complete process.
The kinematic range on DL is reduced by the detector's coverage and affected by its acceptance and resolution. Cross sections based on DL are subject to experimental limitations and are not comparable with results achieved by other experiments. By transforming data from DL to HL, such experimental dependencies can almost be eliminated.
On the other hand, the transition from PL to HL requires the hadronisation process to be quantified. Since the fragmentation of partons to hadrons is due to the strong force at

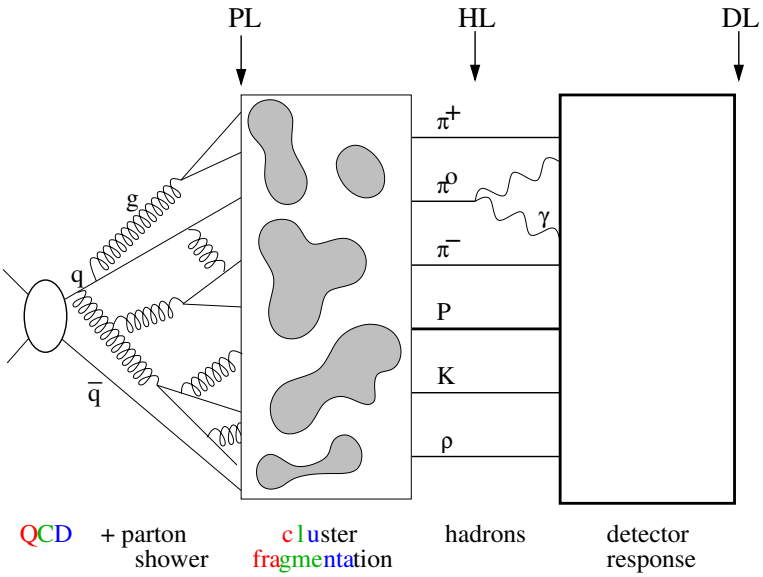

Figure 4.1: Illustration of parton level (PL), hadron level (HL) and detector level (DL).

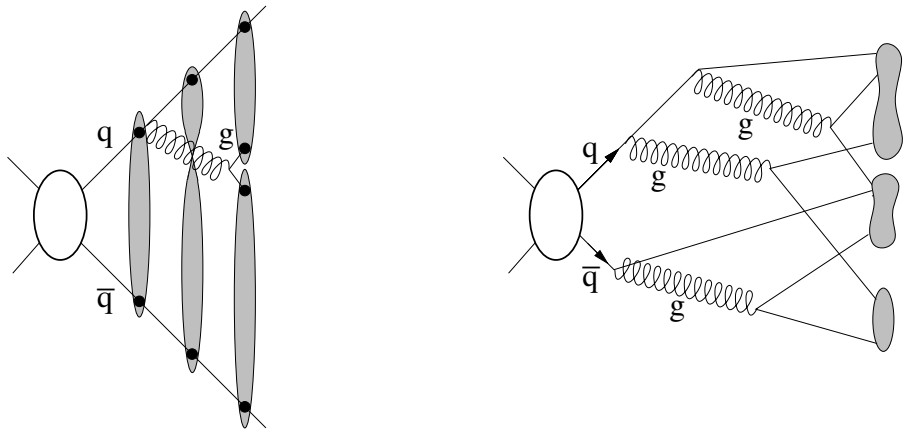

Figure 4.2: String *(left)* and cluster fragmentation *(right)*.

large distances, where α_S is large, it is beyond the scope of pQCD calculations. Additional theoretical models (e.g. *string* or *cluster* fragmentation model, see Fig. 4.2) are needed to describe the process of hadronisation, and therefore the hadronisation is included in the theoretical modelling.
For the above reasons the experimental results are compared with theoretical predictions at an intermediate level, i.e. on HL. The transformation of experimental data from DL to HL is achieved using Monte Carlo (MC) simulations: Events of the initial process are generated based on pQCD and final state partons from this interaction are evolved according to a hadronisation model. Subsequently the interaction of hadrons with detector material and the response of the detector components are simulated. This is iterated for large numbers of events to obtain predictions based on statistical analyses. The generation procedure is sketched in Fig. 4.3. MC simulations provide information on PL, HL and DL. In this analysis, MC simulations are used for two purposes:

- to transform experimental data from DL to HL
  (by calculating *correction factors* and *acceptances*, see Sec. 9.3);
- to transform NLO pQCD calculations from PL to HL
  (by calculating *hadronic corrections*, see Sec. 12.2).

Two MC programs were used: RAPGAP MC for both purposes mentioned above, and POMWIG MC to provide a systematic check of the hadronic corrections obtained with RAPGAP.

4.2 RAPGAP

Event generation, simulation and reconstruction

Diffractive events in PHP were generated with RAPGAP v3.00 [43]. For the proton and photon, the structure functions CTEQ 5M1 [44] and GRV-G-VO [18], respectively, were used. At the time the MC sample was generated, only the H1 LO fit2 [24] was available for the diffractive parton distributions. Events were generated separately for direct and resolved PHP. Three different subsets were produced for direct PHP, corresponding to the processes shown in Fig. 1.7 (top row):

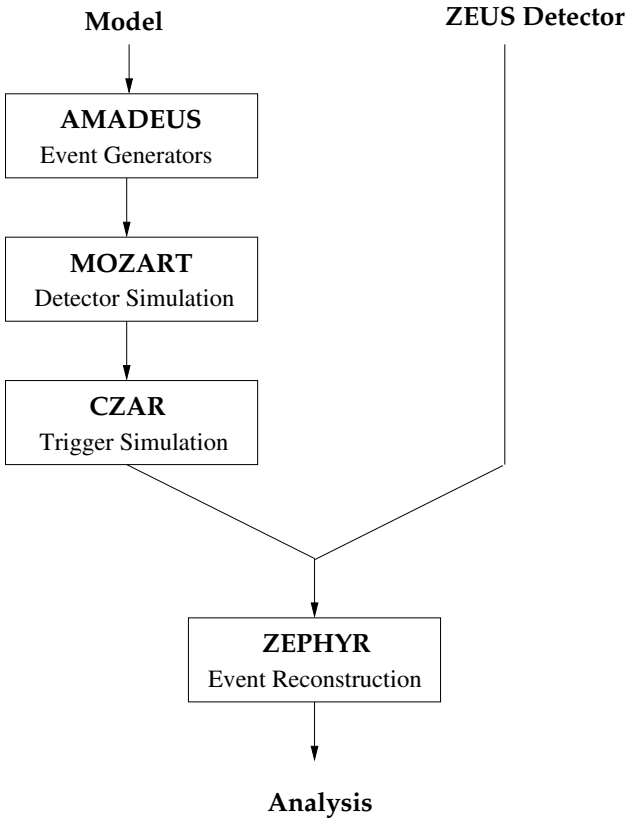

Figure 4.3: Generation procedure of MC events: A MC program is interfaced to the program AMADEUS for automatic event generation at ZEUS. Subsequently, the response of the ZEUS detector to the final state hadrons and the trigger system are simulated by MOZART and CZAR, respectively. Finally, events are reconstructed with ZEPHYR.

- $q\bar{q}$-production of light quarks: u, d, s;
- $q\bar{q}$-production of heavy quarks: c;
- QCD-Compton scattering.

Resolved PHP includes all the processes given in Tab. 4.1, corresponding to the LO contributions shown in Fig. 1.7 (middle / bottom row), where the main contribution results from the process with gluons in the initial state. The kinematic range of the simulated processes was

processes & luminosity $\mathcal{L}_{\text{RAPGAP}}$			
direct PHP *(dir)*			resolved PHP *(res)*
u, d, s *(lq)*	c-quark *(hq)*	QCD-Compton *(qcdc)*	
$\gamma + g \to q + \bar{q}$		$\gamma + q \to g + q$	$g+g \to q+\bar{q}$, $q+\bar{q} \to q+\bar{q}$ $g+g \to g+g$, $q+\bar{q} \to g+g$ $g+q \to g+q$, $q+q \to q+q$
$160.66\,\text{pb}^{-1}$	$162.06\,\text{pb}^{-1}$	$321.24\,\text{pb}^{-1}$	$124.70\,\text{pb}^{-1}$

Table 4.1: Subprocesses simulated with RAPGAP and generated luminosity.

Kinematic cuts
$Q^2 < 1.0\,\mathrm{GeV}^2$
$t \ < 1.0\,\mathrm{GeV}^2$
$p_T^{min} = 5\,\mathrm{GeV}$
(except for QCD-C)

Table 4.2: Kinematic cuts applied to the event generation in RAPGAP MC.

chosen according to the cuts given in Tab. 4.2. Parton showers are included according to the Altarelli-Parisi splitting functions [14].

Fragmentation model

Hadronisation in RAPGAP is based on the string fragmentation model [45, 46] as depicted in (Fig. 4.2a). In this model, pairs of quarks are considered to be connected by a string representing the strong force. As the quarks depart from each other, the colour field between them grows stronger until the production of an additional $q\bar{q}$-pair becomes favourable. The colour of the new $q\bar{q}$-pair can create a colourfree gap between the quarks, and free mesons can be formed (Fig. 4.2a). More complicated scenarios assume the existence of *diquark*-pairs and allow the production of baryons to be explained. The length of the string between two quarks corresponds to the energy stored in the colour field and can be tuned to describe the suppression of heavy-quark production.

Generated luminosity

The luminosity for the four simulated processes is given in Tab. 4.1.

4.3 POMWIG

Another MC generator was used to test if, and to what extent, hadronic corrections depend on the hadronisation model implemented in the MC simulation. For this purpose, the POMWIG MC program [47] was chosen which uses the cluster fragmentation model [45] (see Fig. 4.2b). POMWIG v1.2 is a modification to HERWIG v5.9 [48] for the simulation of diffractive processes in DIS. The modification takes advantage of the formal similarity between the exchange of a Pomeron in ep collision and the exchange of a photon in ee collisions, as depicted in Fig. 4.4: In both cases a colourless object (γ or $I\!P$) is radiated from an unmodified particle (e or p) and the radiated object is considered to interact hadronically.
Hence the diffractive process can be simulated by replacing the incident proton by an electron and exchanging the photon flux and structure function by those of the Pomeron. Naturally, this procedure is restricted to processes in which the radiated γ interacts directly, i.e. not as a source of partons as in resolved PHP. The overlapping region with direct PHP is constrained by $10^{-5} < Q^2 \ (< 1.0\,\mathrm{GeV}^2)$ so that hadronisation can only be tested in a reduced range of kinematics. The authors of POMWIG also emphasize that "POMWIG *fails* [...] *in the highest* $z_{I\!P}$ *bins, that is at low diffractive masses*" [47].
The program code of POMWIG was modified to run with the new HERWIG release v6.04 [48] and interfaced to AMADEUS.

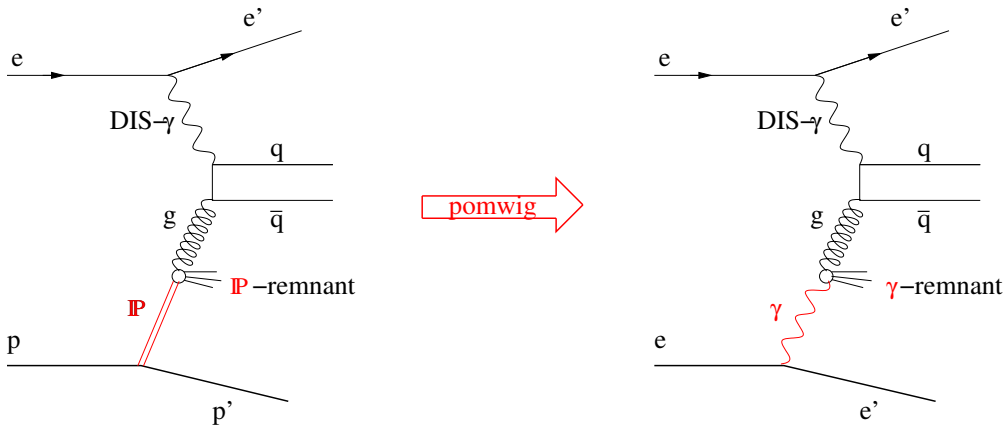

Figure 4.4: Simulation of the diffractive exchange in POMWIG

Event generation, simulation and reconstruction

Events were generated using HERWIG IPROC 9130, i.e. boson-gluon-fusion of light (u, d, s) and c-quarks and QCD-Compton scattering in neutral current DIS. The simulations of soft underlying events, i.e. soft remnant fragmentation was excluded. By default, POMWIG uses the diffractive structure function H1 LO fit 2 (NSTRU = 9). The $I\!P$ flux was parametrised according to Eqn. 1.8 where values obtained by the H1 collaboration [24] were used as default parameter:

$$\alpha_{I\!P} = 1.20, \quad \alpha_{I\!P}\prime = 0.26, \quad B_{I\!P} = 4.6\,.$$

The kinematic range was selected by the cuts summarised in Tab. 4.3.

Kinematic cuts
$10^{-5} < Q^2 < 2.0\,\mathrm{GeV}^2$
$10^{-6} < t < 5.0\,\mathrm{GeV}^2$
$10^{-4} < x_{I\!P} < 0.30$
$p_T^{min} = 2.5\,\mathrm{GeV}$
$-12.0 < \eta^{jet} < 12.0$

Table 4.3: Kinematic cuts applied to the event generation in POMWIG MC.

Fragmentation model

POMWIG does not modify the HERWIG program code for the simulation of the hadronisation process. HERWIG – and therefore POMWIG – is based on the cluster fragmentation model [**?**]: In a first step, gluons within a shower are split to produce $q\bar{q}$-pairs. Subsequently, quarks become *pre-confined* in colourless clusters (Fig. 4.2b), which decay into hadrons.

Generated luminosity

In total 10^6 events were generated, corresponding to a luminosity of $\mathcal{L}_{\mathrm{Pomwig}} = 363.50\,\mathrm{pb}^{-1}$.

Chapter 5

Reconstruction of kinematic variables

The energy scale uncertainty of the CAL, coupled with differences between data and MC simulations, is the dominant effect on the systematic uncertainty in jet measurements at ZEUS: CAL energy uncertainties of $\pm(3-5)\%$ lead to jet energy uncertainties of $\sim \pm(10-20)\%$ [49]. Therefore a good reconstruction of the energy is essential. In this chapter, the energy reconstruction and corrections applied to the CAL and jet energies are discussed. In addition, experimental observables for the kinematic variables y_{JB}, $x_{I\!P}$, x_γ, $z_{I\!P}$ and M_X are introduced.

5.1 CAL cell energy

The energy deposits measured in the calorimeter were corrected for attenuation in inactive detector material between the interaction point IP and the CAL as well as for differences of data and MC in the years 1998-2000 [50] according to Tab. 5.1. The CAL is also affected by different sources of noise which are reduced by the following means:

- sometimes only one of the two photomultipliers of a CAL cell returns a large signal; such *mini sparks* are removed by an imbalance cut on the signals of the photomultipliers;
- *hot cells* can be detected by calibration of the CAL with the radiation from ^{238}U, and a frequently updated list of hot cells is taken into account for analyses;
- signals of isolated cells below a certain energy threshold are ignored ($E_{EMC} < 100\,\text{MeV}$, $\quad \text{E}_{\text{HAC}} < 150\,\text{MeV}$).

CAL section	FCAL		BCAL		RCAL	
scale	1.00		1.05		1.022	
subsection	FEMC	FHAC	BEMC	BHAC	REMC	RHAC
HFS scale	1.024	0.941	1.003	1.044	1.0	1.0

Table 5.1: CALCORR table - correction factors applied to cell energy measurement in data to account for differences with MC, and additional scaling factors for the hadronic final state (HFS) for 1998-2000.

5.2 ZUFOs

5.2.1 CAL energy measurement and CTD track reconstruction

The *hadronic final state* (HFS) has a charged particle and neutral particle component. The energy of both components is measured by the CAL, whereas the momentum of charged particles is also measured by the CTD.
The CAL has finite granularity but a large angular coverage and an accurate measurement of energy is provided by its cells. The shape of *clusters* of cells additionally allows some particles to be identified by their characteristic signature, e.g. in e and μ. However, its resolution becomes poor for low momentum particles, which are likely to get absorbed in inactive material in front of the CAL, e.g. the solenoid coil. In contrast, the CTD track reconstruction provides a precise measurement of particle momentum, especially at low momentum, but is restricted to charged particles and limited in the forward direction where particles traverse only few superlayers before leaving the CTD via the front plate at low angles (Tab. 5.2).
The combination of tracking and calorimeter information significantly improves the reconstruction of the HFS. Internally, the term ZEUS *Unidentified Flying Objects* (ZUFO) [51] is used for such combined energy-track objects while the term *Energy Flow Object* (EFO) is more common in ZEUS publications. The algorithm to combine energy and track information is described in the following.

	CTD	CAL
Measurement	charged momentum	charged and neutral energy
Angular coverage	$15° - 164°$	$2.6° - 176.2°$
Granularity	n.a.	worse in forward direction
Resolution	degrading for high momentum	degrading for low energy

Table 5.2: Complementarity of CAL and CTD measurements.

5.2.2 Clustering of CAL cells

As first step, adjacent cells in the EMC, HAC1 and HAC2 sections are clustered layer by layer into *cell islands*, where a logarithmic energy weight is used to account for the exponential decline of the shower energy distribution from the shower maximum [51]. In the second step of the algorithm, the resulting 2-dimensional cell islands are combined to 3-dimensional objects, *cone islands*, by starting from the outer HAC and processing inwards.

5.2.3 Matching of CTD tracks with CAL clusters

In a subsequent step, good tracks are extrapolated to the inner surface of the calorimeter and matched to cone islands (Fig. 5.1) if the distance of closest approach is either $< 20\,\text{cm}$ or smaller than the island radius. Here the term *good tracks* means that the track

- originates from primary vertex;
- traverses at least 4 superlayers of the CTD;

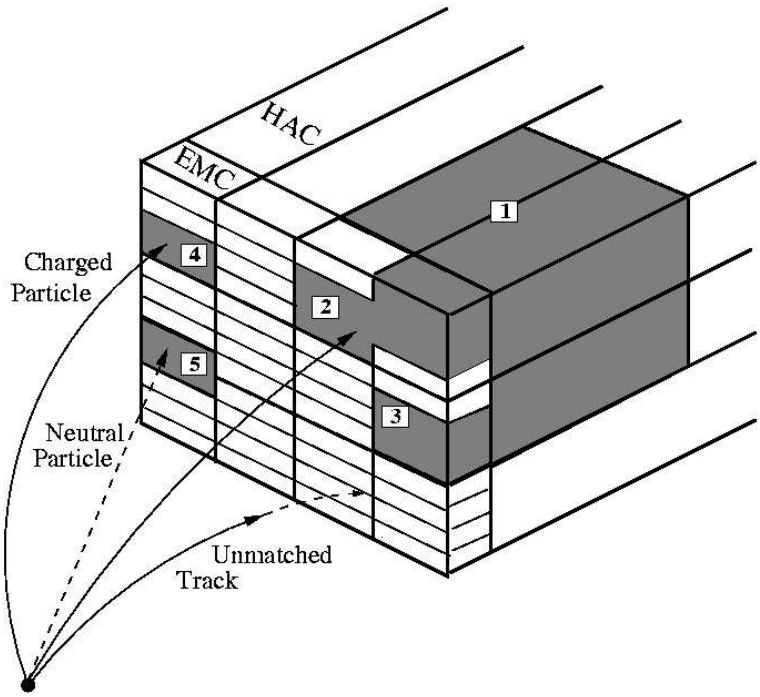

Figure 5.1: Illustration of CAL Clustering and matching: (1) a cone island (2-5) cell islands partly associated with tracks – taken from [51].

- has a p_T between $0.1 < p_T < 20\,\text{GeV}$
  ($p_T < 25\,\text{GeV}$ for particles traversing at least 7 superlayers).

For CAL clusters not matched with a track (e.g. for neutral particles) and for CTD tracks not associated with a cluster (e.g. if the particle momentum is too small to reach the CAL), information of the corresponding detector will be used. In case of good tracks not associated

islands	tracks	detector used
0	1	CTD
1	1	CTD
1	2	CTD
1	3	CTD
2	1	CTD
2	2	CTD
1	0	CAL
1	>0	CAL
1	1	CTD & CAL
2	1	CTD & CAL

Table 5.3: Decision table for CAL-CTD matching. For the last two cases, angular information is obtained from the CTD tracks whereas the energy information is taken from the CAL. In case of a 1-to-1 matching, the decision which detector(s) will be used, depends on the resolution of momentum and energy *(see text)*.

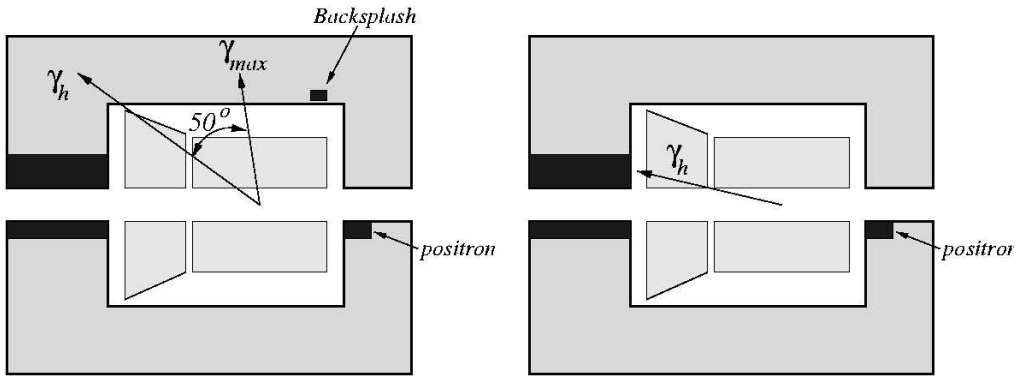

Figure 5.2: Schematic picture of calculation of γ_{max} from hadronic angle γ_h – taken from [51].

with a CAL object, the energy will be determined on the assumption that the particle is a pion. For a 1-to-1 matching, the momentum will be used if the track momentum resolution is better than the island energy resolution ($\sigma(p)/p < \sigma(E)/E$) or if the energy deposit is due to the associated track ($E/p < 1.0 + 1.2\,\sigma(E/p)$). Additional requirements apply for more complicated track-island matches (Tab. 5.3) and for particles with properties of muons [49, 52].

5.2.4 Backsplash correction

Small energy deposits in the detector at large polar angles have a large contribution to the hadronic system $\delta_h = (E - p_z)_h$ and hence a large effect on the reconstruction of y_{JB}[1] which is calculated from δ_h:

$$y_{JB} = \frac{\delta_h}{2E_e} = \frac{(E - p_z)_h}{2E_e}$$

However such energy deposits are often caused by other mechanisms than the *ep*-interaction:

- scattering in the inner part of the detector in front of the CAL, e.g. in the beampipe or the inner wall of the CTD;
- high energy showers in the FCAL causing production of low energy neutral particles (photons or neutrons) that traverse the detector in any direction;
- noisy CAL cells;
- overlay events.

These effects are summarised under the term *backsplash* [52, 54]. At small values of $y_{JB} \lesssim 0.3$, such deposits in the rear side of the detector can strongly bias the δ_h measurement. A procedure to remove contributions from backsplash was developed in [52] and is based on the observation that backsplash is characterised by low CAL energy and no associated track: A polar angle γ_{max} is calculated according to $\gamma_{max} = \gamma_h + \gamma_{\text{offset}}$ (see Fig. 5.2), where γ_h is

[1] The index indicates the reconstruction of y by the Jacquet-Blondel method [53].

the energy-weighted mean of all ZUFOs *(hadronic angle)* and γ_{offset} is a phenomenological parameter and was found to yield best results for $\gamma_{\text{offset}} = 50°$. Subsequently all clusters with $\gamma > \gamma_{max}$ without a vertex track and less than 3 GeV are removed unless their energy is > 1.5 GeV and the timing is consistent with a particle originating from the vertex. Finally γ_h and γ_{max} are recalculated. The procedure is iterated until the difference of γ_h between two iterations is $< 1\%$ or the number of iterations is larger than 3.
The procedure yields good agreement of data and MC in DIS [52]. For PHP, more soft particles from the *ep* interaction are expected and the application of backsplash correction is problematic. The first version of the analysis was performed with ZEUS code that did not allow backsplash correction to be switched off completely. A new release of ZEUS code provided such an option. The influence of the backsplash correction was investigated and found to have effects on the cross section at the order of up to 5%. Final results were hence obtained with a new version, i.e. without backsplash correction.

5.2.5 ZUFO energy correction

Reconstructed ZUFOS still need to be corrected for energy loss in the detector due to inactive material. A formerly recommended version was derived by J. Vossebeld and A. Ochs *(VO-corrections)* [55–57] and compared with a new method *(DM-corrections)* [58, 59] which was implemented in the ZEUS code recently.

ZUFO energy correction by Vossebeld & Ochs

A formerly recommended version for ZUFO energy correction was invented by J. Vossebeld [55]. It assumes that CAL-based ZUFOs are affected by energy loss due to inactive material whereas CTD-based ZUFOs are considered to provide an accurate measurement of a particle's energy. Later, the method was improved by A. Ochs [57].
Corrections were determined separately for data as well as for the HERWIG and ARIADNE MC programs[2] in different bins of θ. These bins reflect the detector geometry, in particular the so-called *supercracks*, i.e. the intersections between FCAL, BCAL and RCAL.

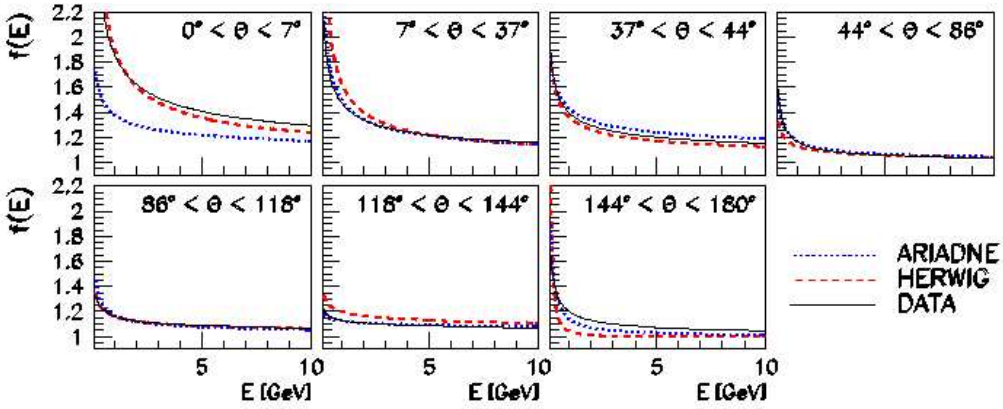

Figure 5.3: VO-corrections over E_{zufo} in 7 different bins of θ reflecting the coverage of FCAL, BCAL, RCAL and the intersections between them – taken from [56].

[2]HERWIG uses cluster fragmentation whereas ARIADNE uses string fragmentation (Fig. 4.2)

The correction factors (see Fig. 5.3) were derived from a sample of neutral current events with $Q^2 > 100\,\mathrm{GeV}^2$ and either high p_T^{lepton} or high y, and were tested with an independent PHP MC sample, where the scattered lepton is not detected in the CAL.
In the first version of this analysis, the VO corrections were used. For low ZUFO energy, E_{zufo}, these correction factors are unreasonably high ($\sim 1.5-2.8$). In addition, the correction factors differ for data and ARIADNE MC[3], in particular at low polar angles $\theta < 7^\circ$ ($\eta < 2.8$). The combination of this features turned out to have a problematic impact on one of the selection variables, η^{max} (see Sec. 5.4), which is calculated from $E_{zufo} > 400\,\mathrm{MeV}$.

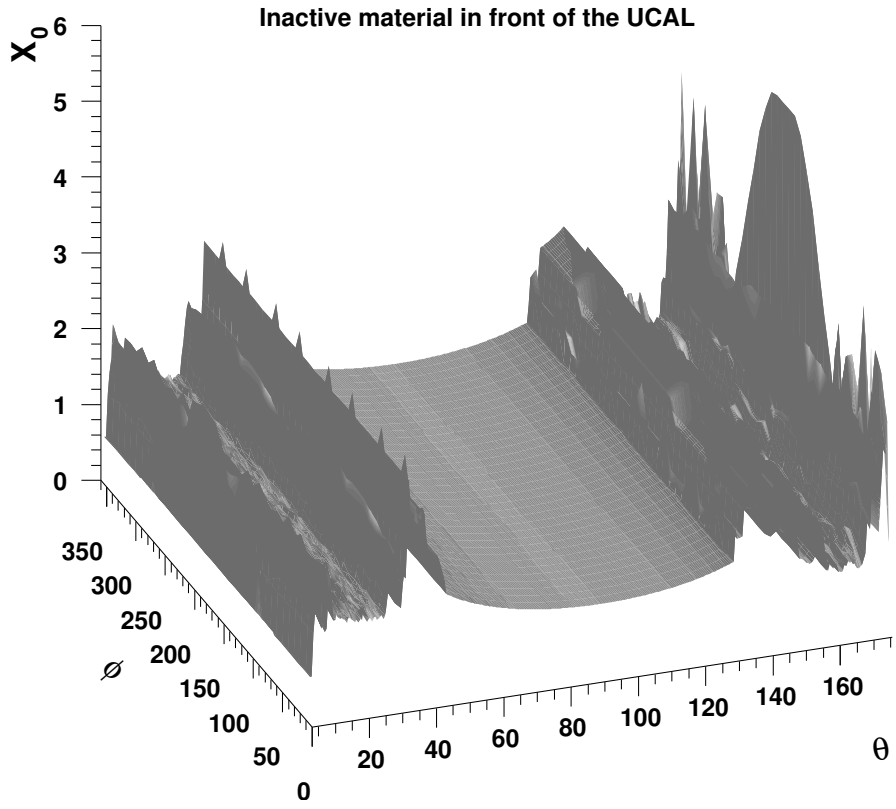

Figure 5.4: Inactive material in front of the uranium calorimeter (UCAL) in units of the radiation length X_0 in the $(\theta - \phi)$ plane, as implemented in the simulation of the detector – taken from [59].

ZUFO energy correction with DMCO

For above reasons, another method for the correction of the ZUFO energy was tested in addition. This recently available method is based on a map of the radiation length of inactive material (e.g. the beampipe, the tracking devices and the solenoid) between the interaction point and the CAL (Fig. 5.4). Correction factors were derived with a PYTHIA MC sample [60] of dijet events in $b\bar{b}$ photoproduction and parametrised as a function of the energy and polar angle of the particles.
For comparison with the VO corrections, the *dead material* (DM) correction factors have been

[3]The correction factors for ARIADNE MC were used for RAPGAP MC because both MC programs use the same hadronisation model.

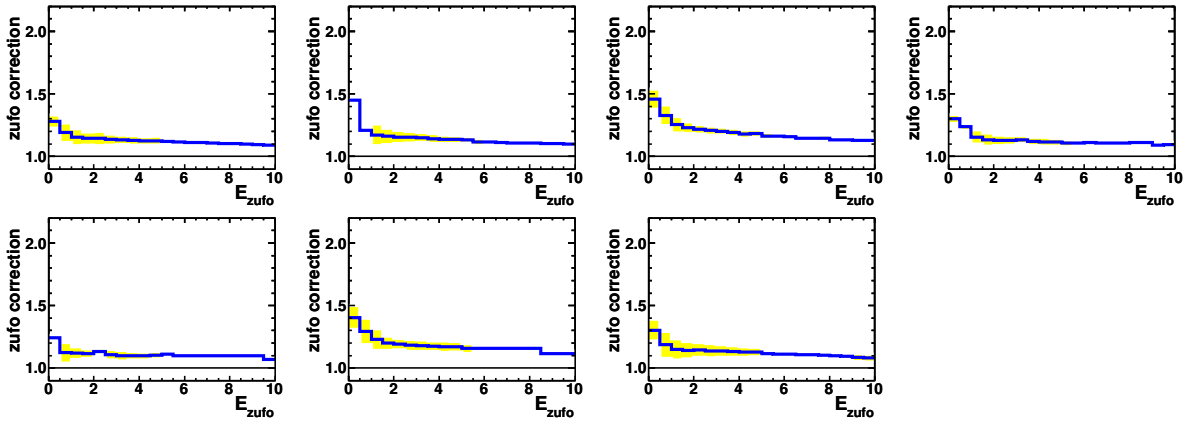

Figure 5.5: Corrections factors for DMCO over E_{zufo} in the same 7 bins of θ as in Fig. 5.3, reflecting the coverage of FCAL, BCAL, RCAL and the intersections between them – in each bin, a Gaussian fit was performed in the range $[1.0, 1.8]$; peak values are given by the dots (—), the 1σ-deviation is indicated by the band.

determined in the same binning and are shown in Fig. 5.5. Unlike the VO corrections, they do not display problematically high correction factors.

5.3 Jets

While pQCD allows processes at parton level to be calculated, experimental measurements are based on detector responses to hadrons (see Sec. 4.1). In order to compare experimental measurements with theoretical predictions, adequate properties need to be defined homogeneously on DL, HL and PL. Such properties are usually derived from abstract objects, so-called *jets* [61]: Assuming that partons fragment in a spray of hadrons whose total energy and mean direction reflect – within some uncertainties – the energy and direction of the original parton, these hadrons (or their detector response) can be combined in phase space by different procedures, i.e. *jet algorithms*.

5.3.1 Jet algorithms

Though different approaches are possible, any jet algorithm needs to fulfill two general conditions, namely *collinear safety* and *infrared safety* which can be deduced from general theoretical and experimental considerations [62]:

- Observables need to be collinear safe, i.e. for any n-parton configuration, the observable is not affected by replacing any massless parton by an exactly collinear pair of massless partons.
  [This requirement avoids collinear divergence in pQCD. From the experimental point of view, two parallel particles hitting the same CAL cell cannot be resolved and the jet algorithm should not depend significantly on the resolution of collinear particles, i.e. the angular resolution of the detector.]

- Observables need to be infrared safe, i.e. for any n-parton configuration, the observable is not affected by adding a infinitely soft parton.
  [This requirement avoids soft divergence in theory and bias from the threshold of a CAL cell or CAL noise in the experiment.]

Cone algorithm

The concept of early jet algorithms attempts to model the generation process of particles by assuming that the decaying products are bundled within a cone around the direction of the original parton. These *cone algorithms* aim to maximise the transverse energy flow E_T through a cone of radius R

$$R = \sqrt{(\Delta\eta)^2 + (\Delta\phi)^2}.$$

Here $\Delta\eta$ and $\Delta\phi$ are the differences of pseudorapidities and azimuthal angles[4] with respect to the jet direction and R is usually set to $R = 1$. Problems arise in case of overlapping jets. According to the *Snowmass Accord* [63], two jets are merged if the overlapping energy exceeds 75 % of the total energy of the jet with the lower energy. Otherwise two jets are formed and the common cells are assigned to the nearest jet. However, the jet properties depend on the number of particles in the overlap region and hence differ for parton, hadron and detector level. Agreement between hadron and parton level can be achieved by introducing a separation radius R_{sep} as suggested by [64]. The value of R_{sep}, however, is not given by theory and remains a phenomenological parameter which may be different for different sources of jet production.

Cluster algorithm

Another approach discards all information on the physical origin of particles and solely considers their distribution in phase space phenomenologically. In these so-called *cluster algorithms*, a distance quantity is defined and objects are clustered according to this quantity. This sort of algorithm is used for most purposes nowadays.
In the k_t cluster algorithm, which is used in this analysis, the distance is defined as the momentum of the softer particle transverse to the axis of the harder particle [65]:

1. For every pair (i, j) of particles, a distance d_{ij} is defined according to:

   $$d_{ij} = \min(\mathrm{E_T^i}, \mathrm{E_T^j})^2 \cdot \mathrm{R_{ij}^2} \qquad (\ \approx \min(\mathrm{E^i}, \mathrm{E^j})^2 \cdot \theta_{\mathrm{ij}}^2 \approx \mathrm{k_t^2}\ )$$

   as well as a distance d_{ib} for each particle i relative to the beam particles b:

   $$d_{ib} = (E_T^i)^2 \cdot R^2$$

   Again R is usually set to $R = 1$ for theoretical reasons [61].

[4] of partons, hadrons, ZUFOs, CAL cells or whatever is defined as input for the jet algorithm

2. If $\min(\mathrm{d_{ib}}) < \min(\mathrm{d_{ij}})$, then jet i is *complete*, otherwise, particles i and j are merged and replaced by a particle k with E_T, η and ϕ calculated from particle i, j according to

$$\begin{aligned} E_T^k &= E_T^i + E_T^j \,, \\ \eta^k &= \frac{E_T^i \cdot \eta^i + E_T^j \cdot \eta^j}{E_T^k} \,, \\ \phi^k &= \frac{E_T^i \cdot \phi^i + E_T^j \cdot \phi^j}{E_T^k} \,. \end{aligned}$$

3. The procedure is iterated, i.e. all d_{ib} and d_{ij} are recalculated and the merging of particles is continued until a list of complete particles, *jets*, remains.

The k_t-algorithm has the advantage that it naturally avoids the problem of overlapping jets. It is also unaffected by the initial particle multiplicity and hence equally applicable to both parton and hadron level. Furthermore it is less sensitive to perturbations from soft particles that get re-absorbed in the process of the algorithm.

Although the concept of jets is intuitive and comprehensible, jets are the product of a mathematical procedure and jets found by one algorithm need not correspond to jets found by another algorithm. In the first iteration of this analysis, a cone algorithm was part of the original trigger selection (Sec. 6.1). A subsequent cut on jet variables derived from the k_T-cluster algorithm had a problematic impact and led to the selection of a different trigger bit for this analysis.

5.3.2 Jet variables

Although there is also a variety of internal and external jet properties, only the following external jet variables are used in this analysis:

$$\begin{aligned} E_T^{jet} &= \sum_{i \in jet} E_T^i \,, \\ \eta^{jet} &= \sum_{i \in jet} (E_T^i / E_T^{jet})\, \eta^i \,, \\ \phi^{jet} &= \sum_{i \in jet} (E_T^i / E_T^{jet})\, \phi^j \,. \end{aligned}$$

On all three levels, only the transverse energy of the objects which are input to the jet algorithm, is considered for the reconstruction of jets. Information on the mass of these objects, as far as available on a particular level, is not taken into account.

5.3.3 Correction of the jet energy E_T^{jet}

The reconstruction of the jet energy E_T^{jet} at ZEUS was compared for jets based on cells, ZUFOs and corrected ZUFOs in [57]. As can be seen in Fig. 5.6, the E_T^{DL} of jets calculated from cell energies was on average 20% below their corresponding MC-value on HL (Fig. 5.6 bottom), while the E_T^{DL} of jets based on ZUFOs was still $\sim (10 - 15)\%$ too small (Fig. 5.6 middle).

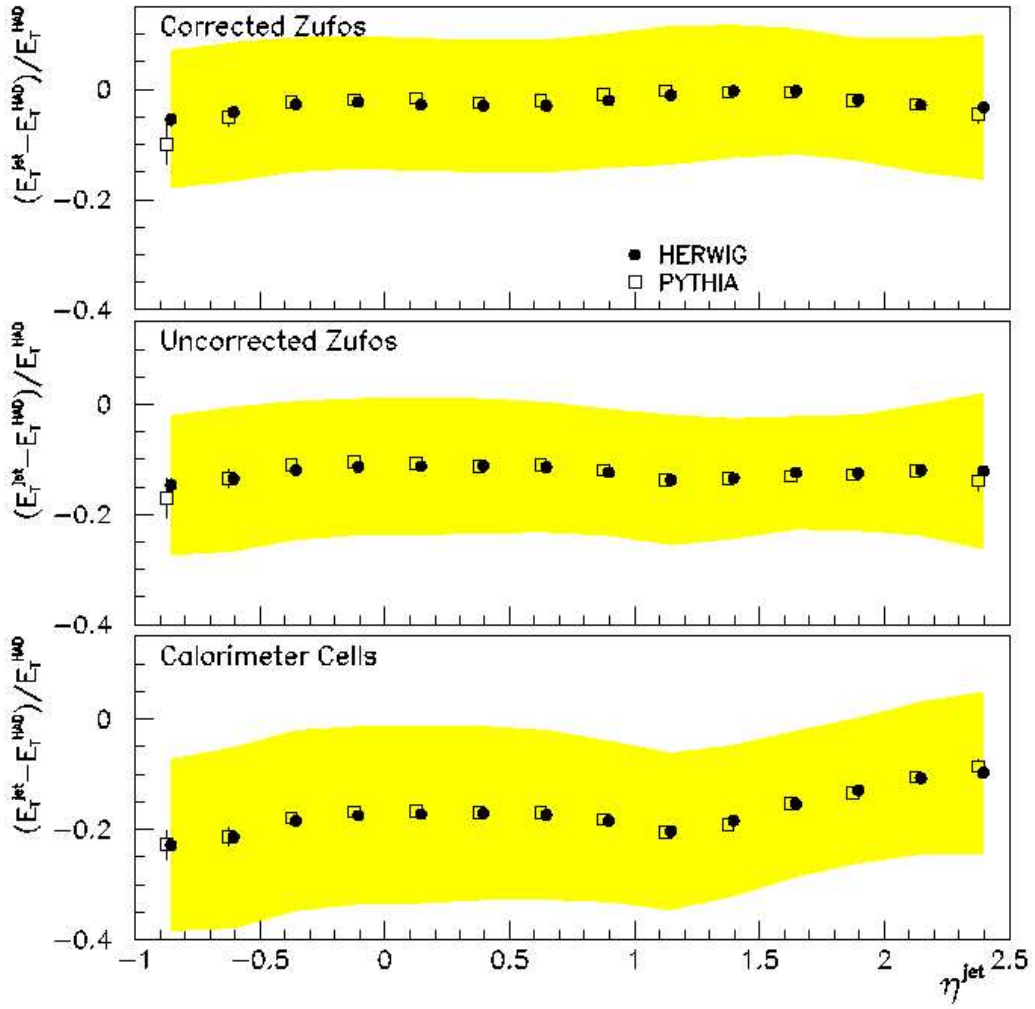

Figure 5.6: Residuals of the jet energy for jets reconstructed on cells *(bottom)*, ZUFOs *(middle)* and VO-corrected ZUFOs *(top)*. The jet energy on DL *(in the figure labelled as E_T^{jet})* is underestimated for cell and zufo jets by $(15-20)\%$ when compared with the jet energy on HL *(in the figure labelled as E_T^{HAD})*, whereas jets calculated from corrected ZUFOs agree within 5% – taken from [57].

Jets reconstructed from corrected ZUFOs (Fig. 5.6 top) yielded better agreement with HL jets although they still underestimate the jet energy by a few percent. Therefore the jet energy E_T^{jet} on DL, as reconstructed by the jet algorithm needs to be corrected, too. This was achieved with the use of the RAPGAP MC described in Sec. 4.2 by the following procedure:

1. Jets on HL and DL were matched in (η, ϕ):
   For each pair i, j of DL- and HL-jets with $E_T^{jet} > 3\,\mathrm{GeV}$, the distance R_{ij} was calculated according to

   $$R_{ij} = \sqrt{(\eta^{\mathrm{jet}\,i} - \eta^{\mathrm{jet}\,j})^2 + (\phi^{\mathrm{jet}\,i} - \phi^{\mathrm{jet}\,j})^2}.$$

   Iteratively, those jets with the smallest R_{ij} were matched, provided that both jets were still unmatched and have a transverse energy of $E_T^{jet} > 3\,\mathrm{GeV}$.

2. The residuals Res,
$$Res = \frac{E_T^{DL} - E_T^{HL\,\text{matched}}}{E_T^{DL}},$$
were calculated for all matched pairs of jets where the jet on DL had to pass the cuts described in Chap. 6, with the exception of the jet cuts. The residuals of the two jets with highest E_T^{jet} on DL were plotted double differentially in bins of E_T^{jet} and η^{jet} as shown in Fig. 5.7.

3. The peak values of the residuals were estimated from a Gaussian fit to the distribution of the residuals:
The peak value was used to be unsensitive to mismatched pairs of jets: If two jets close in (η, ϕ) on HL become combined into a single jet on DL, then the residual calculated from its closest partner on HL can yield in abnormal high values that spoil the mean value of the distribution. Bins with too small statistics were ignored.

4. The peak values were plotted in bins of E_T^{jet} and η^{jet} as shown in Fig. 5.7. Interestingly, the residuals differ less over E_T^{jet} than for the jets with first and second highest E_T^{jet}. However, the ordering of jets on HL and PL can change (Sec. 9.1), and since no information on corresponding jets on HL or PL is available for data, the mean residuals of the jet with first and second highest transverse energy were used to derive correction factors for E_T^{jet}. However, based on the assumption that the ordering of the jets does not change, discriminative correction factors for first and second jet can be used to estimate the systematic uncertainty of the jet correction factors Sec. 11.1.3.

5. The mean residual in bins of E_T^{jet} and η^{jet} was parametrised according to
$$\begin{aligned} E_T^{jet\,corr} &= c_{\text{VO}}(i) \cdot E_T^{jet} \quad \text{with} \\ c_{\text{VO}}(i) &= 0.0343 + 0.006 \cdot (E_T^{jet} - 6.5\,[\text{GeV}]) + 0.006 \cdot \eta^{\text{jet}} \end{aligned}$$
for jets reconstructed on VO-corrected ZUFOs, and
$$\begin{aligned} E_T^{jet\,corr} &= c_{\text{DM}}(i) \cdot E_T^{jet} \quad \text{with} \\ c_{\text{DM}}(i) &= \{0.028,\, 0.036,\, 0.039,\, 0.047,\, 0.050\}\,, \\ \text{and} \qquad i &= \lfloor E_T^{jet} - 6\,[\text{GeV}] \rfloor \end{aligned} \tag{5.1}$$
for jets reconstructed on DM-corrected ZUFOs, for which the residuals were flat in η^{jet}.

The residuals for corrected E_T^{jet} are displayed in Fig. 5.8. Deviations between DL and HL are reduced to $< 1.5\%$.

5.4 Reconstruction of kinematic variables

The exact definitions of the variables y_{JB}, $x_{I\!P}$, M_X, x_γ and $z_{I\!P}$ were given in Tab. 1.1. In the experiment these variables are reconstructed from the energy E and longitudinal momentum

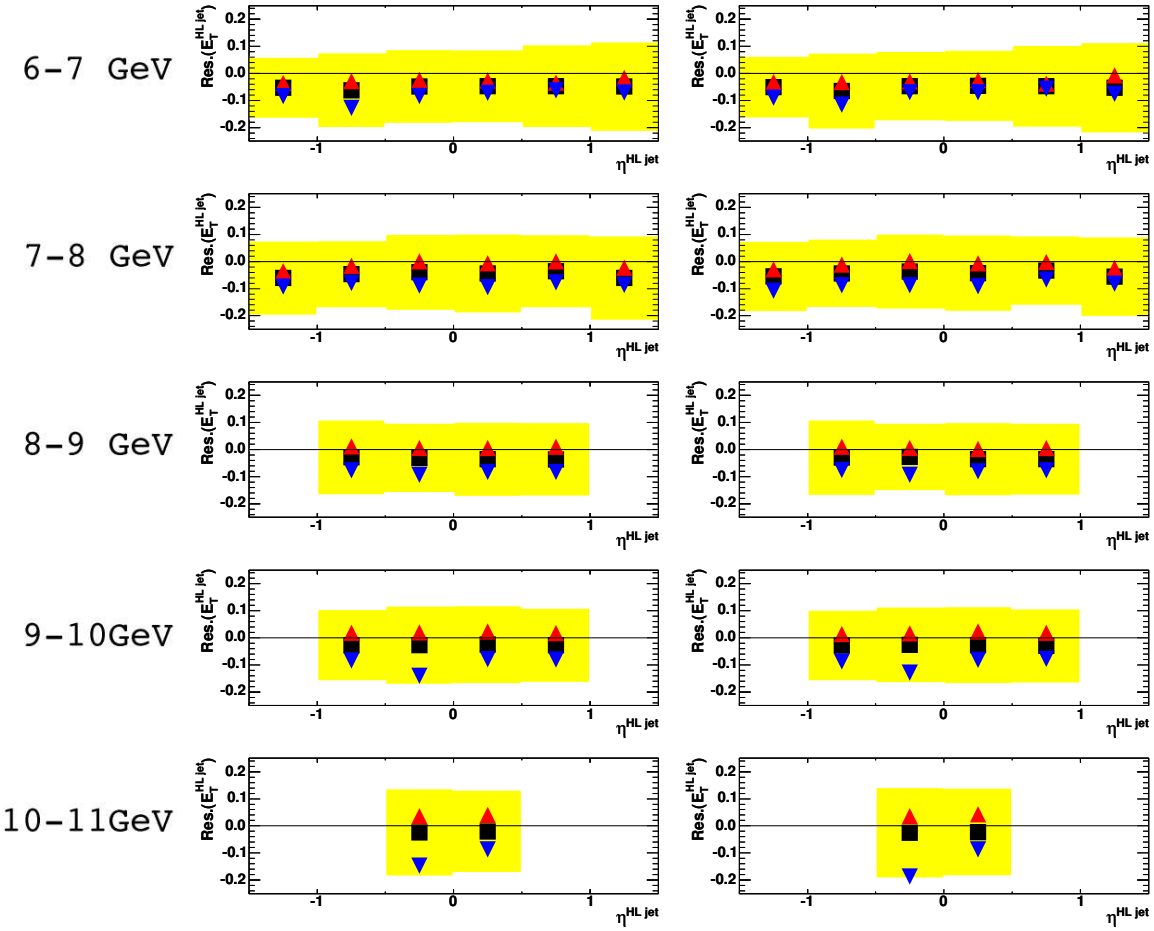

Figure 5.7: Peak values of residuals in bins of η^{jet} and uncorrected E_T^{jet} from $6\,\text{GeV} < E_T^{jet} < 7\,\text{GeV}$ *(top row)* to $10\,\text{GeV} < E_T^{jet} < 11\,\text{GeV}$ *(bottom row)*, for jet with highest E_T^{jet} (▲), second highest E_T^{jet} (▼) and the combination of both jets (■), shown for jets reconstructed on VO-corrected ZUFOs *(left)* and DM-corrected ZUFOs *(right)* before E_T^{jet} correction.

p_z of ZUFOs:

$$y_{JB} = \frac{(E - p_z)_{\text{zufos}}}{2E_e}, \tag{5.2}$$

$$x_{I\!P} = \frac{(E + p_z)_{\text{zufos}}}{2E_p}, \tag{5.3}$$

$$M_X = \sqrt{[(E - p_z) \cdot (E + p_z)]_{\text{zufos}}}\,. \tag{5.4}$$

For Eqn. 5.3 the approximation $Q^2 \approx 0$ was used, since in PHP the electron loses only little of its initial momentum. The squared four-momentum transfer Q^2 cannot be measured directly because the electron is only scattered by a small angle and escapes undetected along the beampipe. As a consequence, the formulae given in Tab. 1.1 can not be used to calculate x_γ and $z_{I\!P}$ on an experimental level. Observable estimators x_γ^{obs} and $z_{I\!P}^{obs}$ can be derived from the ratio of $(E \pm p_z)_{\text{jets}}$ of ZUFOs within jets over $(E \pm p_z)_{\text{zufos}}$ of all ZUFOs where the term *jets* refers to the two leading jets evolving from the hard interaction, i.e. the production of a

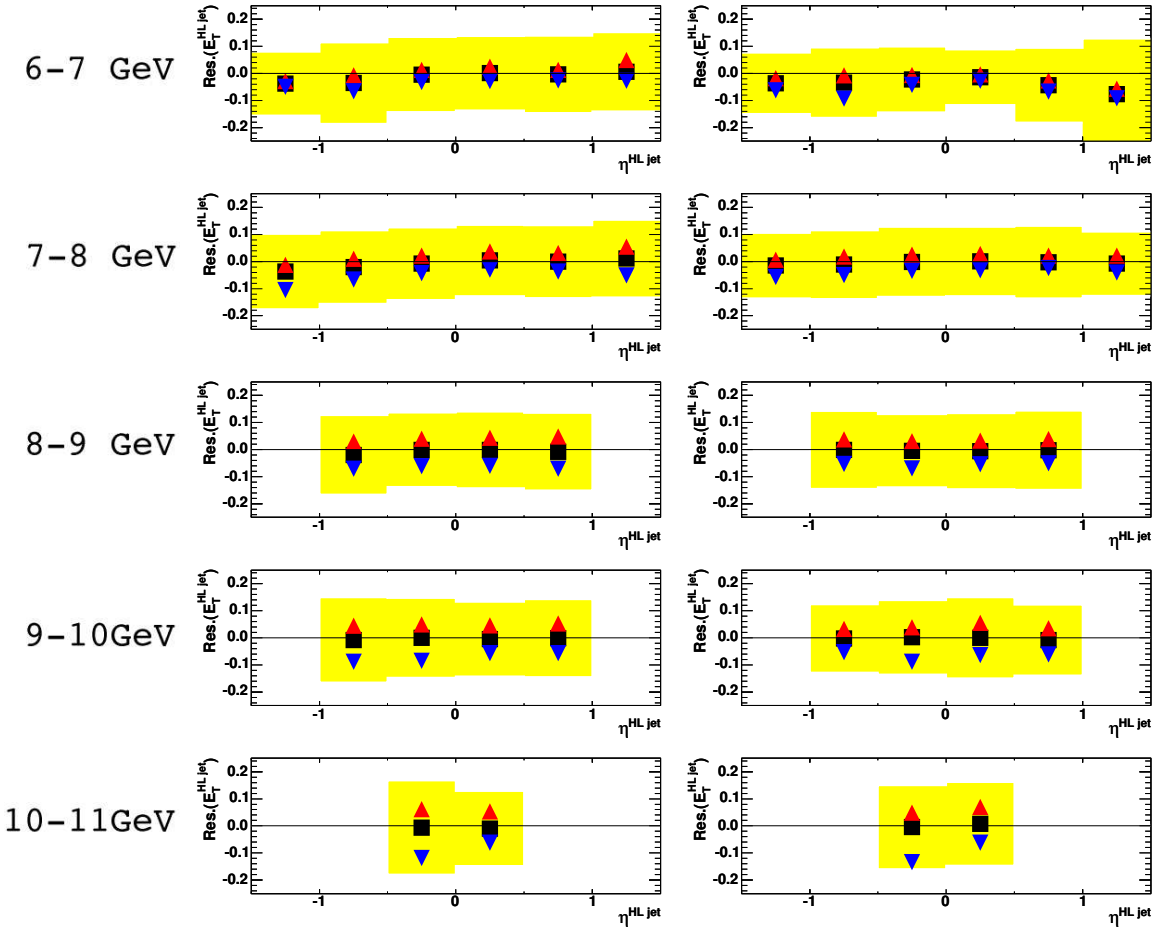

Figure 5.8: Peak values of residuals in bins of η^{jet} and corrected E_T^{jet} from $6\,\text{GeV} < E_T^{jet} < 7\,\text{GeV}$ *(top row)* to $10\,\text{GeV} < E_T^{jet} < 11\,\text{GeV}$ *(bottom row)*, for jet with highest E_T^{jet} (▲), second highest E_T^{jet} and (▼) the combination of both jets (■),, shown for jets reconstructed on VO-corrected ZUFOs *(left)* and DM-corrected ZUFOs *(right)* after E_T^{jet} correction, using mean correction values *(see text)*.

$q\bar{q}$-pair or a qg-pair (Fig. 1.7):

$$\frac{(E \pm p_z)_{\text{jets}}}{(E \pm p_z)_{\text{zufos}}} \simeq \frac{E^{\text{jets}} \cdot (1 \pm \cos\theta)}{(E \pm p_z)_{\text{zufos}}} = \frac{(E_T^{\text{jets}} / \sin\theta) \cdot (1 \pm \cos\theta)}{(E \pm p_z)_{\text{zufos}}} = \\ = \frac{E_T^{\text{jets}} \cdot \tan(\pm\theta/2)}{(E \pm p_z)_{\text{zufos}}} = \frac{E_T^{\text{jets}} \cdot e^{\pm\eta^{jet}}}{(E \pm p_z)_{\text{zufos}}} \qquad (5.5)$$

In the last step, Eqn. 1.2 has been used. From Eqn. 5.5 it follows that

$$x_\gamma^{obs} = \frac{\sum_{k=1,2} E_T^{jet\,k} e^{-\eta^{jet\,k}}}{(E - p_z)_{\text{zufos}}} \quad \text{and} \qquad (5.6)$$

$$z_{I\!P}^{obs} = \frac{\sum_{k=1,2} E_T^{jet\,k} e^{+\eta^{jet\,k}}}{(E + p_z)_{\text{zufos}}} \qquad (5.7)$$

can be used as observables for x_γ and $z_{I\!P}$ on detector level.

Another important variable is η^{max}, which is defined as the pseudorapidity of the most forward ZUFO above a threshold of 400 MeV:

$$\eta^{max} = \max\left[\, \eta_{\text{zufo}} \left(E_{\text{zufo}} > 400\,\text{MeV}\right) \right]. \tag{5.8}$$

The variable η^{max} is associated with the LRG (Sec. 1.8.1) and a cut on η^{max} provides an effective tool to select diffractive events (Sec. 6.5). The threshold in Eqn. 5.8 is necessary to exclude noise from the uranium in the CAL and the dependence on soft particles that can migrate into the LRG and are known to be simulated inadequately in MC [66].
The distribution of η^{max} is shifted towards higher values for MC (Fig. 5.9). This observation holds for the default threshold of 400 MeV as well as an increased and decreased threshold of 300 MeV and 500 MeV, respectively. The η^{max} distribution in MC was not tuned for this analysis. However, the dependence of the cross section on the η^{max}-cut value and the default threshold of $E_{\text{zufo}} > 400\,\text{MeV}$ was studied as a source of systematic errors in Sec. 11.1.5.

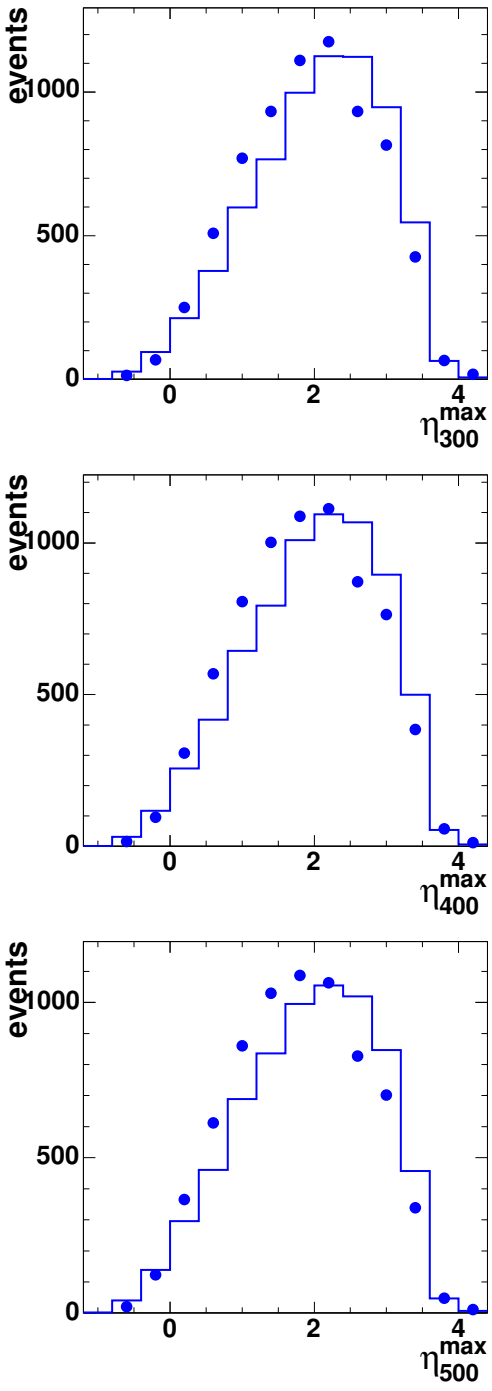

Figure 5.9: Distribution of η^{max} of DMCO corrected ZUFOs above 300 MeV *(left)*, 400 MeV *(middle)* and 500 MeV *(right)* for data (•) and MC (—) with all DL cuts applied with the exception of the cut on $\eta^{max} < 2.8$ – the distribution of MC is shifted to higher values.

Chapter 6

Event selection

6.1 Trigger selection

Data selected by two different triggers were investigated for this analysis: a dijet trigger for PHP (DST 77) and an inclusive jet trigger (DST 72). Events that pass either trigger fulfil the following requirements (see Tab. 6.1):

- a event vertex with $|z_{\text{vtx}}| < 60\,\text{cm}$,
  where z_{vtx} is the z-coordinate of the reconstructed vertex
  relative to the nominal vertex, i.e. at the interaction point $IP = (0, 0, 0)$;
- < 6 *bad tracks*;
  i.e. well-reconstructed tracks not associated with the primary vertex;
- $E - p_z < 75\,\text{GeV}$ or $p_z/E < 1$
  where E and p_z is the energy and longitudinal momentum measured
  in the CAL and p_z is calculated from the reconstructed z-vertex.

Originally, data were selected by the dijet trigger DST 77. This trigger additionally requires that

- ≥ 2 jets are found by a cone algorithm applied on CAL cells with
- a pseudorapidity in the range $|\eta^{jet}| < 2.5$ and
- a transversal jet energy $E_T^{jet} > 4.0\,(4.5)\,\text{GeV}$ for $99e^-p\,(99/00e^+p)$ data.

The latter condition bears potential systematic problems since for the offline event selection a cut on E_T^{jet} reconstructed by a different jet algorithm, the k_T-cluster algorithm (Sec. 5.3.1), is used. Recent studies on the TLT efficiencies [67] showed that MC was not sufficiently tuned to describe the data, in particular at low jet energies E_T^{jet} (Fig. 6.1 top).

trigger	DST 77	DST 72
description	PHP dijet trigger	inclusive jet trigger
synonymous declarations	HPP 14 TLT05 14	HPP 09 TLT05 09
SLT input triggers	HPP SLT 01/02/03	
common cuts	Vertex with $\lvert z_{\text{vtx}}\rvert < 60\,\text{cm}$ < 6 bad tracks $8 < E - p_z < 75\,\text{GeV}$ $E - p_z > 12\,\text{GeV} \quad \| \quad p_z/E < 0.95$	
specific cuts	≥ 2 jets (cone alg.) $\lvert\eta^{jet}\rvert < 2.5$ $E_T^{jet} > 4.0\,(4.5)\,\text{GeV}$	$p_z/E < 1.00$ $E_T^{cone} > 11.0\,\text{GeV}$

Table 6.1: Specification of trigger bits used in this analysis.

The TLT efficiencies were compared with those of the inclusive trigger (DST 72) which has the following specific cuts:

- $p_z/E < 1.0$;
- $E_T^{cone} > 11.0\,\text{GeV}$, where E_T^{cone} is the sum of the transverse energy of all CAL cells with the exception of the FCAL's first inner ring of cells around the beampipe.

No significant discrepancies between data and MC were found for DST 72 (Fig. 6.1 bottom). Furthermore, the TLT efficiencies of this trigger were considerably higher at low E_T^{jet}. Due to these reasons it was decided to use trigger DST 72 for the further analysis.

6.2 Quality cuts

To reject events of poor quality, the following cuts were introduced:

- $-35 < z_{\text{vtx}} < 30\,\text{cm}$;
- ≥ 3 *good tracks*, i.e. tracks with $p_T > 0.2\,\text{GeV}$ in good azimuthal range $15° < \theta < 165°$ for a reconstruction in the CTD with the *number of degrees of freedom* ≥ 10 .

The latter cut was adopted from other trigger bits, where such a quality cut is already implemented. The effect of both cuts on the original data sample can be seen in Fig. 6.2.

6.3 Selection of PHP events

For the MC sample, PHP events were selected by the cut $Q^2 < 1.0\,\text{GeV}^2$. For data, a cut on Q^2 is not possible since the scattered electron e' escapes along the beampipe and is not

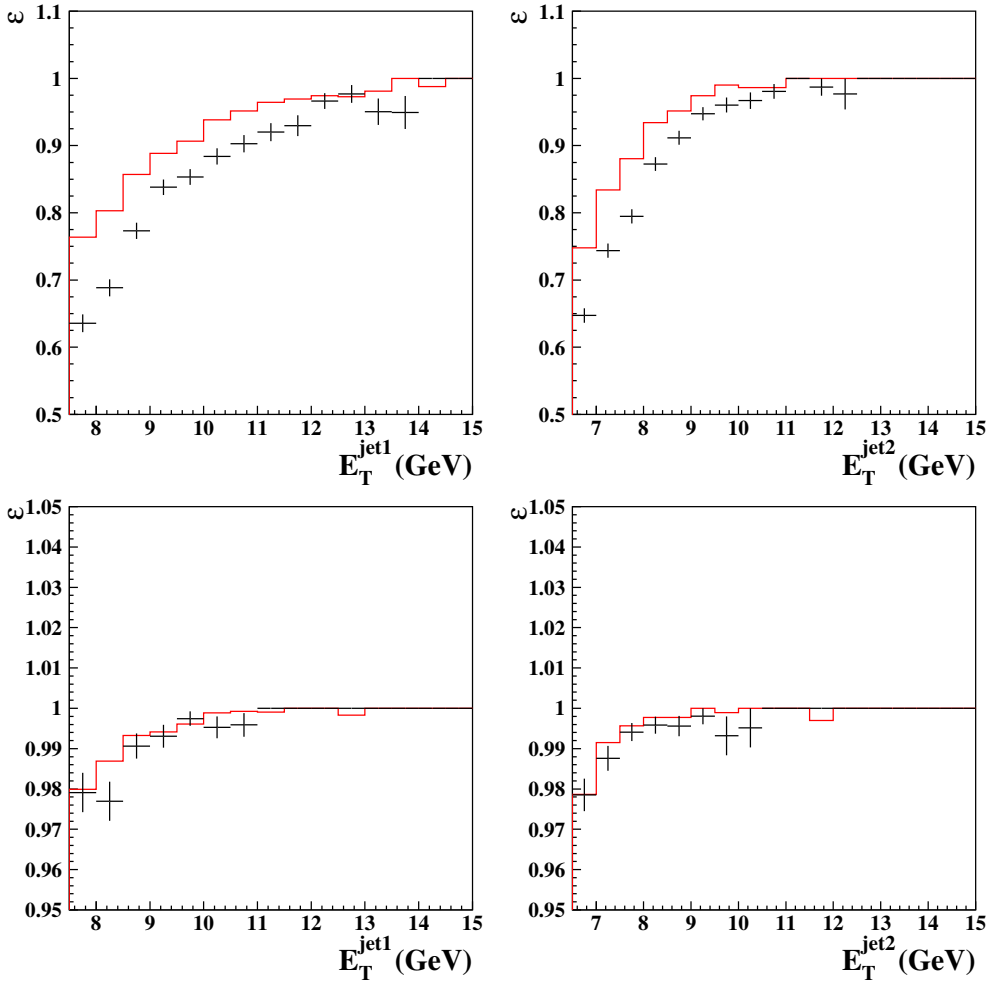

Figure 6.1: TLT efficiencies over jet energies $E_T^{jet\,1}$ *(left)* and $E_T^{jet\,2}$ *(right)* in data (+) and MC (—) for DST 77 *(top)* and DST 72 *(bottom)*– taken from [67].

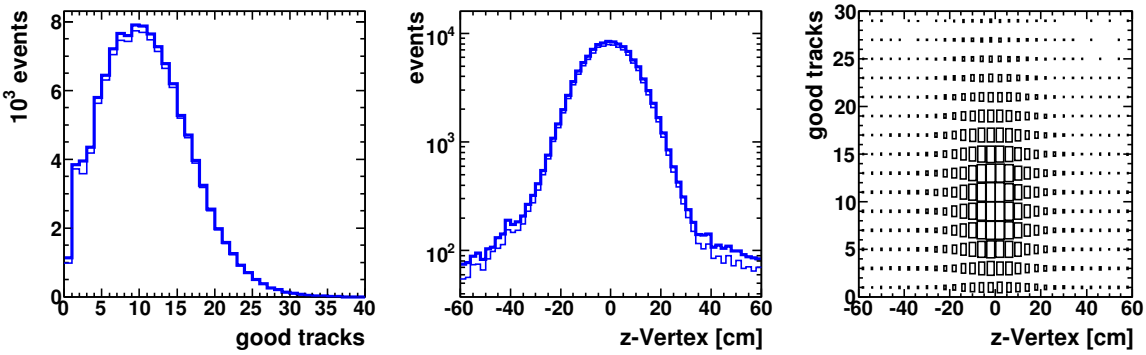

Figure 6.2: Quality cuts – *left:* event distribution of the number of good tracks (*thin line:* after cut on z_{vtx}), *middle:* event distribution of z_{vtx} (*thin line:* after cut on number of good tracks) *right:* correlation plot of good tracks vs. z_{vtx} .

detected. However, most DIS events can be rejected by the requirement that no scattered electron is found in the CAL. The detection and identification of the scattered electron was done with the electron finder SINISTRA that assigns probabilites to any detected electron to be the scattered electron. If the probability of any found candidate was ≥ 0.9 and its y_{el}, calculated as

$$y_{el} = 1 - \frac{E_{e\prime}}{2E_e}(1 - \cos\theta_{e'}) \,,$$

satisfied $y_{el} \leq 0.7$, then the event was excluded.
An additional cut on y_{JB} (Eqn. 5.2) was applied in order to further reduce background from DIS events and beam gas interactions: In cases where the scattered electron is not found by SINISTRA, it is included in the calculation of the hadronic energy and by conservation of energy it follows that

$$y_{JB} = \frac{E - p_z}{2\,E_e} = \frac{2\,E_e}{2\,E_e} = 1 \,.$$

Interactions of beam-protons with residual gas in the beampipe can lead to large energy deposits in the forward region of the detector and have $y_{JB} \approx 0$. For this analysis, a cut of

$$0.2 < y_{JB} < 0.85 \tag{6.1}$$

was used. The number of electron candidates with $y_{el} < 0.7$ (with and without the cut on y_{JB}) as well as the distribution of y_{JB} (with and without the cut on e' candidates) is shown in Fig. 6.3.

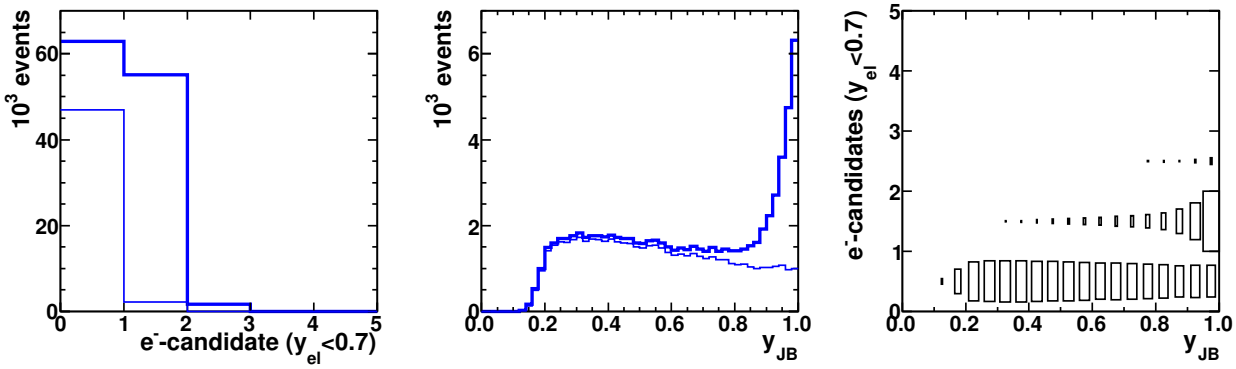

Figure 6.3: PHP cuts – *left:* event distribution of the number of electron candidates with $y_{el} < 0.7$ (*thin line:* after quality cuts and y_{JB}-cut), *middle:* event distribution of y_{JB} (*thin line:* after quality cuts and cut on e' candidates with $y_{el} \lesssim 0.7$), *right:* correlation plot of e' candidates vs. y_{JB} after quality cuts.

6.4 Selection of dijet events

Jets were reconstructed by the k_t-cluster algorithm in the longitudinally invariant inclusive mode run in laboratory frame. At least 2 jets were required in the range

$$-1.5 < \eta^{jet} < +1.5 \tag{6.2}$$

and with a transversal jet energy E_T^{jet} of

$$\begin{aligned} E_T^{jet\,1} &> 7.5\,\text{GeV} \quad \text{for the jet with highest } E_T^{jet}, \\ E_T^{jet\,2} &> 6.5\,\text{GeV} \quad \text{for the jet with second highest } E_T^{jet}. \end{aligned} \tag{6.3}$$

The jet finder was set to run on ZUFOs at DL, on stable hadrons at HL and on final state partons at PL, i.e. on partons after parton shower and (if implemented) gluon splitting. The distribution of $E_T^{jet\,1(2)}$ and $\eta^{jet\,1(2)}$ on DL is shown in Fig. 6.4.

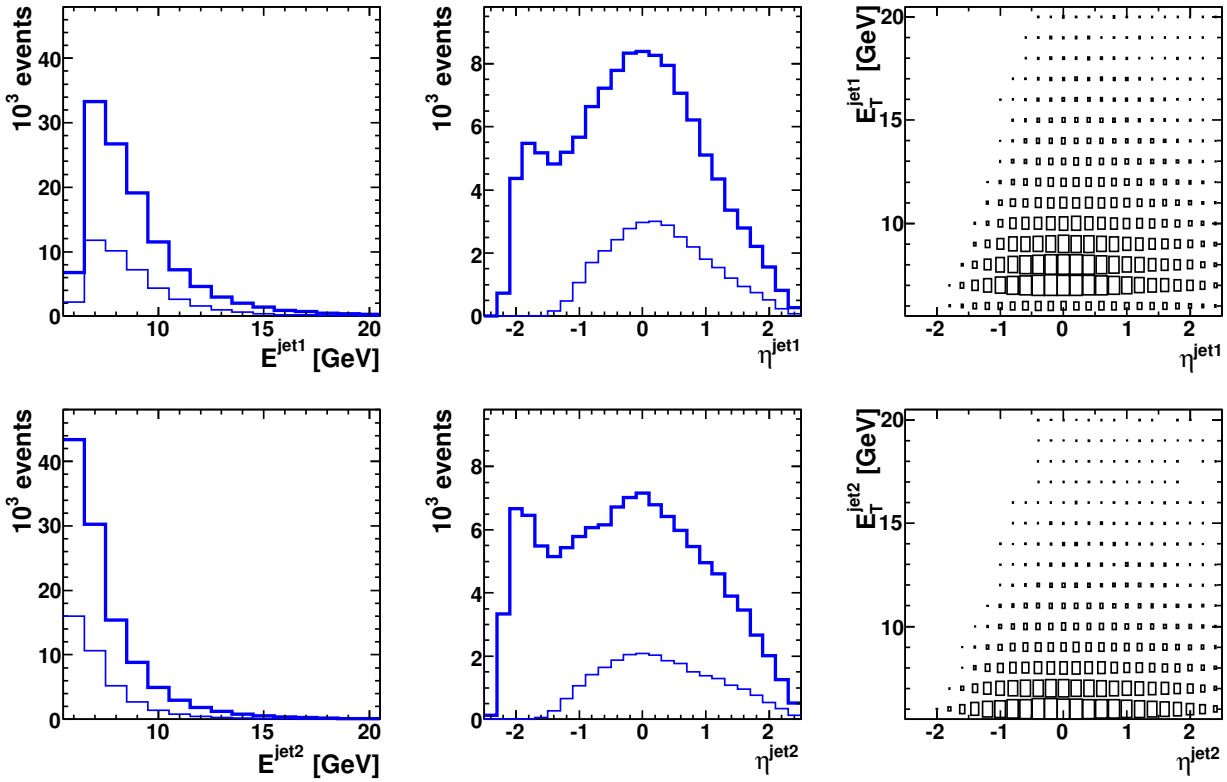

Figure 6.4: Dijet cuts (*top:* 1st jet, *bottom:* 2nd jet) – *left:* event distribution for E_T^{jet} (*thin line:* after quality cuts, PHP cuts and corresponding η^{jet}-cut), *middle:* event distribution for η^{jet} (*thin line:* after quality cuts, PHP cuts and corresponding E_T^{jet}-cut), *middle:* correlation plot of E_T^{jet} vs. η^{jet} after quality cuts and PHP cuts.

6.5 Selection of diffractive events

In this analysis, diffractive events were selected with the LRG method described in Sec. 1.8.1: Due to the colourless exchange, a large rapidity gap is expected between the outgoing proton and the dijet system or a possible remnant of the diffractive exchange. Figure 6.5 shows an example of a diffractive event at the ZEUS detector. Since the scattered proton p' is not detected, the requirement of a LRG is implemented by a cut on the highest observed pseudorapidity η^{max} of an event (Sec. 5.4):

$$\eta^{max}_{\text{ZUFO}} < 2.8\,. \tag{6.4}$$

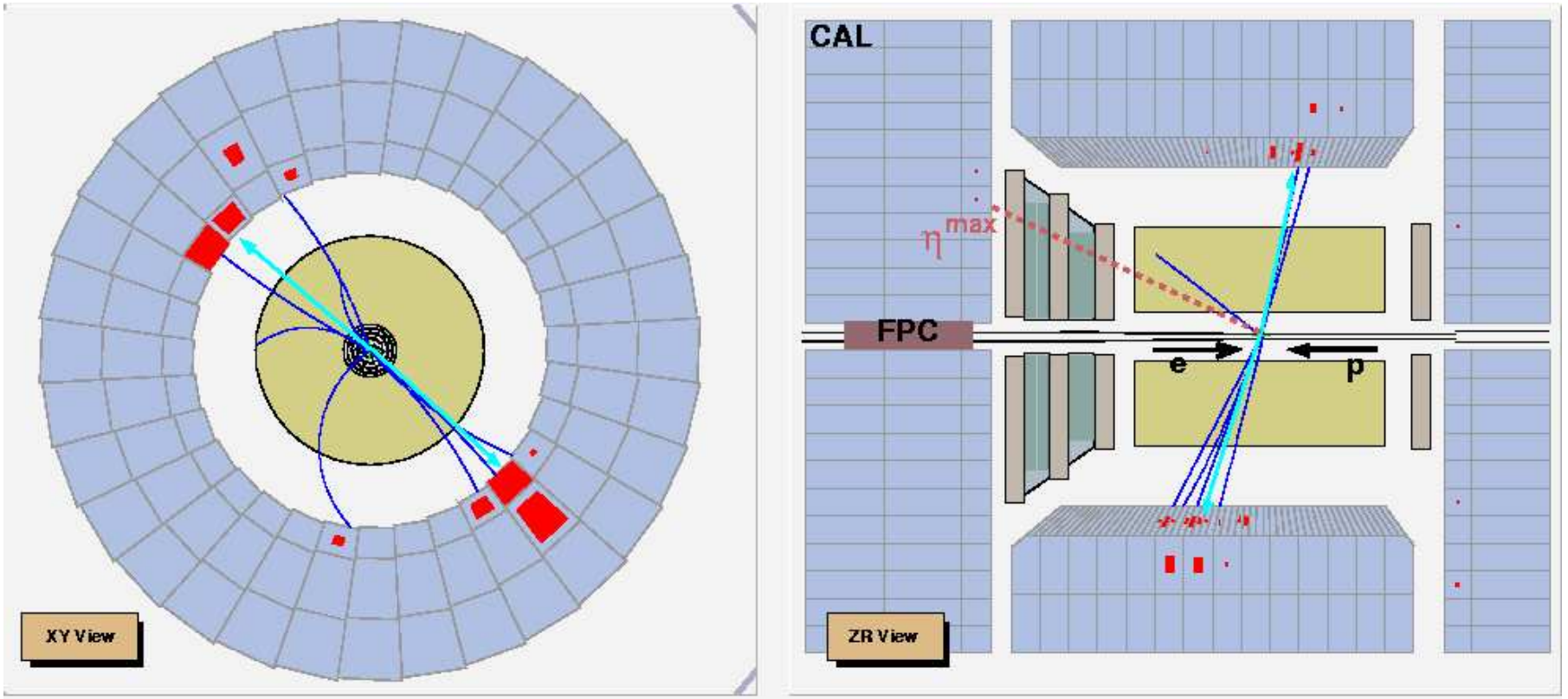

Figure 6.5: Example of a diffractive event in the ZEUS detector – *left:* transverse view, *right:* longitudinal view.

In order to reduce background from proton dissociation at high η, the total energy in the FPC was restricted to values of

$$E_{\mathrm{FPC}}^{total} \;<\; 1.0\,\mathrm{GeV}\,. \tag{6.5}$$

The cuts on the pseudorapidity and the FPC energy were only applied on DL to account for detector acceptance and to reduce background from other sources like non-diffractive photoproduction and beam gas interactions. Since the cuts also reduce the kinematic range of the diffractive signal on DL, the pure, uncontaminated MC sample was used to reconstruct the full kinematic range. For this purpose, the above cuts were not applied to the MC sample on HL and PL. In order to select diffractive events also on those levels, an additional cut on $x_{I\!P}$ was introduced at all three levels of MC as well as on DL of data:

$$x_{I\!P} \;<\; 0.025\,. \tag{6.6}$$

The distributions of E_{FPC}^{total}, $x_{I\!P}$ and η^{max} at DL are shown in Fig. 6.6.

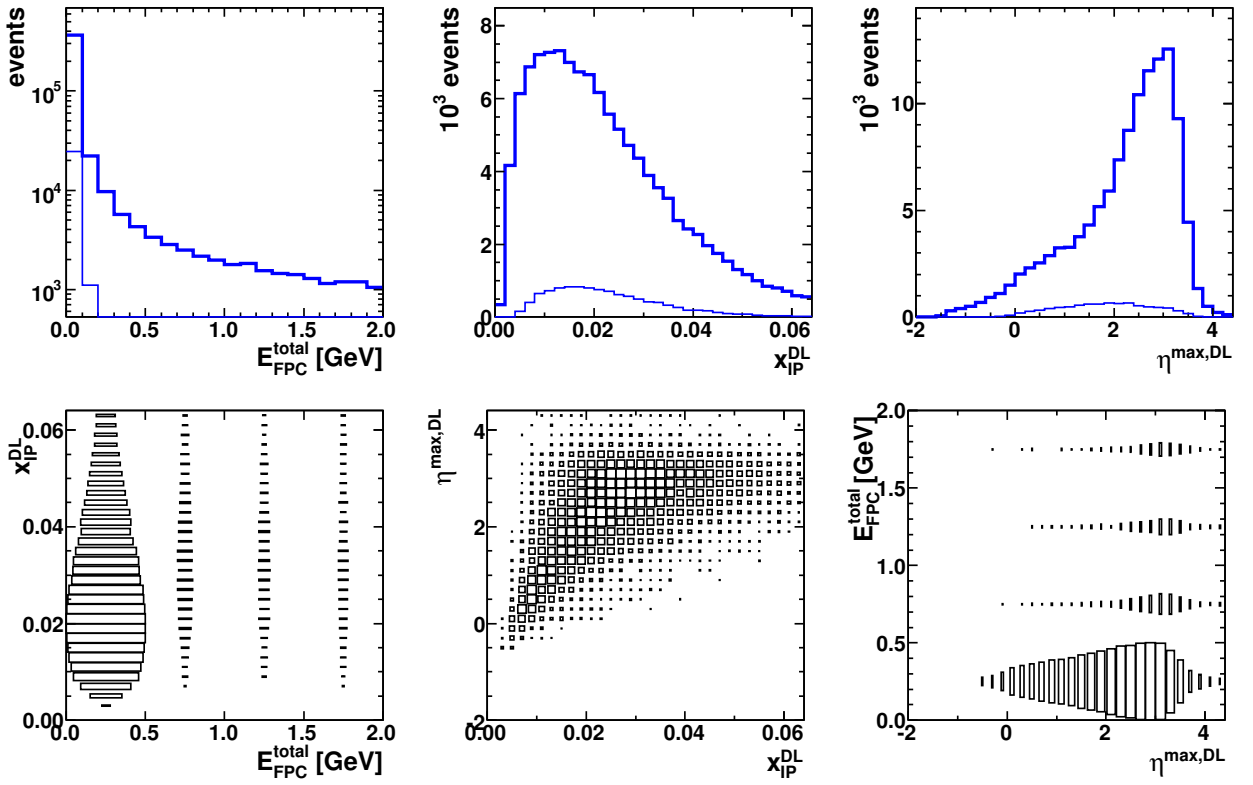

Figure 6.6: Diffractive cuts – *top row:* event distributions for E_{FPC}^{total} *(left)*, $x_{I\!P}^{DL}$ *(middle)* and $\eta^{max,DL}$ *(right)* for all events *(thick line)* and after application of all other selection cuts *(thin line); bottom row:* correlation plots of E_{FPC}^{total}, $x_{I\!P}^{DL}$ and $\eta^{max,DL}$.

6.6 Summary

All cuts that were applied to the data and MC sample are summarised in Tab. 6.2. For MC events, identical cuts were applied to the corresponding variables on HL and PL in order to

obtain comparable MC sets on all three levels, with the exceptions of the η^{max}- and E^{FPC}_{total}-cut which were only applied on DL. Two cuts were implemented to reject background from cosmic events. These cuts are introduced in Sec. 7.2.2 and are shown in Tab. 6.2 for completeness. The cosmic cut is only applied to the data sample.

Quality Cuts	PHP Selection
$-35 < z_{\mathrm{vtx}} < 30\,\mathrm{cm}$ ≥ 3 good tracks	no e^-candidate found, $0.20 < y_{JB} < 0.85$ only MC: $Q^2 < 1.0\,\mathrm{GeV}^2$
Diffractive Selection	Dijet Selection
$x_{I\!P} < 0.025$ *only DL*: $\eta^{max} < 2.8$ $E^{total}_{\mathrm{FPC}} < 1.0\,\mathrm{GeV}$	≥ 2 jets (k_T-algorithm) *with:* $E^{jet}_T > 7.5\,(6.5)\,\mathrm{GeV}$ $-1.5 < \eta^{jet} < 1.5$
Cosmics Rejection *(only data)*	
$\lvert t^{down}_{\mathrm{CAL}} - t^{up}_{\mathrm{CAL}} \rvert > 7.0\,\mathrm{ns}$ *or* 2 back-to-back hits in BAC: $\Delta R_{2\mu} = \sqrt{(\Delta\theta_{2\mu} - \pi)^2 + (\Delta\phi_{2\mu} - \pi)^2} < 0.5$	

Table 6.2: Overview on the offline selection cuts and the rejection cuts described in Sec. 7.2.2.

Chapter 7

Sources of background

7.1 Background from *ep*-related processes

Sources of *ep*-related background were investigated by S. Kagawa [67]. Therefore only the results of the studies on *ep*-background will be summarised briefly.

7.1.1 Non-diffractive background

Non-diffractive dijet events in PHP were simulated with PYTHIA MC [60]. Since a large rapidity gap is exponentially suppressed for non-diffractive processes, events that passed all selection cuts were accumulated in the highest bin of η^{max}, accounting for $\sim 12.5\%$ of this bin's content. The total background from non-diffractive events was estimated to be of the order of 5% and was not subtracted.

7.1.2 Proton dissociative background

Although a proton can dissociate as an aftereffect of a diffractive scattering, the large amount of p-dissociative events is predominantly due to non-diffractive processes and has been excluded by the following means:
The cut on the energy in the FPC (Eqn. 6.5) restricts the mass range of the p-dissociative system Y to $M_Y \lesssim 2.3\,\mathrm{GeV}$. The amount of p-dissociative events for $E^{total}_{\mathrm{FPC}} < 1\,\mathrm{GeV}$ was estimated with EPSOFT MC [68] which simulates p-dissociative events in PHP where the exchanged photon fluctuates into a J/Ψ meson. From a fit of RAPGAP MC and EPSOFT MC to data in the range $0 < E^{total}_{\mathrm{FPC}} < 10\,\mathrm{GeV}$, background from p-dissociation was found to account for 14% of all events in data and was subtracted uniformly from all cross sections.

7.2 Background related to other sources

7.2.1 Beam gas and beampipe interactions

Both the proton and electron beam can interact with rest gas in the beampipe as well as with the beampipe itself. Additionally, pions produced due to proton beam interactions upstream of the interaction point decay to muons which run almost parallel to the proton beam,

surrounding it like a halo. Such *halo muons* can traverse the ZEUS detector parallel to the beamline and cause signals in the CTD and the CAL (Fig. 7.3 bottom).
The majority of these events is effectively removed on trigger level by the requirement of a well-reconstructed vertex close to the interaction point and timing information from different detectors. They are additionally suppressed by the cut on the number of good tracks originating from the vertex (Sec. 6.2) and the cut on $y_{JB} > 0.2$ (Sec. 6.3). The remaining contribution from this source of background is assumed to be negligible.

7.2.2 Cosmic events

The data sample can also be contaminated by cosmic events, mostly single muons, that traverse the detector close to the nominal vertex and can fake a dijet signal. Fake dijet events would appear back-to-back in the detector and be accumulated in the highest bins of the x_γ-distribution (Fig. 7.2b). Such a non-uniform background would significantly bias the fit of MC to data as described in Sec. 8.1. Therefore a rejection of cosmic events is required at an early stage.
A wide set of parameters was checked for detection of cosmic candidates, of which two turned out to be highly effective:

1. the mean cell timing of the upper half of the CAL vs. its lower half, because cosmic muons traverse the detector from top to bottom;

2. back-to-back hits in the BAC (Sec. 2.3.2), since the BAC detects mostly muons and primarily those cosmic muons survive the trigger criteria that pass near the nominal interaction point IP.

The time difference $t_{\mathrm{CAL}}^{down} - t_{\mathrm{CAL}}^{up}$ between the averaged cell timing of the lower and upper half of the CAL is plotted in Fig. 7.1. Cut values of

$$\begin{aligned} t_{\mathrm{CAL}}^{down} - t_{\mathrm{CAL}}^{up} &> +7.0\,\mathrm{ns} \quad \text{and} \\ t_{\mathrm{CAL}}^{down} - t_{\mathrm{CAL}}^{up} &< -10.0\,\mathrm{ns} \end{aligned} \tag{7.1}$$

were found to reject clear cosmic events without removing non-cosmics. The cut on negative time differences was introduced due to a small number of questionable events with erroneous time reconstruction (left-sided tail in Fig. 7.1 left). This cut, however, does not sufficiently reject cosmics that traverse the detector at almost horizontal angles and only result in a small time difference $t_{\mathrm{CAL}}^{down} - t_{\mathrm{CAL}}^{up}$.
Therefore an additional cut on back-to-back muons was implemented: For each pair of BAC hits, angular distances $\Delta\phi_{2\mu}$, $\Delta\theta_{2\mu}$ and $\Delta R_{2\mu}$ were calculated, defined by

$$\begin{aligned} \Delta\phi_{2\mu} &= \phi_{\mu_1} - \phi_{\mu_2} \qquad (0 < \phi < 2\pi)\,, \\ \Delta\,\theta_{2\mu} &= \theta_{\mu_1} + \theta_{\mu_2} \qquad (0 < \theta < \pi)\,, \\ \Delta R_{2\mu} &= \sqrt{(\Delta\theta_{2\mu} - \pi)^2 + (\Delta\phi_{2\mu} - \pi)^2}\,. \end{aligned}$$

A small value of $\Delta R_{2\mu}$ indicates that 2 hits in the BAC are found in opposite direction in both θ and ϕ. Events with $\min(\Delta R_{2\mu}) \leq 1.0$ were checked by eye, and a cut value of

$$\min(\Delta R_{2\mu}) < 0.5^{+0.4}_{-0.2} \tag{7.2}$$

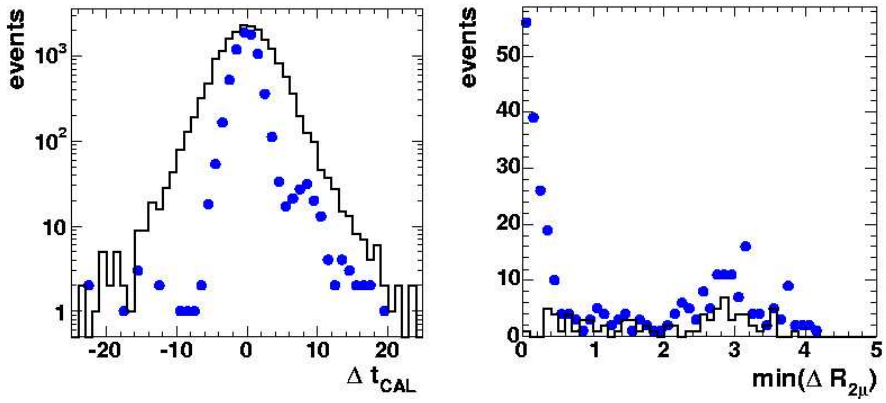

Figure 7.1: Variables for rejection of cosmic events – *left:* time difference $\Delta t_{\mathrm{CAL}} = t_{\mathrm{CAL}}^{down} - t_{\mathrm{CAL}}^{up}$ *right:* angular deviation $\Delta R_{2\mu}$ from π for hits in BAC – both distributions show a distinct secondary peak at $\Delta t_{\mathrm{CAL}} \approx 9\,\mathrm{ns}$ and $\min(\Delta R_{2\mu}) \approx \pi$ for data (•) which is not seen in MC(—) and due to cosmic events.

was found to ensure a clear identification of cosmic events. A secondary peak at $\Delta R_{2\mu} \approx \pi$ is mainly due to halo muons in the BAC which usually do not affect the CTD-and CAL-measurement, and were not removed.
About 0.9% of all events have more than two BAC hits (Fig. 7.2 left). For these events the combinatoric probability to find back-to-back hits increases. However, such events mostly result from cosmic showers or halo muons (Fig. 7.3 middle) and should be rejected, too.

In total, 189 cosmics were identified and removed by the cut on CAL timing and back-to-back hits in the BAC. All cosmic events were displayed and checked event-by-event; only four candidates were found to be questionable. 6990 events of the data sample pass the cosmic cuts as non-cosmics.
This method *(= method A)* was also compared with another method *(= method B)* in which the jet timing relative to the time of the initial *ep* interaction was calculated from the cell

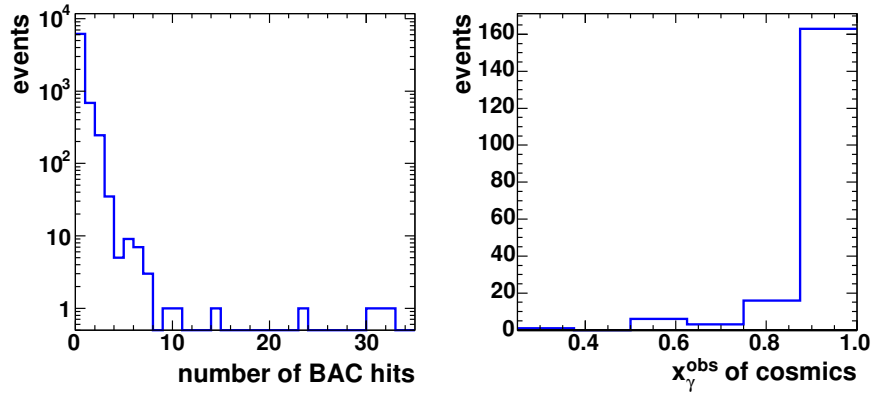

Figure 7.2: Number of hits in BAC for all data events *(left)*, and x_γ^{obs}-distribution of detected cosmics *(right)*.

timing of the CAL, and a cut on the jet timing was applied according to

$$\begin{aligned} |t^{jet\,1} - t^{jet\,2}| &> 6\,\text{ns} \qquad \text{or} \\ |t^{jet\,1(2)}| &> 20\,\text{ns}\,. \end{aligned}$$

Method A detected 116 out of 125 cosmic events which were found by method B; only one of the nine undetected candidates was a clear cosmic event. Method A also detected a distinct class of cosmic events which remained undetected with method B. Furthermore, method A is technically easier to apply. The numbers of events detected by methods A and B are summarised in Tab. 7.1.
An example of a cosmic event, a cosmic shower and a halo muon are shown in Fig. 7.3. The cuts for rejection of cosmic events are not applied to the MC sample.

		back-to-back hits in BAC	
		yes	no
CAL timing	bad	107 (66)	39 (24)
	good	43 (26)	6990 (9)

Table 7.1: Events rejected by / passing cuts of method A (CAL timing and orientation of BAC hits); in total, 6990 events of the data sample remain. The numbers in parantheses add up to the number of 125 events which were identified as cosmic events with method B (jet timing).

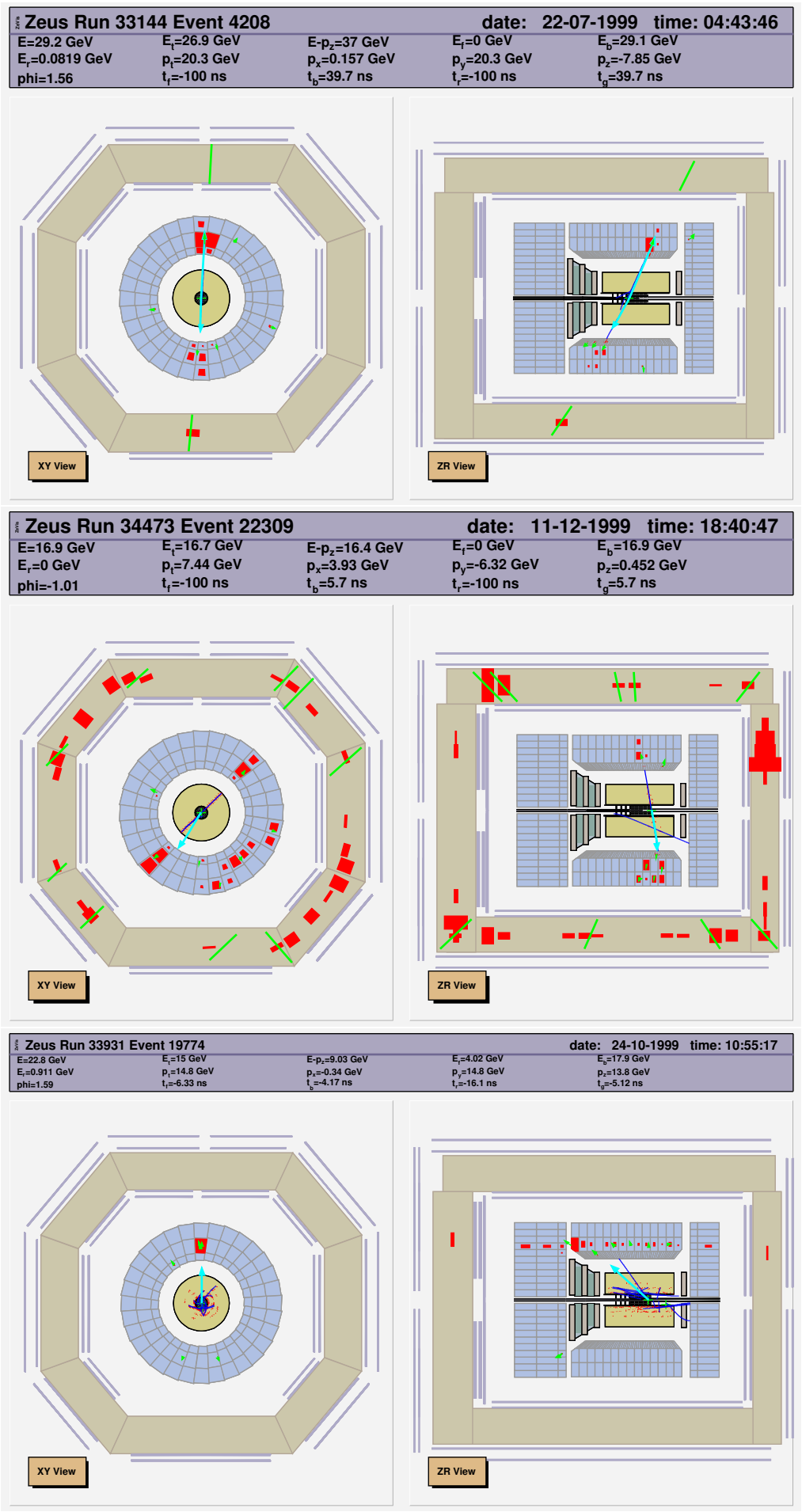

Figure 7.3: Example of a cosmic event only found by method A *(top)*, of a cosmic shower *(middle)* and a halo muon traversing the CAL *(bottom)*.

Chapter 8

Tuning of the MC sample

In this chapter the assembling of the RAPGAP MC sample will be described: The LO MC sets for the different processes stated in Sec. 4.2 need to be combined into one MC sample (Sec. 8.1) and normalised to the data (Sec. 8.2). The MC also needs to be corrected for deficiencies in the simulation of the generated processes (Sec. 8.3).

8.1 Fitting of MC to data

The RAPGAP MC sample used for this analysis consists of four subsets (Tab. 4.1): one MC set for the contribution of resolved PHP (in the following referred to as *resolved MC*) (Fig. 8.1 left) and three sets for contributions from direct PHP, i.e. light quark production *(lq)*, charm quark production *(hq)*, and QCD-Compton scattering *(qcdc)*. The processes for direct PHP were combined into one set of *direct MC* (Fig. 8.1 middle, right). The relative contributions from direct and resolved MC were determined by a least-squares fit to the data to the x_γ^{obs} distribution which naturally separates *direct enriched* ($x_\gamma \geq 0.75$) from *resolved enriched* ($x_\gamma < 0.75$) regions of PHP. The fit was performed in the range [0.25, 1.0] and allowed two

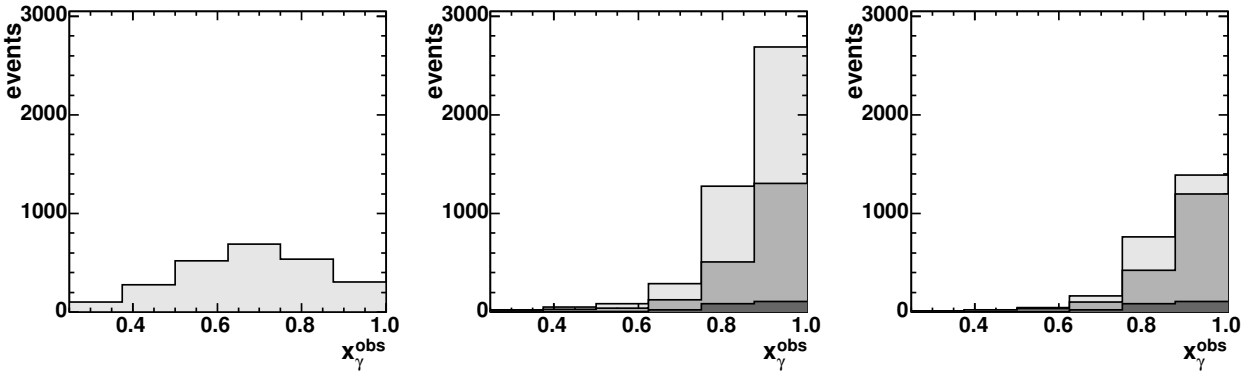

Figure 8.1: MC sets for resolved PHP *(left)*, and direct PHP: contribution from different processes in direct PHP are shown accumulative *(middle)* and separately *(right)* for liqht quark production *(light grey)*, charm quark production *(medium grey)* and QCD-Compton scattering *(dark grey)*.

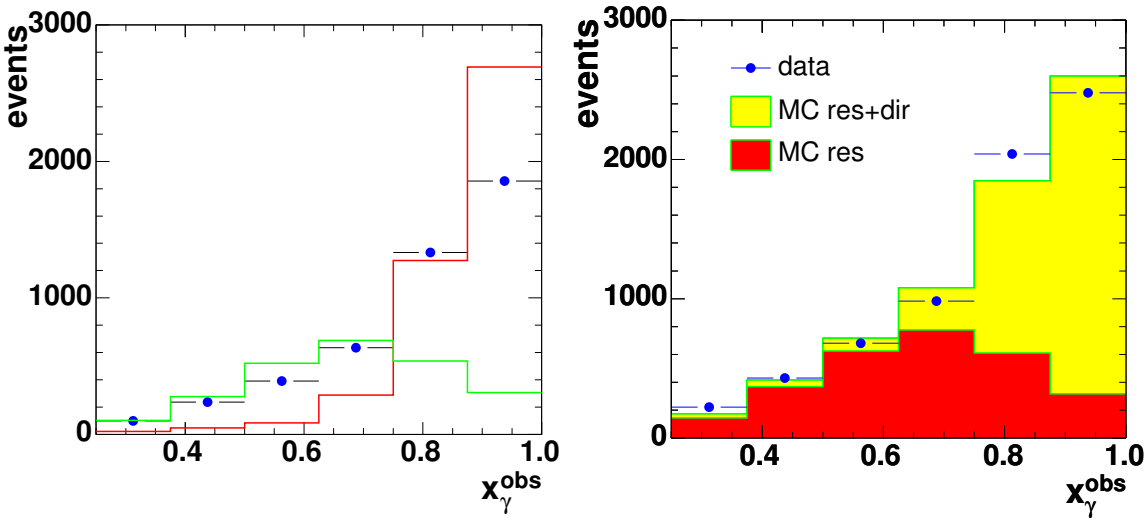

Figure 8.2: Distribution of x_γ^{obs} — *left:* before fit for data (•) and separately for MC samples of direct and resolved PHP (*black line:* MC dir, *grey line:* MC res); *right:* after fit for data, resolved MC and the sum of resolved and direct MC.

fit parameters, f_{dir} and f_{res}, for the contribution from direct and resolved PHP:

$$f_{\text{dir}} \cdot \left(\frac{N_{\text{MC lq}}}{\mathcal{L}_{\text{MC lq}}} + \frac{N_{\text{MC hq}}}{\mathcal{L}_{\text{MC hq}}} + \frac{N_{\text{MC qcdc}}}{\mathcal{L}_{\text{MC qcdc}}} \right) + f_{\text{res}} \cdot \frac{N_{\text{MC res}}}{\mathcal{L}_{\text{MC res}}} = \frac{N_{\text{data}}}{\mathcal{L}_{\text{data}}} . \tag{8.1}$$

Here N gives the number of events passing all cuts on DL. The fit (Fig. 8.2) yielded the following results:

$$\begin{aligned} f_{\text{dir}} &= 0.590 \pm 0.013 , \\ f_{\text{res}} &= 0.718 \pm 0.021 , \end{aligned} \tag{8.2}$$

i.e. a ratio of $45,1\% : 54.9\%$ for the contributions from direct and resolved MC.

8.2 Normalisation of MC to data

Since only LO is taken into account for the generation of MC events, the need of a scaling (or normalisation) factor is expected. The most basic concept assumes a constant normalisation factor for the full range of x_γ^{obs}.
The above fit of MC to data includes such an overall MC normalisation factor, c_{norm}, which can be introduced in Eqn. 8.1 according to

$$c_{\text{norm}} \cdot \left[f'_{\text{dir}} \cdot \left(\frac{N_{\text{MC lq}}}{\mathcal{L}_{\text{MC lq}}} + \frac{N_{\text{MC hq}}}{\mathcal{L}_{\text{MC hq}}} + \frac{N_{\text{MC qcdc}}}{\mathcal{L}_{\text{MC qcdc}}} \right) + f'_{\text{res}} \cdot \frac{N_{\text{MC res}}}{\mathcal{L}_{\text{MC res}}} \right] = \frac{N_{\text{data}}}{\mathcal{L}_{\text{data}}} , \tag{8.3}$$

where f'_{dir} and f'_{res} conserve the relative contributions of direct and resolved PHP as well as the lumi-weighted number of events :

$$\left[\frac{f'_{\text{dir}}}{f'_{\text{res}}} = \frac{f_{\text{dir}}}{f_{\text{res}}} \quad \wedge \quad \frac{f'_{\text{dir}} + f'_{\text{res}}}{2} = 1 \right] \quad \Longrightarrow \quad c_{\text{norm}} = \frac{f_{\text{dir}}}{f'_{\text{dir}}} = \frac{f_{\text{res}}}{f'_{\text{res}}} = \frac{f_{\text{dir}} + f_{\text{res}}}{2} .$$

With the results obtained in Eqn. 8.2, this gives

$$\begin{aligned} c_{\text{norm}} &= 0.654\,, \\ f'_{\text{dir}} &= 0.903\,, \\ f'_{\text{res}} &= 1.097\,. \end{aligned} \tag{8.4}$$

i.e. a general MC normalisation factor of 0.673 with the same ratio as given in Sec. 8.1.

8.3 Reweighting of $z_{I\!P}$

In the left column of Fig. 8.3, the variable $z_{I\!P}^{obs}$ is shown for direct enriched and resolved enriched PHP in the final binning determined in Sec. 9.1. Since the distribution of $z_{I\!P}^{obs}$ in data is not simulated well by MC, a reweighting of the MC sample in bins of $z_{I\!P}^{obs}$ was advised (see also Sec. 8.4). The reweighting to data was performed separately for the regions enriched with direct PHP and resolved PHP. As a result of the reweighting, data and MC agree almost perfectly in all subsequent plots of $z_{I\!P}^{obs}$.

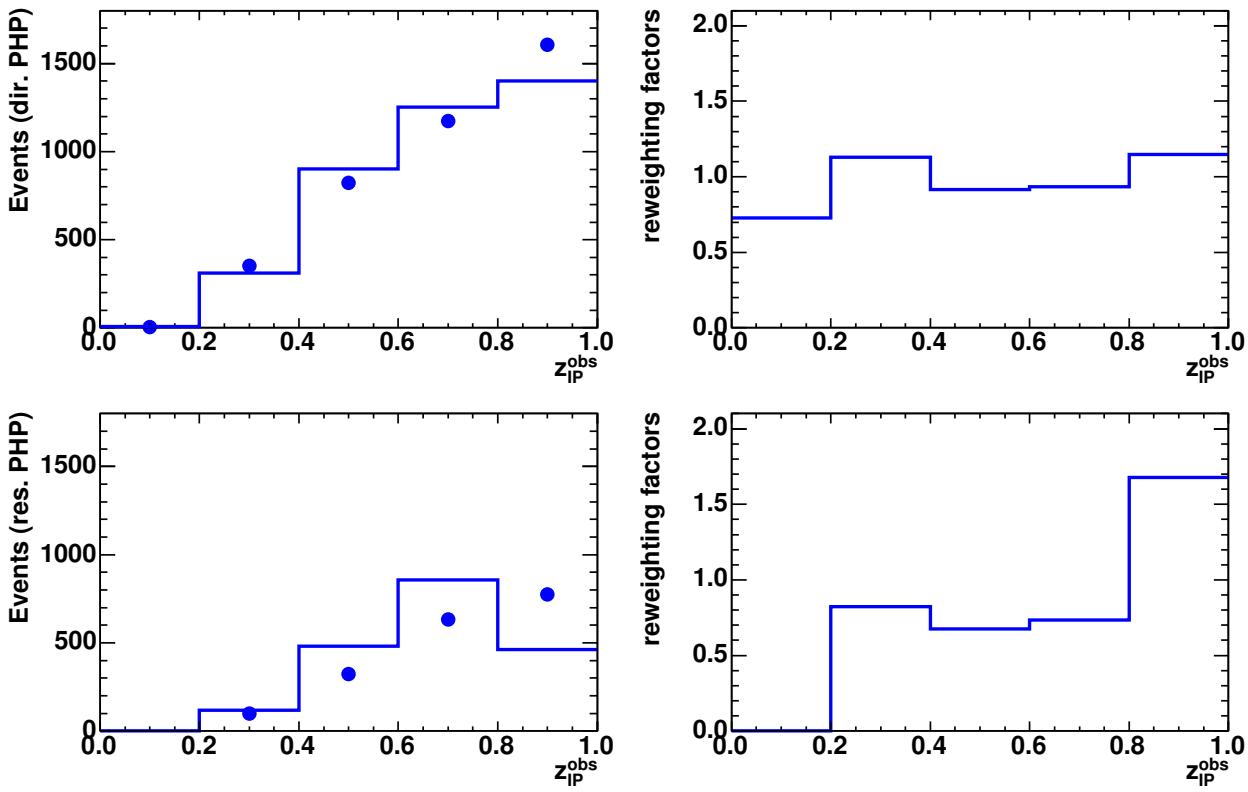

Figure 8.3: Reweighting of MC to data in bins of $z_{I\!P}^{obs}$ for direct enriched *(top row)* and resolved enriched PHP *(bottom row)*. The $z_{I\!P}^{obs}$-distributions for data (•) and MC (—) are shown in the *left column*, the reweighting factors for MC in the *right column*.

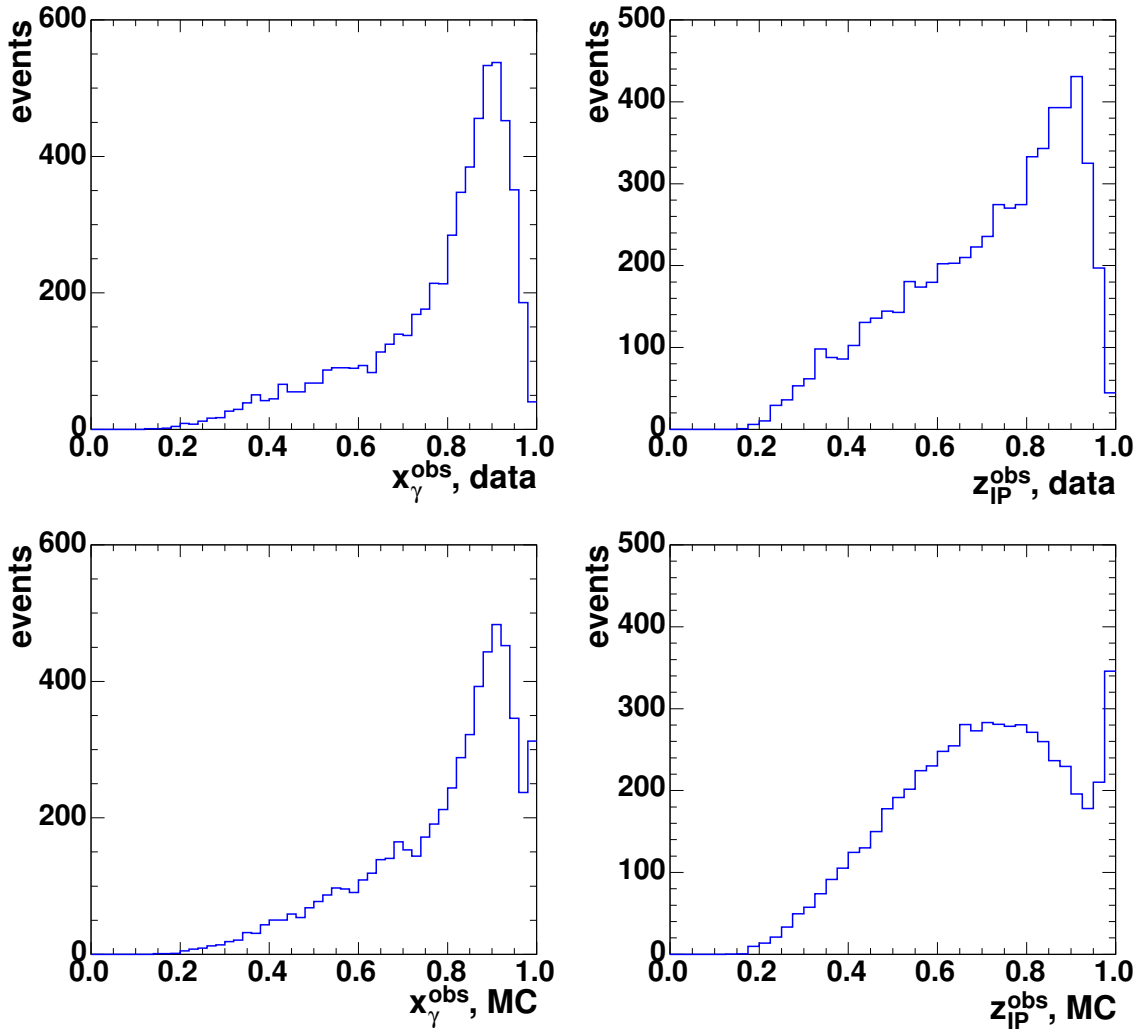

Figure 8.4: Distribution of x_γ^{obs} *(left column)* and $z_{I\!P}^{obs}$ *(right column)* for data *(top row)* and MC *(bottom row)* on DL – the distributions for MC reveal a secondary peak at high x_γ^{obs} and $z_{I\!P}^{obs}$.

8.4 Discussion of fitting and reweighting

A fine binning of x_γ^{obs} and $z_{I\!P}^{obs}$ before reweighting reveals that these variables are not described adequately by the RAPGAP MC (see Fig. 8.4): Both variables show secondary peaks at $x_\gamma^{obs} \simeq 1$ and $z_{I\!P}^{obs} \simeq 1$ which are not present in data. These peaks are mainly due to the MC sample for charm quark production[1] and are strongly correlated with each other (Fig. 8.6, top left) and weakly correlated with M_X (Fig. 8.6, top middle, right). On HL the peaks appear as an excess of D^* events. The peaks can be understood qualitatively when assuming that for the production of a (massive) $c\bar{c}$-pair in PHP, almost all available energy is required and hence, $x_\gamma^{obs} \sim 1$ and $z_{I\!P}^{obs} \sim 1$ is favoured.
The peaks could be an artefact of the parameters which were used for the generation of the MC: To calculate the matrix elements in pQCD, a hard scale is required. For all MC sets but

[1]The peaks are also visible in the MC sample for resolved PHP which is a combination of the processes generated separately for direct PHP, including charm quark production.

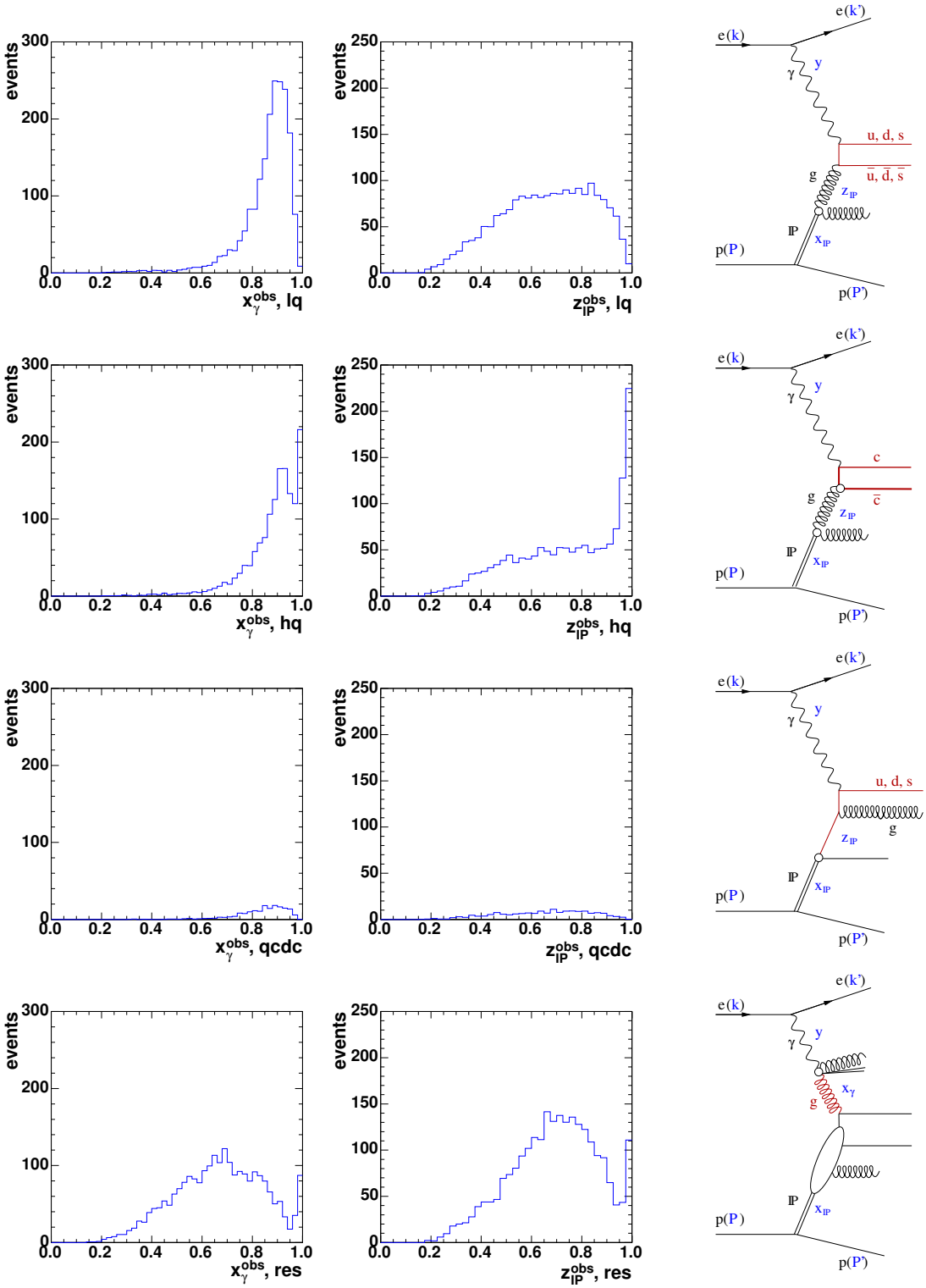

Figure 8.5: Distribution of x_γ^{obs} *(left column)* and $z_{I\!P}^{obs}$ *(middle column)* and the dominant MC process *(right column)* for production of light quark, charm quark, QCD-Compton scattering and resolved PHP *(from top to bottom)*. The blob in the lower diagram indicates integration over all simulated processes.

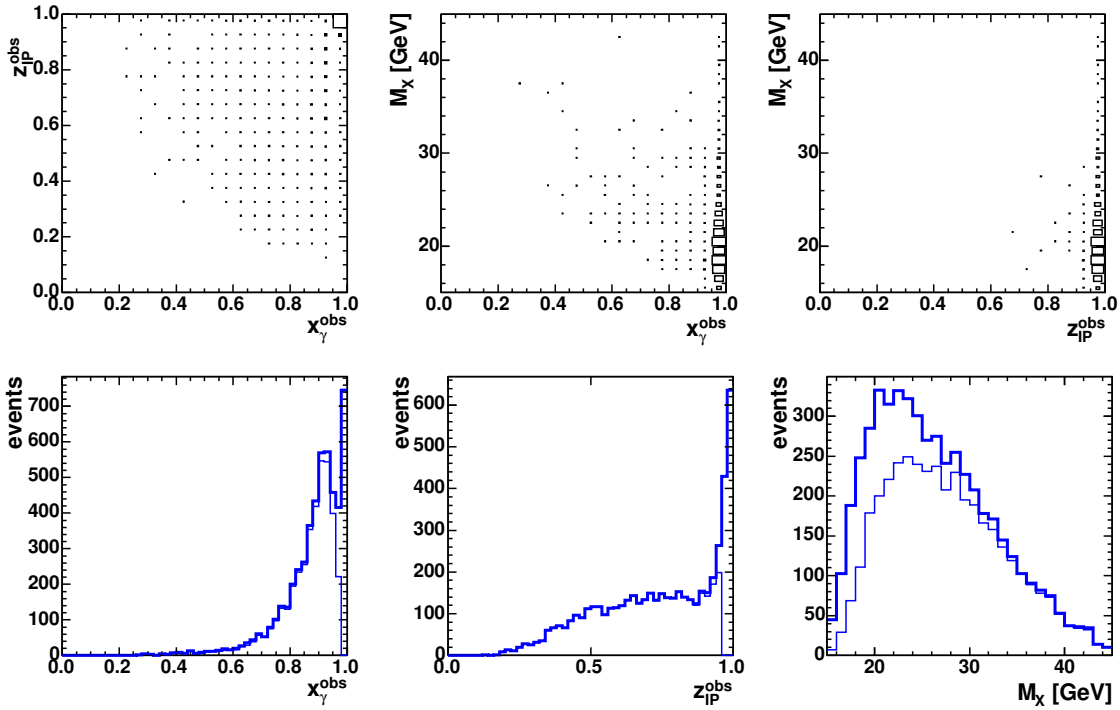

Figure 8.6: Details of the secondary x_γ^{obs}- and $z_{I\!P}^{obs}$-peak in MC sample of charm quark production — *top row:* Correlation plot for $z_{I\!P}^{obs}$ vs. x_γ^{obs} *(left)*, M_X vs. x_γ^{obs} with a cut on $z_{I\!P}^{obs} > 0.96$ *(middle)*, and M_X vs. $z_{I\!P}^{obs}$ with a cut on $x_\gamma^{obs} > 0.98$ *(right); bottom row:* distributions of x_γ^{obs}, $z_{I\!P}^{obs}$ and M_X without *(thick line)* and with *(thin line)* an additional cut on $x_\gamma^{obs} < 0.98 \;\vee\; z_{I\!P}^{obs} < 0.96$.

the one for charm quark production, the hard scale was defined by a minimal $\hat{p_T}^2 > 5\,\mathrm{GeV}^2$ of the partons of the initial process (Fig. 1.7). For the MC set for charm quark production, however, the squared quark mass m_c^2 was taken.
The secondary peak in x_γ^{obs} strongly bias the fit of MC to data: By excluding events with

$$x_\gamma^{obs} > 0.98 \;\wedge\; z_{I\!P}^{obs} > 0.96$$

from the MC sample of charm quark production (percentage $\approx 12.6\%$, for comparison percentage in data: 0.4%), the fit in x_γ^{obs} yields much better agreement of data and MC (Fig. 8.7), and results in equal contributions from direct and resolved PHP:

$$\begin{aligned} c_{\mathrm{norm}} &= 0.679\,, \\ f'_{\mathrm{dir}} &= 0.989\,, \\ f'_{\mathrm{res}} &= 1.011\,. \end{aligned} \tag{8.5}$$

The effect of the peak in $z_{I\!P}^{obs}$ on the reweighting factors was found to be less eminent. Since the peaks are present on both DL and HL, the effect on the acceptances is also negligible.
The treatment of the secondary peak in the MC sample of charm quark production is currently under discussion in the diffractive physics group at ZEUS.

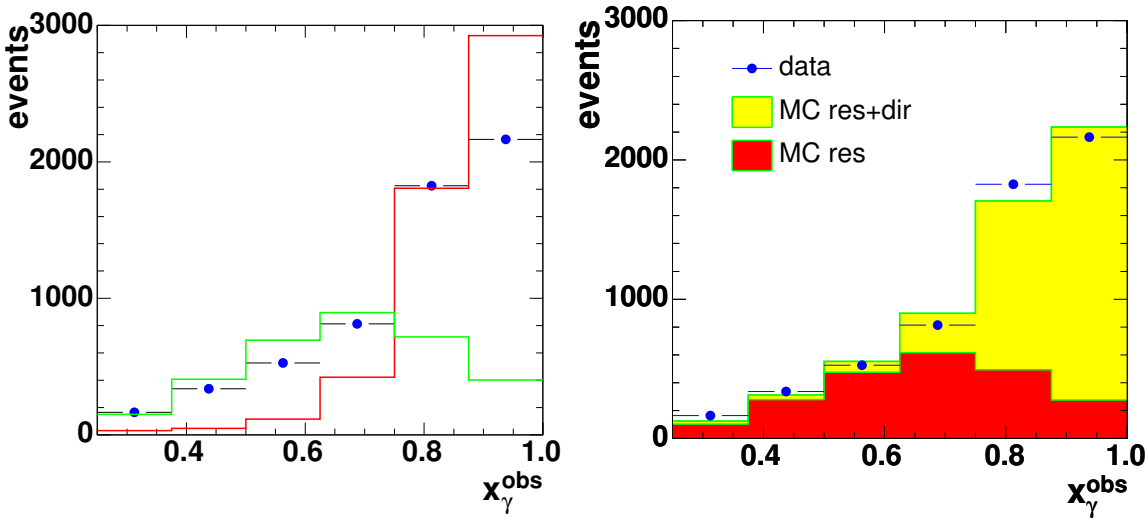

Figure 8.7: Fitting of MC (—) to data (•) in x_γ^{obs} with an additional cut of $x_\gamma^{obs} < 0.98 \ \vee \ z_{I\!P}^{obs} < 0.96$ on the MC sample for charm quark production.

Chapter 9

Control plots

For the reconstruction of hadronic cross sections, information at DL needs to be transformed to HL. In this analysis this transformation is performed with the bin-by-bin method. The application of this method requires good agreement of data and MC on DL (Sec. 9.2) with bin widths given by the resolution of the variables (Sec. 9.1) and their statistical error. Acceptances, which are also needed for the calculation of the cross sections on HL, are presented in Sec. 9.3 along with efficiencies and purities for the chosen set of variables.

9.1 Resolution

The resolution R of a variable v is given by

$$R = v^{DL} - v^{HL}$$

and is an indicator of the reconstruction quality of this variable. Resolutions for the chosen set of variables y_{JB}, x_γ^{obs}, $x_{I\!P}$, $z_{I\!P}^{obs}$, M_X, $E_T^{jet\,1}$, $\eta^{jet\,1}$, $E_T^{jet\,2}$ and $\eta^{jet\,2}$ are shown in Figs 9.1 and 9.2 as 2-dimensional contour plots (left column) and as 1-dimensional distributions (middle column). Additionally, event rates for MC on DL and HL in the chosen binning are shown in the right column.
The resolution of η^{jet} displays a broadening for values between $-0.8 < \eta^{jet\,1(2)} < +0.8$. This is due to *jet switching*, i.e. jets mismatched on DL and HL in cases where the secondary jet on one level is the highest energetic jet on the other level. For jets matched on DL and HL, no such broadening is observed (Fig. 9.3). Information on HL is not available for data, however, and therefore jet matching is not applicable for the reconstruction of the hadron level.
The resolution of E_T^{jet} is rather low, even for matched pairs of jets (Fig. 9.3). This is strongly affected by the angular resolution of the detector, given by the cell size of the CAL: For the energy reconstruction of ZUFOs, cells are combined to clusters (Sec. 5.2.2), where a distance measurement, based on the cell center, is applied. The energy of particles that hit the edge of a neighbouring cell can bias the calculation of (η, ϕ) or be discarded from a cluster and – subsequently – a jet, leading to an underestimation of the jet energy on DL. On the other hand, two particles that are not combined into one jet on HL, can hit the same CAL cell and be combined into one jet on DL, leading to an overestimation of the jet energy on DL.
From the resolutions in Figs. 9.1 and 9.2 a binning is deduced and proposed in Tab. 9.1. Although this binning seems more adequate than the binning used in a parallel analysis [67]

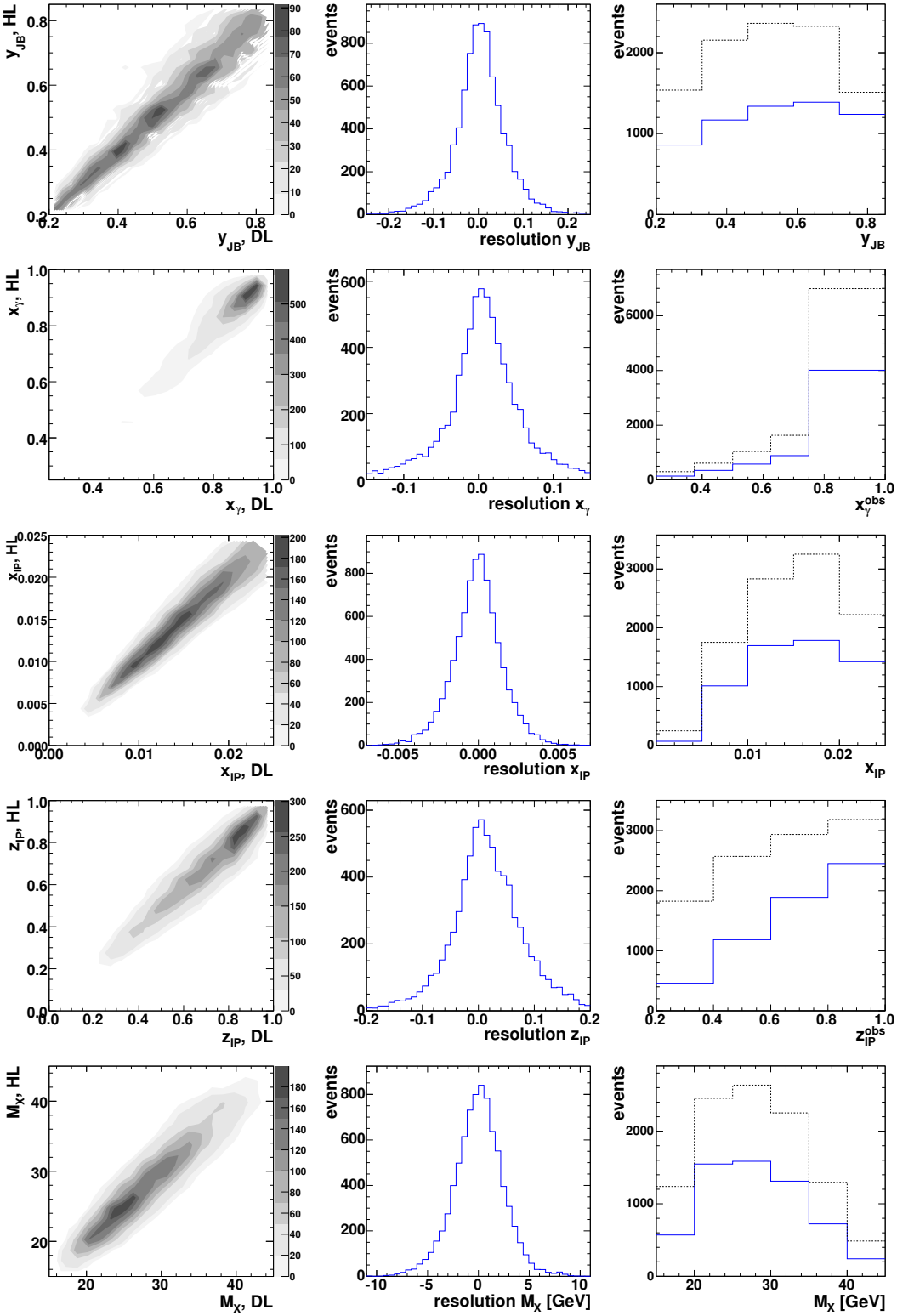

Figure 9.1: Resolution of HL vs. DL *(left column)*, integrated over DL *(middle column)* and event rates of MC *(right column)* on DL *(solid line)* and HL *(dashed line)* for the variables y_{JB}, x_γ^{obs}, $x_{I\!P}$, $z_{I\!P}^{obs}$, M_X.

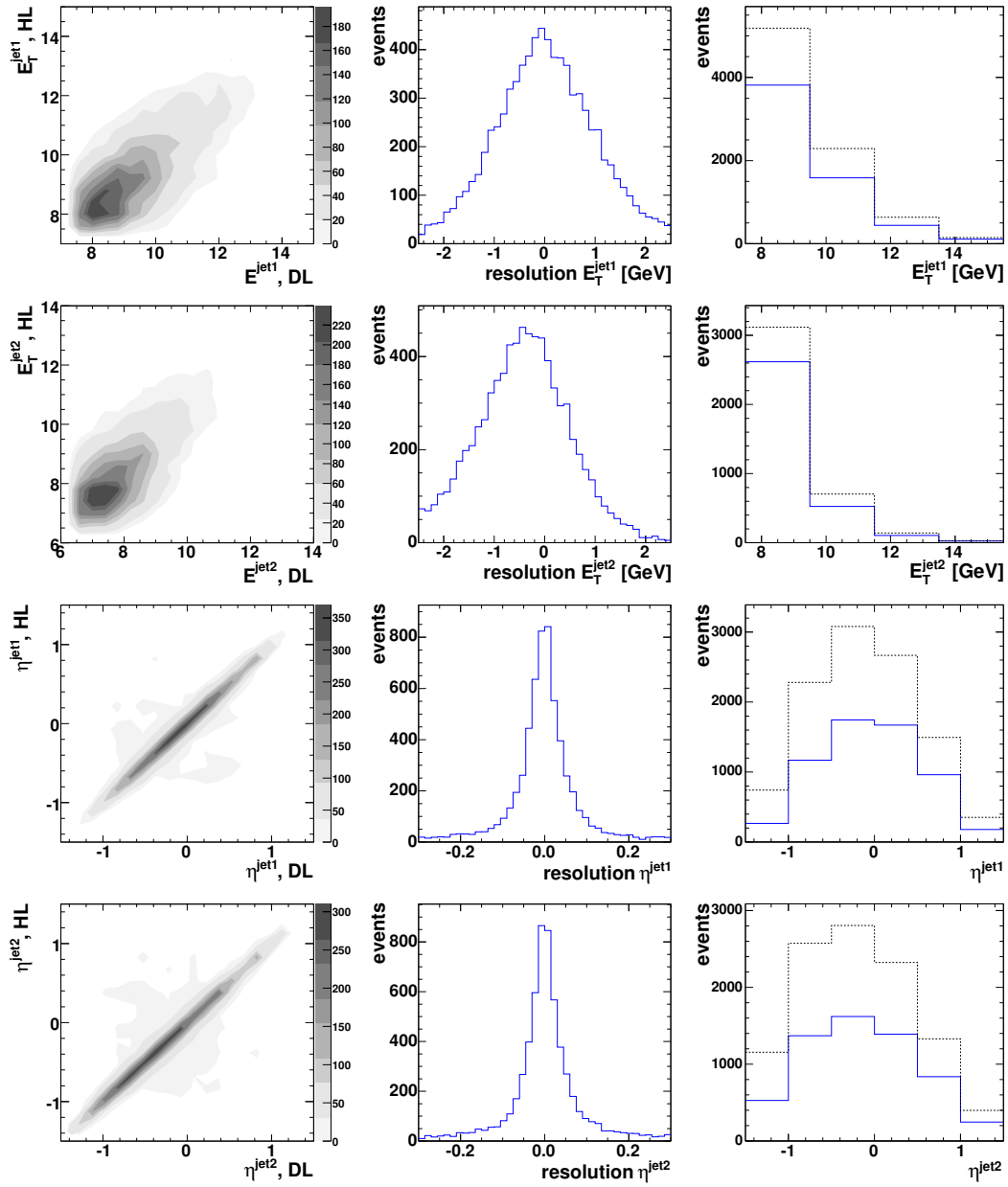

Figure 9.2: Resolution of HL vs. DL *(left column)*, integrated over DL *(middle column)* and event rates of MC *(right column)* on DL *(solid line)* and HL *(dashed line)* for the variables $E_T^{jet\,1}$, $\eta^{jet\,1}$, $E_T^{jet\,2}$ and $\eta^{jet\,2}$.

and consequently, for the NLO predictions [69], the NLO binning was used for comparability of results. With the exception of E_T^{jet}, where the bin width was set to 2 GeV to obtain moderate statistics in at least two bins, the bin width of most variables is only of the order of 1σ of the resolution and a possible source of migration effects. In particular, the two highest bins of x_γ^{obs} needed to be combined into one bin with a width of 0.25 for this reason. Migration in x_γ^{obs} seemed less pronounced for the slightly wider binning proposed in Tab. 9.1.

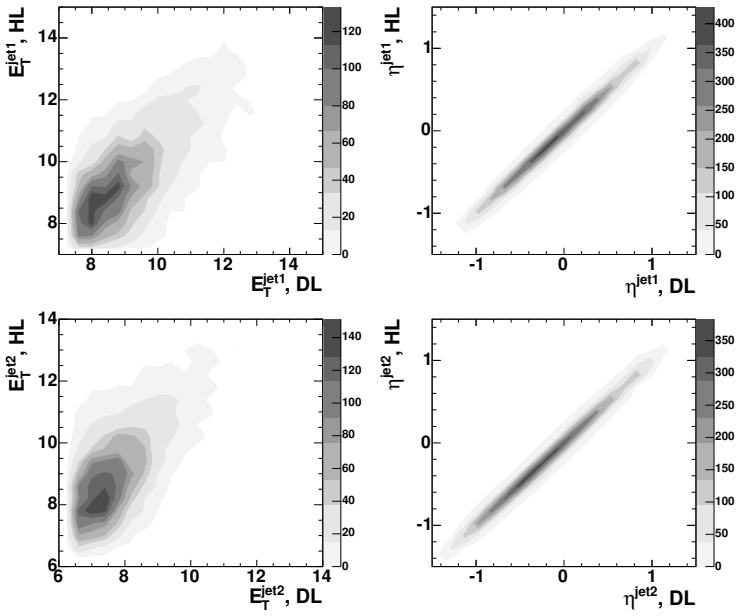

Figure 9.3: Resolution of E_T^{jet} *(left)* and η^{jet} *(right)* for matched jets with highest *(top)* and second highest *(bottom)* E_T^{jet} on DL. As mentioned in Sec. 5.3.3, the E_T^{jet} of the second highest energetic jet is shifted to lower values on DL than the highest energetic jet.

9.2 Event rates

The event rates for data are compared to MC in Fig. 9.4, where the MC was normalised and fitted to data in x_γ^{obs} and reweighted in bins of $z_{I\!P}^{obs}$ as described in the previous chapter. In

	Proposed binning	NLO binning
	bins × bin width *(range)*	bins × bin width *(range)*
y_{JB}	5×0.13 (0.20 to 0.85)	
x_γ^{obs}	5×0.15 (0.25 to 1.0)	$4 \times 0.125, 1 \times 0.25$ (0.25 to 1.0)
$x_{I\!P}$	5×0.005 (0.0 to 0.025)	
$z_{I\!P}^{obs}$	4×0.2 (0.2 to 1.0)	
M_X	4×8 GeV (14 to 46 GeV)	6×5 GeV (15 to 45 GeV)
E_T^{jet}	3×3 GeV (7.5 to 16.5 GeV)	4×2 GeV (7.5 to 15.5 GeV)
η^{jet}	6×0.5 (-1.5 to $+1.5$)	

Table 9.1: Binning as indicated by resolution and statistics *(left)* vs. applied binning *(right)*.

general, the agreement is good.
The $\eta^{jet\,1(2)}$-distribution of MC is shifted to higher (lower) values of η compared with data. This becomes more pronounced in the distribution of $(\eta^{jet\,1} - \eta^{jet\,2})$ (Fig. 9.4 bottom-right)

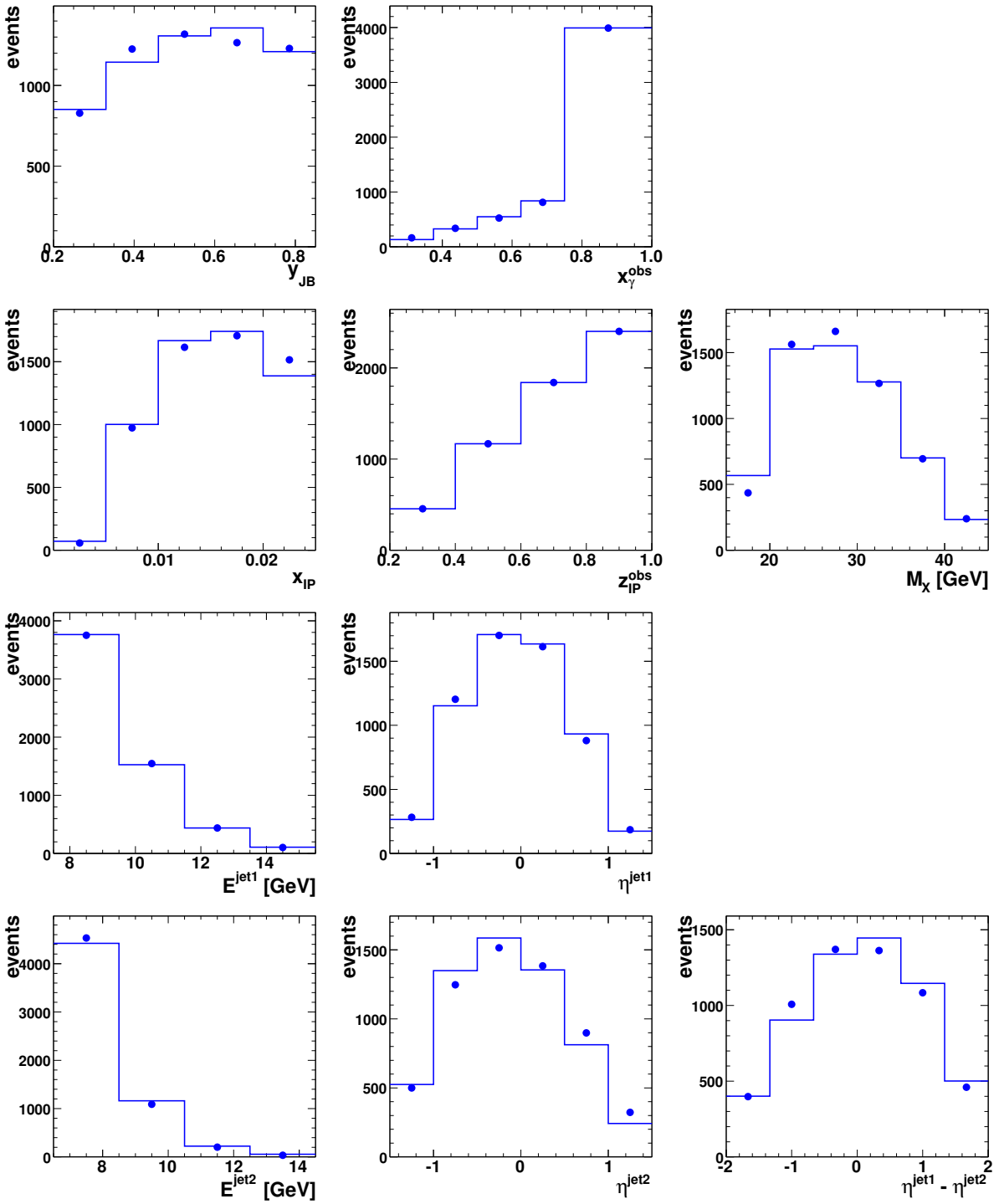

Figure 9.4: Event rates of data and MC on DL for variables y_{JB}, x_γ^{obs}, $x_{I\!P}$, $z_{I\!P}^{obs}$, M_X, $E_T^{jet\,1}$, $\eta^{jet\,1}$, $E_T^{jet\,2}$ and $\eta^{jet\,2}$.

which shows a strong asymmetry for MC jets: On average, more energy seems to be assigned to the leading jet in MC.
An excess of data is also seen for $0.020 < x_{I\!P} < 0.025$ and considered to be mainly due to non-diffractive background (Sec. 7.1.1, [67]).

9.3 Acceptance, efficiency and purity

The total cross section $\sigma_{\rm tot}^{HL}$ for data on HL is evaluated from

$$\sigma^{HL,\rm tot} = \frac{N_{\rm data}^{tot}}{A^{\rm tot} \cdot \mathcal{L}_{\rm data}},$$

where $\mathcal{L}_{data}$ is the total integrated luminosity of data and the acceptance A is defined as the ratio of events N passing the selection cuts on DL and HL in bin i:

$$A^{\rm tot} = \frac{N_{\rm MC}^{DL}}{N_{\rm MC}^{HL}},$$

For fairly good agreement of data and MC on DL, the differential cross section for a given variable can be reconstructed with the bin-by-bin method:

$$A^{bin\,i} = \frac{N_{\rm MC}^{DL\,bin\,i}}{N_{\rm MC}^{HL\,bin\,i}}, \tag{9.1}$$

$$\sigma^{HL\,bin\,i} = \frac{N_{\rm data}^{bin\,i}}{A^{bin\,i} \cdot \mathcal{L}_{\rm data}}. \tag{9.2}$$

Additional information is given by the efficiency ε and purity p, which give the ratio of events reconstructed in the same bin i on both DL and HL to the number of events on HL and DL, respectively:

$$\varepsilon^{bin\,i} = \frac{N_{\rm MC}^{DL\,bin\,i} \cap N_{\rm MC}^{HL\,bin\,i}}{N_{\rm MC}^{HL\,bin\,i}}, \tag{9.3}$$

$$p^{bin\,i} = \frac{N_{\rm MC}^{DL\,bin\,i} \cap N_{\rm MC}^{HL\,bin\,i}}{N_{\rm MC}^{DL\,bin\,i}}. \tag{9.4}$$

Acceptance, efficiency and purity are related by

$$\varepsilon = A \cdot p$$

and are shown for the variables y_{JB}, x_γ^{obs}, $x_{I\!P}$, $z_{I\!P}^{obs}$, M_X, $E_T^{jet\,1}$, $\eta^{jet\,1}$, $E_T^{jet\,2}$ and $\eta^{jet\,2}$ in Figs. 9.5 and 9.6.

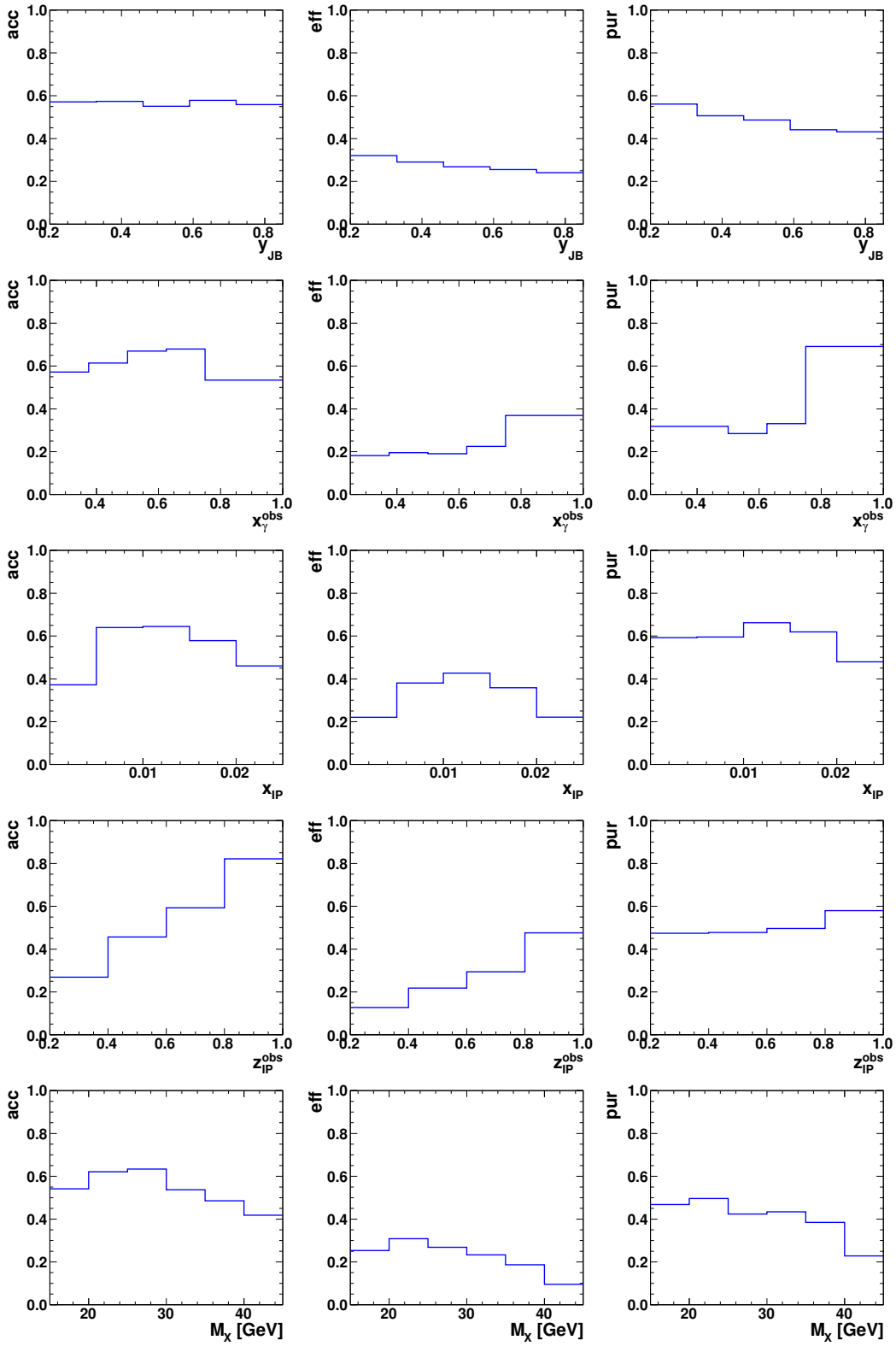

Figure 9.5: Acceptance *(left column)*, efficiency *(middle column)* and purity *(right column)* for the variables y_{JB}, x_γ^{obs}, $x_{I\!P}$, $z_{I\!P}^{obs}$ and M_X.

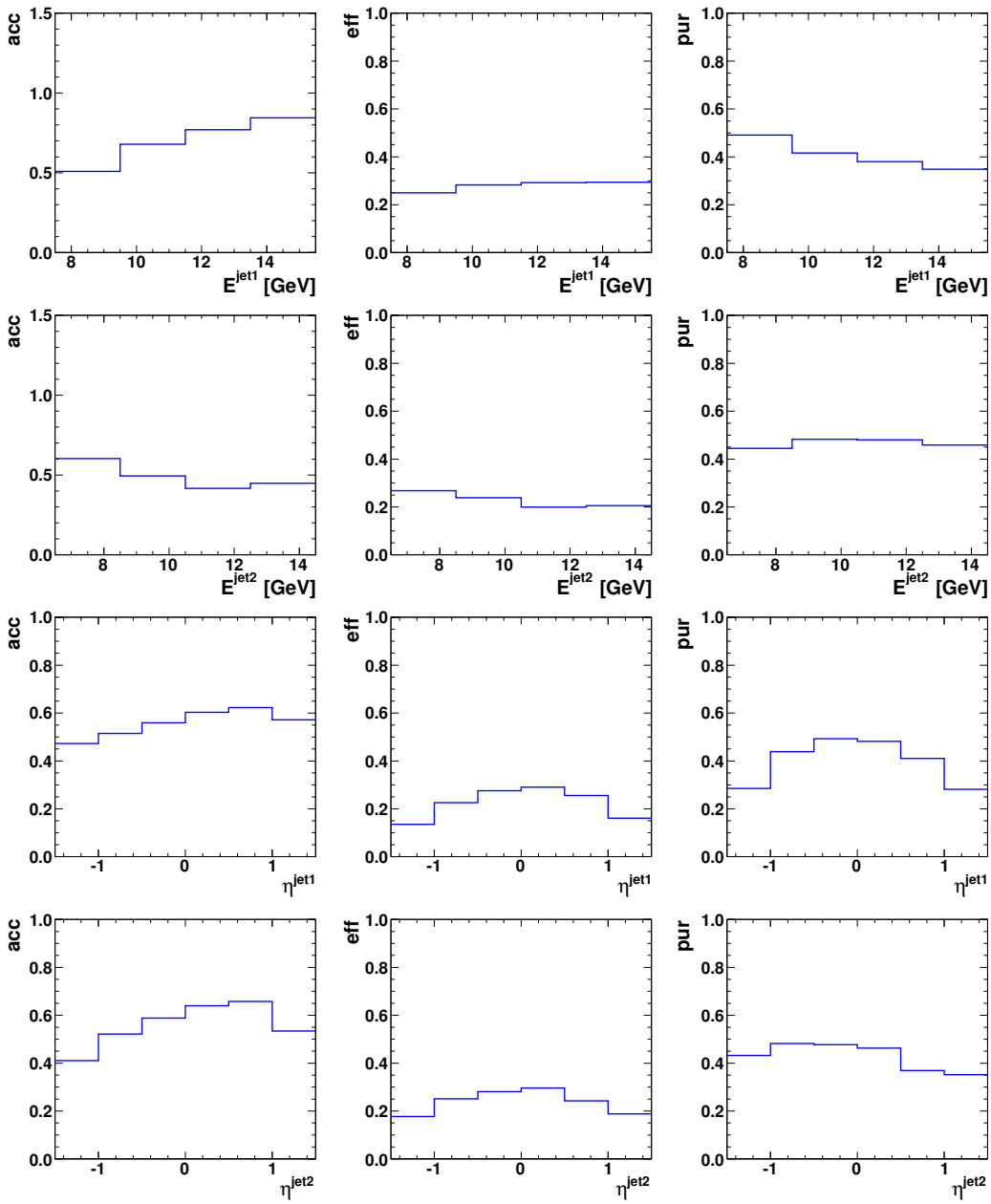

Figure 9.6: Acceptance *left columns)*, efficiency *(middle column)* and purity *(right column)* for the variables $E_T^{jet\,1}$, $\eta^{jet\,1}$, $E_T^{jet\,2}$ and $\eta^{jet\,2}$.

9.4 Effect of VO-corrections on acceptances

The VO-corrections, introduced in Sec. 5.2.5, contained unreasonably high correction factors in the forward bin $\theta < 7^\circ$ ($\eta < 2.8$). As a consequence, almost any ZUFO that passed the CAL noise cut of 100 MeV, was corrected to values above the η^{max}-threshold of 400 MeV and taken into account for the calculation of η^{max}. Since the VO-correction factors were also significantly higher for MC than for data (Fig. 5.3), the calculated η^{max} was higher for MC and fewer MC events passed the cut of $\eta^{max} < 2.8$. Although the HL is not directly affected by this problem, the fit of MC to data in x_γ^{obs} led to a lower normalisation factor and, hence,

to lower event rates of MC on HL after normalisation. Consequently the acceptances were too high and the cross section, based on VO-correction, underestimated by $\sim 10\%$. The VO-corrections were discarded from the further analysis for above reasons.

Chapter 10

Cross sections

10.1 Single differential cross sections

Single differential cross sections are presented in Fig. 10.1 as a function of y_{JB}, x_γ^{obs}, $x_{I\!P}$, $z_{I\!P}^{obs}$, M_X, $E_T^{jet\,1}$, $\eta^{jet\,1}$, $E_T^{jet\,2}$ and $\eta^{jet\,2}$. The systematic and total uncertainty as determined in Sec. 11.1 is indicated by the error bars in each bin[1].
For comparison, the cross sections for LO MC are also given in each plot. Since the MC sample was normalised to data, this comparison only provides a test of the shape of the distributions. In general, good agreement is observed between the data and the LO MC. The distribution of x_γ^{obs} seems slightly steeper in data and is related to the inadequacy of MC at high x_γ^{obs} (Sec. 8.4). The excess of data at high $x_{I\!P}$ is considered to be mainly due to non-diffractive background as discussed in Sec. 7.1.1. The agreement of $z_{I\!P}^{obs}$ is a consequence of the $z_{I\!P}^{obs}$-reweighting of MC and does not bear any physical meaning.
Tables of the cross sections and the statistical and systematic errors can be found in App. D.

10.2 Double differential cross sections

As discussed in Sec. 1.7.2, factorisation is expected to hold for direct PHP but to fail for resolved PHP by theoretical considerations. For this reason, the cross sections were also investigated double differentially for direct enriched ($x_\gamma^{obs} \geq 0.75$) and resolved enriched PHP ($x_\gamma^{obs} < 0.75$).
These cross sections are shown in Figs. 10.2 and 10.3, respectively, for the variables y_{JB}, x_γ^{obs}, $x_{I\!P}$, $z_{I\!P}^{obs}$, M_X, $E_T^{jet\,1}$, $\eta^{jet\,1}$, $E_T^{jet\,2}$ and $\eta^{jet\,2}$. The agreement with RAPGAP LO MC is fairly good and the comparison reveals the same characteristics as described for single differential cross sections. Tables of the cross sections and the statistical and systematic errors can be found in Apps. E and F.

[1]Since the statistical uncertainty is small for most bins and covered by the dot size, the standard depiction of error bars has been reversed for a better visualisation of the statistical uncertainty: The inner error bars indicate the systematic uncertainty, whereas the outer errors bars indicate the systematic and statistical uncertainty added in quadrature. The statistical uncertainties is approximately twice the difference between inner and outer error bars:

$$\Delta\sigma_{total} - \Delta\sigma_{syst} \;=\; \sqrt{\Delta\sigma_{stat}^2 + \Delta\sigma_{syst}^2} - \Delta\sigma_{syst} \;\approx\; \frac{\Delta\sigma_{stat}}{2}\,.$$

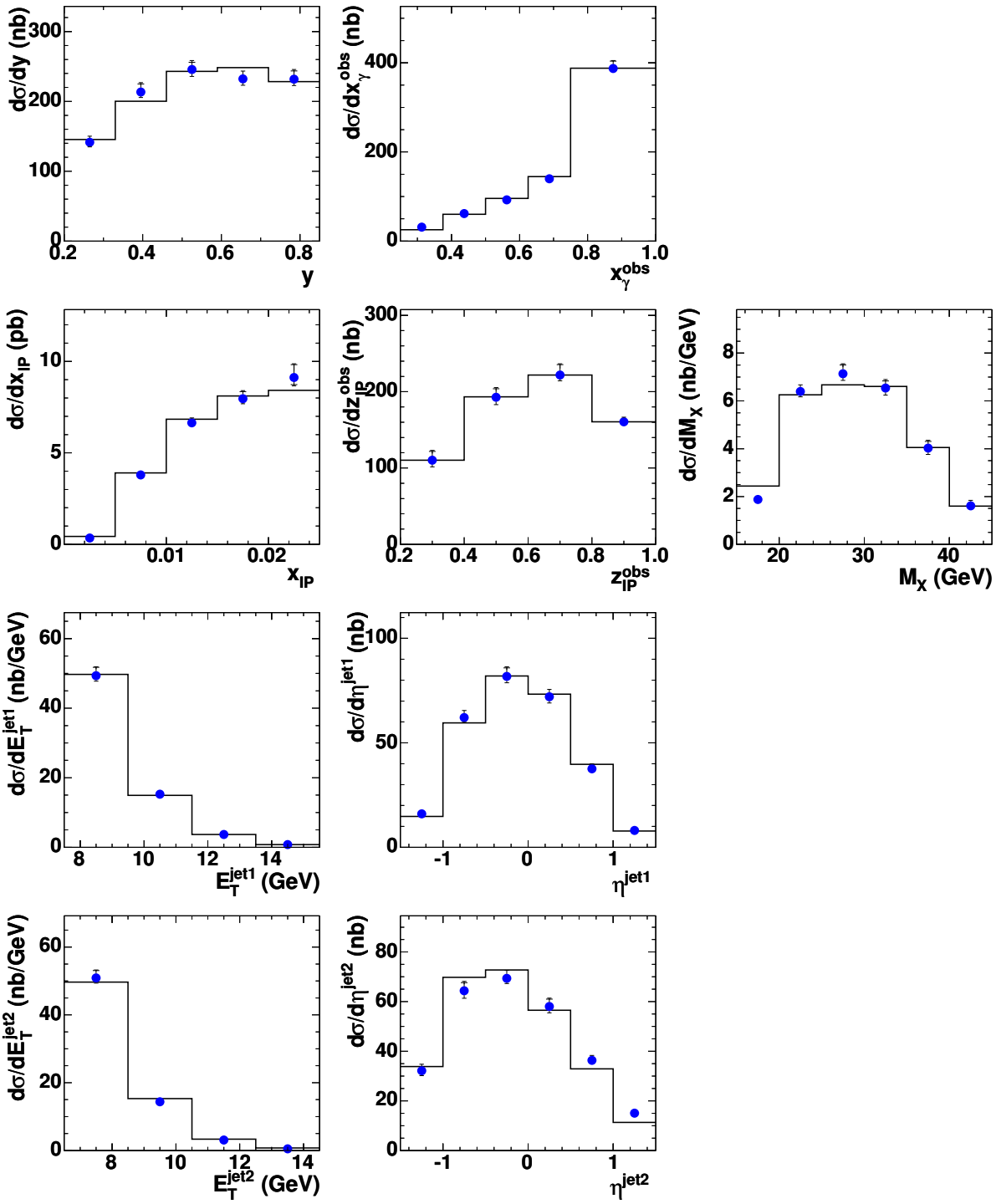

Figure 10.1: Single differential cross sections for data (•) and RAPGAP MC (—) for variables y_{JB}, x_γ^{obs}, $x_{I\!P}$, $z_{I\!P}^{obs}$, M_X, $E_T^{jet\,1}$, $\eta^{jet\,1}$, $E_T^{jet\,2}$ and $\eta^{jet\,2}$ – the inner error bars indicate the systematic uncertainty as determined in Sec. 11.1 while the outer error bars indicate the statistical and systematic uncertainties added in quadrature.

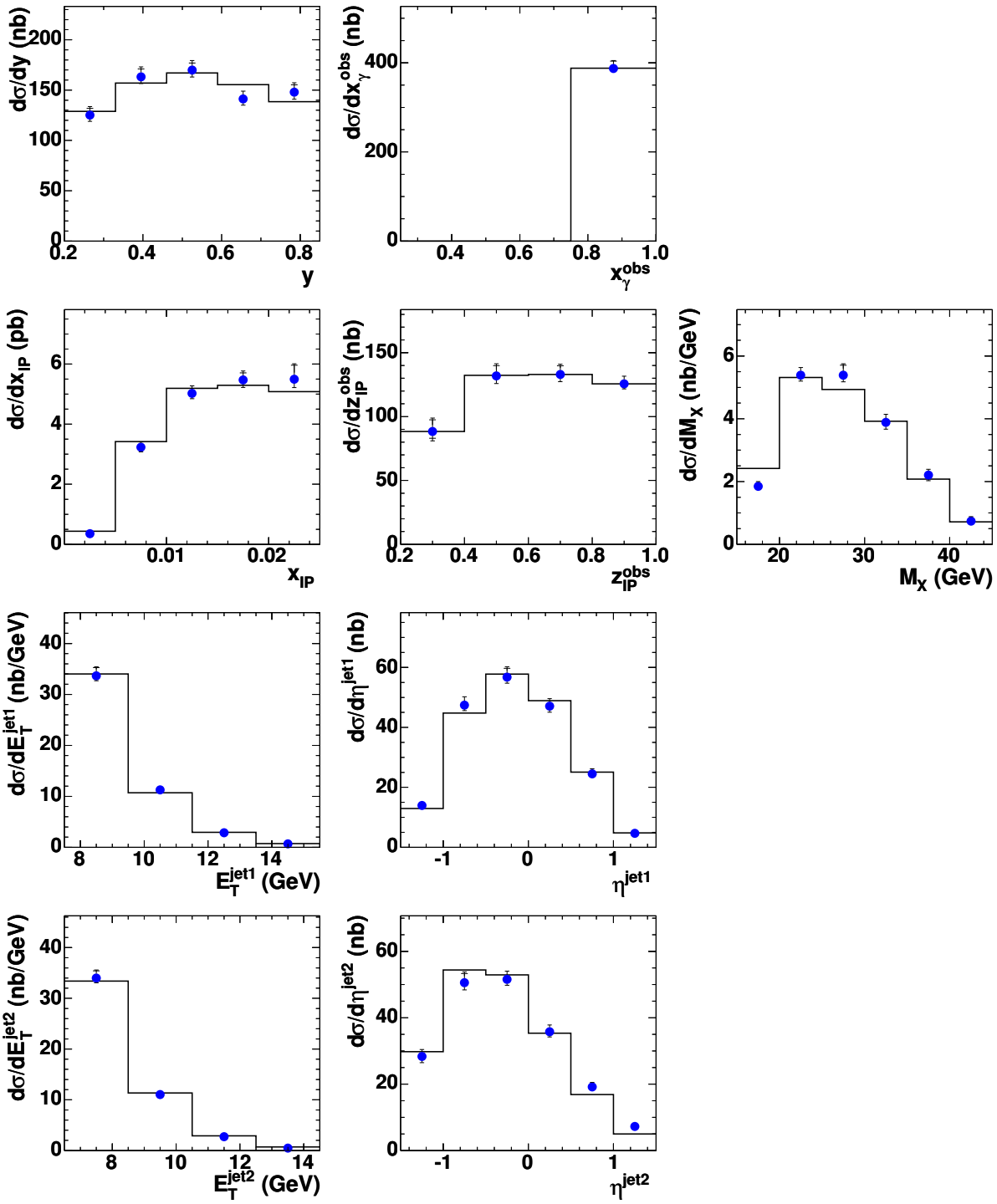

Figure 10.2: Double differential cross sections for data (•) and RAPGAP MC (—) in the range $x_\gamma^{obs} \geq 0.75$ enriched with direct PHP for variables y_{JB}, x_γ^{obs}, $x_{I\!P}$, $z_{I\!P}^{obs}$, M_X, $E_T^{jet\,1}$, $\eta^{jet\,1}$, $E_T^{jet\,2}$ and $\eta^{jet\,2}$ – the inner error bars indicate the systematic uncertainty as determined in Sec. 11.1 while the outer error bars indicate the statistical and systematic uncertainties added in quadrature.

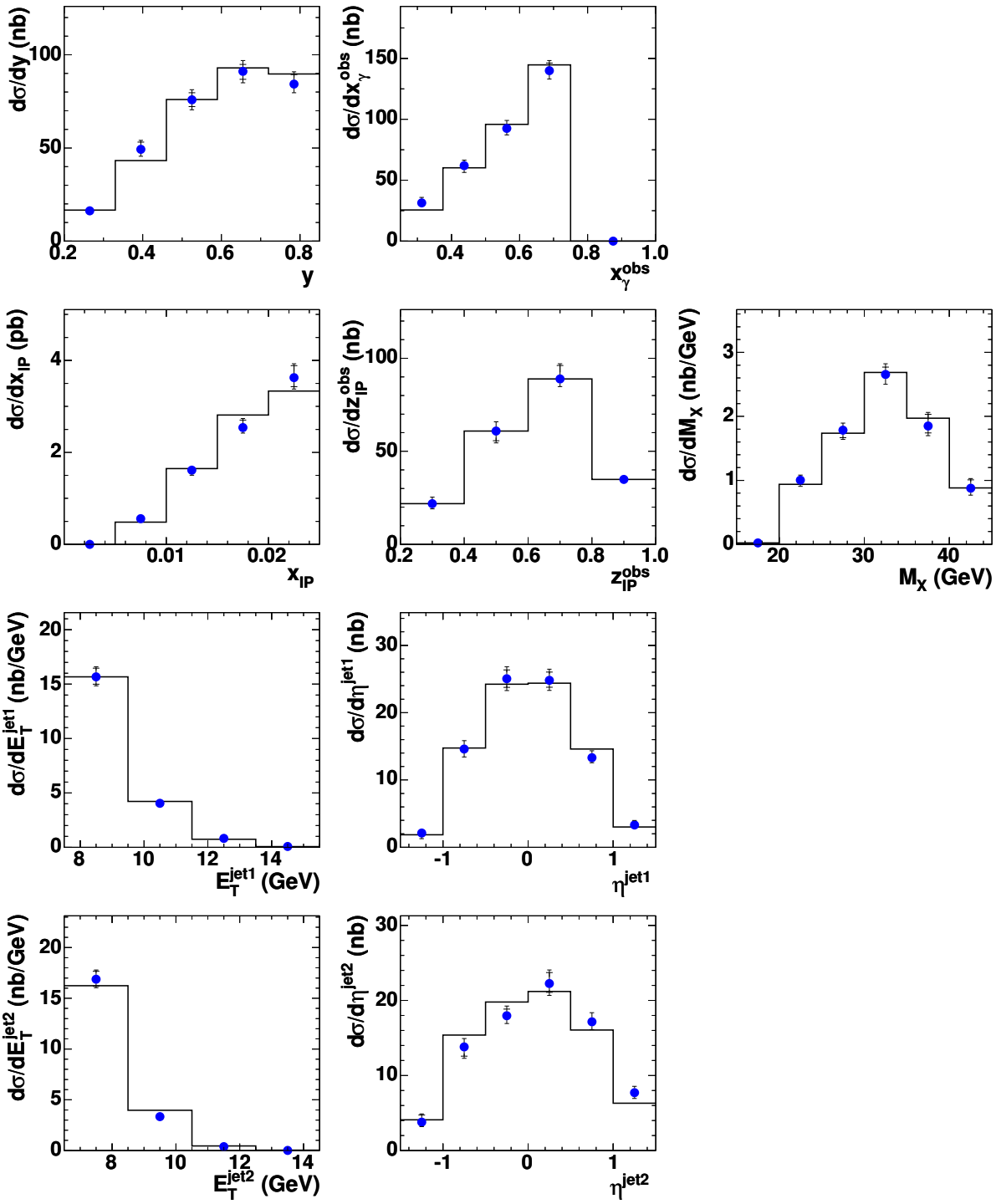

Figure 10.3: Double differential cross sections for data (•) and RAPGAP MC (—) in the range $x_\gamma^{obs} < 0.75$ enriched with resolved PHP for variables y_{JB}, x_γ^{obs}, $x_{I\!P}$, $z_{I\!P}^{obs}$, M_X, $E_T^{jet\,1}$, $\eta^{jet\,1}$, $E_T^{jet\,2}$ and $\eta^{jet\,2}$ – the inner error bars indicate the systematic uncertainty as determined in Sec. 11.1 while the outer error bars indicate the statistical and systematic uncertainties added in quadrature.

Chapter 11

Systematic studies

In this chapter the dependence and influence of systematic biases on the analysis will be investigated. Possible sources of systematic errors are identified in Sec. 11.1. The results of the systematic studies are shown for the full x_γ^{obs} range in App. A and for the range enriched with direct and resolved PHP in Apps. B and C, respectively. Conclusions will be drawn in Sec. 11.2.

11.1 Systematic tests

Systematic dependencies of the experiment and the analysis were investigated in order to determine the total uncertainty of the results. Often the cut values that are used for the selection of the data sample, are varied for this purpose by 1σ of the variable's resolution. However, a simple variation of the cut values was disfavoured, because for some variables a dependency on the cut value is expected: For example, the jet energy E_T^{jet} in PHP provides the hard scale (Eqn. 1.9), comparable to Q^2 in DIS. Moreover, some cut variables might not be independent and the systematic error obtained from one can indirectly affect others and not be combined with the systematic errors derived from a cut variation of those variables.
For this reason, the primary variables which were used for the calculation of the kinematic variables, were modified to study their influence on the results. For each of these systematic modifications, the cross section σ_{sys} was calculated as described in the previous chapters, and its deviation from the central cross section σ_0 was quantified according to

$$\frac{\Delta\sigma}{\sigma} = \frac{\sigma_{sys} - \sigma_0}{\sigma_0}$$

The deviations $\Delta\sigma/\sigma$ are shown for the full x_γ^{obs} range in App. A and for the range enriched with direct and resolved PHP in Apps. B and C, respectively.
The following variables and parameters have been identified as independent and primary to the calculation of the kinematic variables presented in the analysis:

1. the reconstruction of the z vertex in data;

2. the energy uncertainty of ZUFOs;

3. the correction factors for the jet energy E_T^{jet} on DL;

4. the cut on η^{max} which defines the angle of the most forward ZUFOs above an energy threshold;

5. the energy threshold in the calculation of η^{max} ;

6. the cut on y_{JB} .

The systematic tests for these variables are motivated in Sec. 11.1.1 to Sec. 11.1.6 and summarised in Tab. 11.1.

Systematic check	**Variation**	**Applied to**
Shift of z vertex	$\pm 5\,\text{mm}$	data
ZUFO energy Scale uncertainty	CTD: $\pm 0.3\%$ F/BCAL $\pm 1\%$, RCAL $\pm 2\%$	data
Discriminative correction factors for jet 1, 2	*(see Eqn.11.1)*	data, MC
Variation of η^{max} cut	2.8 ± 0.2	data, MC
Variation of η^{max} threshold	$(400 \pm 100)\,\text{MeV}$	data, MC
Variation of upper y_{JB} limit	$0.85 \rightarrow 0.78$	data, MC

Table 11.1: Systematic checks and their variation values.

11.1.1 *z*-Vertex

In the production of dijets in diffractive PHP, the bulk of most events is concentrated in the central region of the detector between $-1.0 \lesssim \eta \lesssim +1.0$. Therefore the calculation of the longitudinal momentum of ZUFOs, $p_{z,zufos}$, and hence the calculation of y_{JB}, $x_{I\!P}$ and M_X (Sec. 5.4) depend on the precise reconstruction of the z vertex.
While the z_{vtx}-distribution in MC peaks at the nominal interaction point IP, i.e. at $z_{vtx} \approx 0.0\,\text{mm}$, a small shift of the peak to $z_{vtx} \approx -3.9\,\text{mm}$ has been observed for data. The effect of this deviation, and the uncertainty of the reconstruction of the z vertex, have been investigated by a shift of $\pm 5\,\text{mm}$ in data.

11.1.2 ZUFO energy scale

The variables y_{JB}, $x_{I\!P}$ and M_X are calculated from the total energy and longitudinal momentum of ZUFOs (Sec. 5.4). The precision of their reconstruction has been investigated by ZEUS previously [70]. The energy scale uncertainty of ZUFOs based on CAL measurements was estimated to be 1% for the FCAL and BCAL, and 2% for the RCAL. For ZUFOs based on CTD tracks, the uncertainty was determined to be 0.3%. The ZUFO energy and momentum have been modified according to these values in order to estimate the effect of the energy scale uncertainty on the cross sections.

11.1.3 E_T^{jet} correction

In Sec. 5.3.3 correction factors for the transverse jet energy, E_T^{jet}, have been determined. It has been observed that in MC the jet with the second highest E_T^{jet} on DL is usually underestimated compared to HL by a larger amount than the jet with the highest E_T^{jet} (Fig. 5.7 and 5.8). Correction factors for E_T^{jet}, which discriminate between first and second jet, are problematic because the percentage of *jet switching* from DL to HL (Sec. 5.3.3) in data cannot be determined. As a systematic check, however, discriminative correction factors can be applied to obtain an upper and lower limit, based on the assumption that jet switching does not occur in data.
Jets with highest and second highest E_T^{jet}, as reconstructed from DM-corrected zufos (Sec. 5.2.5), were corrected in an analogous way to the procedure described in Eqn. 5.1:

$$\begin{aligned} E_T^{jet\,corr} &= c_{\mathrm{DM}}^{jet\,j}(i) \cdot E_T^{jet} \quad \text{with} \\ c_{\mathrm{DM}}^{jet1}(i) &= \{0.048,\ \ 0.068,\ \ 0.083,\ \ 0.091,\ \ 0.125\}\,, \\ c_{\mathrm{DM}}^{jet2}(i) &= \{0.0,\ \ -0.001,\ -0.013,\ -0.015,\ -0.024\}\,, \\ \text{and} \qquad i &= \lfloor E_T^{jet} - 6\,[\mathrm{GeV}] \rfloor\,. \end{aligned} \tag{11.1}$$

11.1.4 Cut on η^{max}

The cut of $\eta^{max} < 2.8$ selects events with a large rapidity gap. As visible in Fig. 6.6, it serves as the main selection criteria of diffractive events in this analysis, and a variation of the cut value by 2.8 ± 0.2 was chosen as a systematic check.

11.1.5 Energy threshold for the η^{max} calculation

The value of η^{max} was calculated from all ZUFOs above an energy threshold of 400 MeV (Sec. 5.4). Although this value is commonly used at ZEUS, it is a rather experimental parameter which possibly depends on the underlying physical process. For this reason, the threshold was modified to (400 ± 100) MeV.

11.1.6 Cut on y_{JB}

The cut of $y_{JB} < 0.85$ was implemented in order to reject DIS events (Sec. 6.3). This cut, adopted to be consistent with a parallel analysis and the NLO predictions, is uncommonly high for ZEUS and extends into the tail of the DIS peak at $y_{JB} \lesssim 1$ (Fig. 6.3). Since this

could cause a bias from DIS events in the data sample, a more conservative cut of $y_{JB} < 0.78$ was introduced as a systematic check.

11.2 Conclusion on systematic studies

The systematic uncertainties based on above modifications are small, typically at the order of less than 2%, with the exception of the systematic errors arising from the cut on η^{max} and y_{JB}.
The largest observed systematic error of $\sim (6-8)\%$ is due to the cut on η^{max} and points to the unsatisfactory simulation of η^{max} in MC (Sec. 5.4, Fig. 5.9). Interestingly, the modification of the energy threshold in the calculation of η^{max} has a negligible effect and hence indicates that the systematic uncertainty could be an effect of the underlying physics and its simulation in the MC program. Further studies on soft particle production and its tuning in MC simulations could reduce the uncertainty due to η^{max} cuts in ZEUS.
The modification of the y_{JB} cut leads to high systematic uncertainties in a few bins. The non-fluctuating shape of the deviations indicate a trend and hence favour a reduction of the cut value. It seems advisable to consider a reduced y_{JB} cut in case of a re-calculation of the NLO predictions.

Chapter 12

Cross section comparison with NLO

In this chapter, cross sections for data are compared to NLO calculations. The NLO predictions are based on a model of M. Klasen and G. Kramer [17] (Sec. 1.7.2) and were calculated with their program for the kinematic range of this analysis by L. Adamczyk [69]. The calculations were performed on PL for the three different dPDFs described in Sec. 1.8. For comparison of the NLO cross sections with those of data (Sec. 12.3), they need to be transformed to HL (Sec. 12.2). The results are summarised in Sec. 12.5.
The program of M. Klasen and G. Kramer provides calculations for the variables y_{JB}, x_γ^{obs}, $x_{I\!P}$, $z_{I\!P}^{obs}$, M_X, $E_T^{jet\,1}$ and $\eta^{jet\,1}$.

12.1 NLO cross sections on PL

The NLO cross sections were calculated separately for processes of direct and resolved PHP. In Fig. 12.1 the sum of these cross sections is shown as filled histograms for the three dPDFs described in Sec. 1.8, i.e. the H1 2002 fit, the Zeus Lps and Zeus Glp fit. The MC cross sections obtained with the H1 LO fit2 (Sec. 1.8.1) are included as a dashed line. For comparison with NLO, the MC samples for direct and resolved PHP were not fitted (Sec. 8.1), normalised (Sec. 8.2) or reweighted to data (Sec. 8.3).
The three different NLO predictions are similar in shape for all but the $z_{I\!P}^{obs}$ distribution and differ significantly in normalisation: The NLO cross sections derived from the Zeus Lps fit account for 78 % of those from the H1 2002 fit whereas the Zeus Glp fit accounts for only 27 %. The different normalisation of the H1 2002 fit and Zeus Lps fit could be affected by the fact that the H1 2002 fit was extracted on data which contain contributions from proton dissociation up to a mass of $M_Y \lesssim 1.6\,\text{GeV}$ whereas the LPS method naturally excludes such contributions. For a recent fit of the H1 collaboration ("H1 2006 fit" [29]), which includes the H1 2002 fit, the contribution of proton background was estimated to be $\approx (23 \pm 16)\%$. The dPDFs of the M_X fit are expected to contain $\approx (30 \pm 3)\%$ [30] background from proton dissociation. These estimated contributions were not subtracted from the NLO cross sections in the figures.

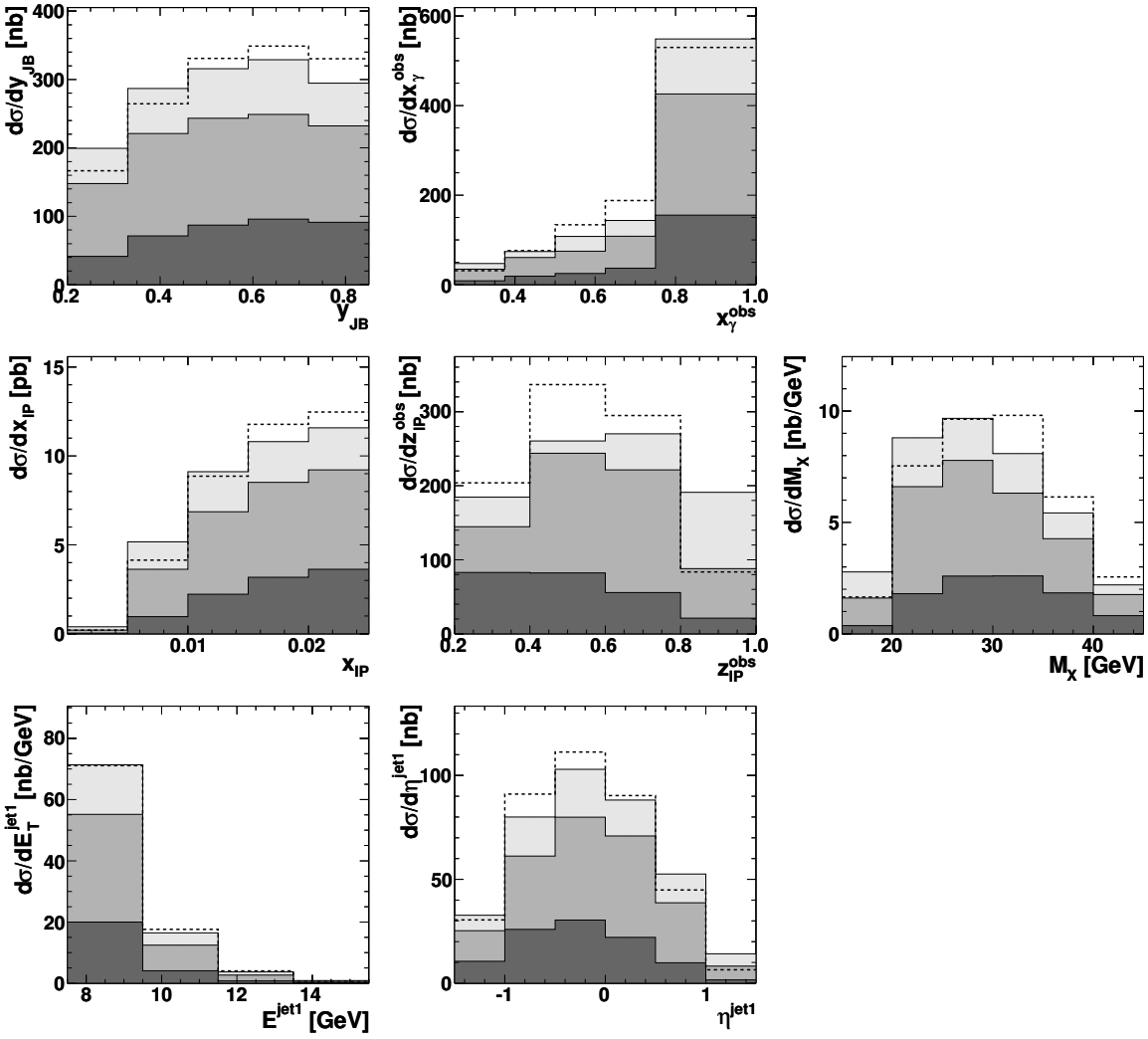

Figure 12.1: NLO cross sections on PL based on H1 2002 fit *(light grey)*, the ZEUS LPS-fit *(medium grey)* and the GLP-fit *(dark grey)*, and unnormalised, unfitted and unreweighted RAPGAP MC based on the H1 LO-fit 2 *(dashed line)*.

12.2 Hadronic corrections

NLO predictions are calculated on PL. For comparability with the measured cross sections of data in Secs. 10.1 and 10.2, the NLO calculations need to be transformed from PL to HL. This is achieved with the bin-by-bin method by calculating hadronic corrections c_{had} from the ratio of MC events, N_{MC}, on HL to PL in bin i:

$$c_{\mathrm{had}} = \frac{N_{\mathrm{MC}}^{HL\,bin\,i}}{N_{\mathrm{MC}}^{PL\,bin\,i}} \,. \tag{12.1}$$

Since no NLO MC was available for diffractive PHP, it was recommended by the diffractive physics group at ZEUS to use the LO RAPGAP MC for determination of the hadronic corrections.

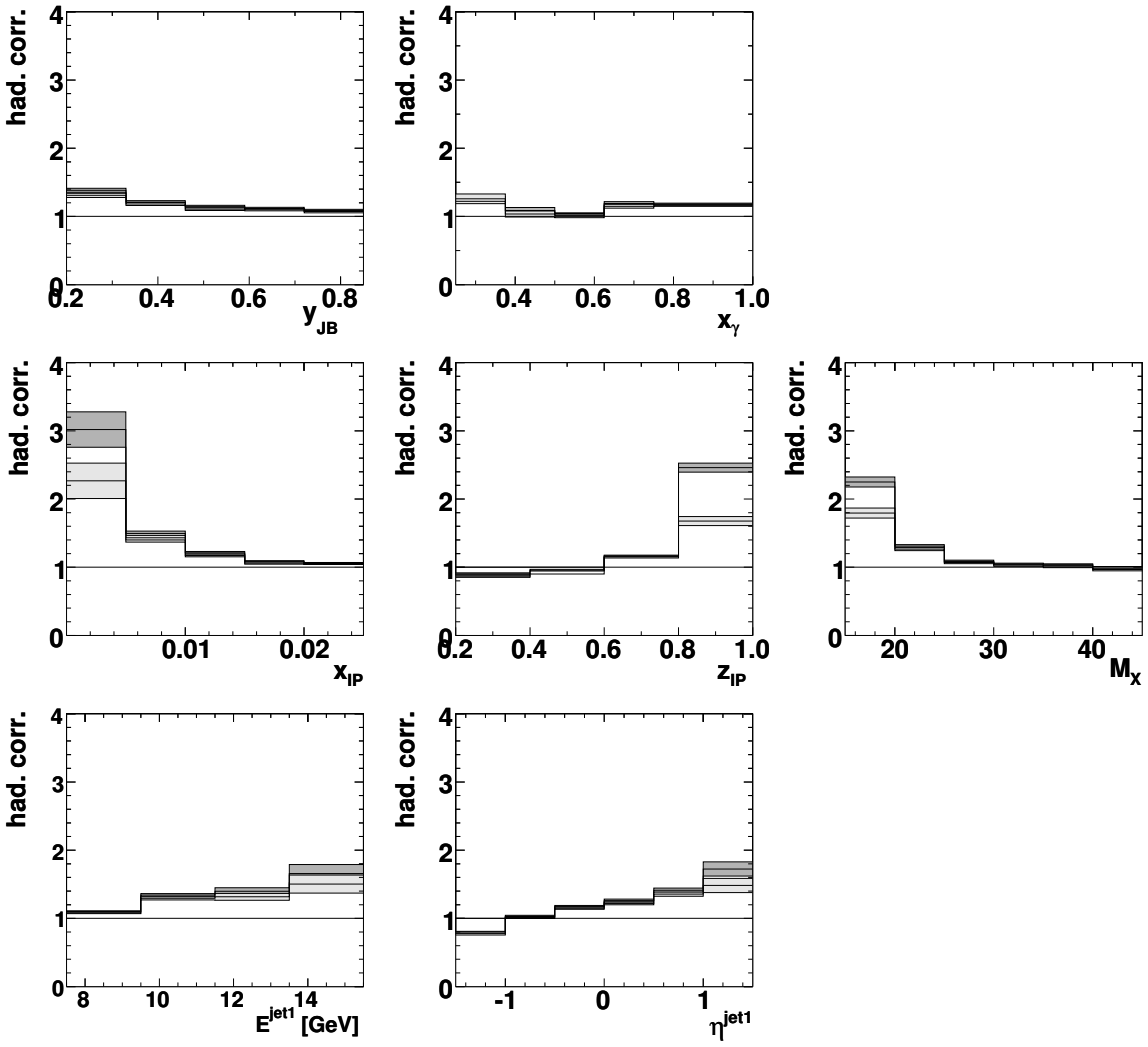

Figure 12.2: Hadronic corrections including error bands for the H1 2002 fit *(light grey)* and the ZEUS LPS fit *(dark grey)* calculated with the reweighted RAPGAP MC (H1 LO-fit 2) for the variables y_{JB}, x_γ^{obs}, $x_{I\!P}$, $z_{I\!P}^{obs}$, M_X, $E_T^{jet\,1}$ and $\eta^{jet\,1}$ — hadronic corrections for the ZEUS GLP fit are similar to those of the ZEUS LPS fit and were omitted for clearer visibility of the other two sets of hadronic corrections.

Hadronic corrections with RAPGAP

In order to account for the observed differences between LO MC and NLO predictions in the distribution of $z_{I\!P}^{obs}$ on PL (Fig. 12.1), the unnormalised and unfitted[1] RAPGAP MC sample was reweighted to the NLO predictions in bins of $z_{I\!P}^{PL}$ in accordance with the method described in Sec. 8.3, i.e. separately for $x_\gamma^{obs} \geq 0.75$ and $x_\gamma^{obs} < 0.75$. For compatibility of results, this reweighting procedure was performed independently for the NLO predictions using the dPDFs from the H1 2002 fit and the LPS fit, before the hadronic corrections were calculated.
Figure 12.2 shows the hadronic corrections which were obtained after the $z_{I\!P}^{PL}$ reweighting

[1]The fitting parameters for direct and resolved PHP were omitted in MC because no fitting was applied to the direct and resolved contributions of the NLO calculations. The constant normalisation factor cancels out in the calculation of the hadronic corrections.

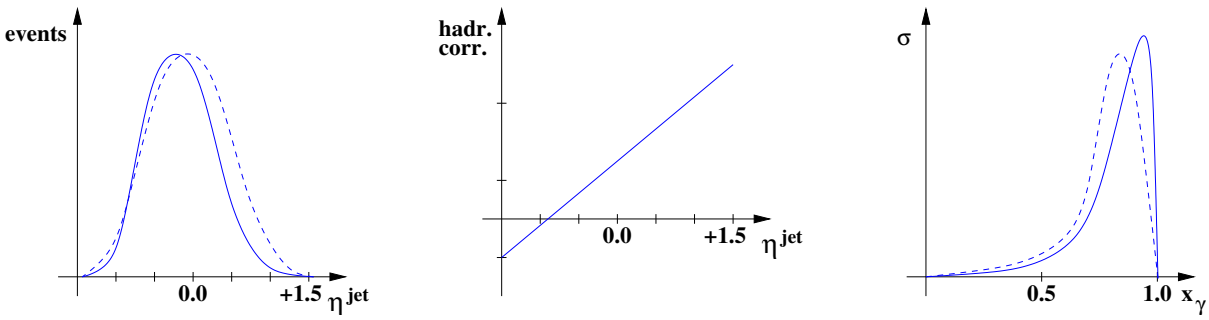

Figure 12.3: Schematic illustration of the effect of the η^{jet}-shift on x_γ^{obs}: The distribution of η^{jet} indicates a shift to larger η^{jet} from PL to HL *(left)* which causes a rise in the hadronic corrections over η^{jet} *(middle)*; the more negative η^{jet}_{PL} in the exponent of Eqn. 12.2 results in a higher x_γ^{obs} on PL *(right plot)*.

to the NLO predictions based on the H1 2002 fit and the ZEUS LPS fit, respectively. The hadronic corrections differ from unity by $\lesssim 20\%$ in the range of high statistics for all variables with the exception of $z_{I\!P}^{obs}$. A systematic increase is observed for η^{jet1} which can be understood qualitatively as a result of the hadronisation process: On PL, the partons are well separated in $(\eta,\, \phi)$ and tend to be assigned to different jets. During hadronisation, formerly asymptotically free partons of the $I\!P$-remnant and the dijet system become connected by a colour field and, consequently, bundled in phase space. Additionally, secondary particles are produced in the angular range between the initial partons of the dijet system and the $I\!P$-remnant, and allow the jet algorithm to maximise the jet energy by combining hadrons of formerly well-separated partons of the $I\!P$-remnant into one of the jets.
The shift to larger η^{jet1} from PL to HL (Fig. 12.3, left) significantly affects the calculation of x_γ^{obs} and $z_{I\!P}^{obs}$ on PL which exponentially depend on η^{jet1}:

$$x_\gamma^{obs} = \frac{\sum_{k=1,2} E_T^{jet\,k} e^{-\eta^{jet\,k}}}{(E-p_z)_{\text{partons}}}\,, \tag{12.2}$$

$$z_{I\!P}^{obs} = \frac{\sum_{k=1,2} E_T^{jet\,k} e^{+\eta^{jet\,k}}}{(E+p_z)_{\text{partons}}}\,. \tag{12.3}$$

The more negative η^{jet}_{HL} in the exponent of Eqn. 12.2 results in a higher x_γ^{obs} (Fig. 12.3, right) and smaller $z_{I\!P}^{obs}$ on PL. Indeed the distribution of $z_{I\!P}^{obs}$ displays the largest observed discrepancy (Fig. 12.2) in the highest bin of $z_{I\!P}^{obs} > 0.8$. The large hadronic corrections in the lowest bin of $x_{I\!P}$ and M_X could also be affected by edge effects in the generation of MC events in the range of low statistics, indicated by the error bands in the Fig. 12.2.

Hadronic corrections with POMWIG

The large hadronic corrections observed in a few bins motivated investigation of the influence of the fragmentation model on the hadronic corrections. The hadronisation process in RAPGAP is simulated by the string fragmentation model (Sec. 4.2). An alternative is POMWIG [47] which is based on HERWIG [48] and uses cluster fragmentation (Sec. 4.3).
POMWIG was originially developed for diffraction in DIS. Although it is not applicable for resolved PHP (compare Sec. 4.3), the hadronic corrections calculated from POMWIG can serve

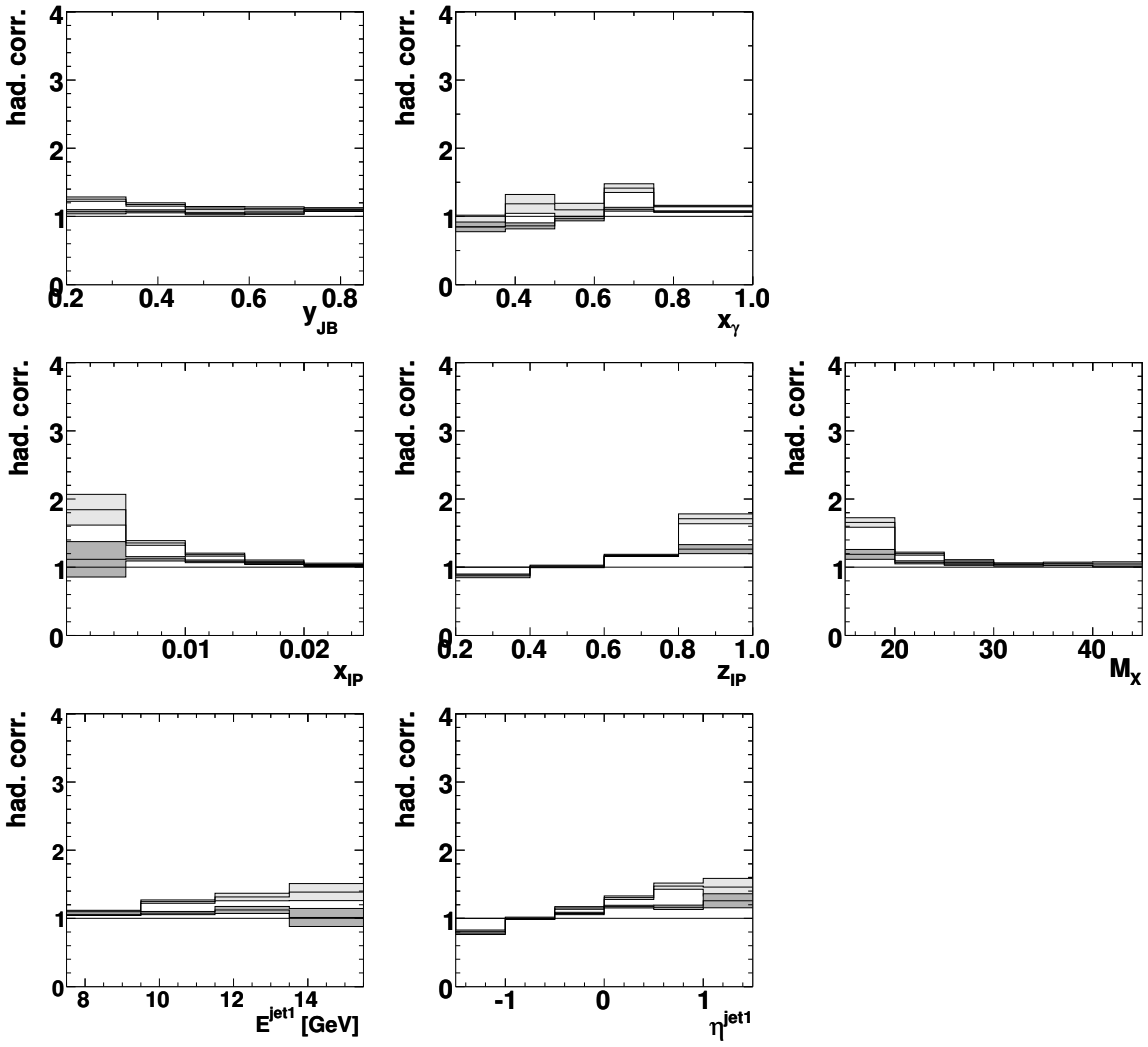

Figure 12.4: Hadronic corrections including error bands calculated with the reweighted RAPGAP MC *(light grey)* and reweighted POMWIG MC *(dark grey)* for processes of direct PHP, shown for the variables y_{JB}, x_γ^{obs}, $x_{I\!P}$, $z_{I\!P}^{obs}$, M_X, $E_T^{jet\,1}$ and $\eta^{jet\,1}$ – both RAPGAP and POMWIG use H1 LO-fit 2 and were reweighted to the NLO prediction based on the H1 2002 fit in bins of $z_{I\!P}^{obs}$.

as a systematic check for those derived from processes of direct PHP in RAPGAP. For comparability, the PL of POMWIG was reweighted in bins of $z_{I\!P}^{obs}$ to the direct contributions of RAPGAP PL in this x_γ^{obs}-range before the same reweighting as for RAPGAP was applied.
The hadronic corrections determined with POMWIG and direct processes of RAPGAP are shown in Fig. 12.4. Although the hadronic corrections are generally smaller for POMWIG, they show the same dependencies for η^{jet1}, high $z_{I\!P}^{obs}$ and low M_X. An additional reweighting in a variable affected by the electron vertex was suggested. Since there is only one bin for $x_\gamma^{obs} > 0.75$, the variable y_{JB} was chosen. However, a double differential reweighting of the PL of POMWIG in bins of $z_{I\!P}$ and y_{JB} only resulted in changes below 2% to the hadronic corrections and was omitted again.

12.3 Single differential cross sections

Single differential cross sections for data were already presented in Sec. 10.1. In Fig. 12.5 they are compared to the NLO predictions based on the H1 2002 fit, the ZEUS LPS fit and the ZEUS GLP fit, where the NLO cross sections were transformed to HL.
All three NLO predictions need a normalisation factor in order to describe the cross sections of the data. The normalisation factor (Tab. 12.1) is closer to unity for the ZEUS LPS fit (≈ 0.80) than for the H1 2002 fit (≈ 0.63) and the ZEUS GLP fit (≈ 2.24). The different normalisation factors could partly reflect different contributions from proton dissocation, which is contained in the data of the H1 2002 fit and ZEUS GLP fit, excluded in the data of the ZEUS LPS fit and estimated and subtracted in the data of this analysis (Sec. 7.1.2).
The shape of the distributions is slightly better described by the ZEUS LPS fit than by the H1 2002 fit and ZEUS GLP fit.

12.4 Double differential cross sections

The cross sections on HL are also compared to NLO predictions for the direct enriched range ($x_\gamma \geq 0.75$) in Figs. 12.6 and 12.7 and for the resolved enriched range ($x_\gamma < 0.75$) in Fig. 12.8.

Cross section of direct enriched PHP

The same conclusions as for the single differential cross sections also hold for the cross sections in the range of direct enriched PHP (Fig. 12.6): Again, the NLO predictions fail to give the correct normalisation of the cross sections. Here the normalisation factors (Tab. 12.1) are ≈ 0.61 for the H1 2002 fit, ≈ 0.77 for the ZEUS LPS fit and ≈ 2.11 for the ZEUS GLP fit. The shape of the data cross sections is adequately described by all three NLO predictions with the exception of $z_{I\!P}^{obs}$.
In addition, the influence of the fragmentation model on the hadronic correction has been investigated for the range of direct enriched PHP, where the missing contribution of resolved PHP in the POMWIG MC sample is less important. For this purpose hadronic corrections obtained from RAPGAP MC (using *string fragmentation*) and POMWIG MC (using *cluster fragmentation*) have been applied to the PL of the LPS-based NLO prediction, normalised to the data by a factor of 0.8 (Fig. 12.7). For the RAPGAP MC sample, the hadronic corrections were derived from direct and resolved contributions in the range $x_\gamma \geq 0.75$. These hadronic corrections differ by less than 2.5% from those derived from direct contributions only. Therefore the hadronic corrections obtained from the POMWIG MC sample, although not containing resolved contributions, were taken as an appropriate estimate of hadronic corrections for processes of both direct and resolved PHP. The shaded area in Fig. 12.7 hence shows the uncertainty of the fragmentation model on the NLO predictions at HL. The differences of the shapes between the data and the normalised NLO cross sections are covered by the uncertainty of the fragmentation model with the exception of high values of y_{JB}.

Cross section of resolved enriched PHP

In the range of resolved enriched PHP (Fig. 12.8), the normalisation factors (Tab. 12.1) are larger than for direct enriched PHP, ≈ 0.71 for the H1 2002 fit, ≈ 0.93 for the ZEUS LPS fit

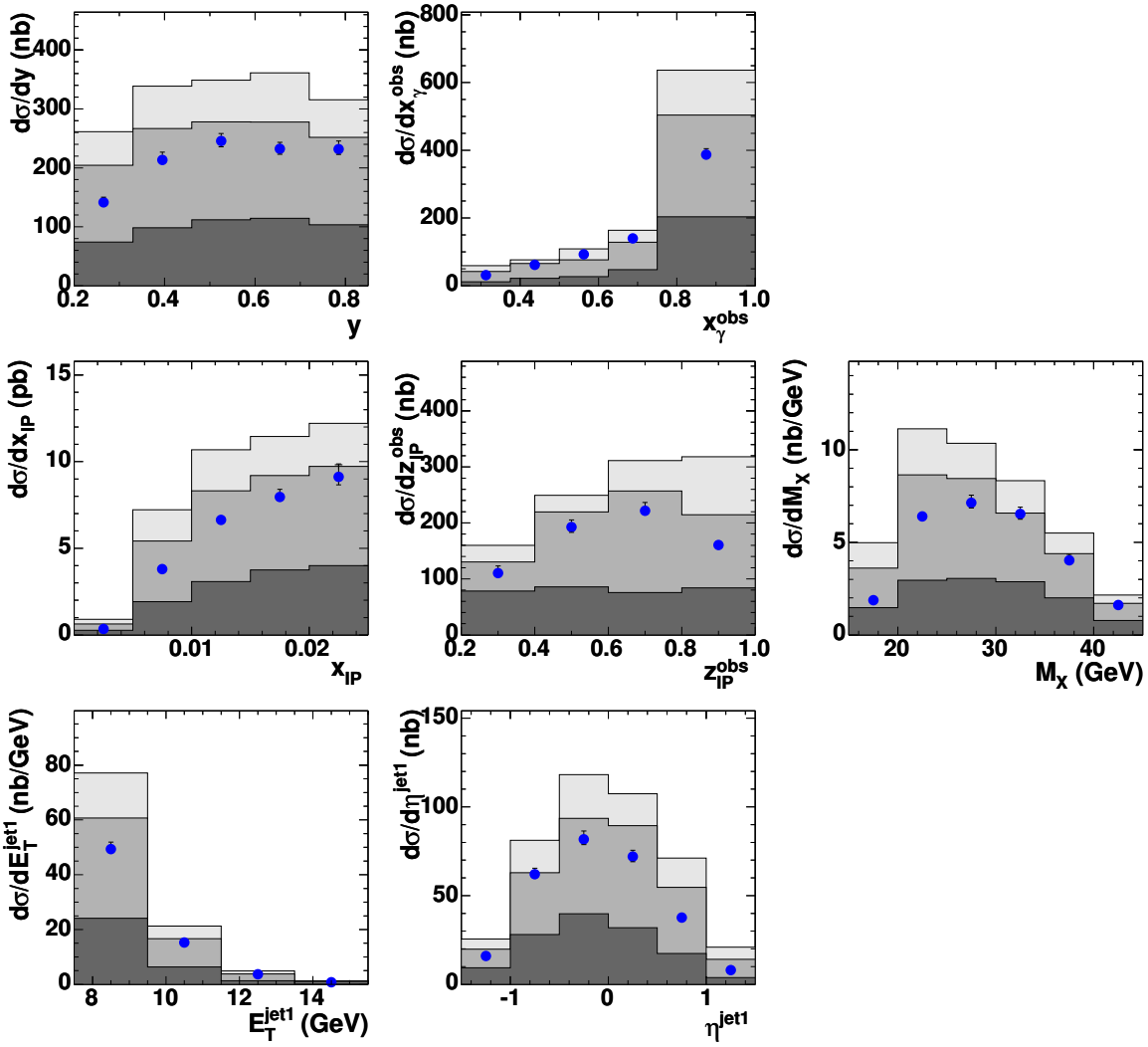

Figure 12.5: Single differential cross sections for data (•) and NLO predictions based on the H1 2002 fit *(light grey)*, the ZEUS LPS-fit *(medium grey)* and the ZEUS GLP-fit *(dark grey)* for the variables y_{JB}, x_γ^{obs}, $x_{I\!P}$, $z_{I\!P}^{obs}$, M_X, $E_T^{jet\,1}$ and $\eta^{jet\,1}$ – the inner error bars indicate the systematic uncertainty as determined in Sec. 11.1 whereas the outer error bars indicate the statistical and systematic uncertainty added in quadrature.

and ≈ 2.92 for the ZEUS GLP fit. The shape of the distributions is adequately described by all NLO predictions but seems to favour the H1 2002 fit. This conclusion, however, has to be taken with caution as the data were corrected to HL with a MC sample based on the H1 LO fit 2, which is more similar to the H1 2002 fit than to the ZEUS LPS fit. Moreover, the uncertainty of the dPDFs increases rapidly for $z_{I\!P} > 0.4$.

12.5 Conclusions on NLO comparison

Single and double differential cross sections of data have been compared to three NLO predictions based on different dPDFs. The shape of the shown variables do not strikingly indicate that one of the NLO predictions is to be preferred.

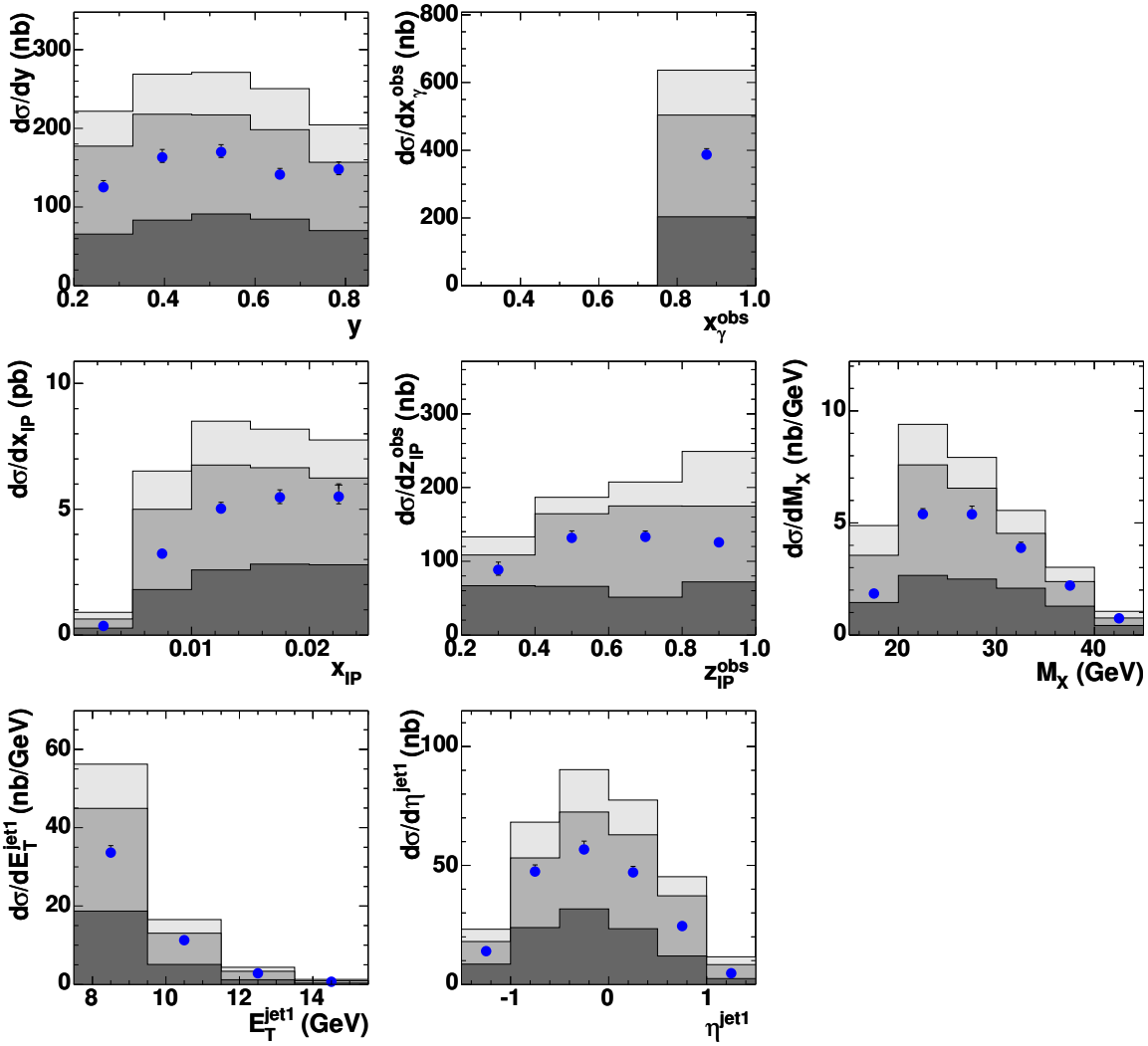

Figure 12.6: Double differential cross sections for data (•) and NLO predictions based on the H1 2002 fit *(light grey)*, the ZEUS LPS-fit *(medium grey)* and the ZEUS GLP-fit *(dark grey)* in the range $x_\gamma^{obs} \geq 0.75$ for the variables y_{JB}, x_γ^{obs}, $x_{I\!P}$, $z_{I\!P}^{obs}$, M_X, $E_T^{jet\,1}$ and $\eta^{jet\,1}$ – the inner error bars indicate the systematic uncertainty as determined in Sec. 11.1 whereas the outer error bars indicate the statistical and systematic uncertainty added in quadrature.

All three NLO predictions need a normalisation factor in order to reproduce the cross sections of the data. The normalisation factors are summarised in Tab. 12.1. However, the large spread of the presently available NLO predictions does not allow conclusions on suppression of both direct and resolved PHP or resolved PHP only.

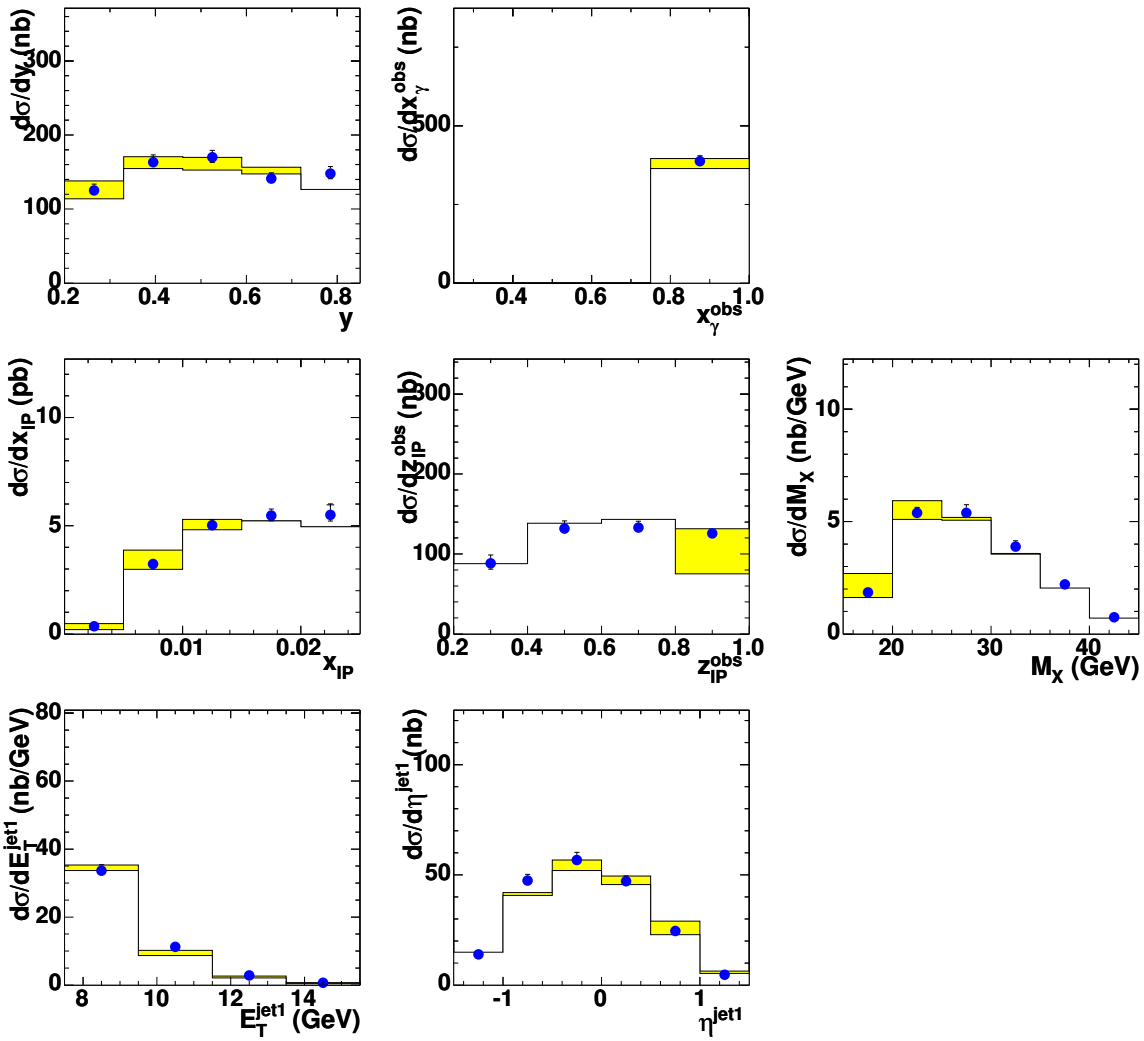

Figure 12.7: Double differential cross sections for data (•) and the normalised and LPS-based NLO predictions (—) in the range $x_\gamma^{obs} \geq 0.75$ for the variables y_{JB}, x_γ^{obs}, $x_{I\!P}$, $z_{I\!P}^{obs}$, M_X, $E_T^{jet\,1}$ and $\eta^{jet\,1}$ – the inner error bars indicate the systematic uncertainty as determined in Sec. 11.1 whereas the outer error bars indicate the statistical and systematic uncertainty added in quadrature; the shaded band indicates the variation of the fragmentation model *[upper edge:* RAPGAP *(string fragmentation), lower edge:* POMWIG *(cluster fragmentation).]*

NLO prediction	assumed p dissociation	normalisation factor		
		full x_γ^{obs}	$x_\gamma^{obs} \geq 0.75$	$x_\gamma^{obs} < 0.75$
H1 2002 fit	$(23 \pm 16)\%$	0.63	0.61	0.71
ZEUS LPS fit	*n.a.*	0.80	0.77	0.93
ZEUS GLP fit	$(30 \pm 3)\%$	2.24	2.11	2.92

Table 12.1: Assumed p-dissociative background of NLO predictions and normalisation factors for agreement with data.

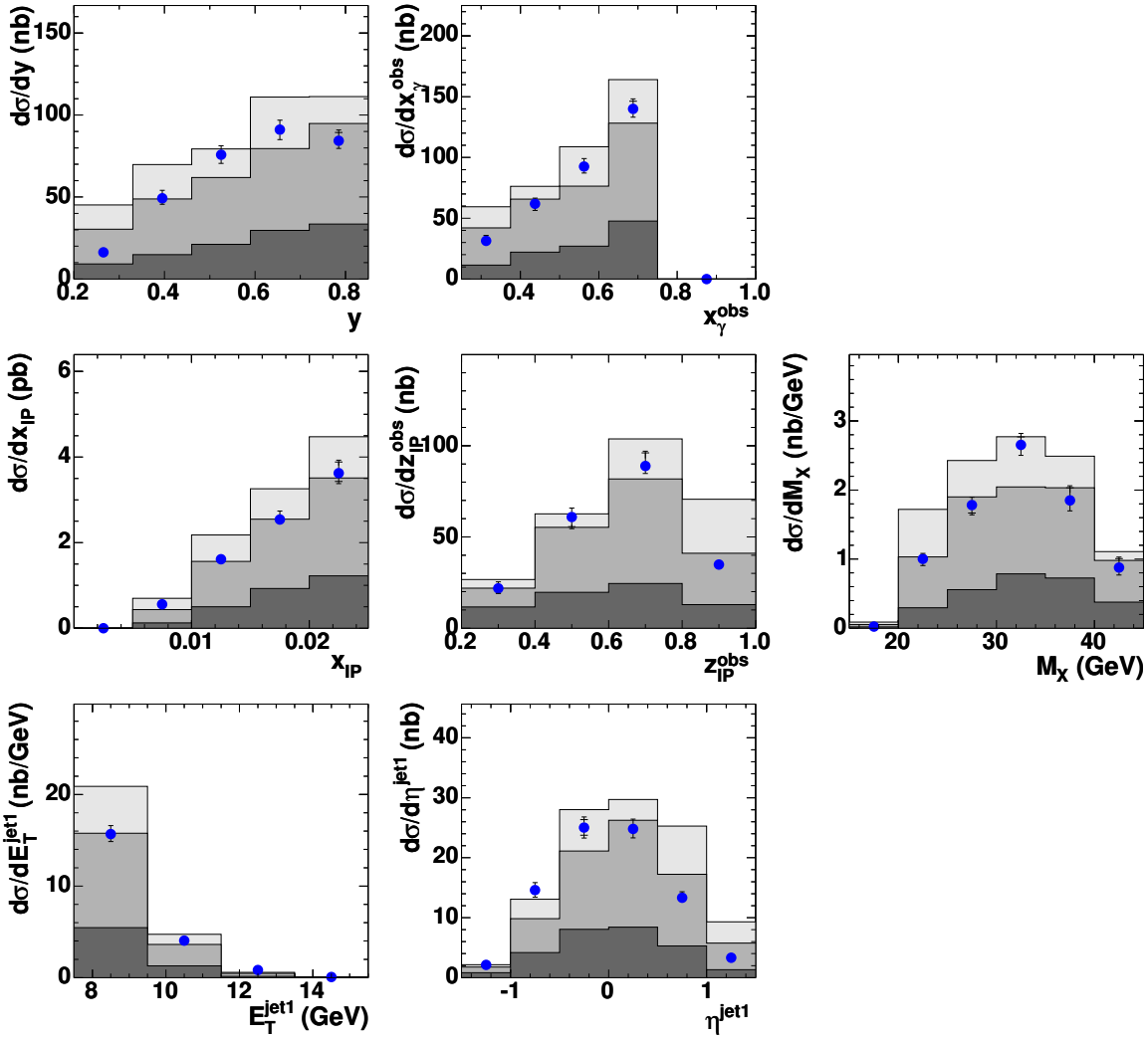

Figure 12.8: Double differential cross sections for data (•) and NLO predictions based on the H1 2002 fit *(light grey)*, the ZEUS LPS-fit *(medium grey)* and the ZEUS GLP-fit *(dark grey)* in the range $x_\gamma^{obs} < 0.75$ for the variables y_{JB}, x_γ^{obs}, $x_{I\!P}$, $z_{I\!P}^{obs}$, M_X, $E_T^{jet\,1}$ and $\eta^{jet\,1}$ – the inner error bars indicate the systematic uncertainty as determined in Sec. 11.1 whereas the outer error bars indicate the statistical and systematic uncertainty added in quadrature.

Chapter 13

Conclusions

Dijet events in diffractive photoproduction have been selected from $77.1\,\mathrm{pb}^{-1}$ of ZEUS data. Two different triggers for data selection were tested of which one was found to be preferable for this analysis. Dijet events with a transverse jet energy of $E_T^{jet1(2)} > 7.5\,(6.5)\,\mathrm{GeV}$ and a pseudorapidity between $-1.5 < \eta^{jet1(2)} < +1.5$ were analysed in the kinematic range given by $0.2 < y_{JB} < 0.85$ and $x_{I\!P} < 0.025$.

Great effort has been spent in the reconstruction of the kinematic variables. The backsplash correction which has been a formerly built-in part of the ZEUS reconstruction code, was noted to be inappropriate for this analysis and was switched off. A formerly recommended method of ZUFO correction has been found to be unsuitable for diffractive analyses and was replaced by a recently available method. Both results have been adopted by other analyses which have been repeated without backsplash correction and with the new method for energy correction of ZUFOs. In addition, the reconstruction of the jet energy has been investigated and improved.

For an enhanced extraction of the diffractive signal, an easily applicable method for rejection of cosmic events has been developed, tested and applied.

Cross sections for dijets in diffractive photoproduction have been determined as functions of the variables x_γ, y_{JB}, $x_{I\!P}$, $z_{I\!P}$, M_X, $E_T^{jet\,1}$, $\eta^{jet\,1}$, $E_T^{jet\,2}$ and $\eta^{jet\,2}$ for the full x_γ-range as well as double-differentially, i.e. for the range enriched with direct ($x_\gamma^{obs} \geq 0.75$) and resolved ($x_\gamma^{obs} < 0.75$) photoproduction.

The data have been compared to leading-order Monte Carlo simulation and three next-to-leading order QCD predictions based on different diffractive parton density functions. These predictions were given on parton level, and the influence of the fragmentation model on the transformation to hadron level has been investigated.

Both single and double differential cross sections of the data are found to agree well in shape with those of the normalised Monte Carlo simulation. The shapes of the single differential distributions agree also reasonably with all three predictions at next-to-leading order. However, their normalisation fails, both for single and double differential cross sections. Due to the large spread of the presently available dPDFs, there is at present no clear answer to the question whether factorisation breaking in diffractive photoproduction is observed in the data. It is planned to determine the diffractive parton density functions in a global fit including all data sets.

The experimental results have been approved by the ZEUS Collaboration and presented at international conferences. A paper on this analysis is in progress.

Acknowledgements

Firstly and above all, I would like to thank Prof. Ewald Paul for his kind supervision and intense interest in my analysis as well as the many prolific and friendly discussions on details and collaborative battles for the best possible formulations in the thesis. His continuous support, encouragement and personal care made this analysis a pleasant and enjoyable journey. Moreover, I would like to thank him as well as Prof. I.C. Brock and Prof. E. Hilger for taking care of the financial aspects and raising funds for conference attendances, and even more for their comments, which have been very valuable and appreciated, and their questions on details of the analysis, which prooved more than once to open the doors to yet unnoticed effects and to contain the core for deeper understanding.
I'm grateful to Prof. U. Thoma, Prof. H.R. Petry and Prof. B. Diekkrüger for their interest and the time they spent on the thesis and the disputation – to whatever judgement they might come.
I'd also like to thank my current and former physic coordinators and mentors, namely Prof. Michele Arneodo and Dres. A. Bruni, Kerstin Borras, Jo Cole, Marta Ruspa, Uta Stoesslein and Yuji Yamazaki, who helped with many suggestions and comments, and I'm grateful for their continuous interest and eagerness to discuss the topics of this analysis.
The time of work on hardware, detector-sitting and on-call duty would have been considerably harder without Alexej Stifoutkine, and I am glad that I could rely on his expertise, sense for strikingly easy solutions and friendly help at any time.

I am glad that I could work with a group of colleagues of whom many became friends over the years. Although all of them contributed by their spirit and good mood, in terms of this analysis I would like to thank in particular Joachim Tandler and Oliver Kind, whose helpfulness didn't even end - and actually once started - at a quarter past three in the night over the phone when one of them returned from Bonn's famous cocktail bar.
My temporary and former colleagues at the DESY in Hamburg – Ingo Bloch, Stefan Goers, Markus Jüngst, Benjamin Kahle, Peter Irrgang, Oliver Maria Kind, Ursula Meyer, Verena Schönberg, Joachim Tandler, Kai Voss, Howie Wessoleck and Michał Własenko – I would like to thank for vivid discussions, their company and nourishing conversation during right-to-the-contrary lunch at Hoheisel's canteen.

I would also like to thank especially, though not exclusively, the following people:
Aaron Habsburg who incited me to trump him with those additional two-letters-and-a-dot, Dirk Ortmann and Marc Lilienkamp for smoothing the worst abuses of English grammar, Yvonne Dreisbach and Jens Optenhoefel (and again, Oliver) for their endless hospitality, Katrin Hahn for these unexpected "blind dates" that brightened otherwise dull and workful evenings, and all of them, in particular Aaron, for pulling my feet back on solid ground when my head was somewhere up in the physical sky.
The latter maybe a bit rough at times, though. (It's physics. Not chemistry. Thanks.)

Last but by all means not least, I would like to heartly thank my parents and my sister for their love, motivation and buffering of the blahs which seem to come along inevitably with such a project every now and then. But most of all, I'd like to thank them for being exactly as they are.

Appendix A

Systematic errors of cross sections in the full x_γ^{obs}-range

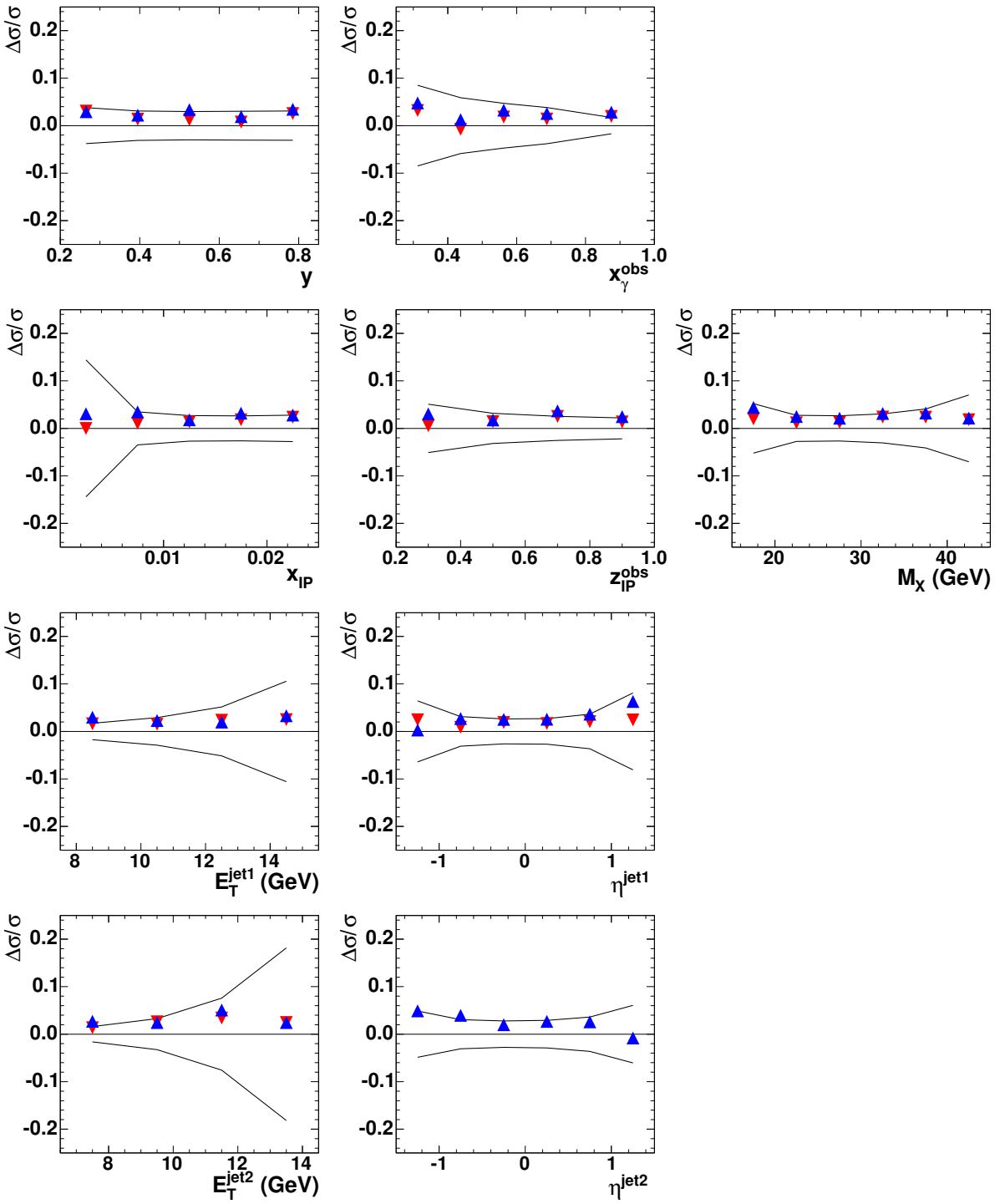

Figure A.1: Systematic errors of a z-vertex shift by $+5\,\mathrm{mm}$ (▲) and $-5\,\mathrm{mm}$ (▼), shown for the variables y_{JB}, x_γ^{obs}, $x_{I\!P}$, $z_{I\!P}^{obs}$, M_X, $E_T^{jet\,1}$, $\eta^{jet\,1}$, $E_T^{jet\,2}$ and $\eta^{jet\,2}$ – the solid lines indicate the statistical errors.

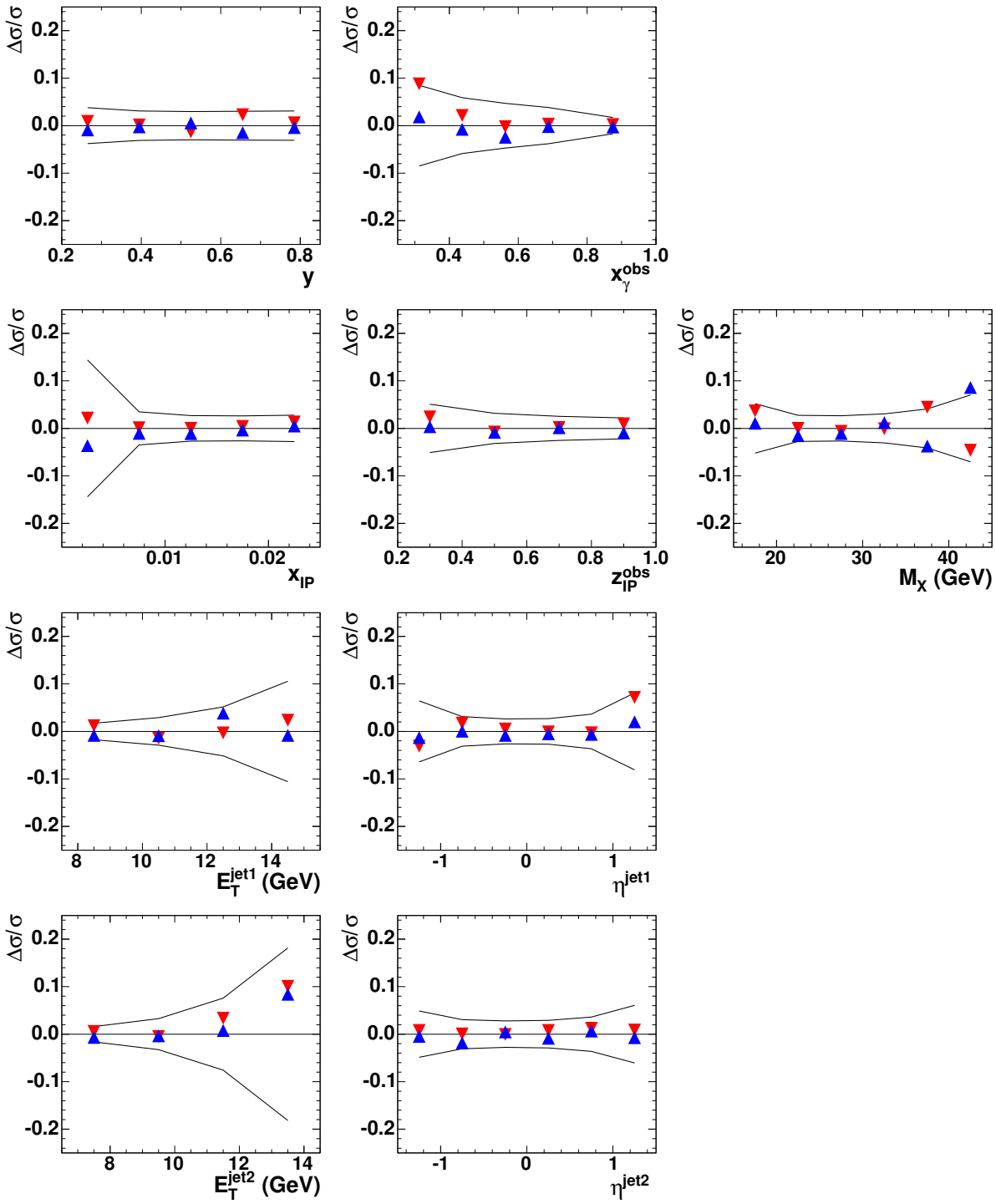

Figure A.2: Systematic errors of ZUFO energy increased (▲) and decreased (▼) as described in Sec. 11.1.2, shown for the variables y_{JB}, x_γ^{obs}, $x_{I\!P}$, $z_{I\!P}^{obs}$, M_X, $E_T^{jet\,1}$, $\eta^{jet\,1}$, $E_T^{jet\,2}$ and $\eta^{jet\,2}$ – the solid lines indicate the statistical errors.

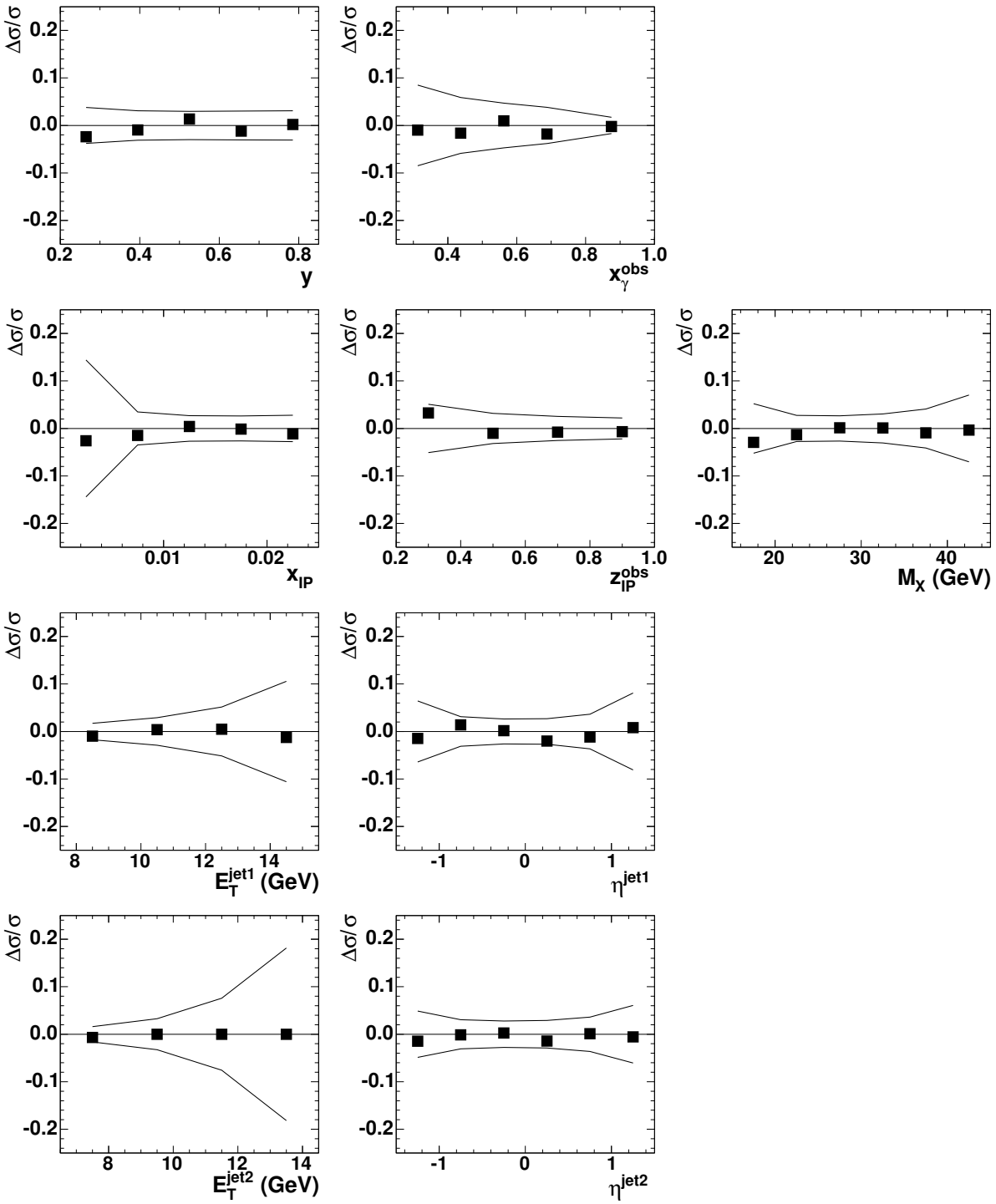

Figure A.3: Systematic errors of a discriminative E_T^{jet} correction for first and second jet (■), shown for the variables y_{JB}, x_γ^{obs}, $x_{I\!P}$, $z_{I\!P}^{obs}$, M_X, $E_T^{jet\,1}$, $\eta^{jet\,1}$, $E_T^{jet\,2}$ and $\eta^{jet\,2}$ – the solid lines indicate the statistical errors.

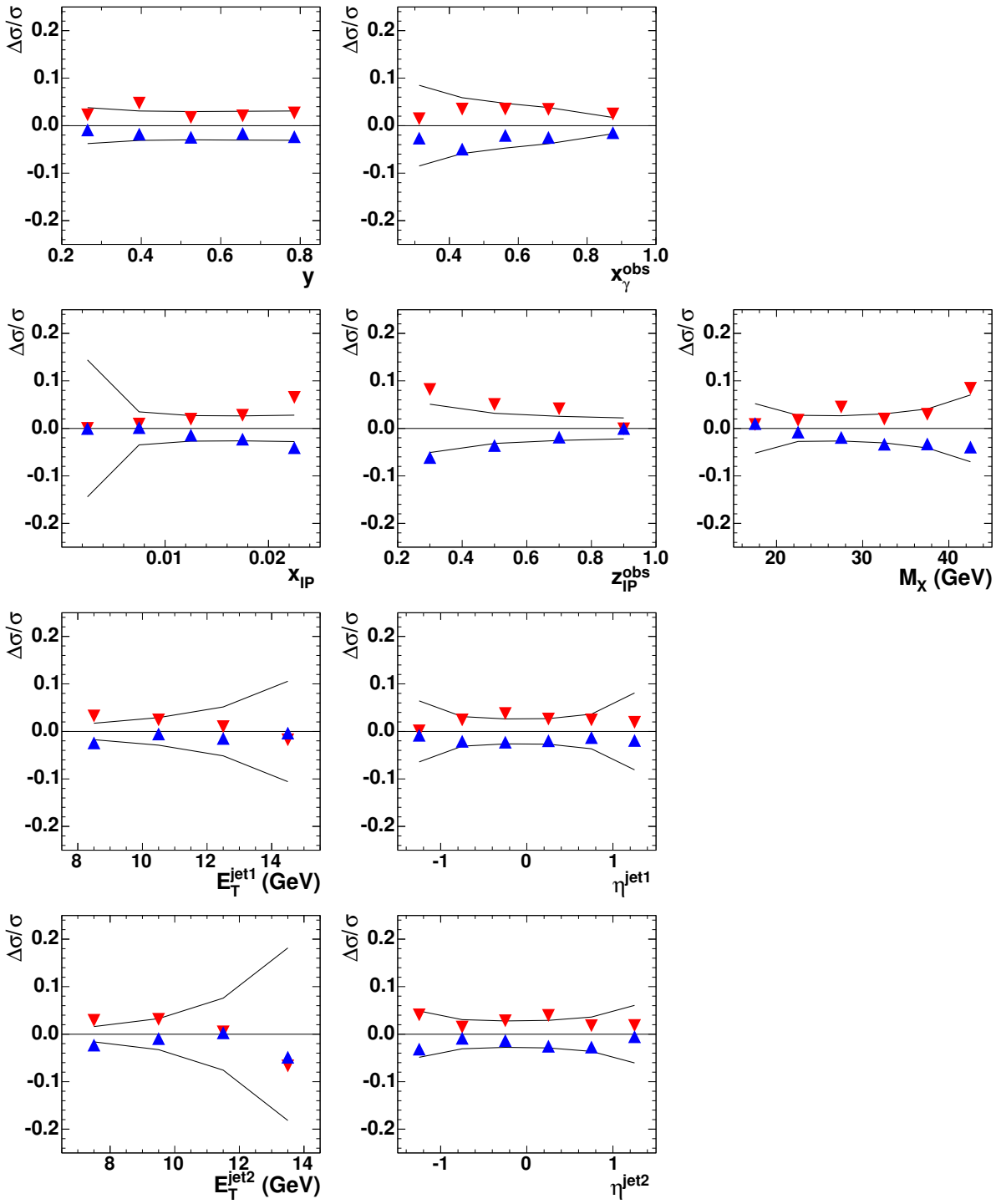

Figure A.4: Systematic errors of the cut on η^{max} increased to $\eta^{max} < 3.0$ (▲) and decreased to $\eta^{max} < 2.6$ (▼), shown for the variables y_{JB}, x_γ^{obs}, $x_{I\!P}$, $z_{I\!P}^{obs}$, M_X, $E_T^{jet\,1}$, $\eta^{jet\,1}$, $E_T^{jet\,2}$ and $\eta^{jet\,2}$ – the solid lines indicate the statistical errors.

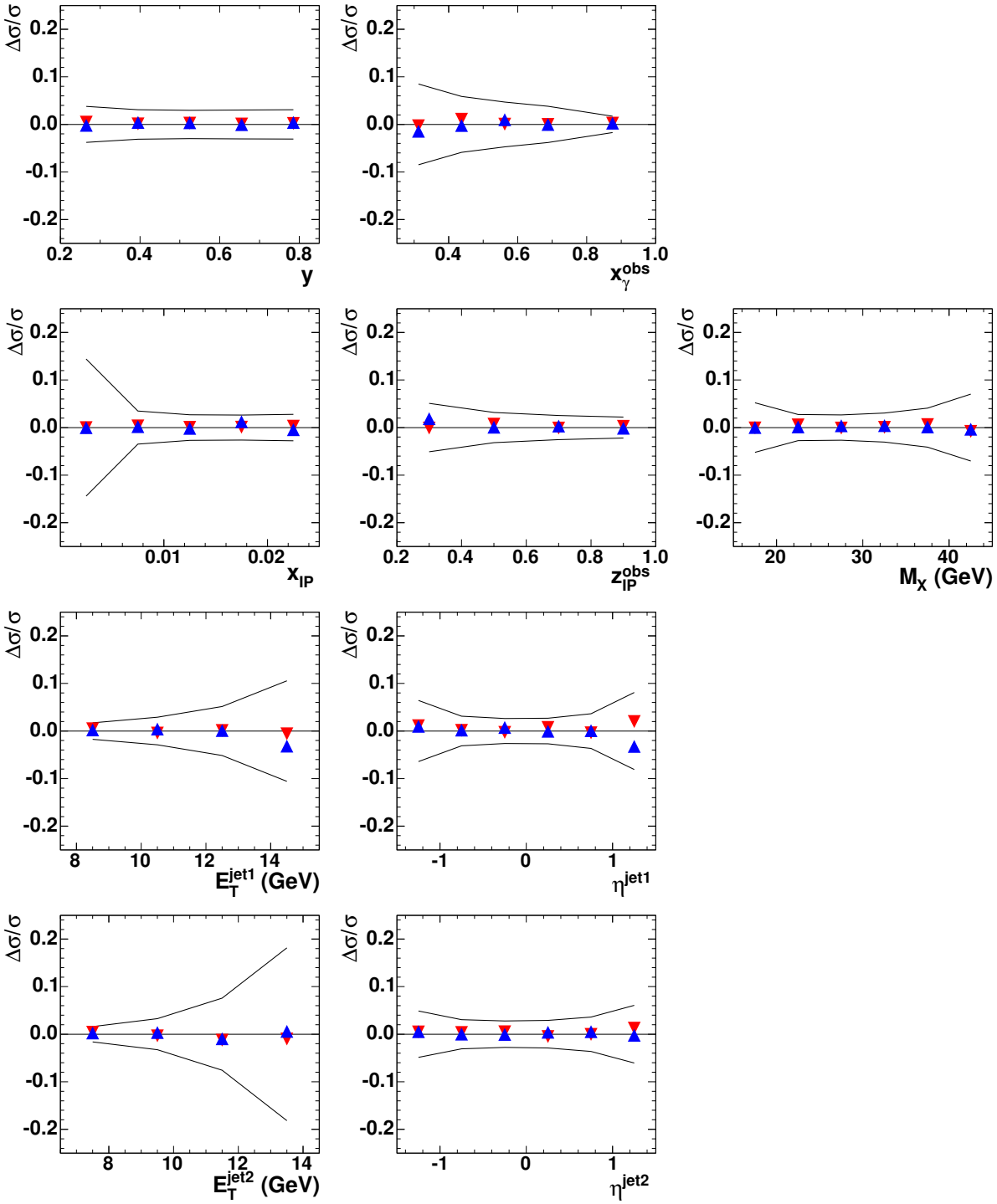

Figure A.5: Systematic errors of the energy threshold, which is used for the calculation of η^{max}, increased to 500 MeV (▲) and decreased to 300 MeV (▼), shown for the variables y_{JB}, x_γ^{obs}, $x_{I\!P}$, $z_{I\!P}^{obs}$, M_X, $E_T^{jet\,1}$, $\eta^{jet\,1}$, $E_T^{jet\,2}$ and $\eta^{jet\,2}$ – the solid lines indicate the statistical errors.

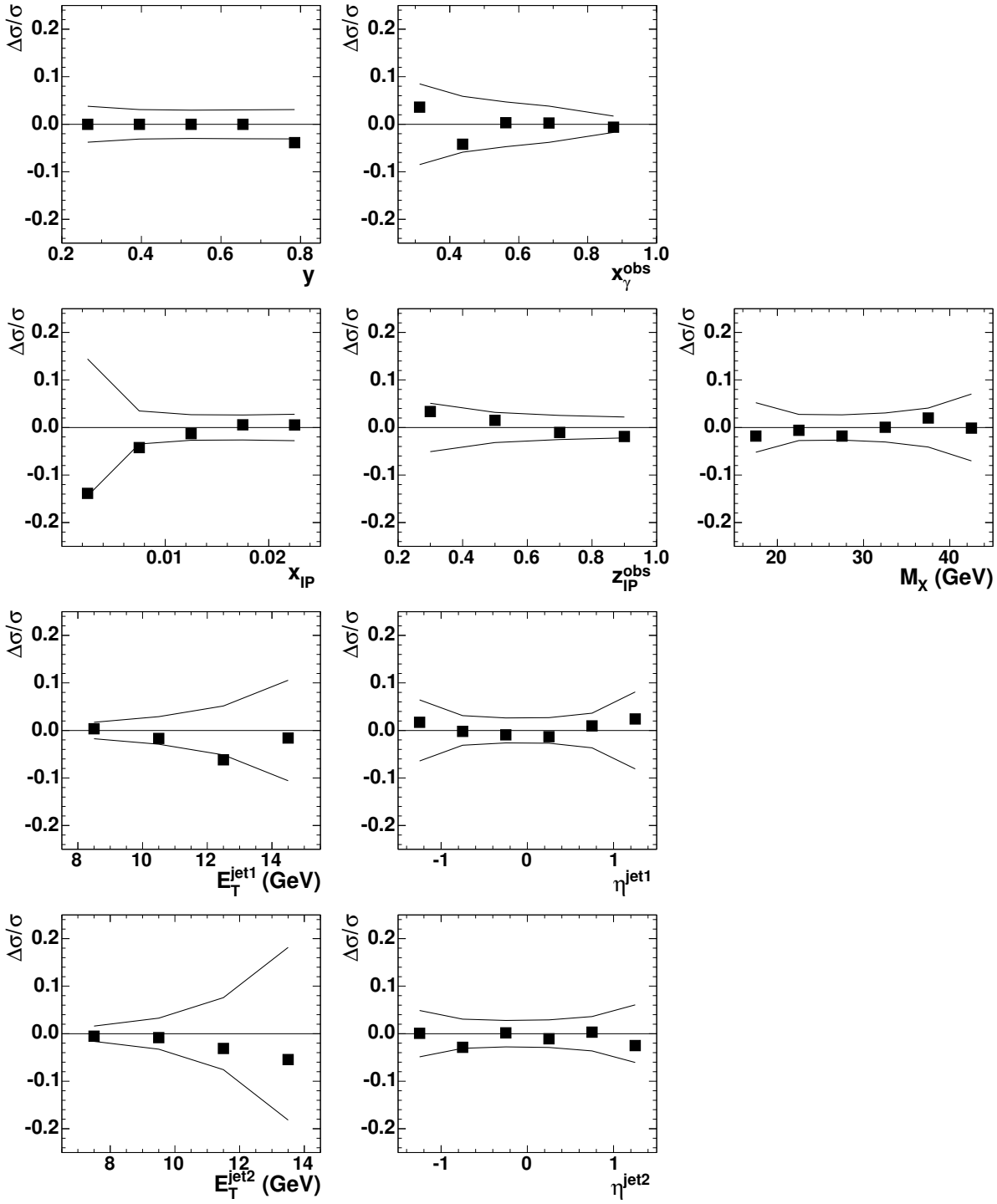

Figure A.6: Systematic errors of a reduced cut of $y_{JB} < 0.78$ (■) shown for the variables y_{JB}, x_γ^{obs}, $x_{I\!P}$, $z_{I\!P}^{obs}$, M_X, $E_T^{jet\,1}$, $\eta^{jet\,1}$, $E_T^{jet\,2}$ and $\eta^{jet\,2}$ – the solid lines indicate the statistical errors.

Appendix B

Systematic errors of cross sections in the range $x_\gamma \geq 0.75$

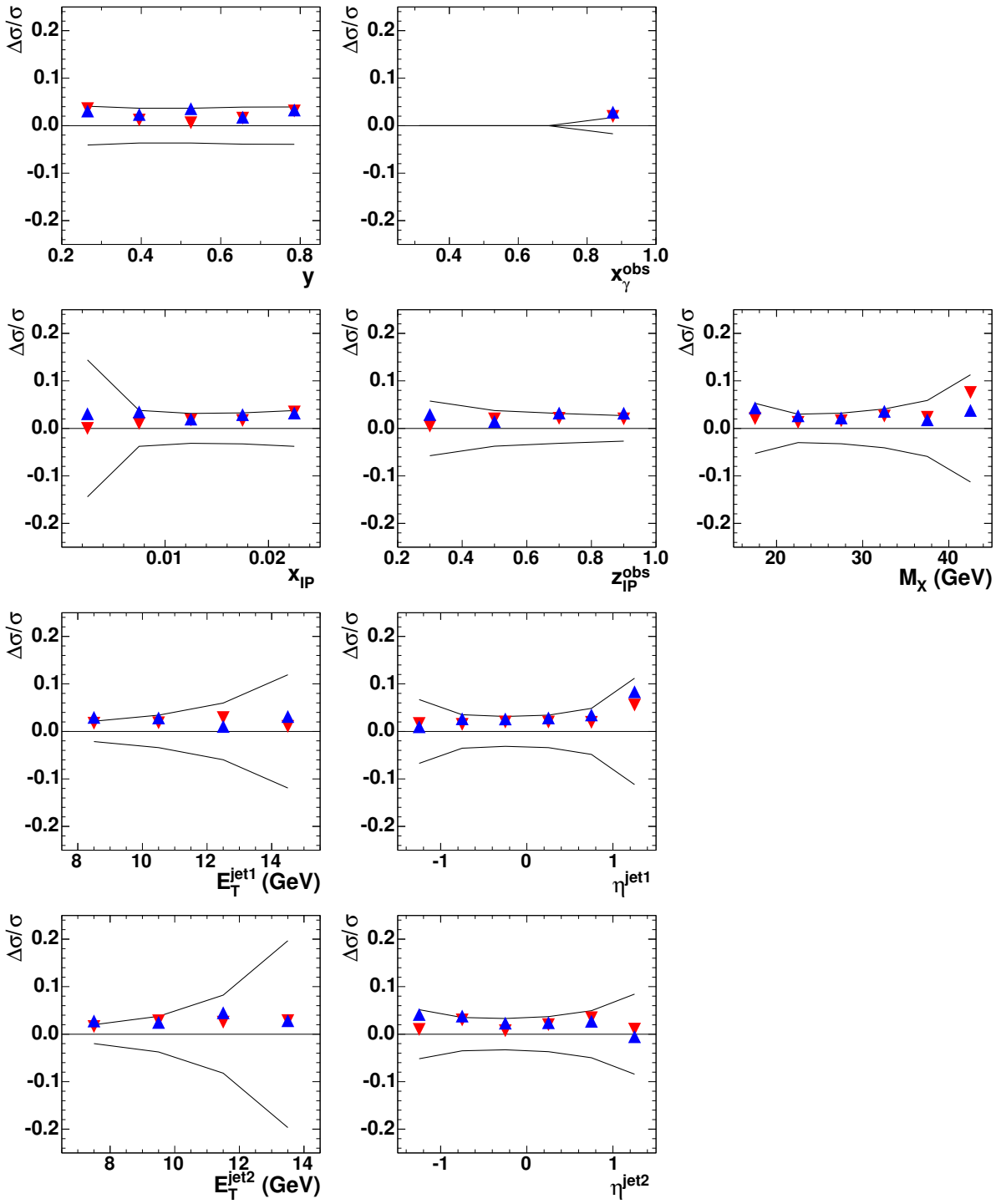

Figure B.1: Systematic errors of a z-vertex shift by $+5\,\mathrm{mm}$ (▲) and $-5\,\mathrm{mm}$ (▼), shown in the range $x_\gamma \geq 0.75$ for the variables y_{JB}, x_γ^{obs}, $x_{I\!P}$, $z_{I\!P}^{obs}$, M_X, $E_T^{jet\,1}$, $\eta^{jet\,1}$, $E_T^{jet\,2}$ and $\eta^{jet\,2}$ – the solid lines indicate the statistical errors.

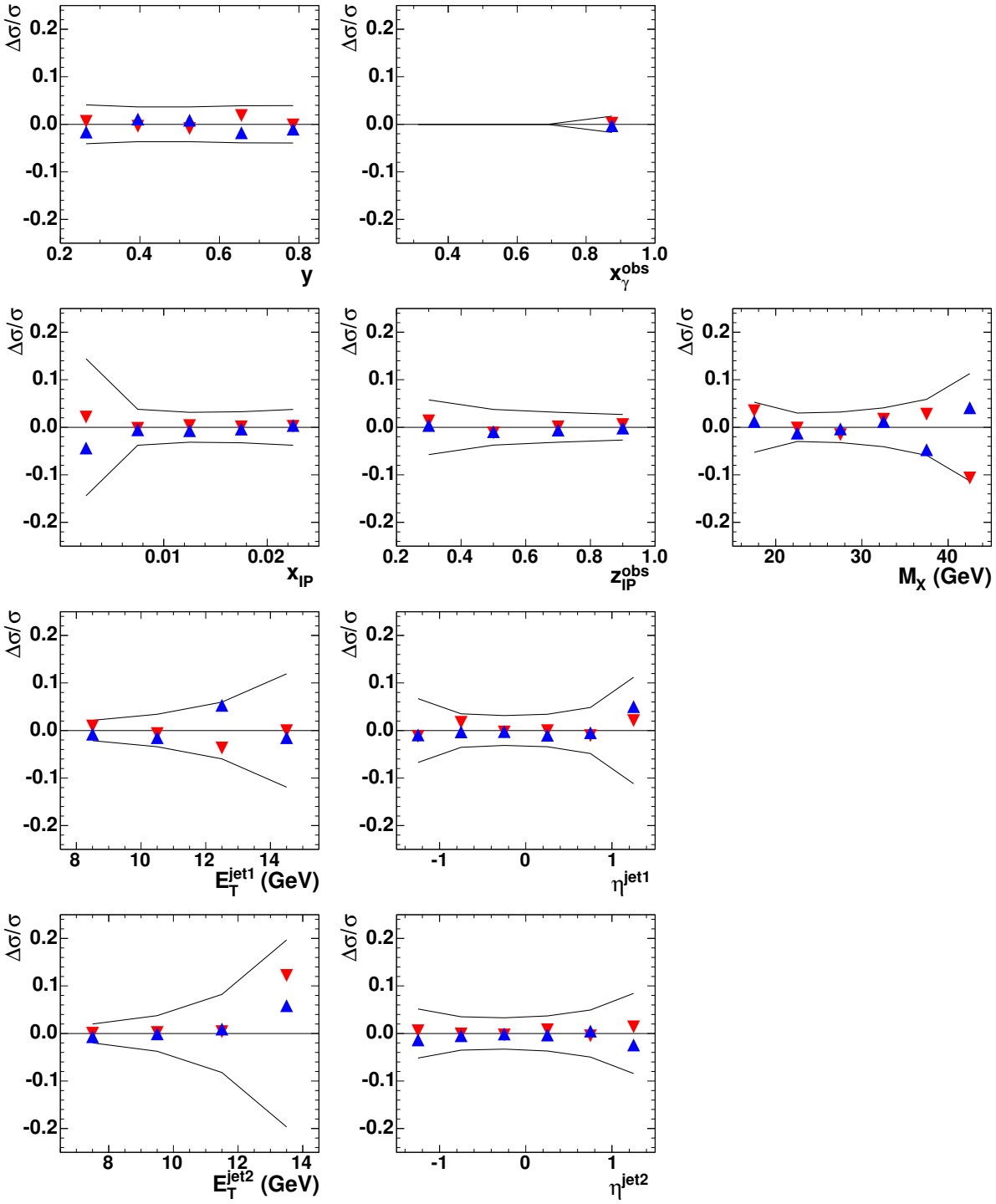

Figure B.2: Systematic errors of ZUFO energy increased (▲) and decreased (▼) as described in Sec. 11.1.2, shown in the range $x_\gamma \geq 0.75$ for the variables y_{JB}, x_γ^{obs}, $x_{I\!P}$, $z_{I\!P}^{obs}$, M_X, $E_T^{jet\,1}$, $\eta^{jet\,1}$, $E_T^{jet\,2}$ and $\eta^{jet\,2}$ – the solid lines indicate the statistical errors.

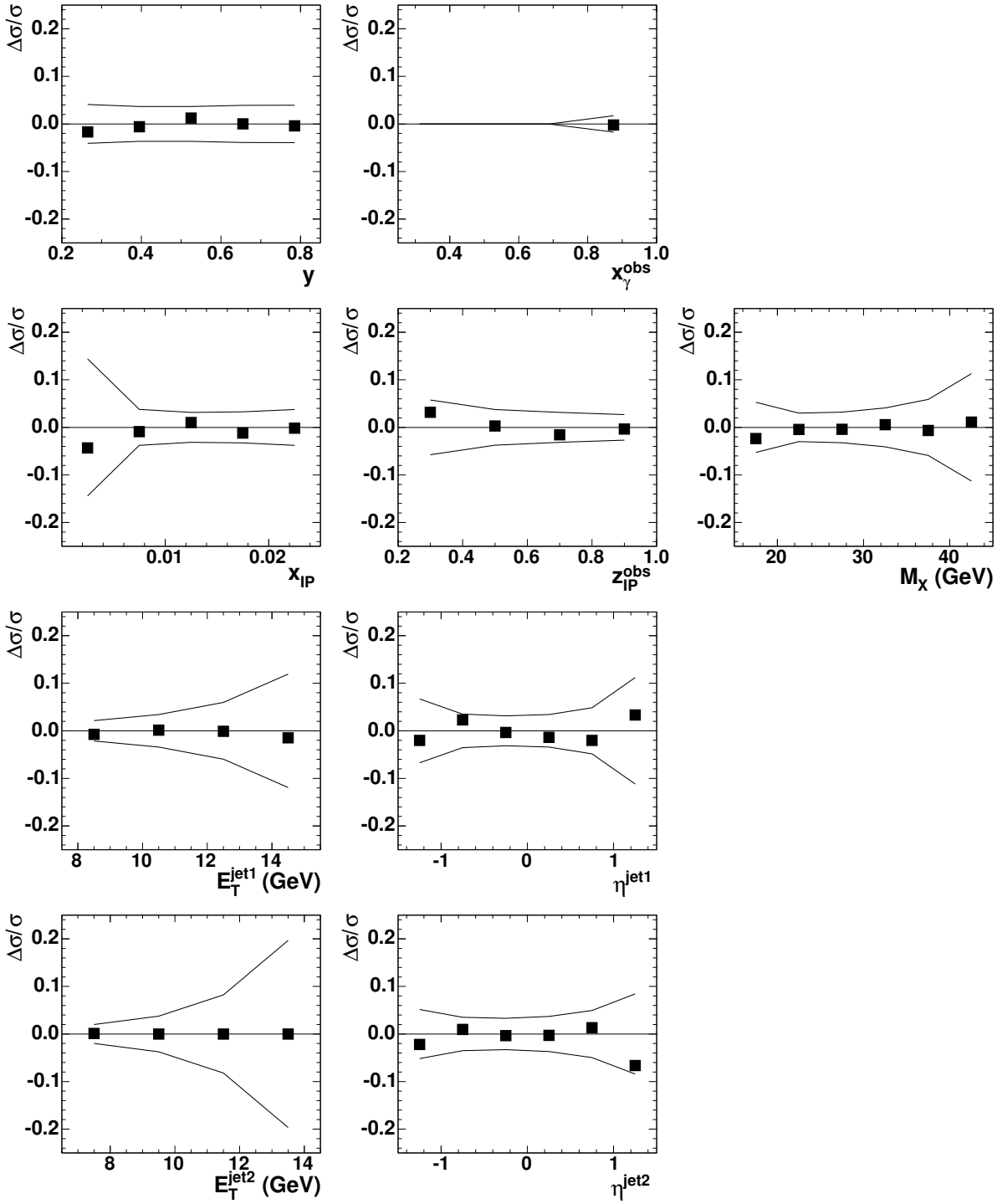

Figure B.3: Systematic errors of a discriminative E_T^{jet} correction for first and second jet (■) shown in the range $x_\gamma \geq 0.75$ for the variables y_{JB}, x_γ^{obs}, $x_{I\!P}$, $z_{I\!P}^{obs}$, M_X, $E_T^{jet\,1}$, $\eta^{jet\,1}$, $E_T^{jet\,2}$ and $\eta^{jet\,2}$ – the solid lines indicate the statistical errors.

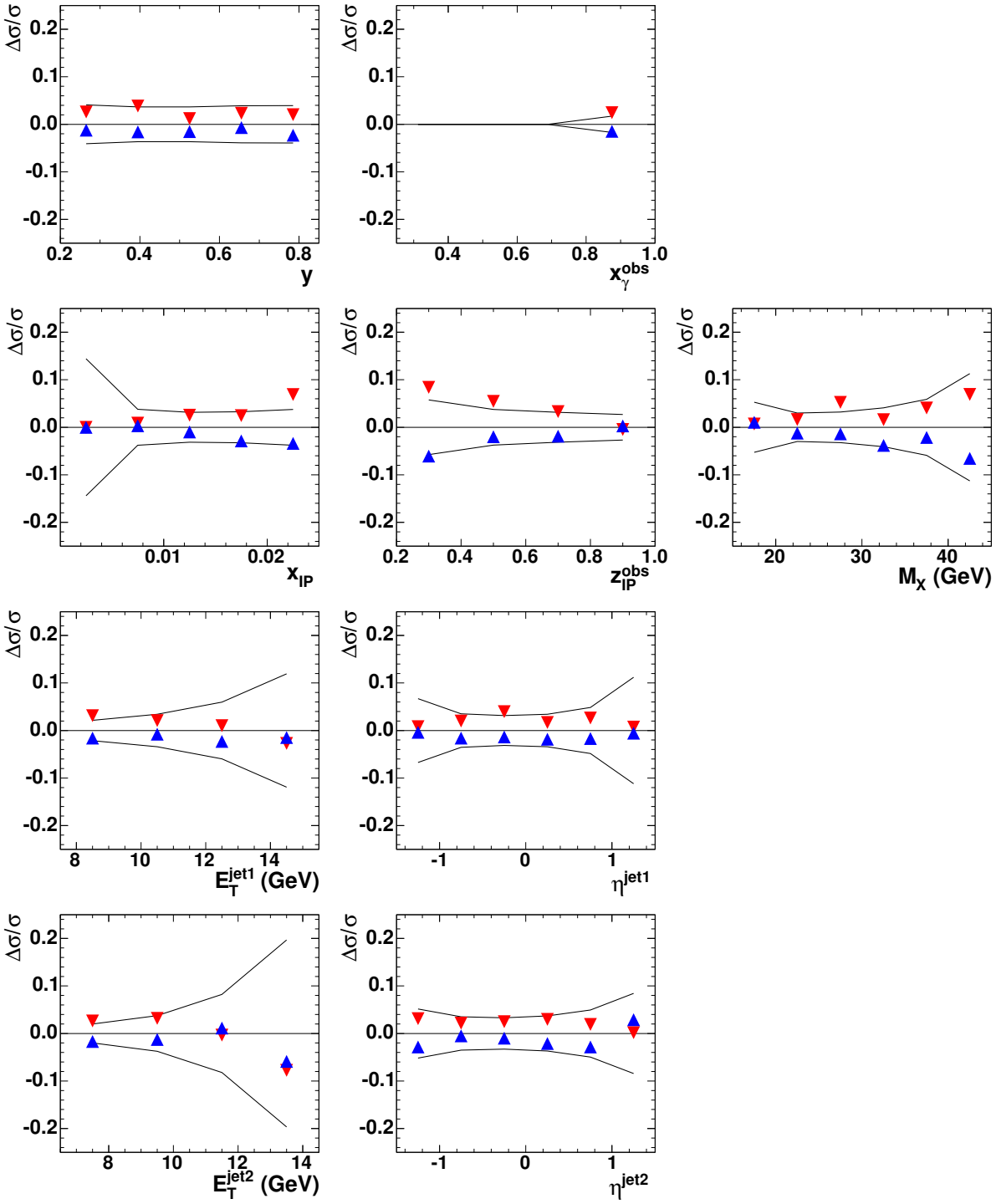

Figure B.4: Systematic errors of the cut on η^{max} increased to $\eta^{max} < 3.0$ (▲) and decreased to $\eta^{max} < 2.6$ (▼), shown in the range $x_\gamma \geq 0.75$ for the variables y_{JB}, x_γ^{obs}, $x_{I\!P}$, $z_{I\!P}^{obs}$, M_X, $E_T^{jet\,1}$, $\eta^{jet\,1}$, $E_T^{jet\,2}$ and $\eta^{jet\,2}$ – the solid lines indicate the statistical errors.

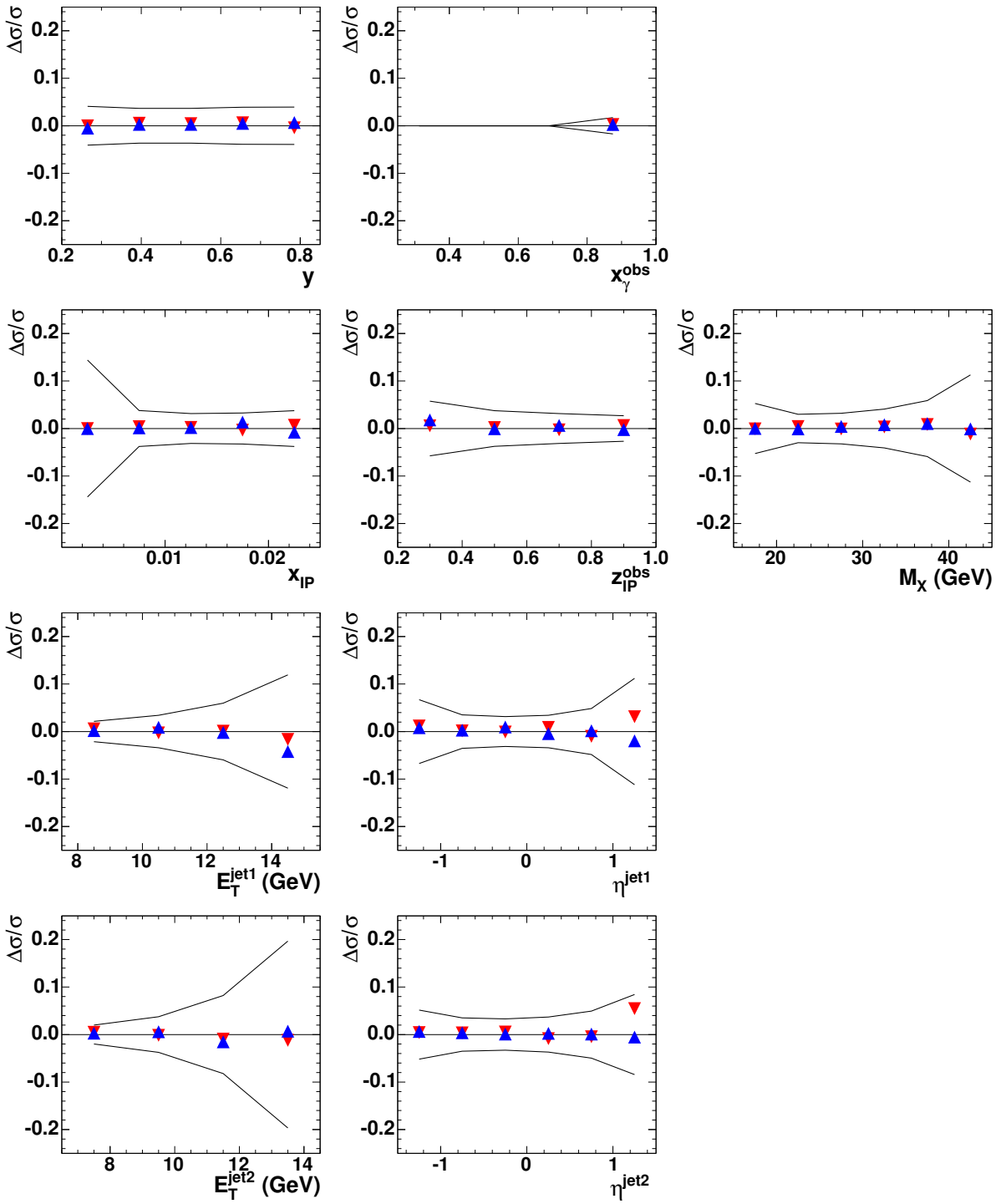

Figure B.5: Systematic errors of the energy threshold, which is used for the calculation of η^{max}, increased to 500 MeV (▲) and decreased to 300 MeV (▼), shown in the range $x_\gamma \geq 0.75$ for the variables y_{JB}, x_γ^{obs}, $x_{I\!P}$, $z_{I\!P}^{obs}$, M_X, $E_T^{jet\,1}$, $\eta^{jet\,1}$, $E_T^{jet\,2}$ and $\eta^{jet\,2}$ – the solid lines indicate the statistical errors.

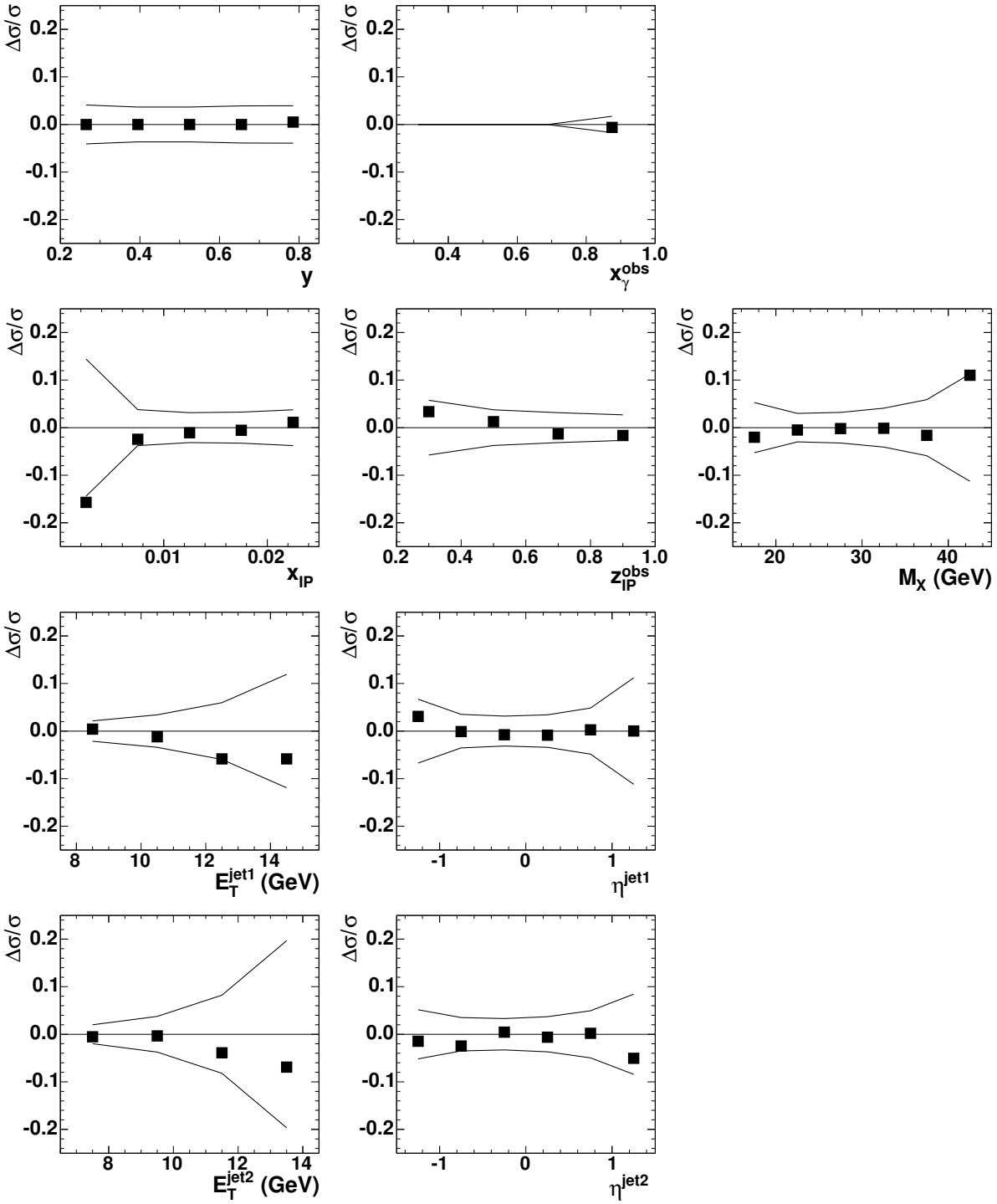

Figure B.6: Systematic errors of a reduced cut of $y_{JB} < 0.78$ (■) shown in the range $x_\gamma \geq 0.75$ for the variables y_{JB}, x_γ^{obs}, $x_{I\!P}$, $z_{I\!P}^{obs}$, M_X, $E_T^{jet\,1}$, $\eta^{jet\,1}$, $E_T^{jet\,2}$ and $\eta^{jet\,2}$ – the solid lines indicate the statistical errors.

Appendix C

Systematic errors of cross sections in the range $x_\gamma < 0.75$

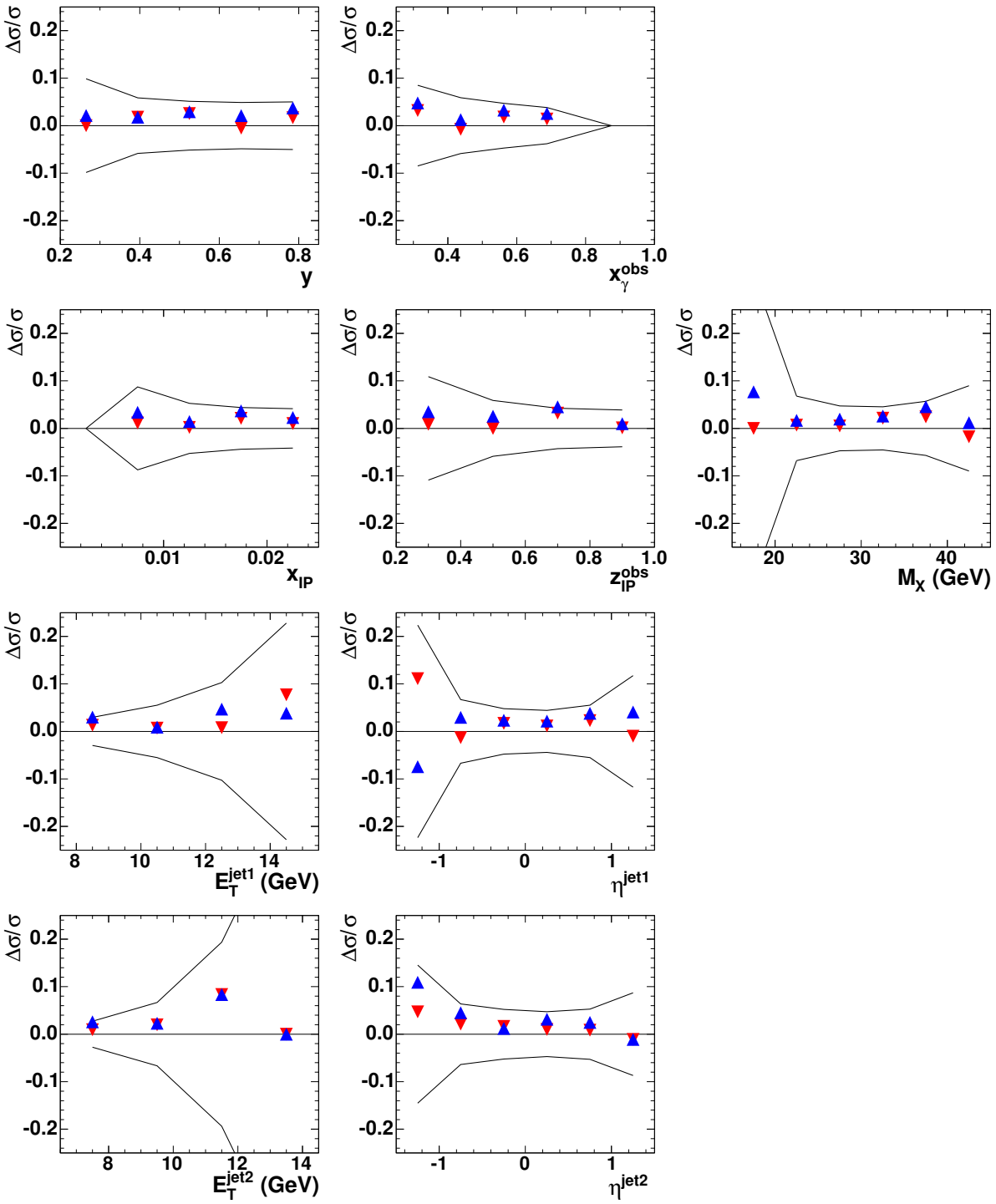

Figure C.1: Systematic errors of a z-vertex shift by $+5\,\mathrm{mm}$ (▲) and $-5\,\mathrm{mm}$ (▼), shown in the range $x_\gamma < 0.75$ for the variables y_{JB}, x_γ^{obs}, $x_{I\!P}$, $z_{I\!P}^{obs}$, M_X, $E_T^{jet\,1}$, $\eta^{jet\,1}$, $E_T^{jet\,2}$ and $\eta^{jet\,2}$ – the solid lines indicate the statistical errors.

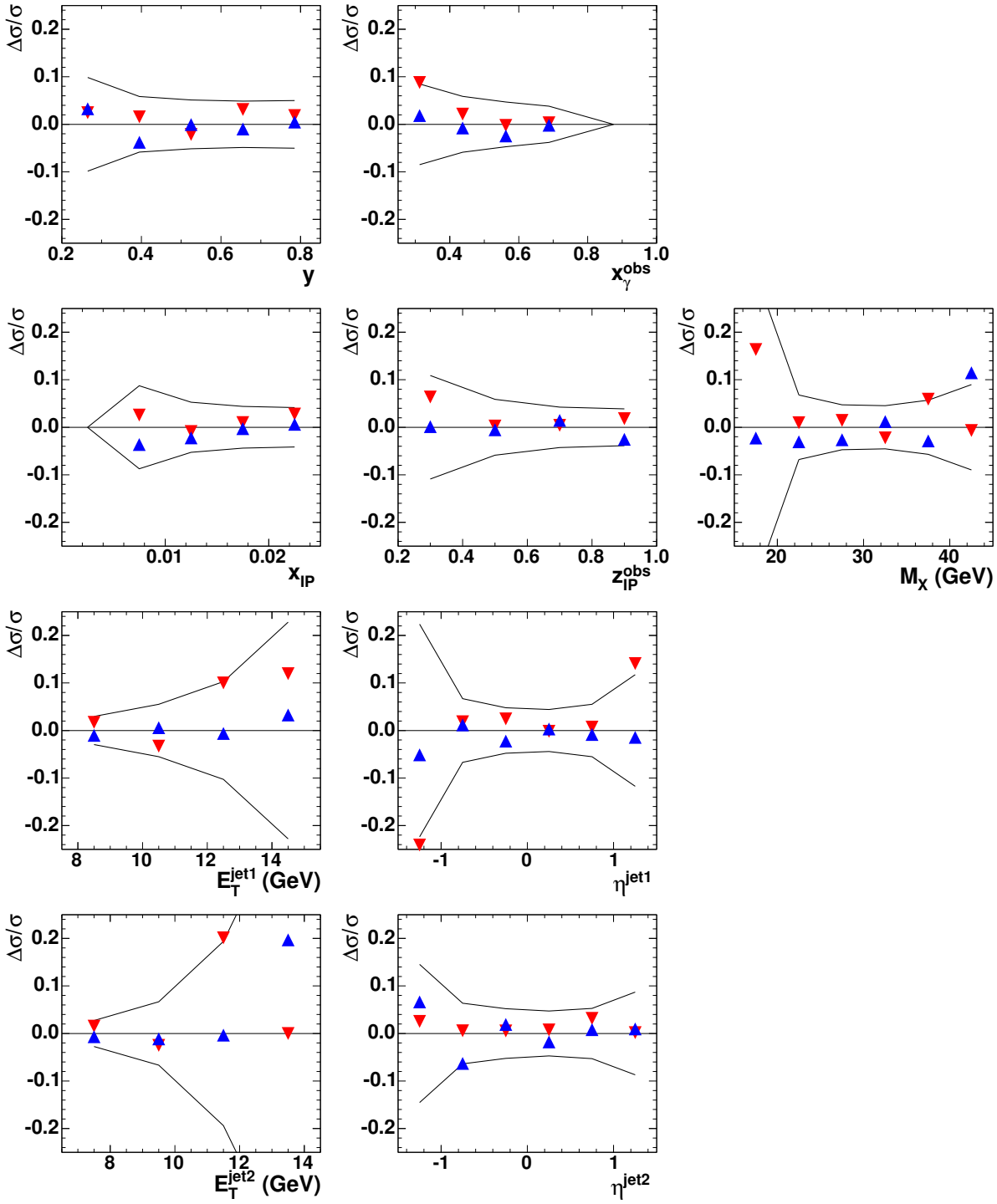

Figure C.2: Systematic errors of ZUFO energy increased (▲) and decreased (▼) as described in Sec. 11.1.2, shown in the range $x_\gamma < 0.75$ for the variables y_{JB}, x_γ^{obs}, $x_{I\!P}$, $z_{I\!P}^{obs}$, M_X, $E_T^{jet\,1}$, $\eta^{jet\,1}$, $E_T^{jet\,2}$ and $\eta^{jet\,2}$ – the solid lines indicate the statistical errors.

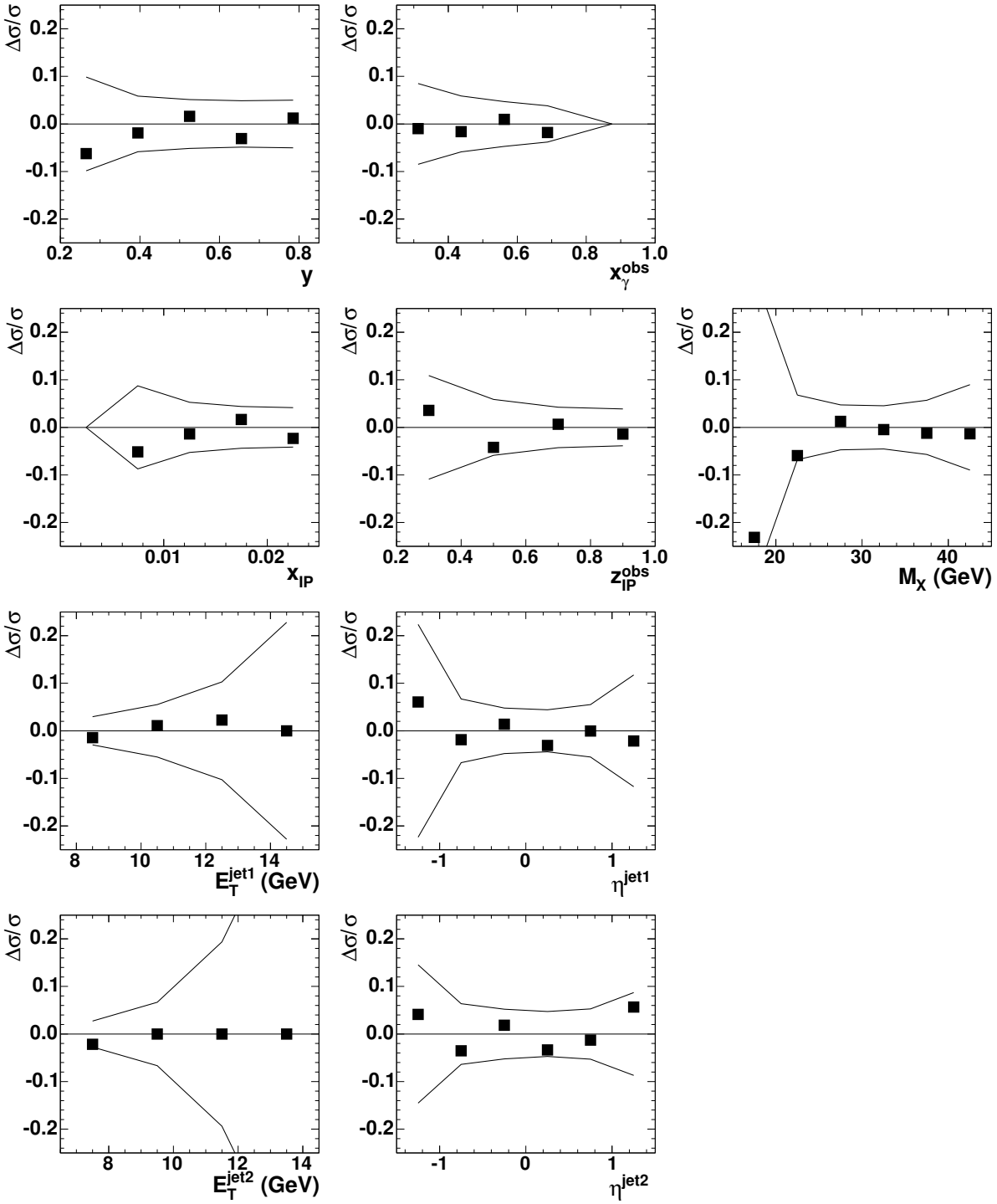

Figure C.3: Systematic errors of a discriminative E_T^{jet} correction for first and second jet (■) shown in the range $x_\gamma < 0.75$ for the variables y_{JB}, x_γ^{obs}, $x_{I\!P}$, $z_{I\!P}^{obs}$, M_X, $E_T^{jet\,1}$, $\eta^{jet\,1}$, $E_T^{jet\,2}$ and $\eta^{jet\,2}$ – the solid lines indicate the statistical errors.

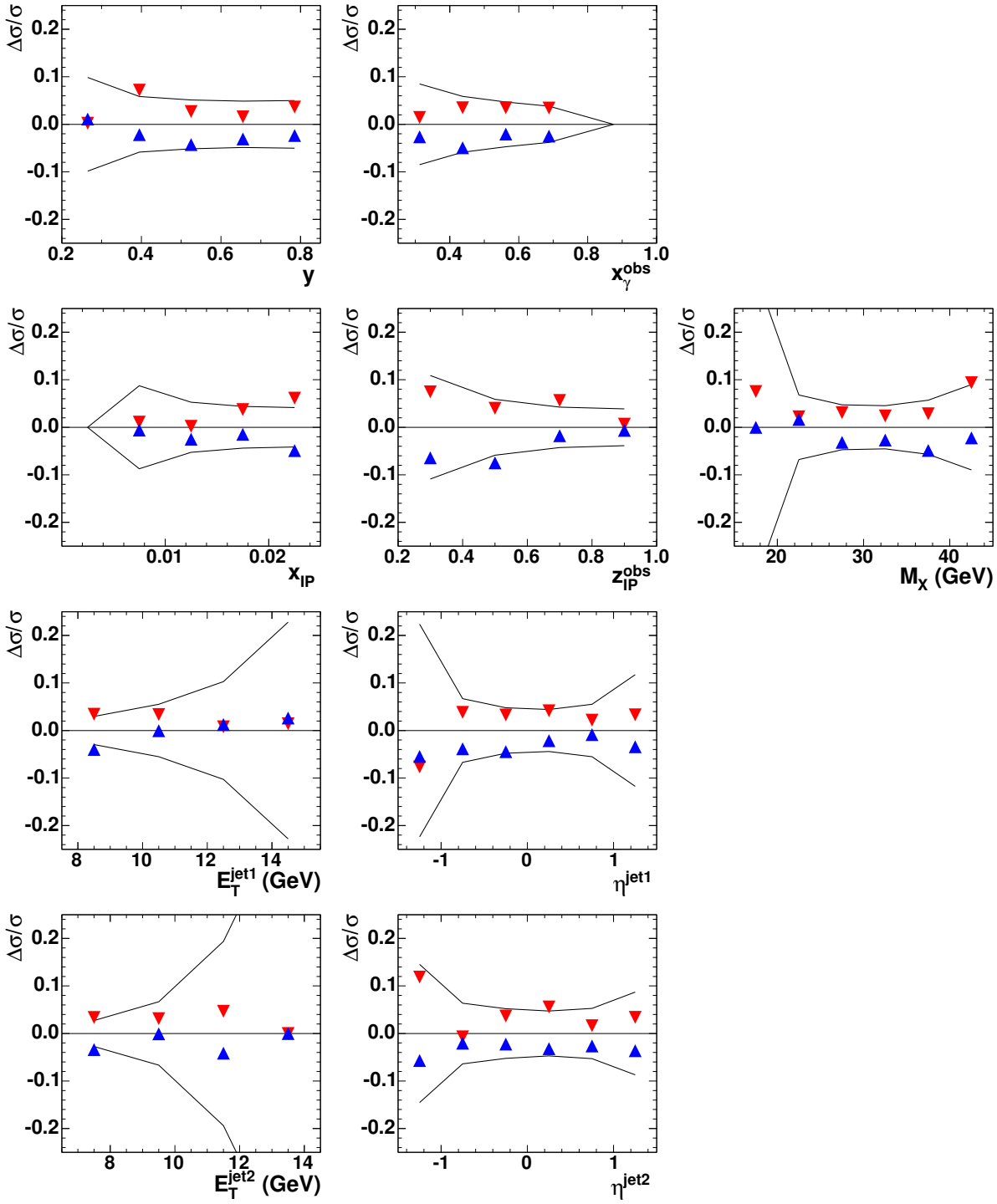

Figure C.4: Systematic errors of the cut on η^{max} increased to $\eta^{max} < 3.0$ (▲) and decreased to $\eta^{max} < 2.6$ (▼), shown in the range $x_\gamma < 0.75$ for the variables y_{JB}, x_γ^{obs}, $x_{I\!P}$, $z_{I\!P}^{obs}$, M_X, $E_T^{jet\,1}$, $\eta^{jet\,1}$, $E_T^{jet\,2}$ and $\eta^{jet\,2}$ – the solid lines indicate the statistical errors.

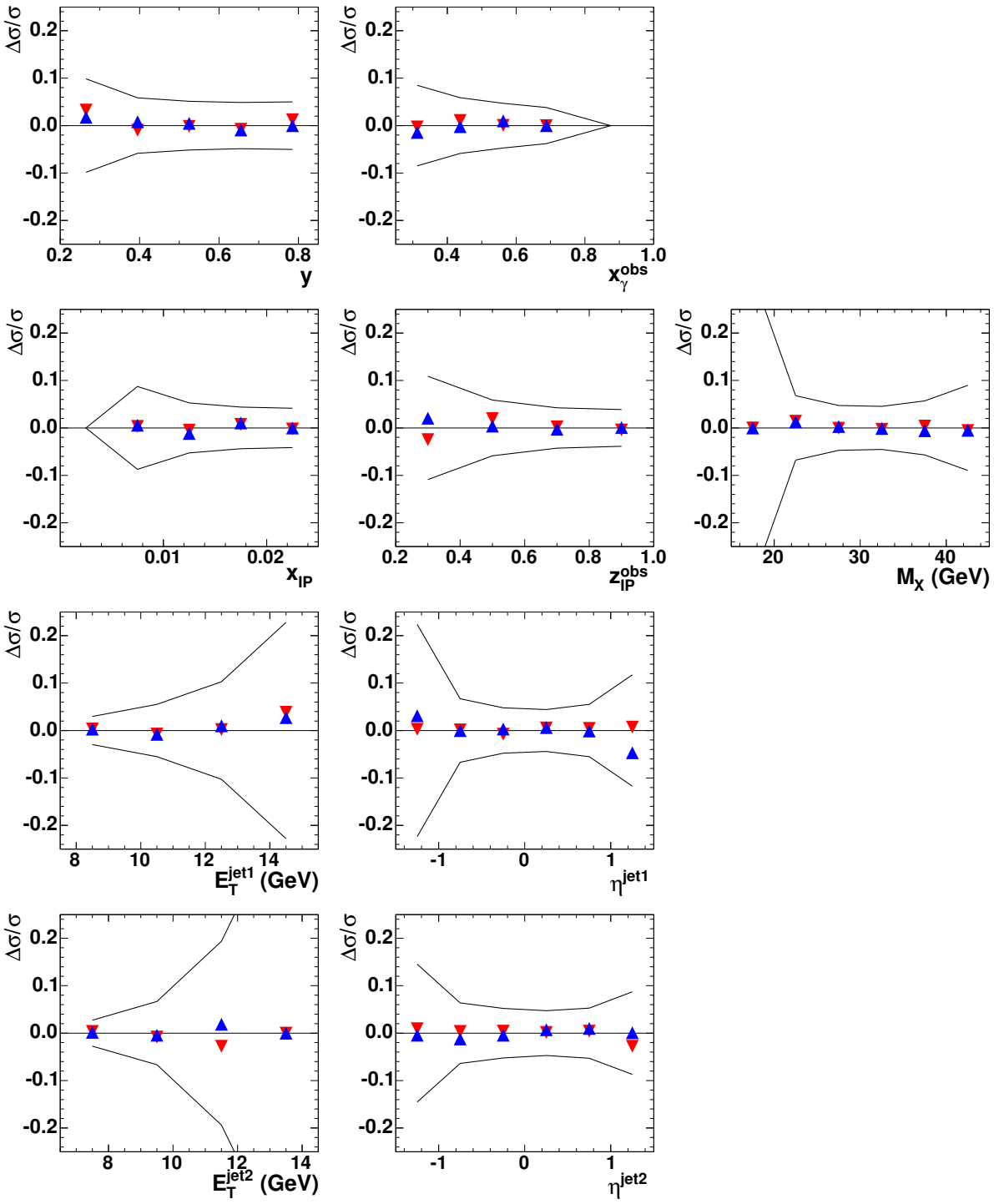

Figure C.5: Systematic errors of the energy threshold, which is used for the calculation of η^{max}, increased to 500 MeV (▲) and decreased to 300 MeV (▼), shown in the range $x_\gamma < 0.75$ for the variables y_{JB}, x_γ^{obs}, $x_{I\!P}$, $z_{I\!P}^{obs}$, M_X, $E_T^{jet\,1}$, $\eta^{jet\,1}$, $E_T^{jet\,2}$ and $\eta^{jet\,2}$ – the solid lines indicate the statistical errors.

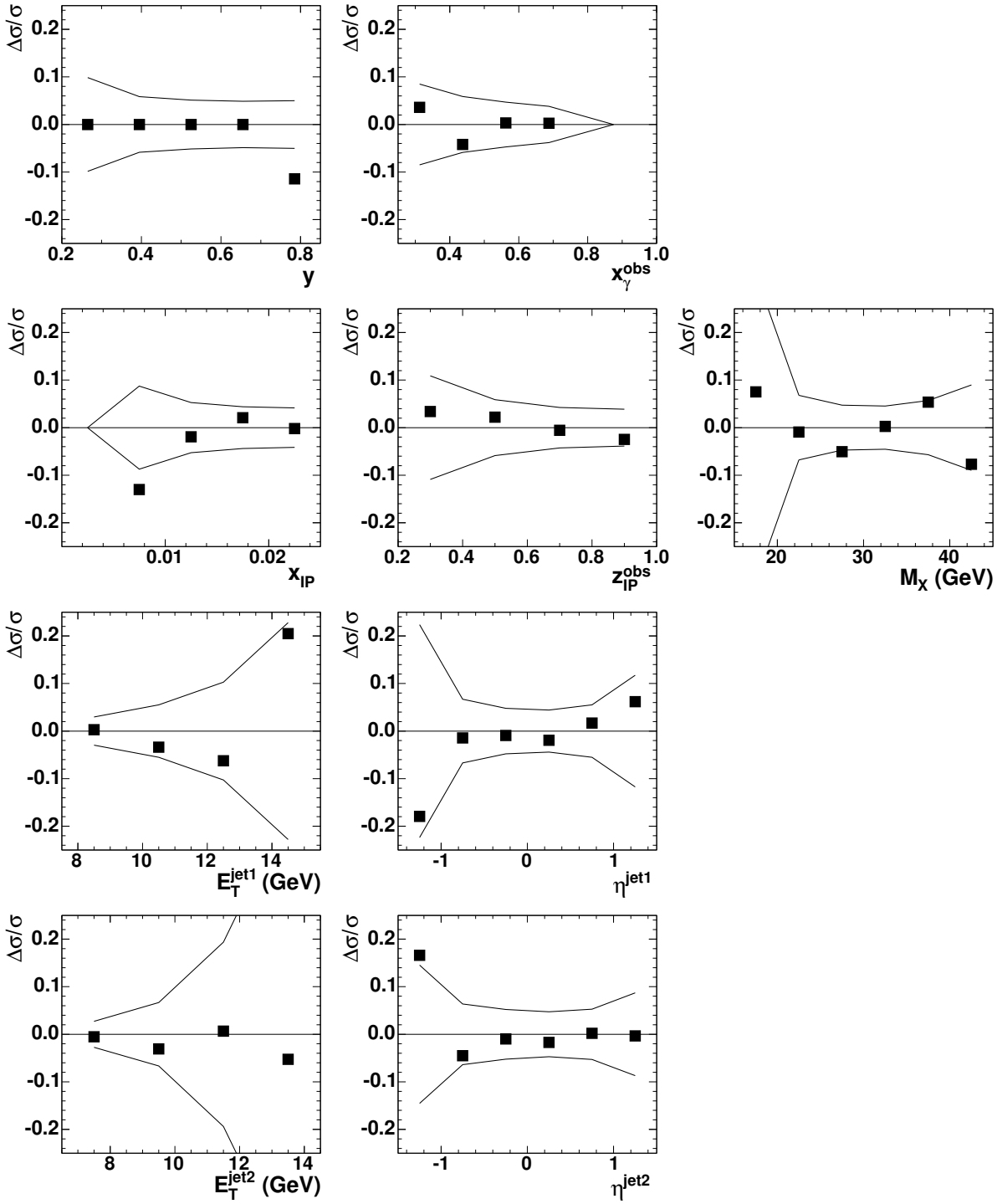

Figure C.6: Systematic errors of a reduced cut of $y_{JB} < 0.78$ (■) shown in the range $x_\gamma < 0.75$ for the variables y_{JB}, x_γ^{obs}, $x_{I\!P}$, $z_{I\!P}^{obs}$, M_X, $E_T^{jet\,1}$, $\eta^{jet\,1}$, $E_T^{jet\,2}$ and $\eta^{jet\,2}$ – the solid lines indicate the statistical errors.

Appendix D

Tables of cross sections and errors for the full x_γ-range

M_X (GeV)	[15.0; 20.0]	[20.0; 25.0]	[25.0; 30.0]	[30.0; 35.0]	[35.0; 40.0]	[40.0; 45.0]
$d\sigma/dM_X$ (nb/GeV)	1.878	6.396	7.140	6.538	4.025	1.611
stat. error	$\pm$0.098	$\pm$0.175	$\pm$0.190	$\pm$0.199	$\pm$0.165	$\pm$0.113
$z_{\text{vtx}} + 5$mm	+0.083	+0.160	+0.153	+0.206	+0.130	+0.035
$z_{\text{vtx}} - 5$mm	+0.038	+0.075	+0.089	+0.157	+0.095	+0.029
$E_{\text{zufo}} \uparrow$	+0.021	$-$0.098	$-$0.077	+0.080	$-$0.149	+0.139
$E_{\text{zufo}} \downarrow$	+0.069	+0.002	$-$0.044	$-$0.005	+0.179	$-$0.074
E_T corr.	$-$0.055	$-$0.085	+0.010	+0.007	$-$0.037	$-$0.006
$E_\eta > 500$GeV	+0.000	+0.010	+0.028	+0.026	+0.005	$-$0.005
$E_\eta > 300$GeV	$-$0.001	+0.036	$-$0.007	+0.003	+0.025	$-$0.013
$\eta^{max} < 3.0$	+0.019	$-$0.049	$-$0.135	$-$0.217	$-$0.132	$-$0.063
$\eta^{max} < 2.6$	+0.015	+0.111	+0.320	+0.128	+0.119	+0.136
$y_{JB} < 0.78$	$-$0.034	$-$0.037	$-$0.128	+0.003	+0.080	$-$0.002
syst. error $\uparrow$	+0.119	+0.212	+0.367	+0.301	+0.281	+0.199
syst. error $\downarrow$	$-$0.064	$-$0.144	$-$0.206	$-$0.217	$-$0.202	$-$0.099
total error $\uparrow$	+0.154	+0.275	+0.413	+0.360	+0.326	+0.229
total error $\downarrow$	$-$0.117	$-$0.227	$-$0.280	$-$0.294	$-$0.261	$-$0.150

Table D.1: Cross sections, statistical and systematic errors as defined in Chap. 11 for M_X.

y	$[0.20; 0.33]$	$[0.33; 0.46]$	$[0.46; 0.59]$	$[0.59; 0.72]$	$[0.72; 0.85]$
$d\sigma/dy$ (nb)	141.5	213.5	245.6	232.3	231.7
stat. error	± 5.3	± 6.6	± 7.3	± 7.1	± 7.2
$z_{\text{vtx}} + 5\text{mm}$	$+4.2$	$+4.7$	$+8.2$	$+4.4$	$+8.0$
$z_{\text{vtx}} - 5\text{mm}$	$+4.3$	$+2.9$	$+3.1$	$+1.7$	$+5.9$
$E_{\text{zufo}} \uparrow$	-1.3	-0.5	$+1.4$	-3.4	-0.9
$E_{\text{zufo}} \downarrow$	$+1.3$	$+0.3$	-3.2	$+5.4$	$+1.4$
E_T corr.	-3.4	-2.0	$+3.3$	-2.8	$+0.5$
$E_\eta > 500\text{GeV}$	-0.3	$+0.9$	$+0.8$	-0.1	$+1.0$
$E_\eta > 300\text{GeV}$	$+0.7$	$+0.2$	$+0.6$	$+0.2$	$+0.5$
$\eta^{max} < 3.0$	-1.3	-3.8	-6.0	-3.8	-5.3
$\eta^{max} < 2.6$	$+3.2$	$+10.1$	$+4.2$	$+4.8$	$+6.1$
$y_{JB} < 0.78$	-0.0	-0.0	-0.0	-0.0	-9.0
syst. error $\uparrow$	$+6.9$	$+11.5$	$+10.4$	$+8.6$	$+11.8$
syst. error $\downarrow$	-3.8	-4.3	-6.8	-5.8	-10.5
total error $\uparrow$	$+8.8$	$+13.3$	$+12.7$	$+11.2$	$+13.8$
total error $\downarrow$	-6.6	-7.9	-10.0	-9.1	-12.7

Table D.2: Cross sections, statistical and systematic errors as defined in Chap. 11 for y.

x_γ^{obs}	$[0.250; 0.375]$	$[0.375; 0.500]$	$[0.500; 0.625]$	$[0.625; 0.750]$	$[0.750; 1.000]$
$d\sigma/dx_\gamma^{obs}$ (nb)	31.41	61.94	92.52	139.9	387.3
stat. error	± 2.66	± 3.64	± 4.36	± 5.3	± 6.6
$z_{\text{vtx}} + 5\text{mm}$	$+1.50$	$+0.79$	$+3.03$	$+3.6$	$+11.0$
$z_{\text{vtx}} - 5\text{mm}$	$+1.00$	-0.48	$+1.67$	$+1.9$	$+7.5$
$E_{\text{zufo}} \uparrow$	$+0.58$	-0.47	-2.25	-0.3	-1.2
$E_{\text{zufo}} \downarrow$	$+2.76$	$+1.32$	-0.21	$+0.4$	$+0.9$
E_T corr.	-0.31	-1.00	$+0.89$	-2.5	-0.9
$E_\eta > 500\text{GeV}$	-0.45	-0.14	$+0.90$	-0.0	$+1.0$
$E_\eta > 300\text{GeV}$	-0.09	$+0.68$	$+0.04$	-0.0	$+1.0$
$\eta^{max} < 3.0$	-0.83	-3.05	-1.88	-3.5	-5.6
$\eta^{max} < 2.6$	$+0.46$	$+2.16$	$+3.21$	$+4.8$	$+9.5$
$y_{JB} < 0.78$	$+1.13$	-2.60	$+0.29$	$+0.4$	-2.4
syst. error $\uparrow$	$+3.57$	$+2.74$	$+4.90$	$+6.3$	$+16.4$
syst. error $\downarrow$	-0.99	-4.19	-2.94	-4.3	-6.3
total error $\uparrow$	$+4.45$	$+4.56$	$+6.55$	$+8.3$	$+17.7$
total error $\downarrow$	-2.84	-5.55	-5.26	-6.8	-9.1

Table D.3: Cross sections, statistical and systematic errors as defined in Chap. 11 for x_γ^{obs}.

$x_{I\!P}$	$[0.000; 0.005]$	$[0.005; 0.010]$	$[0.010; 0.015]$	$[0.015; 0.020]$	$[0.020; 0.025]$
$d\sigma/dx_{I\!P}$ (pb)	0.347	3.796	6.640	7.963	9.125
stat. error	± 0.050	± 0.132	± 0.179	± 0.209	± 0.254
$z_{\text{vtx}} + 5\text{mm}$	$+0.011$	$+0.132$	$+0.121$	$+0.254$	$+0.257$
$z_{\text{vtx}} - 5\text{mm}$	$+0.000$	$+0.041$	$+0.089$	$+0.145$	$+0.215$
$E_{\text{zufo}} \uparrow$	-0.013	-0.039	-0.073	-0.026	$+0.045$
$E_{\text{zufo}} \downarrow$	$+0.008$	$+0.006$	$+0.002$	$+0.032$	$+0.124$
E_T corr.	-0.009	-0.056	$+0.027$	-0.010	-0.104
$E_\eta > 500\text{GeV}$	$+0.000$	$+0.007$	-0.010	$+0.099$	-0.039
$E_\eta > 300\text{GeV}$	$+0.000$	$+0.014$	$+0.003$	$+0.006$	$+0.026$
$\eta^{max} < 3.0$	$+0.000$	$+0.007$	-0.093	-0.179	-0.370
$\eta^{max} < 2.6$	$+0.000$	$+0.035$	$+0.128$	$+0.220$	$+0.596$
$y_{JB} < 0.78$	-0.048	-0.160	-0.086	$+0.046$	$+0.049$
syst. error $\uparrow$	$+0.013$	$+0.144$	$+0.199$	$+0.383$	$+0.698$
syst. error $\downarrow$	-0.051	-0.174	-0.146	-0.181	-0.387
total error $\uparrow$	$+0.052$	$+0.195$	$+0.268$	$+0.436$	$+0.743$
total error $\downarrow$	-0.071	-0.218	-0.231	-0.276	-0.463

Table D.4: Cross sections, statistical and systematic errors as defined in Chap. 11 for $x_{I\!P}$.

$z_{I\!P}^{obs}$	$[0.2; 0.4]$	$[0.4; 0.6]$	$[0.6; 0.8]$	$[0.8; 1.0]$
$d\sigma/dz_{I\!P}^{obs}$ (nb)	110.2	192.7	221.8	160.6
stat. error	± 5.6	± 6.1	± 5.6	± 3.5
$z_{\text{vtx}} + 5\text{mm}$	$+3.4$	$+3.4$	$+8.2$	$+4.0$
$z_{\text{vtx}} - 5\text{mm}$	$+0.6$	$+2.7$	$+5.6$	$+2.2$
$E_{\text{zufo}} \uparrow$	$+0.4$	-1.6	$+0.3$	-1.5
$E_{\text{zufo}} \downarrow$	$+2.7$	-1.5	$+0.4$	$+1.6$
E_T corr.	$+3.6$	-1.9	-1.7	-1.1
$E_\eta > 500\text{GeV}$	$+2.1$	$+0.2$	$+0.7$	-0.2
$E_\eta > 300\text{GeV}$	-0.1	$+1.4$	-0.2	$+0.4$
$\eta^{max} < 3.0$	-6.8	-6.9	-4.1	-0.0
$\eta^{max} < 2.6$	$+9.0$	$+9.7$	$+9.2$	-0.2
$y_{JB} < 0.78$	$+3.7$	$+2.9$	-2.3	-3.0
syst. error $\uparrow$	$+11.5$	$+11.1$	$+13.5$	$+4.8$
syst. error $\downarrow$	-6.8	-7.5	-5.0	-3.6
total error $\uparrow$	$+12.8$	$+12.7$	$+14.6$	$+6.0$
total error $\downarrow$	-8.8	-9.7	-7.5	-5.0

Table D.5: Cross sections, statistical and systematic errors as defined in Chap. 11 for $z_{I\!P}^{obs}$.

E_T^{jet1} (GeV)	[7.5; 9.5]	[9.5; 11.5]	[11.5; 13.5]	[13.5; 15.5]
$d\sigma/dE_T^{jet1}$ (nb/GeV)	49.34	15.28	3.68	0.77
stat. error	±0.86	±0.44	±0.19	±0.08
$z_{\text{vtx}} + 5\text{mm}$	+1.47	+0.35	+0.07	+0.03
$z_{\text{vtx}} - 5\text{mm}$	+0.78	+0.23	+0.09	+0.02
$E_{\text{zufo}} \uparrow$	−0.42	−0.14	+0.14	−0.01
$E_{\text{zufo}} \downarrow$	+0.59	−0.22	−0.01	+0.02
E_T corr.	−0.48	+0.06	+0.02	−0.01
$E_\eta > 500\text{GeV}$	+0.12	+0.06	+0.00	−0.02
$E_\eta > 300\text{GeV}$	+0.24	−0.07	+0.00	−0.00
$\eta^{max} < 3.0$	−1.19	−0.08	−0.05	−0.00
$\eta^{max} < 2.6$	+1.60	+0.37	+0.04	−0.01
$y_{JB} < 0.78$	+0.18	−0.26	−0.23	−0.01
syst. error ↑	+2.40	+0.57	+0.19	+0.04
syst. error ↓	−1.35	−0.38	−0.23	−0.03
total error ↑	+2.55	+0.72	+0.27	+0.09
total error ↓	−1.60	−0.58	−0.30	−0.09

Table D.6: Cross sections, statistical and systematic errors as defined in Chap. 11 for E_T^{jet1}.

E_T^{jet2} (GeV)	[6.5; 8.5]	[8.5; 10.5]	[10.5; 12.5]	[12.5; 14.5]
$d\sigma/dE_T^{jet2}$ (nb/GeV)	50.90	14.36	3.08	0.48
stat. error	±0.82	±0.47	±0.23	±0.09
$z_{\text{vtx}} + 5\text{mm}$	+1.39	+0.35	+0.16	+0.01
$z_{\text{vtx}} - 5\text{mm}$	+0.70	+0.37	+0.10	+0.01
$E_{\text{zufo}} \uparrow$	−0.35	−0.05	+0.02	+0.04
$E_{\text{zufo}} \downarrow$	+0.28	−0.07	+0.10	+0.05
E_T corr.	−0.34	−0.00	+0.00	+0.00
$E_\eta > 500\text{GeV}$	+0.13	+0.05	−0.03	+0.00
$E_\eta > 300\text{GeV}$	+0.22	−0.05	−0.04	−0.00
$\eta^{max} < 3.0$	−1.16	−0.13	+0.01	−0.02
$\eta^{max} < 2.6$	+1.47	+0.45	+0.01	−0.03
$y_{JB} < 0.78$	−0.27	−0.12	−0.10	−0.03
syst. error ↑	+2.17	+0.68	+0.22	+0.07
syst. error ↓	−1.29	−0.20	−0.11	−0.05
total error ↑	+2.32	+0.83	+0.32	+0.11
total error ↓	−1.53	−0.51	−0.26	−0.10

Table D.7: Cross sections, statistical and systematic errors as defined in Chap. 11 for E_T^{jet2}.

η^{jet1}	$[-1.5;-1.0]$	$[-1.0;-0.5]$	$[-0.5;0.0]$	$[0.0;0.5]$	$[0.5;1.0]$	$[1.0;1.5]$
$d\sigma/d\eta^{jet1}$ (nb)	16.02	62.12	81.77	72.04	37.60	8.04
stat. error	$\pm$1.03	$\pm$1.94	$\pm$2.15	$\pm$1.94	$\pm$1.37	$\pm$0.65
$z_{\text{vtx}} + 5$mm	+0.05	+1.70	+2.08	+1.86	+1.37	+0.51
$z_{\text{vtx}} - 5$mm	+0.39	+0.54	+1.54	+1.20	+0.78	+0.20
$E_{\text{zufo}} \uparrow$	−0.20	+0.03	−0.68	−0.36	−0.24	+0.16
$E_{\text{zufo}} \downarrow$	−0.50	+1.09	+0.40	−0.07	−0.11	+0.58
E_T corr.	−0.24	+0.86	+0.14	−1.44	−0.44	+0.07
$E_\eta > 500$GeV	+0.16	+0.13	+0.62	−0.03	+0.03	−0.26
$E_\eta > 300$GeV	+0.18	+0.09	−0.24	+0.54	−0.14	+0.16
$\eta^{max} < 3.0$	−0.13	−1.30	−1.86	−1.40	−0.48	−0.15
$\eta^{max} < 2.6$	+0.02	+1.49	+3.07	+1.88	+0.91	+0.15
$y_{JB} < 0.78$	+0.28	−0.12	−0.74	−0.94	+0.36	+0.20
syst. error $\uparrow$	+0.54	+2.71	+4.08	+2.95	+1.85	+0.86
syst. error $\downarrow$	−0.60	−1.30	−2.13	−2.25	−0.71	−0.30
total error $\uparrow$	+1.16	+3.33	+4.61	+3.54	+2.30	+1.08
total error $\downarrow$	−1.19	−2.34	−3.02	−2.97	−1.55	−0.72

Table D.8: Cross sections, statistical and systematic errors as defined in Chap. 11 for η^{jet1}.

η^{jet2}	$[-1.5;-1.0]$	$[-1.0;-0.5]$	$[-0.5;0.0]$	$[0.0;0.5]$	$[0.5;1.0]$	$[1.0;1.5]$
$d\sigma/d\eta^{jet2}$ (nb)	32.13	64.35	69.40	58.03	36.33	15.02
stat. error	$\pm$1.56	$\pm$1.97	$\pm$1.93	$\pm$1.69	$\pm$1.31	$\pm$0.91
$z_{\text{vtx}} + 5$mm	+1.58	+2.55	+1.39	+1.56	+0.95	−0.12
$z_{\text{vtx}} - 5$mm	+0.45	+1.79	+0.67	+0.94	+0.81	−0.00
$E_{\text{zufo}} \uparrow$	−0.15	−1.19	+0.33	−0.50	+0.24	−0.11
$E_{\text{zufo}} \downarrow$	+0.25	+0.04	−0.05	+0.45	+0.45	+0.13
E_T corr.	−0.48	−0.08	+0.19	−0.84	+0.04	−0.08
$E_\eta > 500$GeV	+0.17	+0.00	−0.03	+0.24	+0.20	−0.03
$E_\eta > 300$GeV	+0.15	+0.23	+0.34	−0.28	−0.02	+0.19
$\eta^{max} < 3.0$	−1.01	−0.55	−0.93	−1.46	−0.99	−0.08
$\eta^{max} < 2.6$	+1.31	+0.96	+1.95	+2.28	+0.65	+0.27
$y_{JB} < 0.78$	+0.02	−1.84	+0.12	−0.63	+0.11	−0.37
syst. error $\uparrow$	+2.12	+3.27	+2.54	+2.96	+1.51	+0.36
syst. error $\downarrow$	−1.13	−2.26	−0.93	−1.88	−0.99	−0.43
total error $\uparrow$	+2.64	+3.82	+3.19	+3.41	+2.00	+0.98
total error $\downarrow$	−1.93	−3.00	−2.14	−2.53	−1.64	−1.00

Table D.9: Cross sections, statistical and systematic errors as defined in Chap. 11 for η^{jet2}.

Appendix E

Tables of cross sections and errors for the range $x_\gamma \geq 0.75$

M_X (GeV)	[15.0; 20.0]	[20.0; 25.0]	[25.0; 30.0]	[30.0; 35.0]	[35.0; 40.0]	[40.0; 45.0]
$d\sigma/dM_X$ (nb/GeV)	1.849	5.391	5.387	3.884	2.205	0.738
stat. error	$\pm$0.098	$\pm$0.162	$\pm$0.173	$\pm$0.159	$\pm$0.130	$\pm$0.083
$z_{\text{vtx}} + 5$mm	+0.080	+0.143	+0.119	+0.139	+0.040	+0.028
$z_{\text{vtx}} - 5$mm	+0.038	+0.068	+0.086	+0.101	+0.051	+0.056
$E_{\text{zufo}} \uparrow$	+0.023	$-$0.067	$-$0.019	+0.048	$-$0.104	+0.030
$E_{\text{zufo}} \downarrow$	+0.064	$-$0.009	$-$0.084	+0.066	+0.061	$-$0.079
E_T corr.	$-$0.043	$-$0.023	$-$0.022	+0.021	$-$0.014	+0.008
$E_\eta > 500$GeV	+0.000	$-$0.003	+0.023	+0.032	+0.023	$-$0.001
$E_\eta > 300$GeV	$-$0.001	+0.022	$-$0.006	+0.012	+0.018	$-$0.009
$\eta^{max} < 3.0$	+0.019	$-$0.066	$-$0.074	$-$0.148	$-$0.047	$-$0.048
$\eta^{max} < 2.6$	+0.012	+0.088	+0.282	+0.062	+0.090	+0.051
$y_{JB} < 0.78$	$-$0.037	$-$0.027	$-$0.011	$-$0.005	$-$0.036	+0.081
syst. error $\uparrow$	+0.114	+0.183	+0.319	+0.204	+0.130	+0.119
syst. error $\downarrow$	$-$0.057	$-$0.101	$-$0.116	$-$0.148	$-$0.121	$-$0.093
total error $\uparrow$	+0.150	+0.244	+0.363	+0.259	+0.184	+0.145
total error $\downarrow$	$-$0.113	$-$0.190	$-$0.209	$-$0.217	$-$0.178	$-$0.125

Table E.1: Cross sections, statistical and systematic errors as defined in Chap. 11 for M_X.

y	$[0.20; 0.33]$	$[0.33; 0.46]$	$[0.46; 0.59]$	$[0.59; 0.72]$	$[0.72; 0.85]$
$d\sigma/dy$ (nb)	125.2	163.2	169.9	141.2	147.9
stat. error	± 5.1	± 6.0	± 6.2	± 5.5	± 5.8
$z_{\text{vtx}} + 5\text{mm}$	$+3.9$	$+3.9$	$+6.0$	$+2.5$	$+4.9$
$z_{\text{vtx}} - 5\text{mm}$	$+4.5$	$+1.9$	$+1.0$	$+2.2$	$+4.5$
$E_{\text{zufo}} \uparrow$	-2.0	$+1.8$	$+1.5$	-2.5	-1.5
$E_{\text{zufo}} \downarrow$	$+0.8$	-0.7	-1.5	$+2.6$	-0.2
E_T corr.	-2.1	-1.0	$+2.1$	$+0.0$	-0.6
$E_\eta > 500\text{GeV}$	-0.6	$+0.5$	$+0.5$	$+0.7$	$+1.0$
$E_\eta > 300\text{GeV}$	-0.0	$+0.9$	$+0.8$	$+0.9$	-0.6
$\eta^{max} < 3.0$	-1.5	-2.6	-2.6	-0.9	-3.4
$\eta^{max} < 2.6$	$+3.3$	$+6.3$	$+2.1$	$+3.3$	$+3.0$
$y_{JB} < 0.78$	-0.0	-0.0	-0.0	-0.0	$+0.8$
syst. error $\uparrow$	$+6.8$	$+7.9$	$+7.0$	$+5.5$	$+7.4$
syst. error $\downarrow$	-3.4	-2.8	-3.0	-2.7	-3.8
total error $\uparrow$	$+8.5$	$+9.9$	$+9.4$	$+7.8$	$+9.4$
total error $\downarrow$	-6.1	-6.6	-6.9	-6.1	-7.0

Table E.2: Cross sections, statistical and systematic errors as defined in Chap. 11 for y.

x_γ^{obs}	$[0.250; 0.375]$	$[0.375; 0.500]$	$[0.500; 0.625]$	$[0.625; 0.750]$	$[0.750; 1.000]$
$d\sigma/dx_\gamma^{obs}$ (nb)	*n.a.*	*n.a.*	*n.a.*	*n.a.*	387.3
stat. error	*n.a.*	*n.a.*	*n.a.*	*n.a.*	± 6.6
$z_{\text{vtx}} + 5\text{mm}$	*n.a.*	*n.a.*	*n.a.*	*n.a.*	$+11.0$
$z_{\text{vtx}} - 5\text{mm}$	*n.a.*	*n.a.*	*n.a.*	*n.a.*	$+7.5$
$E_{\text{zufo}} \uparrow$	*n.a.*	*n.a.*	*n.a.*	*n.a.*	-1.2
$E_{\text{zufo}} \downarrow$	*n.a.*	*n.a.*	*n.a.*	*n.a.*	$+0.9$
E_T corr.	*n.a.*	*n.a.*	*n.a.*	*n.a.*	-0.9
$E_\eta > 500\text{GeV}$	*n.a.*	*n.a.*	*n.a.*	*n.a.*	$+1.0$
$E_\eta > 300\text{GeV}$	*n.a.*	*n.a.*	*n.a.*	*n.a.*	$+1.0$
$\eta^{max} < 3.0$	*n.a.*	*n.a.*	*n.a.*	*n.a.*	-5.6
$\eta^{max} < 2.6$	*n.a.*	*n.a.*	*n.a.*	*n.a.*	$+9.5$
$y_{JB} < 0.78$	*n.a.*	*n.a.*	*n.a.*	*n.a.*	-2.4
syst. error $\uparrow$	*n.a.*	*n.a.*	*n.a.*	*n.a.*	$+16.4$
syst. error $\downarrow$	*n.a.*	*n.a.*	*n.a.*	*n.a.*	-6.3
total error $\uparrow$	*n.a.*	*n.a.*	*n.a.*	*n.a.*	$+17.7$
total error $\downarrow$	*n.a.*	*n.a.*	*n.a.*	*n.a.*	-9.1

Table E.3: Cross sections, statistical and systematic errors as defined in Chap. 11 for x_γ^{obs}.

$x_{I\!P}$	$[0.000; 0.005]$	$[0.005; 0.010]$	$[0.010; 0.015]$	$[0.015; 0.020]$	$[0.020; 0.025]$
$d\sigma/dx_{I\!P}$ (pb)	0.355	3.230	5.026	5.470	5.497
stat. error	± 0.051	± 0.122	± 0.158	± 0.179	± 0.207
$z_{\text{vtx}} + 5\text{mm}$	$+0.011$	$+0.113$	$+0.099$	$+0.160$	$+0.179$
$z_{\text{vtx}} - 5\text{mm}$	$+0.000$	$+0.034$	$+0.088$	$+0.091$	$+0.190$
$E_{\text{zufo}} \uparrow$	-0.016	-0.017	-0.035	-0.020	$+0.021$
$E_{\text{zufo}} \downarrow$	$+0.008$	-0.007	$+0.018$	$+0.004$	$+0.011$
E_T corr.	-0.015	-0.028	$+0.052$	-0.065	-0.008
$E_\eta > 500\text{GeV}$	$+0.000$	$+0.005$	$+0.011$	$+0.074$	-0.042
$E_\eta > 300\text{GeV}$	$+0.000$	$+0.012$	$+0.011$	-0.019	$+0.038$
$\eta^{max} < 3.0$	$+0.000$	$+0.010$	-0.050	-0.158	-0.186
$\eta^{max} < 2.6$	$+0.000$	$+0.028$	$+0.128$	$+0.133$	$+0.379$
$y_{JB} < 0.78$	-0.056	-0.079	-0.053	-0.030	$+0.061$
syst. error $\uparrow$	$+0.013$	$+0.122$	$+0.192$	$+0.239$	$+0.466$
syst. error $\downarrow$	-0.060	-0.086	-0.081	-0.175	-0.191
total error $\uparrow$	$+0.053$	$+0.173$	$+0.249$	$+0.298$	$+0.510$
total error $\downarrow$	-0.079	-0.149	-0.177	-0.250	-0.282

Table E.4: Cross sections, statistical and systematic errors as defined in Chap. 11 for $x_{I\!P}$.

$z_{I\!P}^{obs}$	$[0.2; 0.4]$	$[0.4; 0.6]$	$[0.6; 0.8]$	$[0.8; 1.0]$
$d\sigma/dz_{I\!P}^{obs}$ (nb)	88.4	131.8	133.0	125.7
stat. error	± 5.1	± 5.0	± 4.2	± 3.4
$z_{\text{vtx}} + 5\text{mm}$	$+2.6$	$+1.9$	$+4.3$	$+4.0$
$z_{\text{vtx}} - 5\text{mm}$	$+0.4$	$+2.6$	$+2.8$	$+2.5$
$E_{\text{zufo}} \uparrow$	$+0.4$	-1.2	-0.8	-0.2
$E_{\text{zufo}} \downarrow$	$+1.2$	-1.6	$+0.1$	$+0.7$
E_T corr.	$+2.8$	$+0.4$	-2.1	-0.4
$E_\eta > 500\text{GeV}$	$+1.6$	-0.0	$+0.9$	-0.3
$E_\eta > 300\text{GeV}$	$+0.5$	$+0.3$	-0.4	$+0.8$
$\eta^{max} < 3.0$	-5.3	-2.6	-2.5	$+0.4$
$\eta^{max} < 2.6$	$+7.4$	$+7.2$	$+4.4$	-0.6
$y_{JB} < 0.78$	$+3.0$	$+1.7$	-1.7	-2.1
syst. error $\uparrow$	$+9.1$	$+8.1$	$+6.8$	$+4.9$
syst. error $\downarrow$	-5.3	-3.3	-3.8	-2.2
total error $\uparrow$	$+10.4$	$+9.5$	$+8.0$	$+5.9$
total error $\downarrow$	-7.4	-5.9	-5.6	-4.0

Table E.5: Cross sections, statistical and systematic errors as defined in Chap. 11 for $z_{I\!P}^{obs}$.

E_T^{jet1} (GeV)	$[7.5; 9.5]$	$[9.5; 11.5]$	$[11.5; 13.5]$	$[13.5; 15.5]$
$d\sigma/dE_T^{jet1}$ (nb/GeV)	33.65	11.26	2.84	0.66
stat. error	± 0.72	± 0.38	± 0.17	± 0.08
$z_{\text{vtx}} + 5\text{mm}$	$+1.00$	$+0.32$	$+0.03$	$+0.02$
$z_{\text{vtx}} - 5\text{mm}$	$+0.58$	$+0.20$	$+0.08$	$+0.01$
$E_{\text{zufo}} \uparrow$	-0.26	-0.17	$+0.15$	-0.01
$E_{\text{zufo}} \downarrow$	$+0.31$	-0.07	-0.10	-0.00
E_T corr.	-0.25	$+0.02$	-0.00	-0.01
$E_\eta > 500\text{GeV}$	$+0.07$	$+0.10$	-0.01	-0.03
$E_\eta > 300\text{GeV}$	$+0.19$	-0.03	$+0.00$	-0.01
$\eta^{max} < 3.0$	-0.53	-0.09	-0.07	-0.01
$\eta^{max} < 2.6$	$+1.05$	$+0.23$	$+0.03$	-0.02
$y_{JB} < 0.78$	$+0.14$	-0.13	-0.17	-0.04
syst. error $\uparrow$	$+1.61$	$+0.46$	$+0.18$	$+0.02$
syst. error $\downarrow$	-0.64	-0.25	-0.21	-0.05
total error $\uparrow$	$+1.77$	$+0.60$	$+0.24$	$+0.08$
total error $\downarrow$	-0.97	-0.46	-0.27	-0.10

Table E.6: Cross sections, statistical and systematic errors as defined in Chap. 11 for E_T^{jet1}.

E_T^{jet2} (GeV)	$[6.5; 8.5]$	$[8.5; 10.5]$	$[10.5; 12.5]$	$[12.5; 14.5]$
$d\sigma/dE_T^{jet2}$ (nb/GeV)	34.00	11.04	2.72	0.48
stat. error	± 0.68	± 0.41	± 0.22	± 0.09
$z_{\text{vtx}} + 5\text{mm}$	$+0.95$	$+0.28$	$+0.12$	$+0.01$
$z_{\text{vtx}} - 5\text{mm}$	$+0.54$	$+0.31$	$+0.07$	$+0.01$
$E_{\text{zufo}} \uparrow$	-0.23	-0.01	$+0.03$	$+0.03$
$E_{\text{zufo}} \downarrow$	$+0.01$	$+0.02$	$+0.01$	$+0.06$
E_T corr.	$+0.04$	-0.00	$+0.00$	$+0.00$
$E_\eta > 500\text{GeV}$	$+0.10$	$+0.07$	-0.04	$+0.00$
$E_\eta > 300\text{GeV}$	$+0.16$	-0.02	-0.03	-0.01
$\eta^{max} < 3.0$	-0.57	-0.14	$+0.03$	-0.03
$\eta^{max} < 2.6$	$+0.90$	$+0.35$	-0.01	-0.04
$y_{JB} < 0.78$	-0.18	-0.04	-0.11	-0.03
syst. error $\uparrow$	$+1.43$	$+0.55$	$+0.15$	$+0.07$
syst. error $\downarrow$	-0.64	-0.14	-0.12	-0.06
total error $\uparrow$	$+1.58$	$+0.69$	$+0.27$	$+0.12$
total error $\downarrow$	-0.93	-0.44	-0.25	-0.11

Table E.7: Cross sections, statistical and systematic errors as defined in Chap. 11 for E_T^{jet2}.

η^{jet1}	$[-1.5;-1.0]$	$[-1.0;-0.5]$	$[-0.5;0.0]$	$[0.0;0.5]$	$[0.5;1.0]$	$[1.0;1.5]$
$d\sigma/d\eta^{jet1}$ (nb)	13.94	47.44	56.76	47.11	24.50	4.66
stat. error	± 0.94	± 1.67	± 1.78	± 1.61	± 1.19	± 0.52
$z_{\text{vtx}} + 5\text{mm}$	$+0.14$	$+1.27$	$+1.49$	$+1.34$	$+0.85$	$+0.39$
$z_{\text{vtx}} - 5\text{mm}$	$+0.23$	$+0.70$	$+1.12$	$+0.93$	$+0.47$	$+0.26$
$E_{\text{zufo}} \uparrow$	-0.13	-0.13	-0.13	-0.46	-0.12	$+0.23$
$E_{\text{zufo}} \downarrow$	-0.17	$+0.82$	-0.17	-0.02	-0.26	$+0.10$
E_T corr.	-0.28	$+1.10$	-0.19	-0.65	-0.50	$+0.16$
$E_\eta > 500\text{GeV}$	$+0.11$	$+0.14$	$+0.54$	-0.21	$+0.04$	-0.09
$E_\eta > 300\text{GeV}$	$+0.16$	$+0.07$	-0.05	$+0.41$	-0.25	$+0.15$
$\eta^{max} < 3.0$	-0.05	-0.75	-0.76	-0.86	-0.41	-0.03
$\eta^{max} < 2.6$	$+0.11$	$+0.94$	$+2.24$	$+0.80$	$+0.64$	$+0.03$
$y_{JB} < 0.78$	$+0.43$	-0.05	-0.44	-0.41	$+0.06$	$+0.00$
syst. error $\uparrow$	$+0.56$	$+2.21$	$+2.96$	$+1.86$	$+1.17$	$+0.57$
syst. error $\downarrow$	-0.36	-0.77	-0.93	-1.26	-0.75	-0.09
total error $\uparrow$	$+1.09$	$+2.77$	$+3.46$	$+2.46$	$+1.67$	$+0.77$
total error $\downarrow$	-1.00	-1.84	-2.01	-2.04	-1.41	-0.53

Table E.8: Cross sections, statistical and systematic errors as defined in Chap. 11 for η^{jet1}.

η^{jet2}	$[-1.5;-1.0]$	$[-1.0;-0.5]$	$[-0.5;0.0]$	$[0.0;0.5]$	$[0.5;1.0]$	$[1.0;1.5]$
$d\sigma/d\eta^{jet2}$ (nb)	28.34	50.59	51.57	35.79	19.17	7.24
stat. error	± 1.46	± 1.77	± 1.69	± 1.32	± 0.95	± 0.61
$z_{\text{vtx}} + 5\text{mm}$	$+1.17$	$+1.92$	$+1.19$	$+0.86$	$+0.52$	-0.04
$z_{\text{vtx}} - 5\text{mm}$	$+0.28$	$+1.51$	$+0.37$	$+0.72$	$+0.66$	$+0.08$
$E_{\text{zufo}} \uparrow$	-0.38	-0.24	-0.05	-0.11	$+0.10$	-0.17
$E_{\text{zufo}} \downarrow$	$+0.16$	-0.05	-0.16	$+0.28$	-0.10	$+0.10$
E_T corr.	-0.62	$+0.48$	-0.17	-0.10	$+0.25$	-0.48
$E_\eta > 500\text{GeV}$	$+0.19$	$+0.19$	$+0.06$	$+0.09$	$+0.02$	-0.04
$E_\eta > 300\text{GeV}$	$+0.12$	$+0.18$	$+0.27$	-0.31	-0.09	$+0.39$
$\eta^{max} < 3.0$	-0.80	-0.26	-0.51	-0.75	-0.54	$+0.21$
$\eta^{max} < 2.6$	$+0.88$	$+1.10$	$+1.28$	$+1.06$	$+0.37$	$+0.01$
$y_{JB} < 0.78$	-0.42	-1.26	$+0.23$	-0.23	$+0.04$	-0.36
syst. error $\uparrow$	$+1.52$	$+2.74$	$+1.83$	$+1.57$	$+0.96$	$+0.46$
syst. error $\downarrow$	-1.16	-1.30	-0.57	-0.86	-0.56	-0.63
total error $\uparrow$	$+2.11$	$+3.26$	$+2.49$	$+2.05$	$+1.35$	$+0.77$
total error $\downarrow$	-1.87	-2.20	-1.79	-1.57	-1.10	-0.88

Table E.9: Cross sections, statistical and systematic errors as defined in Chap. 11 for η^{jet2}.

Appendix F

Tables of cross sections and errors for the range $x_\gamma < 0.75$

M_X (GeV)	[15.0; 20.0]	[20.0; 25.0]	[25.0; 30.0]	[30.0; 35.0]	[35.0; 40.0]	[40.0; 45.0]
$d\sigma/dM_X$ (nb/GeV)	0.023	1.003	1.783	2.655	1.850	0.877
stat. error	$\pm$0.007	$\pm$0.068	$\pm$0.084	$\pm$0.121	$\pm$0.105	$\pm$0.079
$z_{\text{vtx}} + 5$mm	+0.002	+0.017	+0.035	+0.069	+0.084	+0.010
$z_{\text{vtx}} - 5$mm	−0.000	+0.007	+0.009	+0.057	+0.044	−0.016
$E_{\text{zufo}} \uparrow$	−0.001	−0.031	−0.047	+0.032	−0.053	+0.101
$E_{\text{zufo}} \downarrow$	+0.004	+0.010	+0.026	−0.059	+0.109	−0.006
E_T corr.	−0.005	−0.060	+0.023	−0.012	−0.023	−0.012
$E_\eta > 500$GeV	−0.000	+0.013	+0.005	−0.003	−0.011	−0.004
$E_\eta > 300$GeV	−0.000	+0.014	−0.001	−0.008	+0.007	−0.005
$\eta^{max} < 3.0$	−0.000	+0.017	−0.056	−0.071	−0.090	−0.020
$\eta^{max} < 2.6$	+0.002	+0.022	+0.055	+0.063	+0.052	+0.082
$y_{JB} < 0.78$	+0.002	−0.009	−0.090	+0.007	+0.099	−0.068
syst. error $\uparrow$	+0.005	+0.040	+0.075	+0.114	+0.183	+0.130
syst. error $\downarrow$	−0.005	−0.068	−0.116	−0.094	−0.108	−0.074
total error $\uparrow$	+0.009	+0.079	+0.112	+0.166	+0.212	+0.152
total error $\downarrow$	−0.009	−0.096	−0.143	−0.153	−0.151	−0.108

Table F.1: Cross sections, statistical and systematic errors as defined in Chap. 11 for M_X.

y	$[0.20; 0.33]$	$[0.33; 0.46]$	$[0.46; 0.59]$	$[0.59; 0.72]$	$[0.72; 0.85]$
$d\sigma/dy$ (nb)	16.3	49.3	75.8	91.1	84.3
stat. error	± 1.6	± 2.9	± 3.9	± 4.4	± 4.2
$z_{\text{vtx}} + 5\text{mm}$	$+0.4$	$+0.9$	$+2.2$	$+1.9$	$+3.1$
$z_{\text{vtx}} - 5\text{mm}$	$+0.0$	$+0.9$	$+1.9$	-0.5	$+1.4$
$E_{\text{zufo}} \uparrow$	$+0.5$	-1.9	-0.0	-0.9	$+0.4$
$E_{\text{zufo}} \downarrow$	$+0.4$	$+0.8$	-1.6	$+2.8$	$+1.5$
E_T corr.	-1.0	-0.9	$+1.2$	-2.8	$+1.0$
$E_\eta > 500\text{GeV}$	$+0.3$	$+0.4$	$+0.4$	-0.9	-0.0
$E_\eta > 300\text{GeV}$	$+0.5$	-0.5	-0.1	-0.7	$+1.0$
$\eta^{max} < 3.0$	$+0.2$	-1.1	-3.2	-2.8	-2.0
$\eta^{max} < 2.6$	$+0.0$	$+3.5$	$+2.0$	$+1.4$	$+3.1$
$y_{JB} < 0.78$	$+0.0$	-0.0	-0.0	-0.0	-9.6
syst. error $\uparrow$	$+1.0$	$+3.9$	$+3.8$	$+3.7$	$+5.1$
syst. error $\downarrow$	-1.0	-2.4	-3.6	-4.2	-9.8
total error $\uparrow$	$+1.9$	$+4.8$	$+5.4$	$+5.8$	$+6.6$
total error $\downarrow$	-1.9	-3.7	-5.3	-6.1	-10.7

Table F.2: Cross sections, statistical and systematic errors as defined in Chap. 11 for y.

x_γ^{obs}	$[0.250; 0.375]$	$[0.375; 0.500]$	$[0.500; 0.625]$	$[0.625; 0.750]$	$[0.750; 1.000]$
$d\sigma/dx_\gamma^{obs}$ (nb)	31.41	61.94	92.52	139.9	*n.a.*
stat. error	± 2.66	± 3.64	± 4.36	± 5.3	*n.a.*
$z_{\text{vtx}} + 5\text{mm}$	$+1.50$	$+0.79$	$+3.03$	$+3.6$	*n.a.*
$z_{\text{vtx}} - 5\text{mm}$	$+1.00$	-0.48	$+1.67$	$+1.9$	*n.a.*
$E_{\text{zufo}} \uparrow$	$+0.58$	-0.47	-2.25	-0.3	*n.a.*
$E_{\text{zufo}} \downarrow$	$+2.76$	$+1.32$	-0.21	$+0.4$	*n.a.*
E_T corr.	-0.31	-1.00	$+0.89$	-2.5	*n.a.*
$E_\eta > 500\text{GeV}$	-0.45	-0.14	$+0.90$	-0.0	*n.a.*
$E_\eta > 300\text{GeV}$	-0.09	$+0.68$	$+0.04$	-0.0	*n.a.*
$\eta^{max} < 3.0$	-0.83	-3.05	-1.88	-3.5	*n.a.*
$\eta^{max} < 2.6$	$+0.46$	$+2.16$	$+3.21$	$+4.8$	*n.a.*
$y_{JB} < 0.78$	$+1.13$	-2.60	$+0.29$	$+0.4$	*n.a.*
syst. error $\uparrow$	$+3.57$	$+2.74$	$+4.90$	$+6.3$	*n.a.*
syst. error $\downarrow$	-0.99	-4.19	-2.94	-4.3	*n.a.*
total error $\uparrow$	$+4.45$	$+4.56$	$+6.55$	$+8.3$	*n.a.*
total error $\downarrow$	-2.84	-5.55	-5.26	-6.8	*n.a.*

Table F.3: Cross sections, statistical and systematic errors as defined in Chap. 11 for x_γ^{obs}.

$x_{I\!P}$	$[0.000; 0.005]$	$[0.005; 0.010]$	$[0.010; 0.015]$	$[0.015; 0.020]$	$[0.020; 0.025]$
$d\sigma/dx_{I\!P}$ (pb)	0.000	0.558	1.613	2.539	3.625
stat. error	± 0.000	± 0.049	± 0.085	± 0.111	± 0.150
$z_{\text{vtx}} + 5\text{mm}$	0.000	$+0.019$	$+0.023$	$+0.094$	$+0.083$
$z_{\text{vtx}} - 5\text{mm}$	0.000	$+0.006$	$+0.003$	$+0.054$	$+0.037$
$E_{\text{zufo}} \uparrow$	0.000	-0.020	-0.036	-0.007	$+0.023$
$E_{\text{zufo}} \downarrow$	0.000	$+0.014$	-0.014	$+0.025$	$+0.101$
E_T corr.	0.000	-0.029	-0.022	$+0.042$	-0.085
$E_\eta > 500\text{GeV}$	0.000	$+0.003$	-0.019	$+0.027$	-0.001
$E_\eta > 300\text{GeV}$	0.000	$+0.002$	-0.007	$+0.019$	-0.008
$\eta^{max} < 3.0$	0.000	-0.003	-0.040	-0.037	-0.178
$\eta^{max} < 2.6$	0.000	$+0.006$	$+0.003$	$+0.094$	$+0.221$
$y_{JB} < 0.78$	0.000	-0.073	-0.031	$+0.053$	-0.006
syst. error $\uparrow$	$+0.000$	$+0.026$	$+0.024$	$+0.164$	$+0.261$
syst. error $\downarrow$	-0.000	-0.081	-0.071	-0.038	-0.197
total error $\uparrow$	$+0.000$	$+0.055$	$+0.088$	$+0.198$	$+0.301$
total error $\downarrow$	-0.000	-0.094	-0.110	-0.117	-0.248

Table F.4: Cross sections, statistical and systematic errors as defined in Chap. 11 for $x_{I\!P}$.

$z_{I\!P}^{obs}$	$[0.2; 0.4]$	$[0.4; 0.6]$	$[0.6; 0.8]$	$[0.8; 1.0]$
$d\sigma/dz_{I\!P}^{obs}$ (nb)	21.9	60.9	88.9	34.9
stat. error	± 2.4	± 3.6	± 3.8	± 1.3
$z_{\text{vtx}} + 5\text{mm}$	$+0.8$	$+1.6$	$+4.0$	$+0.3$
$z_{\text{vtx}} - 5\text{mm}$	$+0.2$	-0.0	$+2.9$	$+0.0$
$E_{\text{zufo}} \uparrow$	$+0.0$	-0.3	$+1.3$	-0.9
$E_{\text{zufo}} \downarrow$	$+1.4$	$+0.2$	$+0.4$	$+0.6$
E_T corr.	$+0.8$	-2.6	$+0.6$	-0.5
$E_\eta > 500\text{GeV}$	$+0.4$	$+0.2$	-0.2	$+0.0$
$E_\eta > 300\text{GeV}$	-0.5	$+1.2$	$+0.2$	-0.2
$\eta^{max} < 3.0$	-1.4	-4.5	-1.6	-0.2
$\eta^{max} < 2.6$	$+1.6$	$+2.4$	$+5.0$	$+0.2$
$y_{JB} < 0.78$	$+0.7$	$+1.4$	-0.5	-0.9
syst. error $\uparrow$	$+2.6$	$+3.4$	$+7.2$	$+0.8$
syst. error $\downarrow$	-1.5	-5.2	-1.7	-1.4
total error $\uparrow$	$+3.5$	$+5.0$	$+8.1$	$+1.5$
total error $\downarrow$	-2.8	-6.3	-4.1	-1.9

Table F.5: Cross sections, statistical and systematic errors as defined in Chap. 11 for $z_{I\!P}^{obs}$.

E_T^{jet1} (GeV)	$[7.5; 9.5]$	$[9.5; 11.5]$	$[11.5; 13.5]$	$[13.5; 15.5]$
$d\sigma/dE_T^{jet1}$ (nb/GeV)	15.67	4.04	0.82	0.07
stat. error	± 0.46	± 0.22	± 0.08	± 0.02
$z_{\text{vtx}} + 5\text{mm}$	$+0.47$	$+0.04$	$+0.04$	$+0.00$
$z_{\text{vtx}} - 5\text{mm}$	$+0.20$	$+0.03$	$+0.01$	$+0.01$
$E_{\text{zufo}} \uparrow$	-0.16	$+0.02$	-0.01	$+0.00$
$E_{\text{zufo}} \downarrow$	$+0.27$	-0.13	$+0.08$	$+0.01$
E_T corr.	-0.22	$+0.04$	$+0.02$	$+0.00$
$E_\eta > 500\text{GeV}$	$+0.05$	-0.03	$+0.01$	$+0.00$
$E_\eta > 300\text{GeV}$	$+0.05$	-0.03	$+0.00$	$+0.00$
$\eta^{max} < 3.0$	-0.62	-0.00	$+0.01$	$+0.00$
$\eta^{max} < 2.6$	$+0.54$	$+0.14$	$+0.01$	$+0.00$
$y_{JB} < 0.78$	$+0.05$	-0.14	-0.05	$+0.02$
syst. error $\uparrow$	$+0.79$	$+0.15$	$+0.09$	$+0.02$
syst. error $\downarrow$	-0.68	-0.20	-0.05	-0.00
total error $\uparrow$	$+0.92$	$+0.27$	$+0.13$	$+0.03$
total error $\downarrow$	-0.82	-0.30	-0.10	-0.02

Table F.6: Cross sections, statistical and systematic errors as defined in Chap. 11 for E_T^{jet1}.

E_T^{jet2} (GeV)	$[6.5; 8.5]$	$[8.5; 10.5]$	$[10.5; 12.5]$	$[12.5; 14.5]$
$d\sigma/dE_T^{jet2}$ (nb/GeV)	16.88	3.34	0.37	0.02
stat. error	± 0.46	± 0.22	± 0.07	± 0.01
$z_{\text{vtx}} + 5\text{mm}$	$+0.44$	$+0.08$	$+0.03$	$+0.00$
$z_{\text{vtx}} - 5\text{mm}$	$+0.16$	$+0.07$	$+0.03$	$+0.00$
$E_{\text{zufo}} \uparrow$	-0.12	-0.04	-0.00	$+0.00$
$E_{\text{zufo}} \downarrow$	$+0.26$	-0.08	$+0.08$	$+0.00$
E_T corr.	-0.37	$+0.00$	$+0.00$	$+0.00$
$E_\eta > 500\text{GeV}$	$+0.03$	-0.02	$+0.01$	$+0.00$
$E_\eta > 300\text{GeV}$	$+0.06$	-0.03	-0.01	$+0.00$
$\eta^{max} < 3.0$	-0.57	-0.00	-0.02	$+0.00$
$\eta^{max} < 2.6$	$+0.57$	$+0.10$	$+0.02$	$+0.00$
$y_{JB} < 0.78$	-0.09	-0.10	$+0.00$	-0.00
syst. error $\uparrow$	$+0.78$	$+0.15$	$+0.09$	$+0.00$
syst. error $\downarrow$	-0.70	-0.14	-0.02	-0.00
total error $\uparrow$	$+0.91$	$+0.27$	$+0.12$	$+0.01$
total error $\downarrow$	-0.83	-0.26	-0.07	-0.01

Table F.7: Cross sections, statistical and systematic errors as defined in Chap. 11 for E_T^{jet2}.

η^{jet1}	$[-1.5;-1.0]$	$[-1.0;-0.5]$	$[-0.5;0.0]$	$[0.0;0.5]$	$[0.5;1.0]$	$[1.0;1.5]$
$d\sigma/d\eta^{jet1}$ (nb)	2.12	14.60	25.04	24.81	13.32	3.32
stat. error	± 0.47	± 0.98	± 1.20	± 1.10	± 0.73	± 0.39
$z_{\text{vtx}} + 5\text{mm}$	-0.16	$+0.44$	$+0.59$	$+0.54$	$+0.51$	$+0.14$
$z_{\text{vtx}} - 5\text{mm}$	$+0.24$	-0.19	$+0.42$	$+0.29$	$+0.30$	-0.03
$E_{\text{zufo}} \uparrow$	-0.11	$+0.17$	-0.56	$+0.08$	-0.11	-0.05
$E_{\text{zufo}} \downarrow$	-0.51	$+0.27$	$+0.61$	-0.04	$+0.09$	$+0.47$
E_T corr.	$+0.13$	-0.27	$+0.35$	-0.76	-0.00	-0.07
$E_\eta > 500\text{GeV}$	$+0.07$	-0.00	$+0.08$	$+0.16$	-0.01	-0.16
$E_\eta > 300\text{GeV}$	$+0.01$	$+0.02$	-0.19	$+0.13$	$+0.06$	$+0.02$
$\eta^{max} < 3.0$	-0.12	-0.56	-1.11	-0.53	-0.11	-0.11
$\eta^{max} < 2.6$	-0.16	$+0.56$	$+0.82$	$+1.03$	$+0.29$	$+0.11$
$y_{JB} < 0.78$	-0.38	-0.21	-0.23	-0.47	$+0.22$	$+0.21$
syst. error $\uparrow$	$+0.28$	$+0.78$	$+1.30$	$+1.22$	$+0.70$	$+0.54$
syst. error $\downarrow$	-0.69	-0.69	-1.28	-1.04	-0.16	-0.21
total error $\uparrow$	$+0.55$	$+1.25$	$+1.77$	$+1.64$	$+1.02$	$+0.67$
total error $\downarrow$	-0.84	-1.19	-1.75	-1.51	-0.75	-0.44

Table F.8: Cross sections, statistical and systematic errors as defined in Chap. 11 for η^{jet1}.

η^{jet2}	$[-1.5;-1.0]$	$[-1.0;-0.5]$	$[-0.5;0.0]$	$[0.0;0.5]$	$[0.5;1.0]$	$[1.0;1.5]$
$d\sigma/d\eta^{jet2}$ (nb)	3.78	13.80	17.96	22.25	17.15	7.71
stat. error	± 0.55	± 0.88	± 0.94	± 1.05	± 0.91	± 0.67
$z_{\text{vtx}} + 5\text{mm}$	$+0.41$	$+0.62$	$+0.22$	$+0.70$	$+0.43$	-0.09
$z_{\text{vtx}} - 5\text{mm}$	$+0.18$	$+0.29$	$+0.29$	$+0.22$	$+0.14$	-0.09
$E_{\text{zufo}} \uparrow$	$+0.25$	-0.87	$+0.34$	-0.39	$+0.14$	$+0.07$
$E_{\text{zufo}} \downarrow$	$+0.10$	$+0.08$	$+0.10$	$+0.17$	$+0.55$	$+0.01$
E_T corr.	$+0.16$	-0.49	$+0.33$	-0.75	-0.22	$+0.44$
$E_\eta > 500\text{GeV}$	-0.02	-0.17	-0.08	$+0.16$	$+0.17$	$+0.01$
$E_\eta > 300\text{GeV}$	$+0.04$	$+0.05$	$+0.08$	$+0.03$	$+0.07$	-0.21
$\eta^{max} < 3.0$	-0.21	-0.28	-0.40	-0.71	-0.45	-0.28
$\eta^{max} < 2.6$	$+0.45$	-0.10	$+0.66$	$+1.24$	$+0.28$	$+0.26$
$y_{JB} < 0.78$	$+0.63$	-0.62	-0.18	-0.38	$+0.04$	-0.03
syst. error $\uparrow$	$+0.95$	$+0.69$	$+0.90$	$+1.46$	$+0.79$	$+0.51$
syst. error $\downarrow$	-0.22	-1.22	-0.44	-1.17	-0.50	-0.37
total error $\uparrow$	$+1.09$	$+1.12$	$+1.30$	$+1.80$	$+1.21$	$+0.84$
total error $\downarrow$	-0.59	-1.51	-1.04	-1.57	-1.03	-0.77

Table F.9: Cross sections, statistical and systematic errors as defined in Chap. 11 for η^{jet2}.

List of Figures

List of Tables

References

[1] Francesco Maria Grimaldi, *Physicomathesis de lumine, coloribus, et iride, aliisque annexis*, Vol. XIV. Vittorio Benati, Bologna, 1665.

[2] M. Arneodo and M. Diehl, hep-ph/0511047 (2005).

[3] V. Barone and E. Predazzi, *High-Energy Particle Diffraction*. Springer, 2002.

[4] ZEUS Collab, M. Derrick et al., Phys. Lett. **B 332**, 228 (1994).

[5] ZEUS Collab., M. Derrick et al., Phys. Lett. **B 315**, 481 (1993).

[6] G. Ingelman and P. Schlein, Phys. Lett. **B 152**, 256 (1985).

[7] J. C. Collins, hep-ph/9705393 (1997).

[8] P.D.B. Collins, *An Introduction to Regge Theory and High Energy Physics*. Cambridge University Press, 1977.

[9] A. Donnachie and P.V. Landshoff, Phys. Lett. **B 296**, 227 (1992).

[10] F.E. Low, Phys. Rev. **D 12**, 163 (1975).

[11] J.D. Bjorken and E.A. Paschos, Phys. Rev. **185**, 1975 (1969).

[12] M. Groys, DESY-thesis 2005-018 (2005).

[13] V.N. Gribov and L.N. Lipatov, Sov. J. Nucl. Phys. **15**, 438 (1972);
L.N. Lipatov, Sov. J. Nucl. Phys. **20**, 94 (1975);
Yu.L. Dokshitzer, Sov. Phys. JETP **46**, 641 (1977).

[14] G. Altarelli and G. Parisi, Nucl. Phys. **B 126**, 298 (1977).

[15] J.C. Collins, Phys. Rev. **D 57**, 3051 (1998);
J.C. Collins, Phys. Rev. **D 61**, 2000 (1998). Erratum;
J.C. Collins, J. Phys. **G 28**, 1069 (2002).

[16] A.B. Kaidalov, V.A. Khoze, A.D. Martin and M.G. Ryskin, Phys. Lett. **B 567**, 61 (2003).

[17] M. Klasen and G. Kramer, hep-ph/0401202 (2004).

[18] M. Glück, E. Reya and A. Vogt, Phys. Rev. **D 45**, 3986 (1992);
M. Glück, E. Reya and A. Vogt, Phys. Rev. **D 46**, 1973 (1992).

[19] CDF Collaboration, T. Affolder et al., Phys. Rev. Lett. **84**, 5043 (2000).

[20] A.B. Kaidalov, V.A. Khoze, A.D. Martin and M.G. Ryskin, Eur. Phys. J. **C 21**, 521 (2001).

[21] J.D. Bjorken, Int. J. Mod. Phys. **A 7**, 4189 (1992);
J.D. Bjorken, Phys. Rev. **D 47**, 101 (1993).

[22] R.P. Feynman, *Photon-Hadron Interactions*. W.A. Benjamin Inc., New York, 1972. Lectures 50-54.

[23] ZEUS Collab., S. Chekanov et al., Eur. Phys. J. **C 38**, 43 (2004).

[24] H1 Collab., C.Adloff et al., Z. Phys. **C 76**, 613 (1997).

[25] H1 Collab., C. Adloff et al., *Measurement and NLO DGLAP QCD Interpretation of Diffractive Deep-Inelastic Scattering at HERA*. Paper 089 submitted to the EPS 2003 Conf., Aachen, Germany, 2003.

[26] ZEUS Collab., S. Chekanov et al., Euro. Phys. J. **C 25**, 169 (2002).

[27] ZEUS Collab., J. Breitweg et al., Eur. Phys. J. **C 6**, 43 (1999);
ZEUS Collab., DESY-04-131 (2004);
ZEUS Collab., S. Chekanov et al., Nucl. Phys. **B 713**, 3 (2005).

[28] H1 Collab., A. Aktas et al., Subm. to Eur. Phys. J. **C** (2006). DESY-06-048.

[29] H1 Collab., A. Aktas et al., Subm. to Eur. Phys. J. **C** (2006). DESY-06-049.

[30] G. Watt (2006). Talk presented at the XIV Int. Workshop on Deep Inelastic Scattering (DIS06), Tsukuba, Japan.

[31] Brian Foster, ZEUS-note 00-42 (2000).

[32] W. Braunschweig et al., Phys. Lett. **B 57**, 407 (1975).

[33] MARK-J collaboration, D.P.Barber et al., Phys. Lett. **43**, 830 (1979).

[34] ZEUS Collab., U. Holm (ed.), *The ZEUS Detector*. Status Report (unpublished), DESY (1993), available on `http://www-zeus.desy.de/bluebook/bluebook.html`.

[35] N. Harnew et al., Nucl. Inst. Meth. **A 279**, 290 (1989);
ZEUS Collab., UK group, C.B. Brooks et al., Nucl. Inst. Meth. **A 283**, 477 (1989);
B. Foster et al., Nucl. Phys. Proc. Suppl. **B 32**, 181 (1993);
B. Foster et al., Nucl. Inst. Meth. **A 338**, 254 (1994).

[36] R. Hall-Wilton et al., *The CTD Tracking Resolution* (unpublished). ZEUS-99-024, internal ZEUS-note, 1999.

[37] B. Bock et al., Nucl. Inst. Meth. **A 344**, 335 (1994);
B. Gutjahr, PhD thesis, BONN-IR-93-17 (1993).

[38] B. Brendenbach et al., *Performance of and Experience with the Zeus Transition Radiation Detector*. To be subm. to Nucl. Inst. Meth. **A**, 2006.

[39] ZEUS Collab., *A Straw-Tube Tracker for ZEUS*, Proposal DESY PRC 98-08, DESY, 1998.

[40] M. Derrick et al., Nucl. Inst. Meth. **A 309**, 77 (1991);
A. Andresen et al., Nucl. Inst. Meth. **A 309**, 101 (1991);
A. Caldwell et al., Nucl. Inst. Meth. **A 321**, 356 (1992);
A. Bernstein et al., Nucl. Inst. Meth. **A 336**, 23 (1993);
A. Caldwell et al., *The Time Calibration of the ZEUS Calorimeter* (unpublished). ZEUS-93-021, internal ZEUS Note, 1993.

[41] ZEUS Collab., FPC group, A. Bamberger et al., Nucl. Inst. Meth. **A 450**, 235 (2000).

[42] J. Andruszków et al., Preprint DESY-92-066, DESY, 1992;
K. Olkiewicz and A. Eskreys, *Off-line Luminosity Calculation in the ZEUS Experiment in 1997, 1998 and 1999* (unpublished). ZEUS-99-44, 1999;
J. Andruszków et al., Acta Phys. Pol. **B 32**, 2025 (2001).

[43] H. Jung, Comp. Phys. Comm **86**, 147 (1995);
H. Jung. DESY Hamburg (2005), available on `http://www.desy.de/~jung/rapgap/`.

[44] H.L. Lai et al., Phys. Rev. **D 51**, 4763 (1995);
CTEQ Coll., G. Sterman et al., Rev. Mod. Phys. **67**, 157 (1995);
CTEQ Coll., H.L. Lai et al., Eur. Phys. J. **C 12**, 375 (2000).

[45] B.R. Webber, hep-ph/9411384 (1994);
M. Schmelling, Physics Scripta **51**, 683 (1995);
B.R. Webber, ECONF C **990809**, 577 (2000).

[46] B. Andersson et al., Phys. Rep. **97**, 31 (1983);
T. Sjöstrand, Comp. Phys. Comm. **39**, 347 (1986).

[47] B.E. Cox, J.R. Forshaw, Comp. Phys. Comm. **144**, 104 (2002).

[48] G. Corcella et al., Journal of High Energy Phys. **01**, 010 (2001);
G. Marchesini, B.R. Webber, G. Abbiendi, I.G. Knowles, M.H. Seymour and L. Stanco, *HERWIG version 5.9*, 1996;
Alexander Kupco, *Cluster Hadronization in HERWIG 5.9*, 1999.

[49] ZEUS Collab., J. Breitweg et al., Eur. Phys. J. **C 11**, 35 (1999).

[50] M. Martinez, ZEUS-note 00-016 (2000).

[51] N. Tuning, ZEUS-note 01-021 (2001).

[52] J. Grosse-Knetter, *Energy Correction for Islands* (unpublished). ZEUS-97-039, internal ZEUS Note, 1997.

[53] F. Jacquet and A. Blondel, *Proceedings of the Study for an ep facility for Europe*, p. 391. (1979).

[54] J. Grosse-Knetter, ZEUS-note 98-031 (1998).

[55] J.H. Vossebeld, *Dijet Photoproduction at High Transverse Energies* (unpublished). PhD Thesis, 1999;
M. Wing. Annecy, France (2000). Proceedings of the IX Int. Conf. on Calorimetry in Part. Phys.

[56] A.H. Ochs. PhD Thesis, 2001.

[57] M. Wing, hep-ex/0206036 (2002).

[58] M. Corradi, M. Turcato, ZEUS-note 2004-005 (2004).

[59] M. Turcato, DESY-thesis 2003-039 (2003).

[60] T. Sjöstrand, PYTHIA 5.7 *and* JETSET 7.4 *Physics and Manual*, 1993. CERN-TH 7112/93;
T. Sjöstrand et al., Comp. Phys. Comm. **135**, 238 (2001).

[61] M.H. Seymour, hep-ph/9506421 (1995).

[62] M.H. Seymour, Nucl. Phys. **B 513**, 269 (1998).

[63] J.E. Huth et al., *Research Directions for the Decade. Proceedings of Summer Study on High Energy Physics, 1990*, E.L. Berger (ed.), p. 134. World Scientific (1992). Also in preprint FERMILAB-CONF-90-249-E.

[64] S.D. Ellis, Z. Kunszt and D.E. Soper, Phys. Rev. Lett. **69**, 3615 (1992).

[65] S. Catani, Yu.L. Dokshitzer, M.H. Seymour and B.R. Webber, Nucl. Phys. **B 406**, 187 (1993).

[66] Y. Yamazaki, private communication, 2006.

[67] S. Kagawa, KEK-report 2005-12 (2005).

[68] M. Kasprzak, ZEUS-note 95-069 (1995).

[69] L. Adamczyk, *NLO predictions for diffractive jets production in PHP*, 2005. Presentation at group meeting.

[70] ZEUS Collab., S. Chekanov et al., Phys. Lett. **B 539**, 197 (2002). Erratum in Phys. Lett. **B 552**, 308 (2003).